ABSTRACT

Title of Document:	THE PLENOPTIC SENSOR
	Chensheng Wu, Doctorate, 2016
Directed By:	Professor Christopher C. Davis, ECE Department, UMCP

In this thesis, we will introduce the innovative concept of a plenoptic sensor that can determine the phase and amplitude distortion in a coherent beam, for example a laser beam that has propagated through the turbulent atmosphere.. The plenoptic sensor can be applied to situations involving strong or deep atmospheric turbulence. This can improve free space optical communications by maintaining optical links more intelligently and efficiently. Also, in directed energy applications, the plenoptic sensor and its fast reconstruction algorithm can give instantaneous instructions to an adaptive optics (AO) system to create intelligent corrections in directing a beam through atmospheric turbulence. The hardware structure of the plenoptic sensor uses an objective lens and a microlens array (MLA) to form a mini “Keplerian” telescope array that shares the common objective lens. In principle, the objective lens helps to detect the phase gradient of the distorted laser beam and the microlens array (MLA) helps to retrieve the geometry of the distorted beam in various gradient segments. The software layer of the plenoptic sensor is developed based on different applications.

Intuitively, since the device maximizes the observation of the light field in front of the sensor, different algorithms can be developed, such as detecting the atmospheric turbulence effects as well as retrieving undistorted images of distant objects. Efficient 3D simulations on atmospheric turbulence based on geometric optics have been established to help us perform optimization on system design and verify the correctness of our algorithms. A number of experimental platforms have been built to implement the plenoptic sensor in various application concepts and show its improvements when compared with traditional wavefront sensors. As a result, the plenoptic sensor brings a revolution to the study of atmospheric turbulence and generates new approaches to handle turbulence effect better.

THE PLENOPTIC SENSOR

by

Chensheng Wu

Dissertation submitted to the Faculty of the Graduate School of the
University of Maryland, College Park, in partial fulfillment
of the requirements for the degree of
Doctor of Philosophy
2016

Advisory Committee:
Professor Christopher C. Davis, Chair
Professor Thomas E. Murphy
Professor Phillip Sprangle
Professor Jeremy Munday
Professor Douglas Currie

Dedication

To my wife Cuiyin Wu, mother Lijun Lin and father Peilin Wu, for fueling my journey to truth with power, love and passion.

Acknowledgements

This thesis is motivated by Dr. Davis's idea to investigate atmospheric turbulence effects from their effect on a full light field (plenoptic field). Starting in 2012, in a relatively short period of time (3 years), we have opened a new chapter in wavefront sensing and treatment of atmospheric turbulence effects. We have developed a device: the plenoptic sensor, which has surpassed the capacity for extracting optical information of a conventional wavefront sensor.

I also want to thank the Joint Technology Office (JTO) through the Office of Naval Research (ONR) for continuous funding of our research. Without this help, we wouldn't be able to afford the "luxury" costs in experiments.

I must thank all my colleagues that I have been working with in the Maryland Optics Group (MOG), including Mohammed Eslami, John Rzasa, Jonathan Ko, William Nelson, and Tommy Shen.

I must also acknowledge Dr. Larry Andrews and Ronald Phillips in University of Central Florida (UCF) for their generous help and fruitful discussions.

Table of Contents

List of Publications

2016:

1. Chensheng Wu, Jonathan Ko, and Christopher C. Davis, "Using a plenoptic sensor to reconstruct vortex phase structures," Opt. Lett. 41, 3169-3172 (2016).
2. Chensheng Wu, Jonathan Ko, and Christopher C. Davis, "Imaging through strong turbulence with a light field approach," Opt. Express 24, 11975-11986 (2016).
3. W. Nelson, J. P. Palastro, C. Wu, and C. C. Davis, "Using an incoherent target return to adaptively focus through atmospheric turbulence," Opt. Lett.41, 1301-1304 (2016).

2015:

4. Wu, Chensheng, Jonathan Ko, and Christopher Davis. “Determining the phase and amplitude distortion of a wavefront using a plenoptic sensor”. JOSA A.
5. Wu, Chensheng, Jonathan Ko, and Christopher Davis. "Object recognition through turbulence with a modified plenoptic camera." In *SPIE LASE*, pp. 93540V-93540V. International Society for Optics and Photonics, 2015.
6. Wu, Chensheng, Jonathan Ko, and Christopher C. Davis. "Imaging through turbulence using a plenoptic sensor." In *SPIE Optical Engineering+ Applications*, pp. 961405-961405. International Society for Optics and Photonics, 2015.
7. Wu, Chensheng, Jonathan Ko, and Christopher C. Davis. "Entropy studies on beam distortion by atmospheric turbulence." In *SPIE Optical Engineering+ Applications*, pp. 96140F-96140F. International Society for Optics and Photonics, 2015.

8. Nelson, W., C. Wu, and C. C. Davis. "Determining beam properties at an inaccessible plane using the reciprocity of atmospheric turbulence." In *SPIE Optical Engineering+ Applications*, pp. 96140E-96140E. International Society for Optics and Photonics, 2015.
9. Ko, Jonathan, Chensheng Wu, and Christopher C. Davis. "An adaptive optics approach for laser beam correction in turbulence utilizing a modified plenoptic camera." In *SPIE Optical Engineering+ Applications*, pp. 96140I-96140I. International Society for Optics and Photonics, 2015.
10. Nelson, W., J. P. Palastro, C. Wu, and C. C. Davis. "Enhanced backscatter of optical beams reflected in turbulent air." *JOSA A* 32, no. 7 (2015): 1371-1378.

2014:

11. Wu, Chensheng, William Nelson, and Christopher C. Davis. "3D geometric modeling and simulation of laser propagation through turbulence with plenoptic functions." In *SPIE Optical Engineering+ Applications*, pp. 92240O-92240O. International Society for Optics and Photonics, 2014.
12. Wu, Chensheng, William Nelson, Jonathan Ko, and Christopher C. Davis. "Experimental results on the enhanced backscatter phenomenon and its dynamics." In *SPIE Optical Engineering+ Applications*, pp. 922412-922412. International Society for Optics and Photonics, 2014.
13. Wu, Chensheng, Jonathan Ko, William Nelson, and Christopher C. Davis. "Phase and amplitude wave front sensing and reconstruction with a modified plenoptic camera." In *SPIE Optical Engineering+ Applications*, pp. 92240G-92240G. International Society for Optics and Photonics, 2014.

14. Nelson, W., J. P. Palastro, C. Wu, and C. C. Davis. "Enhanced backscatter of optical beams reflected in atmospheric turbulence." In *SPIE Optical Engineering+ Applications*, pp. 922411-922411. International Society for Optics and Photonics, 2014.

15. Ko, Jonathan, Chensheng Wu, and Christopher C. Davis. "Intelligent correction of laser beam propagation through turbulent media using adaptive optics." In*SPIE Optical Engineering+ Applications*, pp. 92240E-92240E. International Society for Optics and Photonics, 2014.

2013:

16. Wu, Chensheng, and Christopher C. Davis. "Modified plenoptic camera for phase and amplitude wavefront sensing." In *SPIE Optical Engineering+ Applications*, pp. 88740I-88740I. International Society for Optics and Photonics, 2013.

17. Wu, Chensheng, and Christopher C. Davis. "Geometrical optics analysis of atmospheric turbulence." In *SPIE Optical Engineering+ Applications*, pp. 88740V-88740V. International Society for Optics and Photonics, 2013.

2012:

18. Eslami, Mohammed, Chensheng Wu, John Rzasa, and Christopher C. Davis. "Using a plenoptic camera to measure distortions in wavefronts affected by atmospheric turbulence." In *SPIE Optical Engineering+ Applications*, pp. 85170S-85170S. International Society for Optics and Photonics, 2012.

List of Tables

List of Figures

List of Abbreviations

AO --- Adaptive Optics

CS --- Curvature Sensor

DM --- Deformable Mirror

DE --- Directed Energy

EBS --- Enhanced Back Scatter

FSO --- Free Space Optics

SH --- Shack-Hartmann

Impacts of this Thesis

Atmospheric turbulence effects have been studied for more than 50 years (1959-present). Solving turbulence problems provides tremendous benefits in fields such as: remote sensing (RS), free space optical (FSO) communication, and directed energy (DE). A great number of studies on turbulence modeling and simulations have been published over the past few decades. Unfortunately, 2 fundamental questions remain unsolved: (1) Every model can tell how things get WORSE, but how do we know which one is correct? (2) How to get things RIGHT (solve turbulence problems)? The answers to these 2 fundamental questions seem surprisingly EASY, but rely on one difficult assumption: the complete knowledge of beam distortion must be known, including the phase and amplitude distortion. Intuitively, given the complex amplitude of the distorted beam, the best model to characterize a turbulent channel can be determined. Similarly, correction algorithms can also be figured out easily. For example, for FSO communications, the phase discrepancy at the receiver can be rectified. For DE applications, one can transmit a conjugated beam to an artificial glint signal on the target site, so that the power of a beam can be best focused near that spot.

The plenoptic sensor is designed as an advanced wavefront sensor. Compared with conventional wavefront sensors, the turbulence regime is extended from weak turbulence distortions to medium, strong and even deep turbulence distortions. In other words, the plenoptic sensor is much more powerful than any conventional wavefront sensor in recording and reconstructing wavefronts of incident beams. With the actual waveform data, the correctness of past atmospheric turbulence models will

be comprehensively examined in addition to indirect statistical data on scintillation and beam wanders. Intelligent and immediate correction become realizable based on the actual waveforms. Therefore, this innovation will greatly reform thoughts, methods and strategies in the field of turbulence studies. Furthermore, it makes the dream of overcoming turbulence effects real and practical.

Chapter 1: Fundamentals of Atmospheric Turbulence

1.1 Fundamental Effects of Atmospheric turbulence

Atmospheric turbulence is generally referred to as the fluctuations in the local density of air. These density fluctuations causes small, random variations in the refractive index of air ranging from 10^{-6} to 10^{-4} [1]. These "trivial" disturbances on light ray trajectories generate a number of significant effects for remote imaging and beam propagation. In general, light rays will deviate from their expected trajectories and their spatial coherence will degrade. Over long propagation distances, the accuracy of delivering signal/energy carried by the wave deteriorates with increased turbulence level and propagation distance. As a result, this limits the effective ranges for RS, FSO and DE applications.

1.1.1 Distortion of coherent beams

When a laser beam propagates through atmospheric turbulence, the inhomogeneity of the air channel's refractive index accumulatively disturbs the phase and amplitude distribution of the beam. The outcomes include:

(1) Fluctuations of signal intensity at the receiver around expected values, known as "scintillation" [2].

(2) The centroid of the beam wanders randomly (referred to as "beam wander") [3].

(3) The beam breaks up into a number of patches (small wavelets that act like plane waves), which is referred to as "beam break-up" [4].

These effects are detrimental to the reliability of free space optical (FSO) communication systems as well as directed energy applications. For example, in FSO systems, beam wander and scintillation effects will degrade the channel capacity by jeopardizing the alignment and disturbing signal quality. In directed energy applications, beam break-up will scatter the energy propagation into diverged and random directions. The beam break-up effect is primarily caused by the reduced spatial coherence of the beam, which can be characterized by the "Fried Parameter" [5]. The spatial coherence length of a laser beam r_0 decays roughly with $L^{-3/5}$:

$$r_0 = \left[0.423k^2 \int_{path} C_n^2(z')dz' \right]^{-3/5} \quad (1)$$

In equation (1), $k=2\pi/\lambda$ is the wavenumber. C_n^2 denotes the strength of atmospheric turbulence [6]. Without employing adaptive optics [7], the Fried parameter r_0 dictates the fundamental limit of spatial coherence of a propagating laser beam. Therefore, it is not difficult to find that a stronger turbulence level or longer propagation distance will cause more distortions of a laser beam.

1.1.2 Distortion of incoherent beams

In normal cases, light sources are incoherent, such as lamps and LEDs (active illumination) and sunlight (passive illumination). Atmospheric turbulence won't cause phase disorder problems for incoherent light sources. However, the degradation of clear and accurate visions of objects will lead to blurring effects and recognition failures. For example, in remote photography, we often find it hard to get a focused image. One can also find distant objects along the road might be shimmering and moving around on a hot summer day. Without loss of generality, the turbulence

effects for incoherent light sources can be analyzed in the same manner as coherent sources. Therefore, we focus our discussions of turbulence primarily on coherent waves. And for some special cases such as imaging through turbulence, we will provide a detailed discussion about turbulence effects on incoherent waves.

1.2 Scintillation

Scintillation is commonly observed as the "twinkling" effect of a star. In a wide sense, scintillation describes the time varying photon flows collected by a fixed optic aperture. Scintillation is often a good indicator for the magnitude of atmospheric turbulence. Intuitively, based on perturbation theory (Rytov method [8]), a larger scintillation value implies that there are more rapid changes in the channel and a smaller scintillation value means the turbulence conditions in a channel are typically weaker and change more slowly.

1.2.1 Causes of scintillation

Due to the fluid nature of air, the turbulence has an inertial range marked by the inner scale (l_0, typical value is 1 mm near the ground) and the outer scale (L_0, typical value is 1 m near the ground). Most turbulence cell structures fall within the inertial range, and inside these temporally stable structures, the refractive index of air can be regarded as uniform. Structures with diameters close to the outer scale of turbulence primarily generate refractive changes on the beam, including diverting the propagation direction of the beam, applying additional converging/diverging effects as well as imposing irregular aberrations on the shape of the beam. Turbulence structures with diameters close to the inner scale often cause diffractive phenomena,

which impose high spatial frequencies terms onto the wavefront. Diffraction effects resulting from these high frequency orders divert part of the beam's energy away from the expected trajectory in further propagation.

The power spectrum of scintillation is largely focused in the frequency range of 10Hz to 100Hz. Low frequency (around 10Hz) scintillation is primarily affected by the refractive behavior of atmospheric turbulence. Higher frequency (around 100Hz) scintillation is primarily affected by the diffractive behavior of atmospheric turbulence. If the beam is sampled at a much higher frequency (for example, 10kHz), neighboring sample points don't show significant variations. This is often called Taylor's hypothesis, where turbulence is regarded as stationary or "frozen" for time scales less than 1ms.

1.2.2 Scintillation analysis

To analytically examine the scintillation effects, a common practice is to calculate the normalized intensity variance collected through a lense's aperture. As:

$$\sigma_I^2 = \frac{\langle I^2 \rangle - \langle I \rangle^2}{\langle I \rangle^2} \tag{2}$$

Intuitively, equation (2) denotes the proportional variation of received power and it helps to classify turbulence levels into 3 major regimes. In the weak turbulence regime (where σ_I^2 <0.3 [8]), equation (2) equals the Rytov variance. In strong turbulence regime (where σ_I^2 >1), the power of the noise signal in the channel is at least the same magnitude as the signal in transmission. And the intermediate level

($0.3<\sigma_I^2<1$), is often called medium turbulence. Weak turbulence is typical for astronomical imaging applications and can be corrected with conventional adaptive optics system or imaging processing algorithms. Medium turbulence is common in horizontal paths for FSO communication applications, where digital signal of on/off can still be reliably sent through the channel. Strong turbulence represents the worst case in turbulence, where there are severe distortions of phase and amplitude distortions on a propagating laser beam. Performing imaging and communication tasks in strong turbulence situations are challenging topics in the field of adaptive optics, and many unique techniques have been developed over the past decade to ameliorate the situation [9] [10] [11].

1.2.3 Scintillation measurement

The commercial device for measuring scintillation is called a scintillometer [12]. In principle, a scintillometer pair (transmitter/receiver) transmits a known signal pattern to the receiver to mimic free space optics (FSO) communication. By detecting the distortion of the received signal, the scintillation index can be calculated either by equation (2), or by calculating the variance of log normal amplitude of intensity. For example, if the transmitter can generate a square wave over time (on/off over time), the receiver is expected to receive the same signal sequence with amplitude modifications. The scintillation amplitude can be determined by comparing the received waveform with the transmitted waveform [13], which profiles the strength of the turbulent channel. An alternative index for scintillation is the refractive index structure constant, C_n^2 (unit: $m^{-2/3}$). The "density" of atmospheric turbulence is determined by the C_n^2 values as the coefficient in the power spectrum density

functions. In practice, it is meaningful to combine C_n^2 measurements with channel length *L* to reflect the actual turbulence effects. Intuitively, the same scintillation effect can either result from strong turbulence level over a short propagation distance or from weak turbulence level over a long propagation distance. In addition, to match with the units of C_n^2, one should note that the correlation of refractive index changes or degrades with $r^{2/3}$ (unit: $m^{2/3}$), often referred as the "2/3" law [14].

1.3 Beam Wander

The centroid of the beam also wanders in propagating though the atmospheric turbulence. Intuitively, the inhomogeneity can be viewed as a wedge effect, which randomly refracts the beam off its propagation axis. A typical example is that one can observe a traffic light shimmering on a hot summer day. This is caused by the vision signals getting distorted by large volumes of turbulent hot air before entering our eyes. Beam wander effect often causes alignment failure in FSO and directed energy applications where the main beam is deviated from the target area.

1.3.1 Causes of beam wander

Beam wander is caused by inhomogeneity in the refractive index of air. Due to Taylor's hypothesis, turbulence is "frozen" when analyzed at high frequencies (more than 1 kHz). The gradient of the refractive index along the transverse plane causes a weak tip/tilt effect on the propagating beam's wavefront profile. The viscidity of air fluid tends to keep similar changes (gradient value) within an inertial range. Therefore, in each small segment of the propagation channel, the primary turbulence effect will tilt the beam with a small angular momentum mimicking the effect of a

random walk. In the long run, the overall beam wander is an aggregated effect of those small random walks.

1.3.2 Beam wander analysis

As the beam wander effect can be effectively modelled as a random walk process [15], it can be treated as a subset of the random walk problem. A good approximation can be expressed as:

$$\left\langle \rho_L^2 \right\rangle = 2.2 C_n^2 l_0^{-1/3} L^3 \tag{3}$$

In equation (3), the LHS represents the RMS value of wandering centroid of the beam. On the RHS, C_n^2 is the index for the strength of turbulence. The inner scale of turbulence is expressed by l_0 and the propagation distance is represented by L. The inertial range of turbulence structures often refers to the range between the inner and outer scales.

1.3.3 Beam wander measurement

Beam wander can be determined by many approaches [16] [17]. Normally, the essential problem is to determine the probability that the beam wander effect will significantly deviate the entire beam from the target aperture [18] (this often causes failures in signal transmission). Therefore, a larger receiving aperture tends to get less affected by the beam wander effect, where the probability of alignment failure drops exponentially with increased aperture sizes (also called aperture averaging effects) [19]. Normally, increasing the aperture size will effectively suppress scintillation and beam wander problems in FSO communication systems.

1.4 Beam Break Up

Beam break up happens as a result of propagation through long turbulent channels (typically for distances over 1 km). The deteriorating spatial coherence of the beam varies from point to point across the beam's transverse profile. For the areas where the beam passes without significant change of coherence, the phase front remains coherent as a patch (a small wavelet that acts like plane waves). Comparatively, for the regions where its coherence breaks down dramatically (temporal spatial coherence length is close to the inner scale of turbulence structure), the beam splits into two or more irregular intensity patterns. As an overall phenomenon, the original coherent beam breaks up into several major patches of different sizes. This result is commonly referred to as beam break-up [20].

1.4.1 Causes of beam break up

Beam break-up is caused by the structural fluctuations in the refractive index of an atmospheric channel. The coherence of the wavefront degenerates fastest at the boundaries of the turbulence structures, while wavefront coherence is maintained within a structure. The deterioration of average coherence length in the wavefront can be estimated by equation (1) as the Fried parameter. Since most of the coherence is still maintained in the patches, the Fried parameter also describes the average size of the coherent sub-wavelets after the beam break-up. In general, the beam break up generates a group of sub-beams that can be treated as coherent wavelets. In other words, the beam breaks down into smaller wavelets, and the geometric wandering of each wavelet makes respective contribution to the final intensity pattern of the arriving beam on the target site. Under these circumstances, the centroid of the beam

doesn't wander much (due to WLLN), but the spatial fluctuations of the beam's intensity distribution is significant.

1.4.2 Beam breakup analysis

Some theoretical analysis predicts that beam breakup only happens at $L>kL_0^2$ [21]. This is obviously incorrect as it doesn't takes into account the turbulence strength. However, if the transmitted beam has spot size of w_0, the beam diameter and range L are related as:

$$2w = \frac{\lambda L}{\pi w_0} + 2w_0 \tag{4}$$

In the diffraction limit, *w* denotes the projected width of the beam without being affected by turbulence. The actual size of a patch can be denoted as S_i, where *i* represents index for the patch at the moment. The following expression serves as a metric for measuring the beam break-up strength:

$$R_b \triangleq \frac{w}{\max\{D_i\}} \tag{5}$$

Equation (5) describes the relation between the projected beam width and the largest patch after the propagation. Intuitively, R_b is a temporal index that describes the lower bound of the beam break up effect. When $R_b \rightarrow \infty$, it means there is no coherence in the beam. On the other hand, if R_b=2, it means that there are at most 4 ($\sim R_b^2$) equal powered dominant patches in the channel that contain major parts of the power of the beam. When R_b^2 is relatively low (<25), it is possible to use adaptive optics to correct the beam to generate a large patch that retains the major power of the beam.

1.4.3 Beam break up measurement

It is technically difficult to study the beam breakup effect by directly make measurements based on equation (5). However, Fourier transforms performed by a thin lens are a convenient tool to reveal the beam breakup effects. Normally, when the arriving beam (distorted by atmospheric turbulence) enters a thin lens with large aperture, each bright spot at the back focal plane of the lens represents a unique patch. Therefore, by counting the bright spot numbers we can retrieve a relatively reliable R_b^2 number, and determine the situation of beam breakup accordingly.

1.5 Theoretical Explanations

Andrews and Phillips [21] have developed a fundamental optical flowchart to theoretically explain atmospheric turbulence effects. In general, the simplest way is to express the complex amplitude of an optical field as U(r, L), where *r* represents the geometric vector in the transverse plane and *L* represents distance in propagation. Therefore, the statistical properties can be described by the following chart:

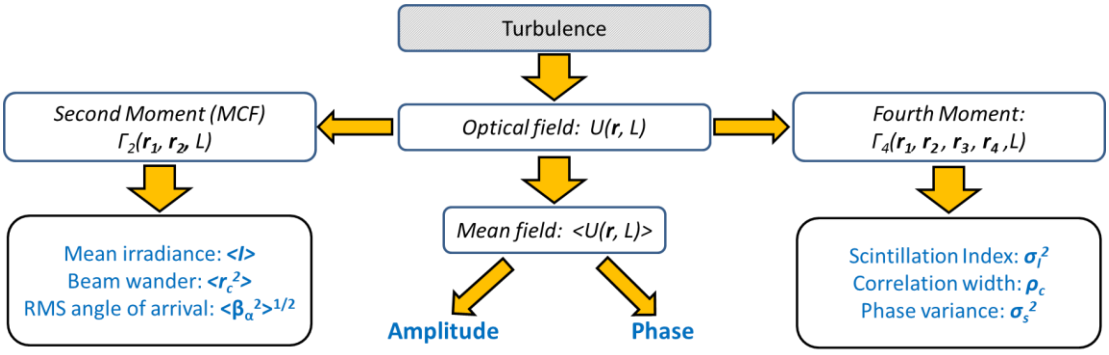

Figure 1. 1: Flow chart of turbulence's primary effects

In the flow chart of figure 1.1, the polarization direction of the laser beam is ignored for simplicity and the light field is given by a complex amplitude *U(r, L)* to represent its magnitude and phase. For polarized beams, it is possible to integrate the analytic methods with unit vectors in the polarization directions.

1.5.1 Second-order statistics

Second order statistical parameters have the same units as irradiance. Intuitively, this means these statistics can be used to indicate a patch's quality, such as the spot size, degree of coherence, spreading angle and wandering range. Without loss of generality, we express a second order statistic as:

$$\Gamma_2(r_1, r_2, L) \triangleq \left\langle U(r_1, L) U^*(r_2, L) \right\rangle \tag{6}$$

Equation (6) describes the field correlation based on the complex amplitude. When equalizing the space vector $\boldsymbol{r_1}$ and $\boldsymbol{r_2}$, the irradiance information is revealed. Accurate analysis of weak turbulence effects is achieved by phase screen models (also known as the Rytov method) [22]. In general, the complex amplitude of the beam affected by turbulence is expressed as:

$$U(r, L) = U_0(r, L) \exp\left[\psi_1(r, L) + \psi_2(r, L) + ...\right] \tag{7}$$

In equation (7), $U_0(\boldsymbol{r}, L)$ is the free space beam at the receiver site, and $\psi(\boldsymbol{r}, L)$ is the complex phase perturbation of the field. In general, the free space beam (U_0) takes any form of beam modes (Gaussian beam, plane wave, spherical and etc.). The real part of ψ denotes the change in the magnitude of the field and the imaginary part controls the phase change of the beam. Theoretically, the Rytov method equalizes the turbulence effect with a phase screen before the receiver. Therefore, the statistics of

atmospheric turbulence is simplified from 3D to 2D. The proof of the simplification can be partially verified by the practice of using adaptive optics (AO) systems in astronomy to correct for the atmospheric turbulence of celestial images [23].

A simple and significant conclusion drawn from second order statistics is expressed as:

$$\Gamma_2(\rho, L) = \exp\left[-\left(\frac{\rho}{\rho_{pl}}\right)^{5/3}\right] \tag{8}$$

Where ρ_{pl} is the reference coherence length defined by the turbulence level, in the case of plane wave and no inertial range, as:

$$\rho_{pl} = (1.46 C_n^2 k^2 L)^{-3/5} \tag{9}$$

The power index for coherence length degeneration is commonly regarded as the Kolmogorov law [24] which sets the base line that all theoretical models for atmospheric turbulence should satisfy.

The second order statistics can also be used to estimate the beam width [25], beam wander [26], and angle of arrival fluctuations [27]. However, in most experiments the strength of the turbulence (C_n^2) can't be consistently obtained by differing approaches and measurements.

1.5.2 Fourth-order statistics

The fourth order statistics have the same units as irradiance squared, which equals the variance of irradiance. Intuitively, it can be used to indicate the variation of photon power in an area as well as the coherence between multiple patches. Without loss of generality, the expression for the fourth order statistic is:

$$\Gamma_4(r_1, r_2, r_3, r_4, L) = \langle U(r_1, L) U^*(r_2, L) U(r_3, L) U^*(r_4, L) \rangle \tag{10}$$

And in the form of the Rytov method, equation (10) can be written as:

$$\begin{aligned} \Gamma_4(r_1, r_2, r_3, r_4, L) = {} & U_0(r_1, L) U_0^*(r_2, L) U_0(r_3, L) U_0^*(r_4, L) \\ & \times \left\langle \exp\left[\psi(r_1, L) + \psi^*(r_2, L) + \psi(r_3, L) + \psi^*(r_4, L) \right] \right\rangle \end{aligned} \tag{11}$$

Despite the complexity view of this equation, a common practice in the fourth order statistics studies is to equate $\boldsymbol{r_1 = r_2}$, and $\boldsymbol{r_3 = r_4}$. Therefore, the fourth order statistics can be similarly treated as the second order statistics based on irradiance distributions. The fourth order reveals certain properties such as scintillation [28] and phase structure [29].

1.5.3 Spectral density functions

Spectral density functions are used to mathematically determine the correlation structure of atmospheric turbulence in terms of refractive index fluctuations. For weak turbulence situations, phase screen models as well as Rytov methods have used those spectral density spectra to produce results that resemble actual turbulence situations. However, since the power spectral density function outlines the long term averaged variation values of atmospheric turbulence at steady strength levels, there is no actual match with turbulence happening in reality. In general, the power spectral functions can be classified in 2 ways: power spectrum function in the frequency domain and power spectrum function in the spatial domain.

In the frequency domain, the spectrum property of a random process *x(t)* is described by the covariance function:

$$B_x(\tau) = \langle x(t)\, x^*(t+\tau) \rangle - \langle x(t) \rangle \cdot \langle x(t) \rangle^* \tag{12}$$

And the power spectral density $S_x(\omega)$ can be retrieved through the Weiner-Khintchine relations:

$$S_x(\omega) = \frac{1}{\pi} \int_0^\infty B_x(\tau) \cos(\omega\tau)\, d\tau \tag{13}$$

$$B_x(\tau) = 2 \int_0^\infty S_x(\omega) \cos(\omega\tau)\, d\omega \tag{14}$$

Simply, the power spectral density and the covariance function are Fourier transforms of each other. Similarly, in the spatial domain, we have the relations:

$$\Phi_u(\kappa) = \frac{1}{2\pi^2 \kappa} \int_0^\infty B_u(R) \sin(\kappa R)\, R dR \tag{15}$$

$$B_u(R) = \frac{4\pi}{R} \int_0^\infty \Phi_u(\kappa) \sin(\kappa R)\, \kappa d\kappa \tag{16}$$

In equation (15) and (16), the spatial power spectral density function is represented by $\Phi_u(\kappa)$ and the spatial covariance function is represented by $B_u(R)$. For simplicity, spherical symmetry is assumed in expressing the above equations.

Therefore, the frequency spectral density function indicates how fast the turbulence situation changes and the spatial spectral density function indicates the turbulence structure. For example, if the coherence length is extremely small for the turbulent channel (~1mm), we would expect a very sharp peaked covariance function and a relatively smooth and long-tail power spectral density function. In this circumstance, we would expect the beam to degenerate to a rather incoherent light field and fully developed speckles should be the dominant pattern at the receiver site.

1.6 Challenges for Mathematical Analysis

The mathematical analysis of turbulence structure, however delicate and accurate, can't provide a solution to overcome turbulence problems in reality. For example, in directed energy research, to achieve more power (improve energy delivery efficiency) in the target spot, the actual temporal structure of atmospheric turbulence is needed instead of the theoretical statistical mean values. In FSO communication systems, more signal power can be coupled into the receiver with AO if the temporal dispersion modes are detected. In the remote imaging process, the turbulence effect is embedded in the spatially dependent point spread functions, and intelligent deconvolution can happen if and only if the temporal 4D point spread function are known [30]. Obviously, great improvement can be achieved if the detailed structure of actual turbulence can be determined. And, accordingly, a more thorough and kinetic 3D model of atmospheric turbulence can be built. The following limits on the theoretical studies of atmospheric turbulence should be mentioned.

1.6.1 Model restrictions

Theoretical models don't track the dynamic changes in the turbulence structure. In other words, no model can predict the temporal and spatial result of how the atmospheric turbulence will distort the wavefront and intensity distribution of the beam. Another restriction is the inaccessibility of the models' input. For example, the turbulence level denoted by C_n^2 must be given in order to facilitate the calculation of turbulence effects. But C_n^2 itself is also a factor dependent on the consequence of the turbulence. In other words, it is logically wrong to require C_n^2 first and then

determine the turbulence effect later. Given that turbulence levels are not stationary (even in a time window of a few seconds), theoretical analysis models are more like empirical fitting curves instead of indicators for real time turbulence.

1.6.2 Computation difficulties

Basically, all the working models of turbulence simulations are based on 2D phase screen models. The phase screen models are established based on the Rytov method, where the beam goes through a 2-step process in a segmented propagation distance: free propagation (step 1) and phase screen modification (step 2). These simulation models do provide a seemingly correct result for temporal turbulence effects that satisfy the models' parameters. In the transverse planes that are perpendicular to the propagation axis, the correlation statistics of atmospheric turbulence are still observed. While along the propagation axis, neighboring phase screens are independent. More complex 3D simulation models have been proposed [31] [32], but have proven to be not computational tractable. In other words, the actual turbulence changes occur much faster than the speed of achievable simulation. It is also pointless to feed the simulation with real time data and make predictions of the subsequent behavior of turbulence.

References:

[1] Lawrence, Robert S., and John W. Strohbehn. "A survey of clear-air propagation effects relevant to optical communications." *Proceedings of the IEEE* 58, no. 10 (1970): 1523-1545.

[2] Fried, Do L., G. E. Mevers, and JR KEISTER. "Measurements of laser-beam scintillation in the atmosphere." *JOSA* 57, no. 6 (1967): 787-797.

[3] Andrews, Larry C., Ronald L. Phillips, Richard J. Sasiela, and Ronald Parenti. "Beam wander effects on the scintillation index of a focused beam." In *Defense and Security*, pp. 28-37. International Society for Optics and Photonics, 2005.

[4] Feit, M.D. and, and J. A. Fleck. "Beam nonparaxiality, filament formation, and beam breakup in the self-focusing of optical beams." *JOSA B* 5, no. 3 (1988): 633-640.

[5] Fried, Daniel, Richard E. Glena, John D.B. Featherstone, and Wolf Seka. "Nature of light scattering in dental enamel and dentin at visible and near-infrared wavelengths." *Applied optics* 34, no. 7 (1995): 1278-1285.

[6] Clifford, S. F., G. R. Ochs, and R. S. Lawrence. "Saturation of optical scintillation by strong turbulence." *JOSA* 64, no. 2 (1974): 148-154.

[7] Roddier, Francois. *Adaptive optics in astronomy*. Cambridge University Press, 1999.

[8] Keller, Joseph B. "Accuracy and Validity of the Born and Rytov Approximations*." *JOSA* 59, no. 8 (1969): 1003.

[9] Vorontsov, Mikhail, Jim Riker, Gary Carhart, V. S. Rao Gudimetla, Leonid Beresnev, Thomas Weyrauch, and Lewis C. Roberts Jr. "Deep turbulence effects

compensation experiments with a cascaded adaptive optics system using a 3.63 m telescope." *Applied Optics* 48, no. 1 (2009): A47-A57.

[10] Tyler, Glenn A. "Adaptive optics compensation for propagation through deep turbulence: initial investigation of gradient descent tomography." *JOSA A* 23, no. 8 (2006): 1914-1923.

[11] Vela, Patricio A., Marc Niethammer, Gallagher D. Pryor, Allen R. Tannenbaum, Robert Butts, and Donald Washburn. "Knowledge-based segmentation for tracking through deep turbulence." *IEEE Transactions on Control Systems Technology* 16, no. 3 (2008): 469-474.

[12] Chehbouni, A., C. Watts, J-P. Lagouarde, Y. H. Kerr, J-C. Rodriguez, J-M. Bonnefond, F. Santiago, G. Dedieu, D. C. Goodrich, and C. Unkrich. "Estimation of heat and momentum fluxes over complex terrain using a large aperture scintillometer." *Agricultural and Forest Meteorology* 105, no. 1 (2000): 215-226.

[13] Fugate, Robert Q., D. L. Fried, G. A. Ameer, B. R. Boeke, S. L. Browne, P. H. Roberts, R. E. Ruane, G. A. Tyler, and L. M. Wopat. "Measurement of atmospheric wavefront distortion using scattered light from a laser guide-star." (1991): 144-146.

[14] Roddier, Fran ̧ois. "The effects of atmospheric turbulence in optical astronomy."*In: Progress in optics. Volume 19. Amsterdam, North-Holland Publishing Co., 1981, p. 281-376.* 19 (1981): 281-376.

[15] Wang, Fugao, and D. P. Landau. "Efficient, multiple-range random walk algorithm to calculate the density of states." *Physical Review Letters* 86, no. 10 (2001): 2050.

[16] Smith, Matthew H., Jacob B. Woodruff, and James D. Howe. "Beam wander considerations in imaging polarimetry." In *SPIE's International Symposium on Optical Science, Engineering, and Instrumentation*, pp. 50-54. International Society for Optics and Photonics, 1999.

[17] Dios, Federico, Juan Antonio Rubio, Alejandro Rodríguez, and Adolfo Comerón. "Scintillation and beam-wander analysis in an optical ground station-satellite uplink." *Applied optics* 43, no. 19 (2004): 3866-3873.

[18] Willebrand, Heinz, and Baksheesh S. Ghuman. "Fiber optics without fiber."*Spectrum, IEEE* 38, no. 8 (2001): 40-45.

[19] Fried, David L. "Aperture averaging of scintillation." *JOSA* 57, no. 2 (1967): 169-172.

[20] Mamaev, A. V., M. Saffman, D. Z. Anderson, and A. A. Zozulya. "Propagation of light beams in anisotropic nonlinear media: from symmetry breaking to spatial turbulence." *Physical Review A* 54, no. 1 (1996): 870.

[21] Andrews, Larry C., and Ronald L. Phillips. *Laser beam propagation through random media*. Vol. 1. Bellingham, WA: SPIE press, 2005.

[22] Lane, R. G., A. Glindemann, and J. C. Dainty. "Simulation of a Kolmogorov phase screen." *Waves in random media* 2, no. 3 (1992): 209-224.

[23] Hardy, John W. *Adaptive optics for astronomical telescopes*. Oxford University Press, 1998.

[24] Kobayashi, Michikazu, and Makoto Tsubota. "Kolmogorov spectrum of superfluid turbulence: Numerical analysis of the Gross-Pitaevskii equation with a small-scale dissipation." *Physical Review Letters* 94, no. 6 (2005): 065302.

[25] Dogariu, Aristide, and Stefan Amarande. "Propagation of partially coherent beams: turbulence-induced degradation." *Optics Letters* 28, no. 1 (2003): 10-12.

[26] Recolons, Jaume, Larry C. Andrews, and Ronald L. Phillips. "Analysis of beam wander effects for a horizontal-path propagating Gaussian-beam wave: focused beam case." *Optical Engineering* 46, no. 8 (2007): 086002-086002.

[27] Avila, Remy, Aziz Ziad, Julien Borgnino, Fran ̧ois Martin, Abdelkrim Agabi, and Andrey Tokovinin. "Theoretical spatiotemporal analysis of angle of arrival induced by atmospheric turbulence as observed with the grating scale monitor experiment." *JOSA A* 14, no. 11 (1997): 3070-3082.

[28] Andrews, Larry C., Ronald L. Phillips, and Cynthia Y. Hopen. *Laser beam scintillation with applications*. Vol. 99. SPIE press, 2001.

[29] Andrews, Larry C. "Field guide to atmospheric optics." SPIE, 2004.

[30] Primot, J., G. Rousset, and J. C. Fontanella. "Deconvolution from wave-front sensing: a new technique for compensating turbulence-degraded images."*JOSA A* 7, no. 9 (1990): 1598-1608.

[31] Marshall, Robert, Jill Kempf, Scott Dyer, and Chieh-Cheng Yen. "Visualization methods and simulation steering for a 3D turbulence model of Lake Erie." In *ACM SIGGRAPH Computer Graphics*, vol. 24, no. 2, pp. 89-97. ACM, 1990.

[32] Wu, Chensheng, William Nelson, and Christopher C. Davis. "3D geometric modeling and simulation of laser propagation through turbulence with plenoptic functions." In *SPIE Optical Engineering+ Applications*, pp. 92240O-92240O. International Society for Optics and Photonics, 2014.

Chapter 2: Conventional Wavefront Sensors

In order to detect the complex field amplitude of a coherent wave, one needs to obtain both the phase and magnitude distribution. However, any image sensor can only tell the intensity distribution of the incident light field at the cost of losing phase information. Special optical designs are needed to retrieve the phase information of the beam. In general, an optical system that provides wavefront information about an incident beam is defined as a wavefront sensor. In this chapter, several conventional designs of wavefront sensors will be introduced and discussed.

2.1 Shack Hartmann Sensor

The Shack-Hartmann sensor [1] is a very effective tool for measuring weak wavefront distortions. It has already been successfully applied in the astronomy field to measure the weak distortion generated by the Earth's atmosphere on celestial images [2].

2.1.1 Mechanisms

A Shack-Hartmann sensor is made up of a micro-lens array (MLA) and an image sensor. The basic structure of a Shack-Hartmann sensor can be shown by the following diagram [3]:

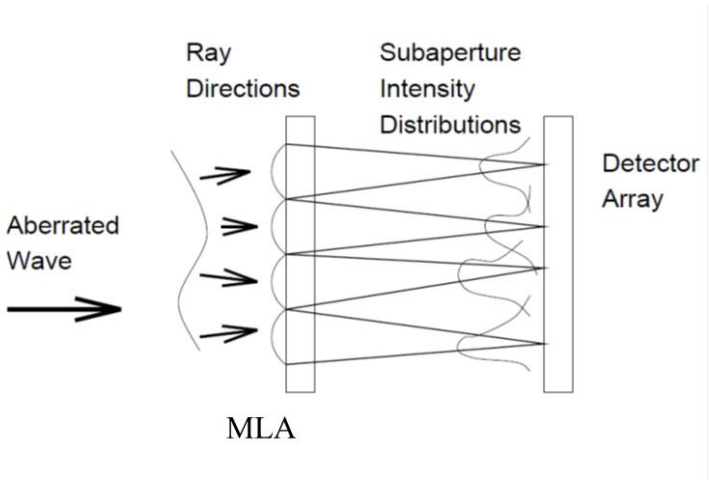

Figure 2. 1:Structure diagram of the Shack-Hartmann sensor

The Shack-Hartmann sensor uses a micro-lens array (MLA) and an image sensor at the back focal plane of the MLA. The incident beam is spatially divided by the MLA lenslet cells into small grid points and the gradient of the local wavefront is reflected by the shift of focal point at the back focal plane of each lenslet. With the assembled local gradient of the wavefront, the global reconstruction of the wavefront can be achieved by satisfying the following constraint:

$$\phi^*(x,y) \triangleq \min\left\{\sum\left\|\nabla\phi(x,y) - g_{SH}(x,y)\right\|^2\right\} \tag{1}$$

In other words, the reconstructed phase front has the minimum mean square error (MMSE) in its gradient when compared with the retrieved local gradient information.

2.1.2 Wavefront reconstructions

The accuracy of the wavefront reconstruction in the Shack-Hartmann sensor depends on the accuracy of local gradient retrieval. In other words, in each MLA cell, the shift of the focus needs to be determined with a certain level of accuracy. The rule of

thumb is to calculate the intensity weighted center for each MLA cell, which can be expressed as:

$$s_x = \frac{\sum_x \sum_y x \cdot I(x,y)}{\sum_x \sum_y I(x,y)}; \quad s_y = \frac{\sum_x \sum_y y \cdot I(x,y)}{\sum_x \sum_y I(x,y)} \tag{2}$$

In general, if the local wavefront distortion is concentrated in tip/tilt, the local image cell under the MLA lenslet will have a sharp focus. If the local distortion is concentrated in higher orders of distortion, the result provided by equation (2) will be inaccurate. To gain more accuracy in revealing local phase front gradient, one can increase the numerical aperture of the MLA unit (enlarge the f/#), so that each pixel shift will correspond with a smaller tip/tilt value. However, the dynamic range of measurable wavefront gradient will be reduced with increased numerical aperture. Theoretically, within the diffraction limits, the sensitivity of the Shack-Hartmann sensor can be infinitely increased. Therefore, the Shack-Hartmann sensor provides a more accurate result in handling weak distortion cases than the results acquired under strong distortions.

On the other hand, smart algorithms in handling more complex local phase front distortions in the Shack-Hartmann sensor have been proposed. For example, adding blob detection before the intensity weighted averaging algorithm to find a more accurate center shift [4]. This helps to remove random high order phase oscillation structures. Also, attempts to extract more complex distortion orders in each cell image of the Shack-Hartmann sensor provide more insight into interpreting the Shack-Hartmann images.

The global result defined by equation (2) states that a reliable wavefront reconstruction should minimize "mismatches" with the retrieved local gradient field on the Shack-Hartmann sensor. Intuitively, if the phase front is assumed to be continuous, the curl of the local phase front gradient should be zero. MMSE is applied in order to assure the non-zero curl of the field.

On a Shack-Hartmann sensor, however, each data point (representing the local gradient of the phase front) is retrieved independently. The curl of the gradient field can result either from the error/inaccuracies of local data or from actual branch points in the distortion (discontinuity of the phase front). We will ignore the branch point problems for the moment, because one can always divide the phase front into continuous blobs and reconstruct them separately. To remove the data error, two approaches are commonly taken by researchers:

(1) Averaging over multiple integral paths.

(2) Solving the MMSE equations.

The first approach is based on the weak law of large numbers (WLLN) [5]. As each data point is independently retrieved, the round-off error with the local gradient should be independent of its neighboring MLA cells. By picking different integral paths, the averaged error will statistically approach a mean value of zero. The second approach is more exact, but may take extra computation power to solve [6] for a large number of phase samples. In fact, the standard approaches have been implanted in imaging processing where an original image can be retrieved from the gradient information.

The averaging path integral can be illustrated by the following diagram:

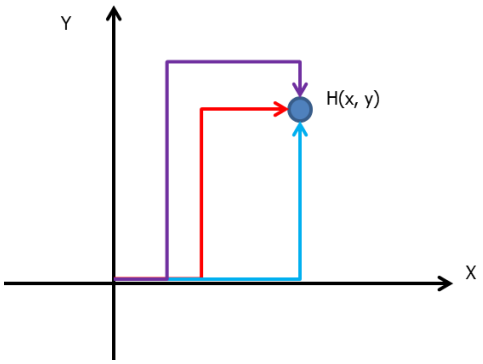

Requirement for adjustment should satisfy:

$$\oint \nabla S(\vec{r}) \cdot d\vec{r} \leq error_{tol}$$

Figure 2. 2: Averaging path integral for Shack-Hartmann sensors

The benefit of averaging path integrals is the convenience of retrieving any arbitrary point on the phase front (without strictly satisfying MMSE).

The solution of MMSE defined by equation (2) can be mathematically described as:

$$\Delta\phi(x,y) = \frac{\partial}{\partial x}\left[g_x(\phi)\right] + \frac{\partial}{\partial y}\left[g_y(\phi)\right] \tag{3}$$

In equation (3), g_x and g_y denote the gradient data retrieved from the Shack-Hartmann sensor. And the above equation in the discrete Fourier transform (DFT) domain can be rewritten as:

$$\left(\omega_x^{\,2} + \omega_y^{\,2}\right)\Phi\left(\omega_x, \omega_y\right) = \mathbb{F}\left\{\frac{\partial}{\partial x} g_x + \frac{\partial}{\partial y} g_y\right\} \tag{4}$$

In equation (4), the right hand side can be directly retrieved from the Shack-Hartmann image, and the left hand side denotes each frequency spectrum point in the Poisson equation defined by equation (3). A discrete Fourier transform is used because of the quantization of image sensors. It can be proved that the result of equation (4) satisfies the MMSE requirement defined by equation (2) under a continuous assumption [7].

For more general cases where branch points are allowed and the phase front is not necessarily continuous, the MMSE result typically leads to a large mismatch [8]. A

common practice is to use the MMSE as a metric to determine the continuity of the phase front by comparing it with a pre-set threshold value. If the MMSE turns out to be larger than the threshold value, the reconstructed wavefront is determined to have branch points. For any arbitrary phase front, one can always break it down into a finite number of continuous segments and apply MMSE separately to realize continuous phase reconstruction and stitch them together.

2.1.3 Limitations

The Shack-Hartmann sensor is effective in revealing wavefront distortions in weak turbulence regimes. In medium and strong turbulence cases, reconstruction errors will show up based on several well-known effects, including scintillation, branch point problems, self-interference and beam break-up. In principle, the fundamental unit of a Shack-Hartmann sensor is the cell image for each lenslet in the MLA. The fundamental unit provides reliable results if and only if it contains a sharp focus. Therefore, the Shack-Hartmann sensor can't interpret cell images with more complex geometric patterns. For example, self-interference happens in strong/deep turbulence where various parts of the beam begin to overlap geometrically due to the beam wander effect. When those interfering patches enter the same MLA cell, the cell image shows more than one focal point and the local gradient is ambiguous. In another case, when a branch point problem happens (typically when the loop sum phase distortion equals a multiple of 2π), the centroid cell at the branch point will be dark and no information can be provided.

The following notes should also be considered when using the Shack-Hartmann sensor to perform wave front reconstruction:

(1) Enlarging the focal length of the MLA improves the angular resolution at the cost of reducing the angular range (and vice-versa).

(2) The dynamic range for each cell is limited by a single pixel (typically ranging from 0 to 255).

Fortunately, one can determine the reliability of the Shack-Hartmann sensor directly by examining the cell images. If a certain number of image cells don't present a distinctive focus, the reconstruction can't be trusted. In other words, the distortion level exceeds the capacity of the Shack-Hartmann sensor.

2.2 Curvature Sensor

The curvature sensor was developed by F. Roddier (since 1988) [9] to measure distributed weak distortion curvatures. Compared with Shack-Hartmann sensors that reveal the tip/tilt of local phase front, the curvature sensor is able to tell the local focus/defocus by taking two images at the same time.

2.2.1 Mechanisms

The diagram of the curvature sensor can be shown by the following figure:

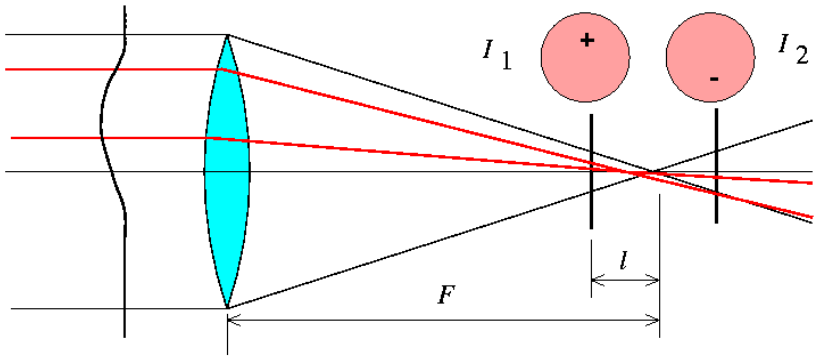

Figure 2. 3: Principle diagram of curvature sensor

Normally, if the incoming wave is a plane wave, the focus of the telescope (represented by the front objective lens in the diagram figure) is able to image a sharp focus at its back focal plane. If the incident plane wave is slightly distorted, the corresponding area will be focused either before the focal plane (if the extra curvature is concave) or after the focal plane (if the extra curvature is convex).

As shown by figure 2.3, two images are taken at symmetric distance (marked by l) from the focal plane. Based on geometric optics, the two images (marked by I_1 and I_2) correspond with the geometry of the objective lens's aperture. Therefore, by analyzing the intensity distribution on I_1 and I_2, one can retrieve the extra curvature distribution of the incident wavefront. Intuitively, for the same arbitrary spot on the pupil image pair I_1 and I_2, the ratio between the brighter spot and the dimmer spot denotes the strength of the extra curvature. The location of the extra curvature is linear with the pupil image's coordinates. As a result, the curvature sensor's function can be revealed by the simplified equation:

$$\frac{I_1(\vec{r})-I_2(\vec{r})}{I_1(\vec{r})+I_2(\vec{r})} = -\frac{\lambda F(F-l)}{2\pi l}\cdot\nabla^2\phi\left(\frac{F\vec{r}}{l}\right) \tag{5}$$

In equation (5), $\boldsymbol{r}$ represents the coordinates in the image plane and F represents the focal length of the telescope (objective lens). The distance between the image plane and the focal plane is marked by l and the wavelength is represented by λ. The Laplacian operator in equation (5) shows that the second order of wavefront distortion (divergence of the phase front gradient) determines the normalized intensity difference for the same geometric spot on the aperture plane.

2.2.2 Wavefront reconstructions

The wavefront reconstruction algorithm for the curvature sensor (CS) is very similar to the reconstruction process of the Shack-Hartmann sensor. In fact, under the continuous phase front assumption, the processing of equation (3) under MMSE requirement aims at extracting the Laplacian of the phase front. The curvature sensor retrieves the same Laplacian of the phase front by using 2 images taken at the same time. Therefore, the reconstruction of the curvature sensor can be solved with the same DFT process:

$$\left(\omega_x{}^2+\omega_y{}^2\right)\Phi\left(\omega_x,\omega_y\right)=-kl\cdot\frac{I_1\left(\frac{F\vec{r}}{l}\right)-I_2\left(\frac{F\vec{r}}{l}\right)}{I_1\left(\frac{F\vec{r}}{l}\right)+I_2\left(\frac{F\vec{r}}{l}\right)} \tag{6}$$

Detailed computer simulation shows that the performances of a Shack-Hartmann sensor and a curvature sensor are almost identical [10].

2.2.3 Limitations

In a similar way as the Shack-Hartmann sensor, the design principle of the curvature sensor is based on perturbation of plane waves under weak turbulence conditions.

When the turbulence gets stronger, complex effects such as self-interference, branch point problems and beam wander effect will greatly compromise the reliability of the curvature sensor. In a wide sense, the curvature sensor's performance equals the Shack-Hartmann sensor. However, the technical challenges of acquiring two images simultaneously brings in extra cost in using the CS.

2.3 Interferometer

An interferometer can be used to determine both the intensity and phase distribution of a distorted beam. In principle, a interferometer uses a reference beam with known phase and intensity distribution to interfere with a distorted beam with the same wavelength. Therefore, by observing the enhancement or degeneration of intensity of the combined beam, the phase information of the distorted beam can be revealed as well as its intensity distribution.

2.3.1 Mechanisms

In general, when two mutually temporally coherent beams of the same wavelength encounter each other, the intensity distribution results from interference and forms steady patterns of intensity enhancement/diminishment depending on the summation of complex field amplitudes of the two beams. Brighter patterns happen for spots where field amplitude are in phase while dimmer patterns happen where the field amplitude are out of phase [11].

The operation of an interferometer can be shown by the following diagram:

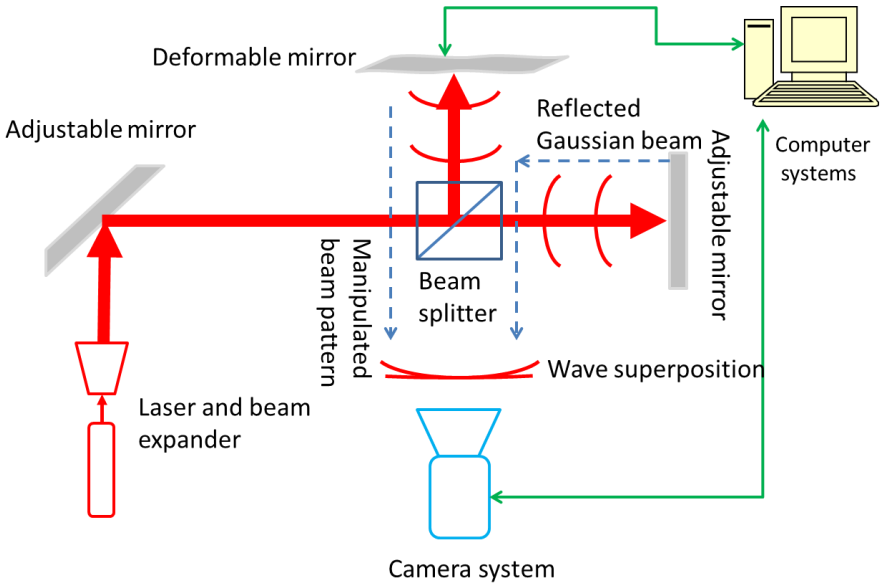

Figure 2. 4: Diagram of an interferometer

In figure 2.4, the distortion is specified by a deformable mirror for simplicity, and in more general cases, the distortion can be caused by beam propagation/reflection in inhomogeneous media. The intensity profile of the distorted beam can be obtained by imaging the beam with a camera system. The phase profile of the distorted beam can be obtained by imaging and analyzing the interference pattern.

Without loss of generality, we can express the phase difference for any arbitrary point by the following equation:

$$I^{\Sigma}(\vec{r}) = \left[I_1(\vec{r}) + I_2(\vec{r}) + 2\cos(\phi_1 - \phi_2)\sqrt{I_1(\vec{r}) \cdot I_2(\vec{r})} \right] \tag{7}$$

In the above equation, the left hand side represents the intensity of the interference pattern. The right hand side of equation (7) writes the interference pattern as the sum of the two beams' intensity plus their interference term. As long as the intensity distributions are retrieved, the relative phase difference between the reference beam

and the distorted beam can be calculated besides a logic error (because the phase difference is expressed in absolute value). The following diagram explains the logic error for interferometer reconstruction:

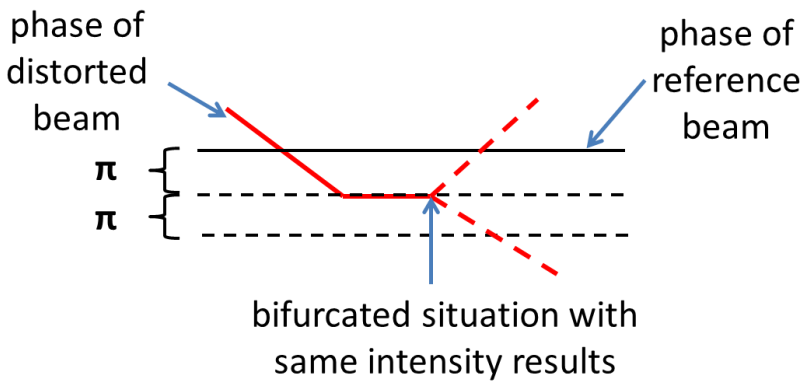

Figure 2. 5: Logic error in interferometer reconstruction

In the above figure, we assume that there is only a phase difference between the two beams, and their intensity distributions are identical. Therefore, where the phases are differenced by π, a dark spot will show up correspondingly (and vice versa). However, for brighter pixels near the dark spot, we find there are two equivalent way to express the variation trend of the phase change. This is regarded as a "logic error" as one of the two choices is wrong in wavefront reconstruction. In general, for weak phase distortions, "logic error" can be corrected while for strong phase distortions, the logic error prevents reliable wavefront reconstruction because of the large number of ambiguities.

2.3.2 Wavefront reconstructions

Interferometers are useful tools to reveal simple patterns of phase changes. In general, the reference beam is assumed to be uniform in both phase and intensity. The best

reconstruction can be achieved when the beam to be measured has similar intensity distribution. Various approaches have been proposed to reconstruct the phase of the distorted beam [12] [13] [14]. For simplicity, we only demonstrate a quick and robust method based on the curl shapes of the dark lines (line with lowest intensities). Without loss of generality, this approach is called "contour reconstruction". Intuitively, each dark curve denotes that the spots on the line are out of phase with the reference beam.

The contour reconstruction takes the following steps:

(1) Index marking: mark each dark curve with integers and neighboring curves should be different by ±1. Note: the marking may not be unique due to the logic error.

(2) Interpolation, multiply the indices for the dark curves by 2π and interpolate a curve between neighboring curves and mark the phases by the averaged phase. Note: now each neighboring curves will have phase difference of π.

(3) Repeat step (2) iteratively for smaller phase difference of $\pi/2$, $\pi/4$, $\pi/8$, ... until the resolution requirement is satisfied.

The "contour reconstruction" is simple and effective in revealing the basic phase information based on image processing approaches. In principle, it takes advantage of the deterministic properties of dark lines and assumes that the phase changes between them are linear. More complex methods to retrieve detailed phase information is available, but more computation resources are required in order to perform the reconstruction instantly (<1ms).

2.3.3 Limitations

The connection between the interferometer, the Shack-Hartmann sensor and the curvature sensor is that they respectively reveal the phase front based on reference value, first order of phase front and the second order of phase front. In a wide sense, those three types of wavefront sensors have the same effectiveness based on their correlated mathematical principles.

The limitations of interferometer in measuring atmospheric turbulence are also evident:

(1) An extra mutually temporally coherent reference beam with known or controllable phase and amplitude information is required.

(2) The size of the reference beam needs to be larger than the distorted beam in order to minimize logic errors.

(3) The intensity knowledge of the distorted beam is required, which involves imaging the distorted beam simultaneously.

(4) The logic error is inevitable whenever there is a contour line that extends to the geometric boundary of the reference beam, making the reconstruction non-deterministic.

(5) Beam wander can cause misalignment between the reference beam and the distorted beam.

Admittedly, an interferometer can directly reveal detailed small phase changes. However, its limitations prevent the practical uses of interferometers in sensing atmospheric turbulence in open paths. Intuitively, the interferometers used in the near

field might not be a good candidate for measuring beam distortions in strong and deep turbulence, which is typically classified as the far field and contains phase distortions that are much larger than 2π.

2.4 Orthogonal Polynomial Point Detector

A new thought on the wavefront detection [15] can effectively speed up the detection and reconstruction process by interpolating the phase front as a summation of low order Zernike polynomials. This approach uses a series of phase plates that match the basic orders of Zernike polynomials (all the phase plates have fixed radius as common observing windows). For an arbitrary incident wavefront, the mode matching (in phase distribution) will cast the power in each mode onto its corresponding point detector. Therefore, the power concentration in each basic Zernike mode is revealed directly and the wavefront distortion is the summation of those Zernike polynomials. The concept of the design can be back traced to holographic wavefront sensors [16] proposed by G.P. Andersen.

2.4.1 Mechanisms

The fundamental structure of the Orthogonal Polynomial Point Detector (OPPD) in wave front sensing can be shown as:

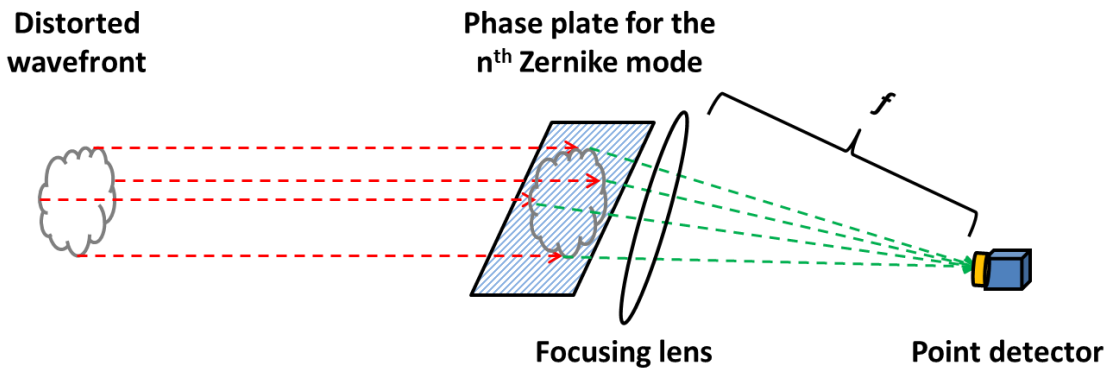

Figure 2. 6: Structure diagram of OPPD

Because 2 identical copies of the wave front can be achieved with one beam splitter, the diagram shown by figure 2.6 can detect the first 2^n Zernike polynomials with 2^n-1 beam splitter and 2^n branches. Based on the 2^n data acquired on the point detectors, the wavefront distortion is summed without any complex computation.

2.4.2 Wavefront reconstructions

The wavefront reconstruction can be directly written as:

$$\phi(x,y) = \sum_{i=1}^{2^n} C_i Z_i(x,y) \tag{8}$$

In equation (8), the real number detected by the i^{th} point detector is expressed as C_i, and $Z_i(x, y)$ represents the i^{th} Zernike polynomial. As each point detector can operate as fast as 100 kHz, the wavefront reconstruction by OPPD can reach 100 kHz.

2.4.3 Limitations

Theoretically, OPPD can reach very high speed wavefront sensing for weak phase distortions. However, for strong phase distortions in medium to strong turbulence cases, OPPD is not effective. Intuitively, if the beam only suffers from large tip/tilt

and a stronger turbulence doubles the tip/tilt, one needs to increase the number of branches in OPPD by 2^n. In fact, the complexity of the OPPD system increases exponentially in response to increased level of turbulence.

A few other limitations need to be considered:

(1) Interfering beam patterns can't be reconstructed by OPPD.

(2) When the coherence length of the wavefront degenerates to be much smaller than the aperture size of OPPD, the result is unreliable.

(3) Free space lasers can't be strictly characterized by low orders Zernike models [17].

(4) Actual size of the point detector needs to be considered.

(5) Synchronization of the point detectors is challenging.

Although the OPPD has proved to be effective in some fiber laser systems, more complex research needs to be done to fit into sensing long range beam distortion by atmospheric turbulence. However, the advantage of OPPD's high speed and concise algorithm is potentially promising.

2.5 Light field sensor

Light field cameras [18] [19] have been invented to acquire images that can be readjusted for different focal depths. To achieve the refocusing, more information than that in a simple an image needs to be recorded. Therefore, this type of light field camera records elements that are more fundamental than image pixels: individual light rays. Alternatively, if the light rays of a laser beam are recorded, the atmospheric distortion can be measured in a more fundamental way. Similarly, one

type of plenoptic camera (CAFADIS) based on the light field principles have been proposed and demonstrated by JM Rodr ́guez-Ramos [20] [21] [22] in the Canary Islands (Spain) to image and observe atmospheric turbulence effect at the same time for celestial objects. This significant achievement has demonstrated that light field imaging principles have the potential to acquire more information than conventional wavefront sensors.

2.5.1 Mechanism

The light field sensor is made up of an imaging lens set and a microlens array (MLA) in front of the image sensor. The MLA is placed at the imaging plane of the imaging lens set while the image sensor locates at the back focal plane of the MLA. The light field sensor can be shown by the following diagram:

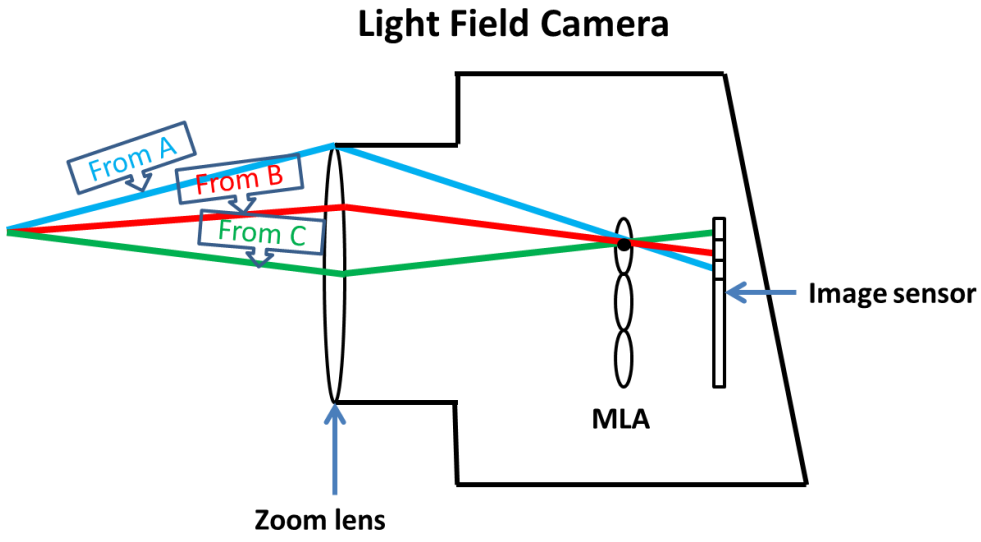

Figure 2. 7: Diagram of the light field camera

In this diagram of the light field camera, the MLA samples the original image by a normal camera's configuration as if each MLA cell acts like a pixel. After the MLA, the rays coming through the same MLA unit will continue propagating and hit corresponding pixels on the image censor at the back focal plane of the MLA. Therefore, the image on the MLA plane can be interpreted ray by ray. By picking different pixels under the same MLA unit, once can choose an object that lies at a different depth in the field.

Based on the variable refocus ability of the light field, the atmospheric turbulence effect can be extracted by analyzing the stableness of images at different focal depths. For example, by analyzing the image wandering effect for objects that are 100m, 200m, and 300m away from the camera helps to reveal the distributive strength of turbulence in each depth. Also, the scintillation of distributed parts of a refocused image facilitates the analysis of a detailed turbulence structure over the transverse plane.

2.5.2 Wavefront reconstructions

Without loss of generality, we assume that the image at different depths in the channel is a horizontal line with fixed length [23]. When turbulence get involved, the horizontal line begin to show primary distortions in the vertical direction, while in horizontal direction, the length of the line change is regarded as secondary changes (and normally regraded as constant). Therefore, the gradient of the wavefront along the vertical direction can be retrieved by the ratio of vertical displacement versus the

length of the line. The following expression can be used to reconstruct the wavefront distortion in linear format:

$$t(x) = -\frac{L \cdot [y'(x) - y_0(x)]}{l_x} \tag{9}$$

In equation (9), $y'(x)$ is the pixel location along the reference line, while $y_0(x)$ is the expected pixel location along the reference line. The actual length of the reference line is expressed by L, while its length in pixels is expressed by l_x. The negative sign corresponds with the typically reversed image in the light field camera. Intuitively, the wavefront reconstruction classifies all the orthogonal distortion of line features as turbulence distortion. For example, if an uplift of a horizontal line is observed, the wavefront must have tilted down to cause the corresponding change. The scaling factor L/l_x, helps to calibrate image reconstruction at various focal depths. Without loss of generality, the wavefront reconstructions of the light field camera have extra capacity to analyze the progressive changes caused by atmospheric turbulence along the propagation direction.

2.5.3 Limitations

The limitations for light field camera are obvious: (1) the indirect imaging approach is very complicated; (2) direct imaging of a coherent beam provides meaningless information (in the next chapter, we will show how the plenoptic sensor is developed based on light field cameras to solve this problem). Intuitively, distributed objects with excellent features along the channel are required, which are commonly unavailable in a real environment. And the light field approach has to reconstruct the

features in each focal stack, analyze the distortions from expected results and derive the actual magnitude and direction of turbulence distortions. Therefore, the first point addresses the fact that this approach requires an ideal condition to extract turbulence information, which is impractical. For the second point, the point spread function (PSF) of a conventional light field camera is formed in each cell. This causes severe incompatibility in directly imaging a distorted beam. As there is no actual "point" in a propagating beam, the PSF formed in each cell carries no meaning. Since patches (small wavelets that act like plane-waves in the near field) with similar propagation momentum within a distorted beam will typically fall into the same MLA cell, the image acquired in the cell will result from interference and leads to ambiguity. Therefore, the light field camera's passive sensing techniques can't be directly applied to sensing coherent laser beams. However, the plenoptic sensor to be introduced in the next chapter overcomes these shortcomings and can be applied directly to image and analyze a distorted laser beam.

2.6 Cooperative Sensors

The idea of cooperative sensors is to examine the distortion with wavefront sensors of various configurations, and combine their reconstruction results to enlarge the solution set. For example, one can use 2 Shack-Hartmann sensors where the MLAs are of the same size but different f/#. The MLA with larger numerical aperture (NA) can sense the weak phase front distortion delicately, while its lack of dynamic range is compensated by the other MLA with smaller NA (worse resolution but more dynamic range). As discussed in section 2.1.3, the self-check mechanism of Shack-

Hartmann sensors enables a merged result: the strengths of angular resolution and dynamic range are obtained at the same time.

2.6.1 Mechanisms

In principle, the cooperative sensor is a stitching of results provided by non-identical sensors. For simplicity, the mutual information (where two sensors agree on each other) is marked as $I(\Phi_1,\Phi_2)$ [24], and the information provided by the sensors respectively is $H(\Phi_1)$, $H(\Phi_2)$. Then, when their result is stitched, a more detailed results containing $H(\Phi_1)+H(\Phi_2)- I(\Phi_1,\Phi_2)$ can be obtained.

2.6.2 Wavefront reconstructions

The wavefront reconstruction is achieved by using the following steps:

(1) For areas reliably detected by more than one sensor, use the result that maximizes the consensus.

(2) For areas that are reliably detected by only one of the sensors, use that sensor's result.

Point (1) requires that for overlapping areas, the sensors should agree with each other. Intuitively, this solves the areas covered by $I(\Phi_1,\Phi_2)$ in the 2 sensor scenario. Point (2) states that without consensus, individual reconstruction should be trusted. This solves for areas indicated by $H(\Phi_1) - I(\Phi_1,\Phi_2)$ and $H(\Phi_2)- I(\Phi_1,\Phi_2)$in the 2 sensor scenario.

2.6.3 Limitations

A multi-sensor system will inevitably have a more complex hardware structure than conventional single sensor systems. Meanwhile, the synchronizing process where all sensors are required to operate at the same speed is not easily realizable. In fact, the multi-sensor system may be required to operate at the speed of the slowest branch. In addition, examining compatibility between devices is difficult. For example, it is hard to determine whether a Shack-Hartmann sensor and a curvature sensor are compatible with each other. Since those two sensors are mathematically identical, one can't extract significantly "more" information by combining their results.

References:

[1] Platt, Ben C. "History and principles of Shack-Hartmann wavefront sensing." *Journal of Refractive Surgery* 17, no. 5 (2001): S573-S577.

[2] Hardy, John W. *Adaptive optics for astronomical telescopes*. Oxford University Press, 1998.

[3] Dayton, David, Sergio Restaino, John Gonglewski, Joe Gallegos, Scot McDermott, Steve Browne, Sam Rogers, Mohan Vaidyanathan, and Mike Shilko. "Laboratory and field demonstration of a low cost membrane mirror adaptive optics system." *Optics Communications* 176, no. 4 (2000): 339-345.

[4] Jiang, Wenhan, Hao Xian, and Feng Shen. "Detection error of Shack-Hartmann wavefront sensors." In *Optical Science, Engineering and Instrumentation'97*, pp. 534-544. International Society for Optics and Photonics, 1997.

[5] Petrov, Valentin V. "Limit theorems of probability theory." (1995).

[6] Buzbee, Billy L., Gene H. Golub, and Clair W. Nielson. "On direct methods for solving Poisson's equations." *SIAM Journal on Numerical analysis* 7, no. 4 (1970): 627-656.

[7] Sun, Jian, Jiaya Jia, Chi-Keung Tang, and Heung-Yeung Shum. "Poisson matting." *ACM Transactions on Graphics (ToG)* 23, no. 3 (2004): 315-321.

[8] Martin, Rainer. "Noise power spectral density estimation based on optimal smoothing and minimum statistics." *Speech and Audio Processing, IEEE Transactions on* 9, no. 5 (2001): 504-512.

[9] Roddier, Francois, and C. Roddier. "Curvature sensing and compensation: a new concept in adaptive optics." In *European Southern Observatory Conference and Workshop Proceedings*, vol. 30, p. 667. 1988.

[10] Rigaut, François, Brent L. Ellerbroek, and Malcolm J. Northcott. "Comparison of curvature-based and Shack–Hartmann-based adaptive optics for the Gemini telescope." *Applied Optics* 36, no. 13 (1997): 2856-2868.

[11] Wyant, James C. "Use of an ac heterodyne lateral shear interferometer with real–time wavefront correction systems." *Applied Optics* 14, no. 11 (1975): 2622-2626.

[12] Schnars, Ulf, and Werner P.O. Jüptner. "Digital recording and reconstruction of holograms in hologram interferometry and shearography." *Applied Optics* 33, no. 20 (1994): 4373-4377.

[13] Elster, C., and I. Weingärtner. "Exact wave-front reconstruction from two lateral shearing interferograms." *JOSA A* 16, no. 9 (1999): 2281-2285.

[14] Deng, Yuqiang, Zubin Wu, Lu Chai, Ching-yue Wang, Keisaku Yamane, Ryoji Morita, Mikio Yamashita, and Zhigang Zhang. "Wavelet-transform analysis of spectral shearing interferometry for phase reconstruction of femtosecond optical pulses." *Optics Express* 13, no. 6 (2005): 2120-2126.

[15] Haumann, H-J., Harald Kobolla, Frank Sauer, Juerg Schmidt, Johannes Schwider, Wilhelm Stork, Norbert Streibl, and Reinhard Voelkel. "Optoelectronic interconnection based on a light-guiding plate with holographic coupling elements." *Optical Engineering* 30, no. 10 (1991): 1620-1623.

[16] Andersen, Geoff P., Luis Dussan, Fassil Ghebremichael, and Kenny Chen. "Holographic wavefront sensor." *Optical Engineering* 48, no. 8 (2009): 085801-085801.

[17] Noll, Robert J. "Zernike polynomials and atmospheric turbulence." *JOSA* 66, no. 3 (1976): 207-211.

[18] Ng, Ren, Marc Levoy, Mathieu Brédif, Gene Duval, Mark Horowitz, and Pat Hanrahan. "Light field photography with a hand-held plenoptic camera."*Computer Science Technical Report CSTR* 2, no. 11 (2005).

[19] Ramos, José Manuel Rodriguez, Fernando Rosa González, and José Gil Marichal-Hernández. "Wavefront aberration and distance measurement phase camera." U.S. Patent Application 12/161,362, filed January 18, 2007.

[20] Rodríguez-Ramos, J. M., et al. "2D-FFT implementation on FPGA for wavefront phase recovery from the CAFADIS camera." *SPIE Astronomical Telescopes+ Instrumentation*. International Society for Optics and Photonics, 2008.

[21] Rodríguez, J. M., et al. "The CAFADIS camera: a new tomographic wavefront sensor for Adaptive Optics." *1st AO4ELT conference-Adaptive Optics for Extremely Large Telescopes*. EDP Sciences, 2010.

[22] Rodríguez-Ramos, J. M., et al. "Wavefront and distance measurement using the CAFADIS camera." *SPIE Astronomical Telescopes+ Instrumentation*. International Society for Optics and Photonics, 2008.

[23] November, Laurence J. "Measurement of geometric distortion in a turbulent atmosphere." *Applied Optics* 25, no. 3 (1986): 392-397.

[24] Cover, Thomas M., and Joy A. Thomas. *Elements of information theory*. John Wiley & Sons, 2012.

Chapter 3: The Plenoptic Sensor

The plenoptic sensor [1] is an unconventional imaging tool that maps a light field into its 4D phase space. It records the scattered light field and performs data mining to find and track patterns inside the light field. With the recovered light field, multiple functions can be applied such as: retrieving the phase front and amplitude changes in the laser beam, correcting a distorted image, and decoding optic communication signals. Many conventionally complicated problems turn out to be extremely simple within the framework of a plenoptic sensor. In this chapter, we will discuss the plenoptic sensor's mechanisms and associated algorithms.

3.1 Basics in light field cameras

The light field camera is an innovation in imaging technique that records the light field of an image formation process instead of directly imaging the object. This indirect imaging technique provides extra degrees of freedom to perform image processing. For example, the blurring areas in conventional imaging devices can be refocused to be sharp on a light field camera [2]. And the image can be tilted slightly in a semi-3D way to allow for multiple viewing angles [3].

3.1.1 Light field rendering

Traditional 2D imaging models treat each resolution point of an object as a fundamental building block. Without occlusions, each illuminated point spherically "scatters" a fan of rays in all possible angles. A good imaging process converges the

rays back into a sharp point, while blurring defects in the imaging process refer to the points with blurred features.

In the advanced light field imaging models, the "blurring points" turn out to be informative. This is because the formation of the blurring points has been decomposed into individual rays as more fundamental building blocks. The requirements for an imaging lens to produce sharp point spread function are no longer needed. In other words, rays originating from the same point do not necessarily need to converge in the light field imaging system. In fact there are no "blurring" problems in the light field models [4] because all rays can be back traced and edited.

For simplicity, light field rendering is the recording and reconstruction of light rays. To express the light field explicitly, the concept of the plenoptic function that can uniquely define each ray [5] [6] provides great convenience. In general, the plenoptic function is a cluster of parameters and functions that can define the ray's interactions and propagation behavior in a specified coordinate system. For example, in the Cartesian coordinate system, the 4D phase space $(x, y, \theta_x, \theta_y)$ for any arbitrary point on plane $Z=z_0$ can define the ray behavior in free space propagation. In the 4D phase space, x and y represent the ray's interception point with plane $Z=z_0$, θ_x and θ_y represents the ray's propagation angle with regard to the plane normal of $Z=z_0$. In addition, the light rays can carry wavelength information (λ) to express "color" properties and photon density information (ρ) to express local brightness. If two or more rays are intercepted by the same pixel, functions are needed to describe their interactions such as interference (coherent) or color mixing (incoherent).

Without loss of generality, the plenoptic function can be treated as a "class" for ray objects [7], which contains all the necessary components to specify optic events of interest. The lowest order of a plenoptic function is 4D [8] that projects the linear trajectory of rays in absence of refraction and reflection. For simplicity we use the following plenoptic function for light field rendering:

$$P \triangleq \rho\left(x, y, \theta_x, \theta_y\right) \tag{1}$$

Evidently, the plenoptic function contains all the information of 2D imaging models as a point spread function can be easily expressed by:

$$s\left(x, y\right) = \iint_{\theta_x, \theta_y} \rho\left(x, y, \theta_x, \theta_y\right) d\theta_x d\theta_y \tag{2}$$

In equation (2), ρ represents the corresponding light field of a point source. Similarly, the image formation in the light field model is expressed as:

$$I\left(x, y\right) = \iint_{\theta_x, \theta_y} \rho^2\left(x, y, \theta_x, \theta_y\right) d\theta_x d\theta_y \tag{3}$$

A more rigid model is to consider the actual polarization of the field, which replaces the photon density with the complex field amplitude:

$$I\left(x, y\right) = \sum_i \iint_{\theta_x, \theta_y} E_i\left(x, y, \theta_x, \theta_y\right) d\theta_x d\theta_y \cdot \iint_{\theta_x, \theta_y} E_i^*\left(x, y, \theta_x, \theta_y\right) d\theta_x d\theta_y \tag{4}$$

In equation (4), both incoherent and coherent conditions have been taken care of. Intuitively, equation (3) and (4) state that images are formed by applying integrals of the plenoptic function over its angular space on the image plane.

A significant convenience of using the plenoptic function is that optic events are computationally tractable. For example, a spherical wave can be described by the plenoptic function as radially outgoing rays. The field magnitude of a spherical wave

degenerates as 1/r, where r is the radical distance. Traditional geometric optics models begin to show problems with increased distance from the point source as rays diverge spatially. However, with plenoptic functions, one can always modify the number of rays in the system: 1) rays leaving the domain of interest will be deleted; 2) rays can be added by interpolation to increase resolution. In the case of the spherical light wave of a point source, one can linearly interpolate rays at increased radical distances to assure adequate spatial resolutions. In fact, besides a few trivial differences, the plenoptic function is equivalent to the wave analysis in computational optics [9].

3.1.2 Image reconstruction

Image reconstruction in the light field camera refers to the transformation from light field images to actual images of objects. Technically, the maximum number of rays that can be acquired by a light field camera is determined by the resolution of the image sensor. As discussed in section 3.1.1, enriched ray information acquired through interpolation and computed/synthetic images can be achieved with image reconstruction algorithms.

The image formation of a light field camera can be shown as [10]:

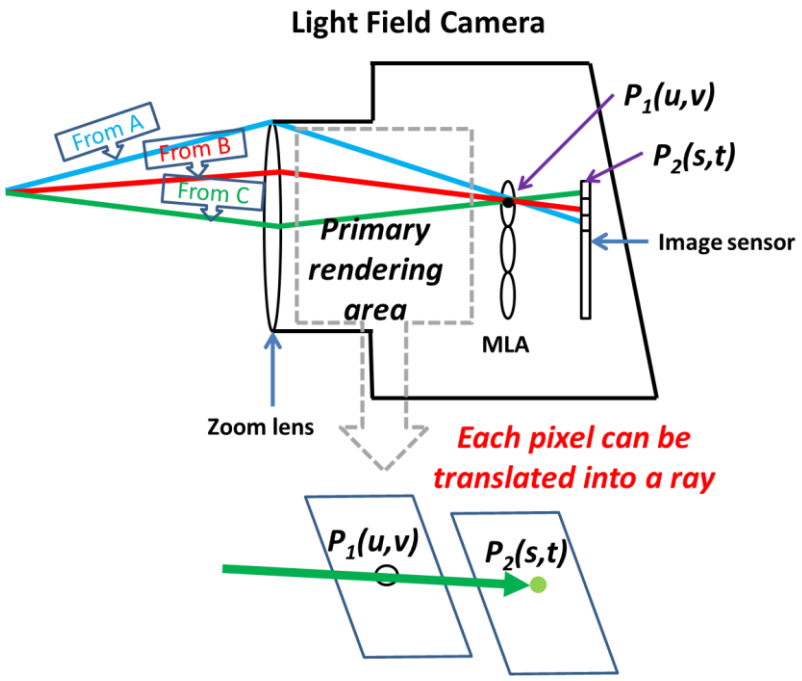

Figure 3. 1: Diagram of light field rendering inside a light field camera

In figure 3.1, we show that the center of a MLA cell is treated as a local retrieval center and the straight line between the retrieval center and a local pixel interprets a ray. Theoretically, each pixel represents a ray. By back tracing the rays to the primary rendering area (area between the zoom lens and the MLA), the primary plenoptic function can be established. The image and geometric dot array of the MLA centers contains all the necessary information of the light field camera. If the density of light rays is not adequate in the primary rendering area, interpolations can be added. Similarly, one can add a calibration process to account for the small aberrations caused by the MLA cells.

The fundamental ray interaction rule in the plenoptic function is free and linear propagation in a free space. To reconstruct the light field in the real world (outside the light field camera), additional functions need to be added. For example, in figure 3.1,

the light field outside the zooming lenses is retrieved by ray tracing through the lenslet set (with all geometric information known). And a computed scene can be reconstructed through the back tracing by a simulation sweep through the depth of view. In other words, the focused spot at arbitrary depth $z=z_0$ can be determined if rays with similar properties converge to the same geometric spot. Simultaneously, rays passing the vicinity of the same spot but fail to share similar properties with other rays can be intelligently filtered out.

Since most applications focus on the image site instead of the reality site, we narrow our discussions in the primary light field rendering area (inside the light field camera). A more general scenario can be applied by back tracing through the imaging lens to explore objects in the scene. In the primary rendering area, the following benefits are naturally acquired:

(1) An image point focused before/on/after each MLA cell can be determined by the pattern of ray spreading on the image sensor.

(2) The change of focal depth can be correspondingly achieved by computationally making rays converge before/on/after each MLA cell.

(3) Only a little knowledge of the zoom lens such as its f/# is required to reveal the light field changes of an image formation process.

Intuitively, if a perfect image point (sharp point spread function) falls on a MLA cell, the fan of rays matches the f/# of the image lens. If the image point is formed before the MLA cell, the fan of rays will be smaller than the f/# of the image lens. Comparatively, the fan of rays gets larger than the f/# of the image lens happens when the image point is formed behind the MLA cell. Based on the above principles, a

sharp image point can be identified and reconstructed locally by the ray spreading patterns under each MLA cell.

Technically, an all-sharp image can be reconstructed on the light field camera, where points at various focal depths are simultaneously sharp on the image [11]. However, based on human vision principles, the all-sharp image doesn't look natural and even causes some discomfort in viewing. Therefore, for the commercial version Lytro cameras [12], it only allows one specified focal depth that is variable by the user.

3.1.3 Incompatibility with coherent beam sensing

The Lytro camera, unfortunately has failed to achieve great commercial success. The major shortcoming of the light field cameras in its commercial implementation is the sacrifice of high image resolution in exchange for adjustable focal depth. Especially when auto-focusing becomes a standard technique for all digital cameras (including cellphone cameras), the ability of re-acquiring a focused image is less attractive.

The possibility of using the light field camera to perform wavefront sensing has been discussed by Researchers in the Canary Islands (as introduced in chapter 2). However, since all rays inside a laser beam have identical wavelength, the light field image will also be corrupted to some extent like ordinary camera images. Therefore, it can't apply in wavefront sensing directly. Besides, indirect methods such as imaging changes of sharp features (chapter 2.5) of object features are inconvenient.

3.2 Modified plenoptic camera

To acquire an informative image of coherent light sources, two preconditions need to be satisfied:

(1) Avoid interference conditions as much as possible.

(2) The phase front and amplitude information should be interpreted simultaneously.

Point (1) states that when interference is ruled out, each pixel value corresponds with the field amplitude information of one wave component instead of summarized field amplitude of several waves. Otherwise, the interpretation of the pixel value will be complicated. And the single point sample by a pixel can't be used to uniquely define all its wave components. The second precondition (Point 2) states that the complex amplitude of a coherent wave requires both the phase and amplitude distribution of the beam to be measured/retrieved successfully.

In general, the two preconditions can be treated as "coding/mapping" conditions in wavefront sensing that generates a decodable image of the laser beam. Then, a reconstruction process/algorithm is a "decoding" method that interprets the image back to the plenoptic function (that contains the phase front and amplitude distribution) of a laser beam.

Our study shows that by several modifications of the light field camera, it is possible to convert it into a wavefront sensor that can measure the phase and amplitude distortion in a coherent beam. In fact, the modification will cause a light field camera to lose its capacity to refocusat different focal depths but as a tradeoff grant it the ability to image a coherent beam. For convenience, we name the modified light field camera as "a plenoptic camera" as it maps the light field of a laser beam into an image.

3.2.1 Structure diagram

The fundamental structure diagram (2D and 3D) of the plenoptic camera can be shown by the following figures [13] [14]:

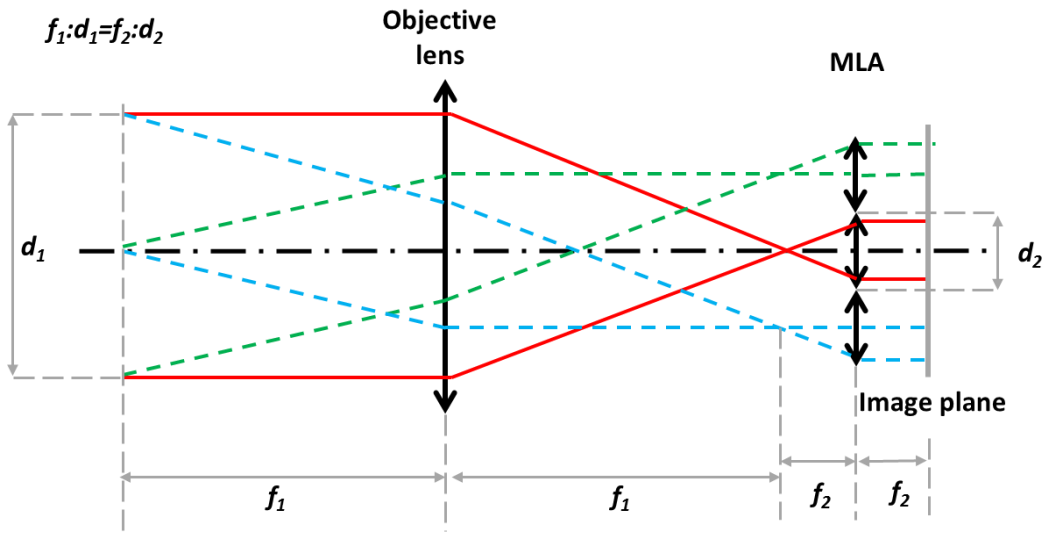

Figure 3. 2: 2D structure diagram of the plenoptic camera

In figure 3.2, f_1 and f_2 are the focal lengths of the objective lens and MLA cell respectively. The diameter of the objective lens is expressed by d_1, and the diameter of the MLA cell is expressed by d_2. Besides, we regulate that $f_1 >> d_2$ to justify the use of paraxial approximation. In fact, the typical ratio between f_1 and d_2 is 2500.

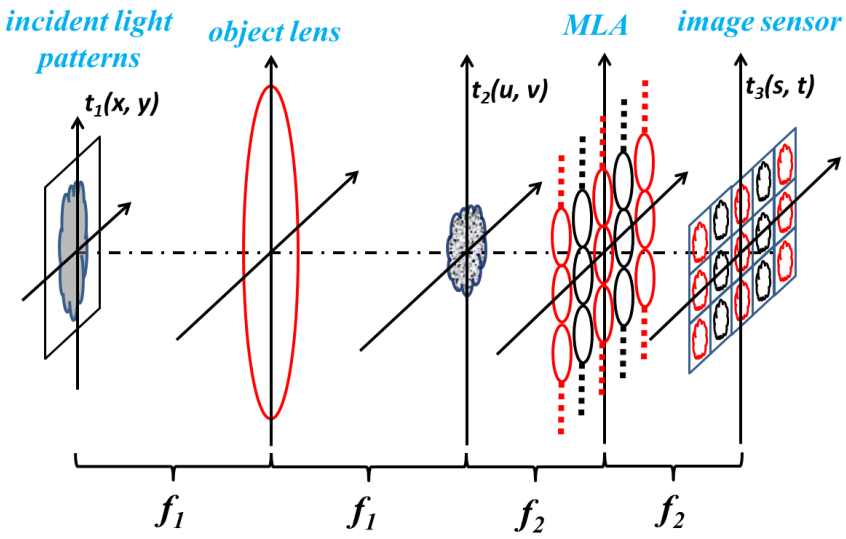

Figure 3. 3: 3D structure diagram of the plenoptic sensor

In figure 3.2 and figure 3.3, we show that a plenoptic camera is made by matching the f/# of the objective lens and the MLA and overlapping the back focal plane of the object lens and the front focal plane of the MLA. In short, the structure of the plenoptic camera can be treated as a mini "Keplerian" telescope array that shares a common objective lens.

Without loss of generality, the plenoptic image is obtained at the back focal plane of the MLA by an image sensor. The entrance pupil of the plenoptic sensor is defined as the front focal plane of the objective lens. The numerical aperture of the objective lens and a MLA cell is matched so that each cell image does not overlap with its neighbors. The requirement of the numerical aperture can be loosened as:

$$NA_{objective} \leq NA_{MLA} \tag{5}$$

However, in order to maximize the viewing aperture, equalization in equation (5) is typically used.

Intuitively, for an arbitrary patch (small wavelet that acts like a plane wave) that incident on the front focal plane of the plenoptic sensor, its phase front will be sampled by the front objective lens into a corresponding MLA cell. And its amplitude information will be sampled by the local MLA cell into an intensity pattern. For any other patch that overlaps geometrically but with slightly different propagation direction, it will be mapped to a different MLA cell and the interference pattern is avoided. Therefore we can use the MLA cell index to represent the phase information and the relative patterns inside a MLA cell to represent the intensity information.

3.2.2 Analysis with geometric optics

The matching of numerical aperture can be expressed by:

$$\frac{d_1}{f_1} = \frac{d_2}{f_2} \tag{6}$$

Without loss of generality, we express an arbitrary ray at the entrance of the plenoptic sensor in a 7D plenoptic function:

$$P_1 \triangleq (\rho_1, x_1, y_1, \alpha_1, \beta_1, \varphi_1; z_1) \tag{7}$$

In equation (7), ρ_1 is the photon density of the light ray. z_1 is the location of the entrance plane along the optic axis. The geometric coordinates of the ray at the entrance plane is expressed by x_1 and y_1. The angular information of the ray under paraxial approximation is expressed as α_1 and β_1. The phase of the ray is resembled by φ_1.

Similarly, the corresponding plenoptic function for the same ray at the image plane can be expressed as:

$$P_2 \triangleq (\rho_2, x_2, y_2, \alpha_2, \beta_2, \varphi_2; z_2) \tag{8}$$

Then the relations between P_1 and P_2 can be expressed as:

$$z_2 - z_1 = 2f_1 + 2f_2 \tag{9}$$

$$\rho_2 = \frac{f_1^2}{f_2^2}\rho_1 \tag{10}$$

$$(M, N) \triangleq \left(\left\lfloor \frac{\alpha_1 f_1}{d_2} + \frac{1}{2} \right\rfloor, \left\lfloor \frac{\beta_1 f_1}{d_2} + \frac{1}{2} \right\rfloor \right) \tag{11}$$

$$(x_2, y_2) = (Md_2, Nd_2) - \frac{f_2}{f_1}(x_1, y_1) \tag{12}$$

$$(\alpha_2, \beta_2) = \frac{f_1}{f_2}(\alpha_1, \beta_1) + \frac{d_2}{f_1}(M, N) \tag{13}$$

$$\frac{\partial(\varphi_1 - \varphi_2)}{\partial \alpha_1} = \frac{\partial(\varphi_1 - \varphi_2)}{\partial \beta_1} = 0 \tag{14}$$

Equation (9) and (10) can be easily obtained by the geometric configuration of the plenoptic sensor. The integer pair *(M, N)* in equation (11) represents the corresponding MLA cell that the light ray will propagate through. Equation (12) and (13) can be derived by analyzing the telescope formed by the objective lens and the MLA cell indexed by *(M, N)*. Equation (14) states that the phase change of the ray is stationary against small angular variation (also known as Fermat's principle).

Equation (6) to (14) state the rules of the plenoptic camera in imaging the laser beam in the forward direction (with geometric ray models). Intuitively, a plenoptic camera maps/codes the light field into an image. Similarly, the inverse mapping to "decode" the image can also be explained with geometric ray models. However, since the image sensor has a finite pixel size, quantization effects must be considered.

In general when the ray is sampled by each pixel on the image sensor, its geometric information and its photon contribution are recorded, while angular and phase information of the ray is lost. For simplicity, we can express the image formation of the plenoptic sensor as:

$$I(x_2, y_2) = \gamma S_{\square} \sum_{P_1 \to (x_2, y_2)} \rho_1 \tag{15}$$

In equation (10), γ represents the linear response between the pixel's numerical value and the total number of photons it collects. $S_{\square}$ denotes the size of the pixel. By inverse mapping, the contributive rays for specific pixel with coordinates (x_2, y_2) must satisfy:

$$(M, N) = \left(\left\lfloor \frac{x_2}{d_2} + \frac{1}{2} \right\rfloor, \left\lfloor \frac{y_2}{d_2} + \frac{1}{2} \right\rfloor \right) \tag{16}$$

$$(x_1, y_1) = \frac{f_1}{f_2} \left(M d_2 - x_2, N d_2 - y_2 \right) \tag{17}$$

$$(\alpha_1, \beta_1) \in \frac{d_2}{f_1} \left(M \pm \frac{1}{2}, N \pm \frac{1}{2} \right) \tag{18}$$

Equation (16) determines the cell indices on a plenoptic image. Equation (17) is derived directly from equation (12), and it means each spot on the plenoptic image corresponds with a particular location in the incident beam. Equation (18) is derived from equation (11), which determines the narrow fan of rays that illuminate the same spot on the plenoptic image. For simplicity, we pick the center value in equation (18) for the directional information of the back traced rays. Therefore, the maximum round-off error for rays' angular accuracy is $d_2/2f_1$. Besides, the pixel width $d_{\square}$ can't be infinitively small, and the maximum spatial round off error is $f_1 d_{\square}/2f_2$. For example, given f_1:d_2=2500, $d_{\square}$=6μm and f_1:f_2=100, the maximum spatial and angular round off

errors are 0.3mm and 0.2mrad respectively. Intuitively, if the whole beam is confined by adaptive optics approaches into one image cell on the plenoptic sensor, it means that the arriving beam has maximum divergence of 0.4 mrad in the above configurations. It can also be shown that by increasing f_1, more angular accuracies can be achieved at the cost of losing spatial accuracy and vice versa.

With the acquired plenoptic function of the laser beam, a reconstruction of the phase front can be achieved by inverse mapping the light field to reality (real world). Typically, the reconstruction is performed on the front focal plane of the object lens. Intuitively, by tracking the angular momentum to the entrance pupil, the phase information is acquired. Similarly, by tracking the intensity to the entrance pupil, the field amplitude information is acquired. A simplified 2D phase reconstruction diagram can be shown by the following diagram. Since the reconstruction interprets the rays into binary signals of "1" and "0", we call it a "0^{th} order reconstruction" or "Naïve" reconstruction (because it is extremely simple).

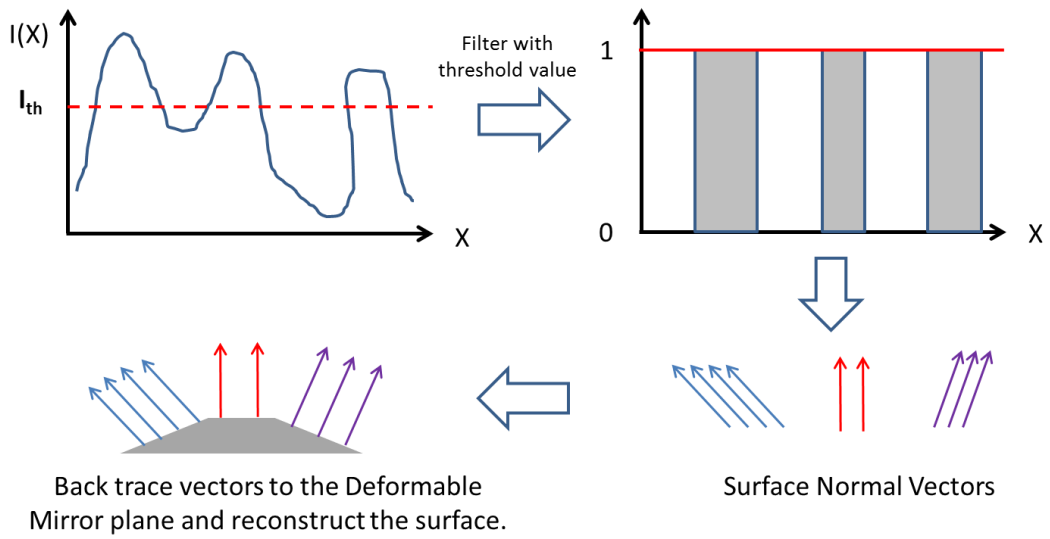

Note: All the information used is $I(X)^0$. Where interferometer need to use $I(X)^1$.

Figure 3. 4: 2D simplified diagram of phase front reconstruction

In figure 3.4, the phase reconstruction algorithm is implemented by back tracing the rays in different cells to the front focal plane. Since the phase distortion scatters the rays into different MLA cells, the back tracing process will determine where the rays originate from in the entrance pupil. Simultaneously, the cell indices carried by the rays represent the distribution of phase distortions. To increase the SNR (signal noise ratio) of the phase front reconstruction, we use a threshold intensity (pixel value) to select pixels that satisfy the minimum illumination condition. More formal reconstruction algorithms will be elaborated on in section 3.4.

3.2.3 Analysis with wave optics

As discussed in section 3.1, the plenoptic function equalizes the wave analysis with adequate resolution. We can also use wave analysis to explain the function of the plenoptic camera by using concepts in Fourier optics [15]. A fundamental conclusion in Fourier optics states that in the paraxial approximation, the complex amplitude of light fields at the front and back focal planes of a lens are Fourier transforms of each

other. The terms “front” and “back” are dictated by the propagation direction of the light. An illustration diagram can be shown as:

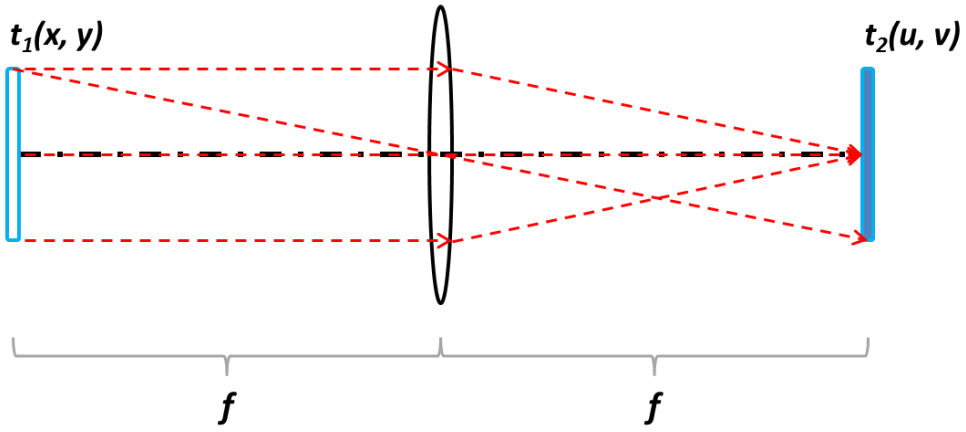

Figure 3. 5: Diagram of basic Fourier optics concept

An analytical formula for the Fourier transform of a thin lens is expressed as:

$$t_2(u,v) = \frac{1}{j\lambda f}\int_{-\infty}^{+\infty}\int_{-\infty}^{+\infty} t_1(x,y)\exp\left(-j\frac{2\pi}{\lambda f}(xu+yv)\right)dxdy \tag{19}$$

In equation (19), $t_1(x, y)$ and $t_2(u, v)$ are the complex amplitude of the field at the front and back focal plane of the thin lens respectively. The focal length is represented by f. A Fourier transform is achieved by regarding the spatial frequency components as:

$$f_x = \frac{u}{\lambda f}, \qquad f_y = \frac{v}{\lambda f} \tag{20}$$

Thus, neglecting aperture limiting effects, the Fourier transform conducted by a thin lens swaps the geometric and angular information of the incident light field. The structure diagram of our plenoptic sensor is replotted in figure 3.6 as:

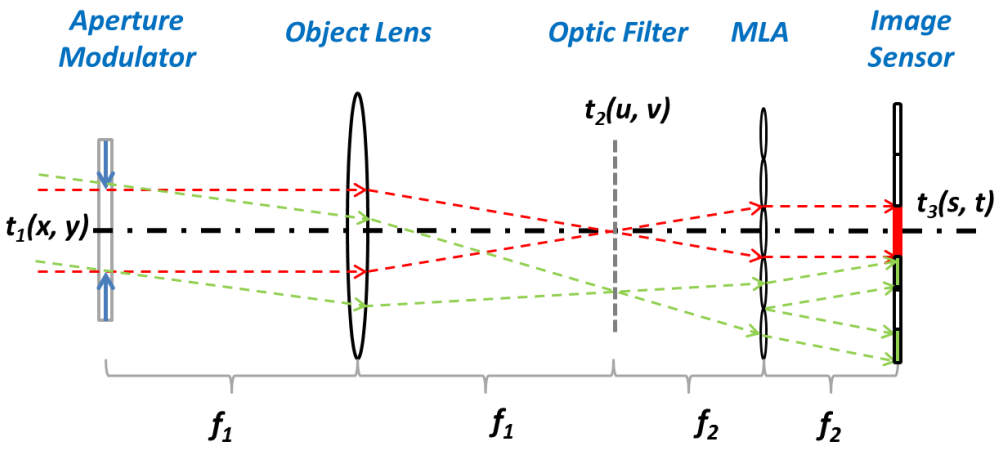

Figure 3. 6: Diagram for wave analysis of the plenoptic sensor

The wave analysis of the objective lens in the plenoptic sensor is the same as in equation (19). However, the Fourier transform by each MLA cell should consider the aperture limiting effects since the width of the light field at the back focal plane of the objective lens is larger than the width of a MLA cell. Thus, a pupil function should be added to the integral when applying equation (19). Without loss of generality, one can express the field of $t_3(s, t)$ as a superposition of transforms performed by each MLA cell:

$$t_3(s,t) = \sum_{M,N} t_3^{M,N}(s',t') \tag{21}$$

In equation (21), the integer pair (M, N) corresponds to the index for each MLA cell in a Cartesian layout. (s', t') are the local coordinates in the domain of each MLA cell with relation to the "global" coordinates (s, t), as:

$$(s',t') = (s - Md, t - Nd) \tag{22}$$

Symbol d in equation (22) represents the pitch of the MLA (spacing between neighboring micro-lens centers). Therefore, the field at the back focal plane of the MLA for each micro-lens can be solved as [14]:

$$t_3^{M,N}(s',t') = \frac{1}{j\lambda f_2}\iint t_2(\mathrm{u}'+\mathrm{Md},\mathrm{v}'+\mathrm{Nd})\,\mathrm{rect}\left(\frac{\mathrm{u}'+\mathrm{s}'}{d}\right) rect\left(\frac{\mathrm{v}'+t'}{d}\right) e^{-\frac{j2\pi}{\lambda f_2}(u's'+v't')}\,du'\,dv' \tag{23}$$

In equation (23), function *rect(*)* denotes the rectangular pupil function for each MLA cell. *(u', v')* are local coordinates for the light field $t_2(u, v)$ viewed by each MLA cell that satisfy the relation:

$$(u',v') = (u - Md, v - Nd) \tag{24}$$

The aperture limiting effect is generally regarded in optics as the "vignetting" effect to indicate the reduced effective aperture for off-axis points. It is reflected in equation (24) by the pupil function. Often "vignetting" effects are treated as disadvantages that should be carefully avoided or compensated for in optic designs. However, these effects serve as an inter-block relation in the plenoptic sensor since the coordinates (*u', v'*) and (*s', t'*) are included in the same pupil function. In other words, each point (*s', t'*) in a MLA cell collects information from a slightly different area on the field of $t_2(u, v)$, where *(u, v)* represent the angular spectrum of the field. Thus the "vignetting" effects provide finer adjustments of angular information in addition to the information provided by the index of the MLA cell *(M, N)*.

Combining equation (22) and (24) one can derive the wave solution for the plenoptic sensor. Due to the limited range of *(M, N)*, one can swap the order of summation and integration. As a result, the general solution is expressed as:

$$\begin{aligned} t_3(s,t) = \frac{1}{j\lambda f_2}\iint t_2(u,v)\sum_{M,N} rect\left(\frac{u+s-2Md}{d}\right) rect\left(\frac{v+t-2Nd}{d}\right) \\ \exp\left\{-j\frac{2\pi}{\lambda f_2}[(u-Md)(s-Md)+(v-Nd)(t-Nd)]\right\} dudv \end{aligned} \tag{25}$$

An intuitive observation from equation (25) is that the effective integral area is a square of size $d \times d$ (d is the pitch length of the MLA) for any pixel with fixed coordinates (s, t). Each integral is based on the value of $t_2(u, v)$ with a linear phase tilt modulation. Thus the intensity obtained on $I_3(s, t)$ is the magnitude of a local Fourier transform with a linear geometric shift depending on the value of (s, t).

For example, if the incoming light field consists of a group of interfering light patches (small "plane waves" with apertures), $t_2(u, v)$ will be a sum of delta functions in the form:

$$t_2(u,v) = \sum_{i=1}^{N} A_i e^{j\varphi_i} \cdot \delta(u - u_i, v - v_i) \tag{26}$$

After propagation through the MLA, the situation can be classified into 2 major cases:

Case 1: All the (u_i, v_i) are distinctive enough that they are observed by different MLA cells.

Case 2: There exists more than one pair (u_i, v_i) that falls in the same domain of a single MLA cell.

In case 1, one can easily determine the first order tilts in the complex amplitude of the field as each patch is imaged by an individual MLA cell. Thus the complex amplitude can be expressed as:

$$t_1(x,y) = \sum_{i=1}^{N} \gamma_0 \frac{\sqrt{I_i} f_2}{f_1} \exp\left(j2\pi d \frac{M_i x + N_i y}{\lambda f_1} + j\varphi_i \right) \tag{27}$$

In equation (27) γ_0 is a constant coefficient relating the optic field strength to the square root of pixel values. $(\gamma_0)^2$ represents the ratio between local wave intensity and corresponding pixel value on an image sensor. I_i is the pixel value for the i^{th} patch that represents the intensity. We arbitrarily neglect the intensity distribution to

emphasize the capability of the plenoptic sensor in extracting the phase gradient. In fact, the intensity distribution is preserved under the transforms of the plenoptic sensor's lens system down to the limit of pixel sizes. However the initial phase information (DC value of phase) is lost as the patches don't interfere with each other when imaged by different MLA cells.

In case 2, if more than one patch propagates through the same MLA cell, their initial phase difference as well as their first order phase tilts can be revealed. Without loss of generality, assume 2 patches with amplitude A_1 and A_2 and phase difference $\Delta\varphi$ are observed by the same MLA cell. Then, the complex amplitude after the MLA cell can be expressed as:

$$t_3^{M,N}(s',t') = \frac{A_1}{j\lambda f_2} rect\left(\frac{u_1 + s' - Md}{d}\right) rect\left(\frac{v_1 + t' - Nd}{d}\right) + \frac{A_2 e^{j\Delta\varphi}}{j\lambda f_2} rect\left(\frac{u_2 + s' - Md}{d}\right) rect\left(\frac{v_2 + t' - Nd}{d}\right) \exp\left\{ j\frac{2\pi}{\lambda f_2}[(u_2 - u_1)s' + (v_2 - v_1)]t' \right\} \quad (28)$$

Note that we have ignored the common phase that has no influence on the image. The corresponding sub-image can be written as:

$$I_3^{M,N}(s',t') = \begin{cases} \eta A_1^2 & (u_1', v_1') \in \{A(s',t')\} \ \textit{while} \ (u_2', v_2') \notin \{A(s',t')\} \\ \eta A_2^2 & (u_1', v_1') \notin \{A(s',t')\} \ \textit{while} \ (u_2', v_2') \in \{A(s',t')\} \\ \eta\left[A_1^2 + A_2^2 + 2A_1A_2\cos(\Delta u \cdot s' + \Delta v \cdot t' + \Delta\varphi)\right] & \textit{both} \in \{A(s',t')\} \end{cases} \quad (29)$$

In equation (29), *{A(s', t')}* is the integral area determined by *(s', t')* from equation (23). We use η as a coefficient representing the linear relation between pixel value

and field intensity to simplify the result. Thus if the two patches are imaged by the same MLA cell, their initial phase difference as well as their first order phase tilt can be retrieved.

An overall relation between complex amplitude of the field and the final image can be derived by combining equation (19) and equation (25). The final result is expressed as:

$$t_3(s,t) = -\frac{1}{\lambda^2 f_1 f_2} \sum_{M,N} \int_{2Md-d/2-s}^{2Md+d/2-s} \int_{2Nd-d/2-t}^{2Nd+d/2-t} \int_{-\infty}^{+\infty} \int_{-\infty}^{+\infty} t_1(x,y)$$
$$\exp\left(-j\frac{2\pi}{\lambda f_1}(xu+yv)\right)\cdot \exp\left(-j\frac{2\pi}{\lambda f_2}(u-Md)(s-Md)\right)\cdot\exp\left(-j\frac{2\pi}{\lambda f_2}(v-Nd)(t-Nd)\right) dxdydudv \quad (30)$$

It is not surprising to find that the geometrical optics approach provides results very close to the analytical result in a wave solution approach, unless the wavefront oscillates at a high spatial frequency. Thus either approach can be used for extracting light field information from the image obtained by the plenoptic sensor. Nevertheless, it is a little more complex to perform the inverse mapping from a plenoptic image to the actual wavefront of the beam. Typically, under the assumption that all the patches in the plenoptic image have a flat phase front (each patch can be assigned a unique value of phase front), we can back propagate the wavelets to the front focal plane of the plenoptic camera and determine the phase difference by a continuity assumption [16] (no step function at the edge of two merging patches in back propagation).

3.3 Plenoptic sensor

The plenoptic sensor is a streaming plenoptic camera that can track the dynamic changes of phase and amplitude distribution in a laser beam. Since atmospheric

turbulence structure changes all the time, it requires adaptive optics to perform instant detection and correction on the distorted phase front. Conventionally, Shack-Hartmann sensors [18] have been proved to be useful in correcting image distortions in astronomy applications when optic signals of a celestial image get weakly distorted in passing through the Earth's atmospheric layer. In horizontal paths on the earth, due to the greatly increased level of turbulence, Shack-Hartmann sensors can't reconstruct the wavefront reliably due to effects (as discussed in section 2.1) of scintillation, self-interference, large oscillation in angle of arrival as well as beam wander effect. Therefore, the plenoptic sensor is developed as a much more powerful wavefront sensor than the Shack-Hartmann sensor.

Without loss of generality, the plenoptic sensor creates a plenoptic function that has an extra parameter of time, expressed as:

$$P_1 \triangleq \left(\rho_1, x_1, y_1, \alpha_1, \beta_1, \varphi_1; z_1, t\right) \tag{31}$$

In equation (31) we add the universal time parameter to track the change of the light field inside a distorted laser beam. In the worst case, when the light fields between neighboring time stamps are irrelevant to each other (which may be caused by a slow frame rate of the sensor or rapid changes in the turbulence), the complexity of the plenoptic function is increased by 1D. With adequate streaming speed, the correlation time τ needs to be considered. Equivalently, this means that frames recorded earlier than τ are independent of the current turbulence situation and can therefore be discarded. In fact, the correlation time serves as the fundamental speed requirement for the plenoptic sensor to sense and figure out a correction solution. Intuitively, if

turbulence changes at 100 Hz, the minimum time budget for the plenoptic sensor is 10ms.

3.3.1 Structure diagram

The structural diagram of the plenoptic sensor can be illustrated by the following figure:

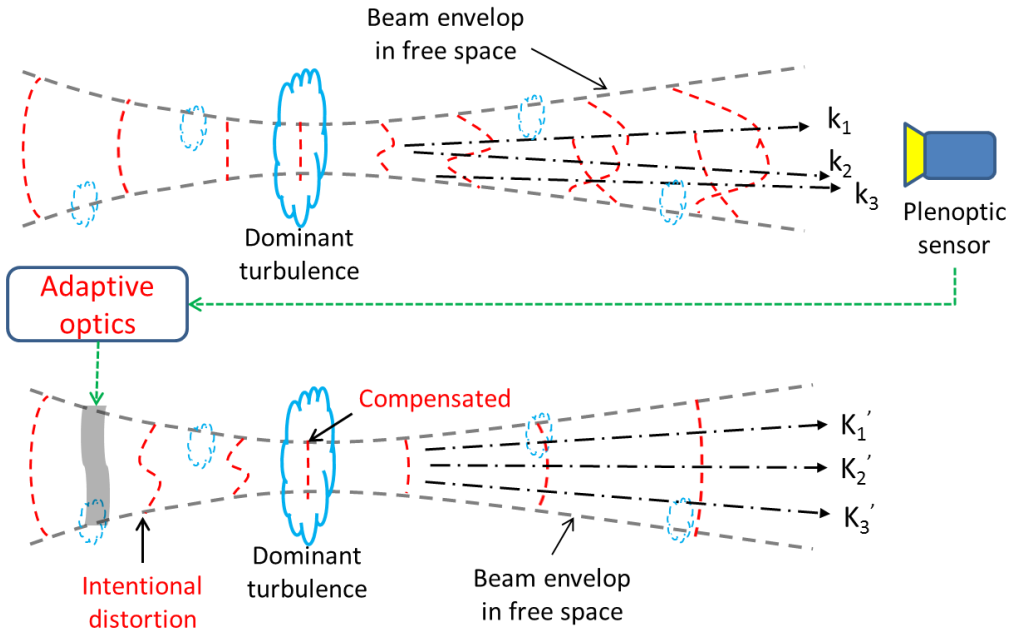

Figure 3. 7: Basic structure diagram of the plenoptic sensor in sensing and correcting laser beam propagation problems

Figure 3.7 show that when a collimated laser beam gets distorted by atmospheric turbulence, it is decomposed into patches that scatter in disordered directions. By using a plenoptic sensor to capture the distribution of those patches and reconstruct the "disorder" patterns (a phase screen that causes the most identical effect), the adaptive optics module can insert a compensation phase screen to bring down the

disorder effects of scattering patches and “deliver” the power of the beam onto intended target.

The time span between the wave front sensing and adaptive optics compensation operation needs to be smaller than the correlation time τ. This time span includes: image acquisition time, algorithm processing time, and set up time for AO system. Therefore, a good arrangement of data structure, streaming controls, information storage and processing help to optimize the efficiency of the AO system in collaborating with the plenoptic sensor.

3.3.2 Streaming controls

The streaming of information in the plenoptic sensor and its cooperative AO system can be shown by the following diagram:

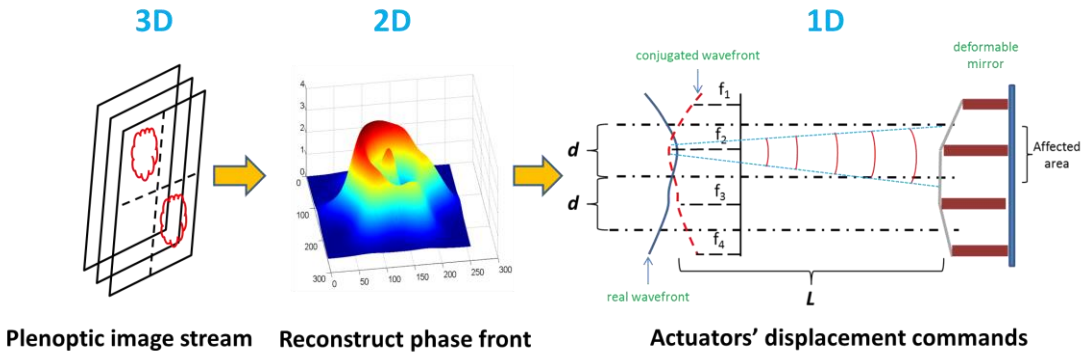

Figure 3. 8: Structure of information stream in the overall wavefront sensing and correcting AO system (integrated with a plenoptic sensor)

Figure 3.8 shows the data flow in the plenoptic sensor, computer (or any computation module), AO device respectively. The data stream on the plenoptic sensor is 3D, as a stream of time varying plenoptic images. On the computer site, each plenoptic image is translated into plenoptic functions and further assembled into the actual phase front

distortions. By the reconstructed wavefront patterns within the correlation time τ, the actual phase front deformation can be credibly determined. On the AO system site, due to the finite number of actuators used to achieve phase front compensation, the reconstructed wavefront deformation is further compressed to a vector array of actuators' displacement commands.

Therefore, a naïve (simple and direct) approach is to arrange the flow in series order (queue). And the overall loop time is determined by:

$$t_{\Sigma} = t_I + t_A + t_D \tag{32}$$

In equation (32), t_I represents the image acquisition time, t_A represents the algorithm processing time and t_D represents the AO device's set up time. Because the data stream is arranged in sequential order, the stack of time in equation (32) means that each data processing stage needs to wait for its previous stage of processing to finish. Evidently, the naïve data flow arrangement makes the sensing and control loop simple and easy to diagnose. Intuitively, at any arbitrary moment only one of the three modules is enabled. It is also clear that if any part of the data processing becomes considerably longer than the others, it becomes the bottleneck for the system's operation speed.

A more advanced data flow control can be arranged by allowing each module to work independently so that the following loop time can be achieved:

$$t_{\Sigma} = \max\{t_I, t_A, t_D\} \tag{33}$$

The following diagram helps to illustrate the achievement of the advanced data stream arrangement (we arbitrarily assume that the computation time is the longest in the loop):

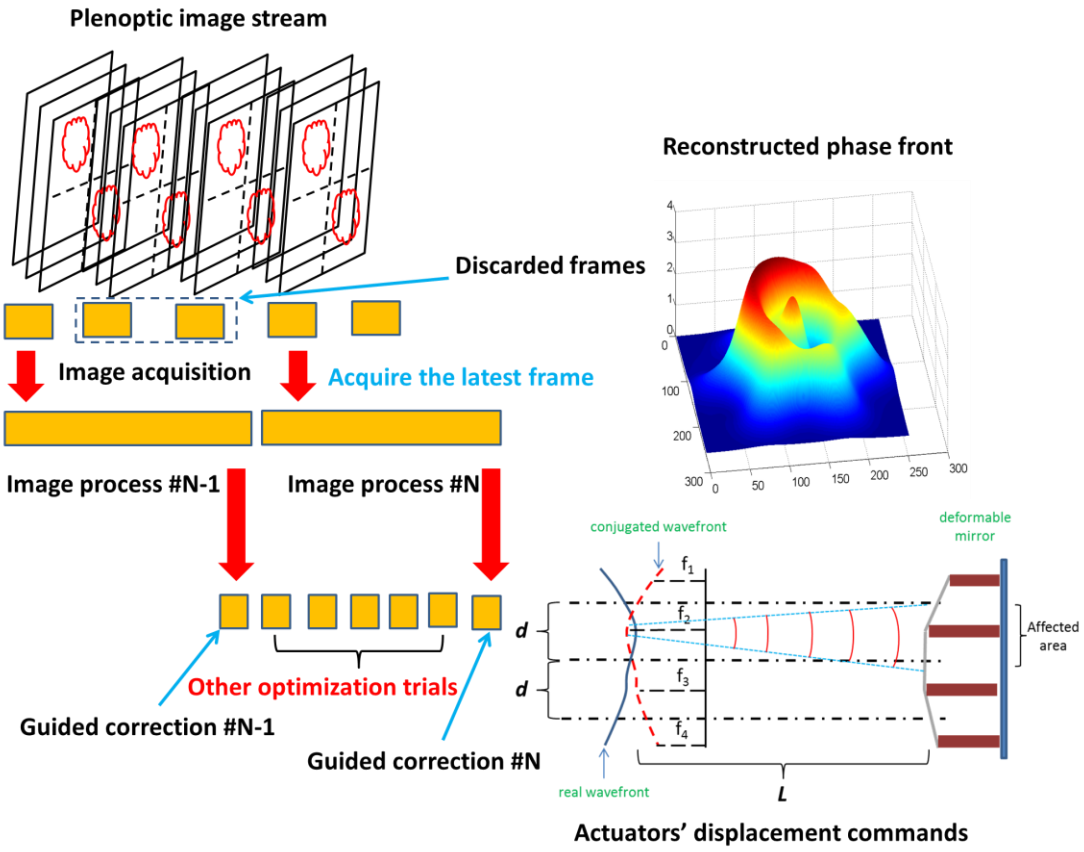

Figure 3. 9: Advanced structure of information stream and data processing

Figure 3.9 shows the advanced arrangement of the data flow structure that can achieve the minimum loop time regulated by equation (33). Assume that the image processing time is the longest (which is typically the case in reality), we can let the plenoptic sensor to work in a free running mode and allow the AO device to perform a few other iteration trials of optimization (such as SPGD [17]) before the computation loop is finished. Therefore, the overall loop time is optimized to be the time consumption of the slowest module in the system. Improvement can be made by further optimizing the slowest module (such as using parallel computing devices to speed up the algorithm). In fact, by redesigning the flow process and using a parallel

reconstruction algorithm, the system can operate at a speed that is comparable with the maximum frame rate of the plenoptic sensor.

3.3.3 Information storage and processing

The plenoptic sensor and its cooperative adaptive optics (AO) system are different devices and each carries certain type of memory storage hardware such as cache, buffer or RAM. Therefore, a careful consideration of the form of data in each processing step is necessary.

Without loss of generality, we can break down the data processing and transmission in the following categories:

(1) Image stream: raw images are acquired on the camera's buffer and copied to the computer's memory.

(2) Light field rendering: the image data stored on the computer site are processed into the plenoptic function of the light field at the entrance pupil of the sensor.

(3) Phase front reconstruction: the most likely (ML) phase front that causes the scattering patterns of the light field are generated on the computer site.

(4) Sending commands to AO: the computer samples the reconstructed phase front based on the format of the AO device and the vector command is sent to each actuator.

Evidently, the computer compresses the plenoptic image flow onto a vector of control commands for the AO device. Therefore, it is of vital importance to perform the processing as swiftly as possible. In general, the algorithm is linear if it satisfies the following relation:

$$\bigcup f\left(P_i\right) = f\left(\bigcup P_i\right) \tag{34}$$

Equation (34) states that in a linear algorithm the set assembly and processing algorithm are interchangeable with each other. Parallel computing can be invoked to speed up the process. Ideally, for a plenoptic image with basic resolution of 1024×1024, the parallel algorithm can be 1 million times faster given 1024^2 threads.

3.4 Reconstruction algorithms

The reconstruction algorithms establish the relations between plenoptic images and certain optic events in the plenoptic sensor's field of view. For the purpose of this chapter in detecting laser beam distortion through random media, we describe the optic event as the phase and amplitude distortions of the beam at the entrance of the plenoptic sensor. Other optic events such as image distortion and partial reflection can be analyzed with specific reconstruction algorithms, which will not be elaborated on in this chapter.

The fundamental translation from a pixel on plenoptic image to a pencil of rays in the light field can be illustrated by the inter-cell indices *(M, N)* that represent which cell the pixel locates in and the intra-cell indices *(S, T)* that represent the location of the pixel inside a cell image. In general we use *I(M, N, S, T)* to represent the pixel, where *I* stands for the pixel value ranged from 0-255 in monochrome 8-bit machine vision cameras. For simplicity, we assume symmetry is satisfied where the center cell is indexed by *(0, 0)* and the center pixel inside a cell is indexed by *(0, 0).*

The phase front tilt can be expressed for the pencil of rays as:

$$\nabla\Phi = \frac{d}{f_1}(M, N) \tag{35}$$

The location of the pencil of rays can be expressed as:

$$\vec{r} = \frac{f_1 d_{\square}}{f_2}(S,T) \tag{36}$$

In equations (35) and (36), d represents the pitch length of the MLA and d□ represents the width of the pixel. The focal length of the objective lens and MLA are represented by f_1 and f_2 respectively. The field intensity of the pencil of rays is represented by $I(M, N, S, T)$. It is evident that the translation algorithm from the plenoptic images to the light field rays is simple and linear. Based on the light field, different algorithms depending on the accuracy and speed requirement of reconstruction are available.

3.4.1 Full reconstruction algorithm

The full reconstruction algorithm is defined if the algorithm has used all the pixels in a plenoptic image. For instance, if the plenoptic image is composed of 1024×1024 pixels, the input of the algorithm is 1 million pixels. Since the entire image is used for reconstruction, the full reconstruction is regarded as "lossless" reconstruction. The detailed steps are shown as:

1. Select an MLA cell and its corresponding block image as a geometric reference.
2. Shift all nonzero block images to the block of the reference image and extend the scalar pixel values to a cluster of vectors with baseline directions extracted from MLA index *(M, N)* and their length proportional to the pixel brightness (ray intensity).
3. Adjust the vectors' direction according to their relative locations in the block due to the "vignetting" effect, or alternatively use equation (16).
4. Back propagate the rays to the depth of the optic event (dominant turbulence location).

5. Filter out rays that are traced out of the reasonable range and rays with abruptly different angles from their geometric neighboring rays (ignore unreasonable rays).
6. Project the beam propagation to the reconstruction plane assuming no turbulence and reshape it in a vector form with the same geometric resolution as in step 4.
7. Combine the ray patterns before and after the "phase screen" to extract the gradients of phase screen.
8. Build the phase screen according to its gradient profile.

Intuitively, the gradients of the phase will cause variations of Poynting vectors in the wave that can be picked up by the plenoptic sensor. Therefore, the phase screen's scattering patterns can be largely retrieved by backward ray tracing. The gradient of phase distortion can be reconstructed as:

$$\nabla_{i,j}\phi(\mathrm{x},\mathrm{y};\mathrm{z}=\mathrm{z}') = -\frac{1}{2}\nabla_{i,j}\phi_{project}(x,y;z=z') + \frac{\iint\limits_{I>I_{th}} I(\mathrm{s},\mathrm{t};\mathrm{z}=2f_1+2f_2)\left[\frac{2nd\cdot(M,N)-n\cdot(\mathrm{s},\mathrm{t})}{f_1}\right]dsdt}{2\iint\limits_{I>I_{th}} I(\mathrm{s},\mathrm{t};\mathrm{z}=2f_1+2f_2)dsdt} \quad (37)$$

The integral area in equation (37) is the area of the PSF (point spread function) for each point source located at *(x, y; z=z')* with *z=z'* indicating the plane of reconstruction. In addition, due to the continuity of a phase screen, an extra layer of filtering can be applied based on the fact that any integral loop of the phase gradient equals zero. In fact, this law should be satisfied for all reconstruction algorithms of a continuous phase screen.

A demonstrative example for the full reconstruction algorithm can be shown by a "defocus" *Z(2, 0)* phase distortion, the reconstruction result is shown as:

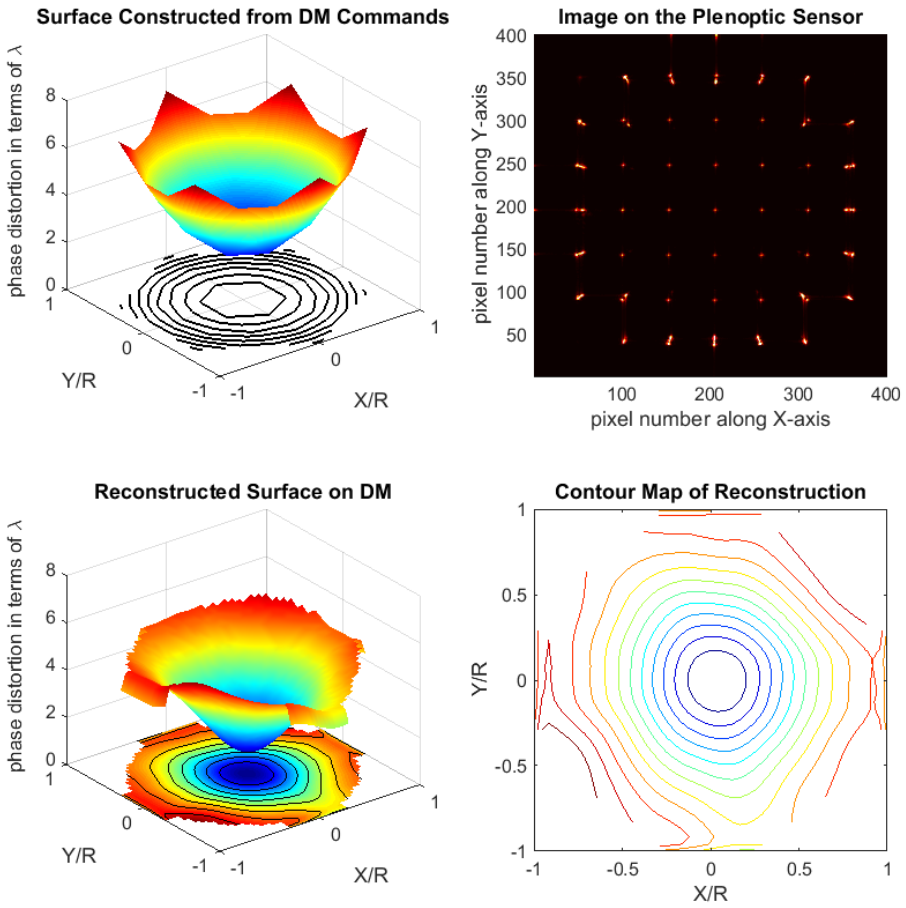

Figure 3. 10: Result for Zernike Z(2,0) phase distortion with full reconstruction algorithm

In figure 3.10, the upper-left plot shows the shape and magnitude of the phase distortion that is applied to the deformable mirror. A contour plot of the deformation is shown on *X*-*Y* plane. The upper-right plot in figure 3.10 shows the image on the plenoptic sensor when a "Defocus" command is sent to the DM. We only show the illuminated blocks on the image sensor. The size of the image sensor (resolution=1024×1024, pixel pitch=5.5μm) supports a maximum number of 18×18 blocks of sub-images. Equivalently, the maximum detectable distortion for the plenoptic sensor is $\pm 1.4\lambda/mm$. In the case of the "Defocus", the furthest block from the center is *(M=4, N=0)* and the corresponding maximum tilt can be calculated as 0.6λ/mm. The "Defocus" can be expressed as:

$$Z_2^0(\rho,\theta) = A \cdot \rho^2 \qquad 0 \le \rho \le 1,\ \theta \in [0, 2\pi) \tag{38}$$

The symbol *"A"* in equation (38) represents the magnitude of the distortion (*A=4095* in the case of "Defocus"), while ρ and θ represent the normalized radius and angle respectively for the Zernike polynomial. Intuitively, the gradient of the "Defocus" function increases symmetrically when the radius ρ increases. The gradient at each spot *(ρ, θ)* is mapped into different blocks of the deformable mirror. Furthermore, the observation that the most outside blocks are illuminated with larger areas reflects that the gradients changes faster when the radius ρ increases.

The lower-left plot in figure 3.10 shows the reconstruction result of the deformable mirror's surface. According to the algorithm steps of single phase screen reconstruction (algorithm 1), the center block of the plenoptic image is selected as the reference block and the reconstruction achieved by examining all the illuminated blocks. The clipping at the edges of the reconstruction are because of the lack of boundary conditions. There is no information about further phase variation outside the edge of the reconstructed surfaces. Therefore, we simply set the reconstructed phase value outside the edges to be zero. A contour plot is presented on the *X*-*Y* plane.

The lower-right plot in figure 3.10is a detailed contour map of the reconstructed surface. The contour plot projects the 3D result of the reconstructed phase screen into a 2D plot and helps to show the details of the reconstruction. In the case of "Defocus", the contour plot shows the concentric rings of the deformation. It looks similar to the contour plot of the commands at the upper-left plot in figure 3.10.

Using the reconstruction algorithm, one can determine:

(1) The geometrical information of light patches (rays) at the plane of distortion. (Algorithm steps 1, 2 and 4)

(2) The angular information of light patches (rays) at the plane of distortion (Algorithm steps 1, 2 and 3)

(3) The phase gradient along the X axis and Y axis. (Algorithm steps 5, 6 and 7)

A detailed explanation of the algorithm can be illustrated by figure 3.11:

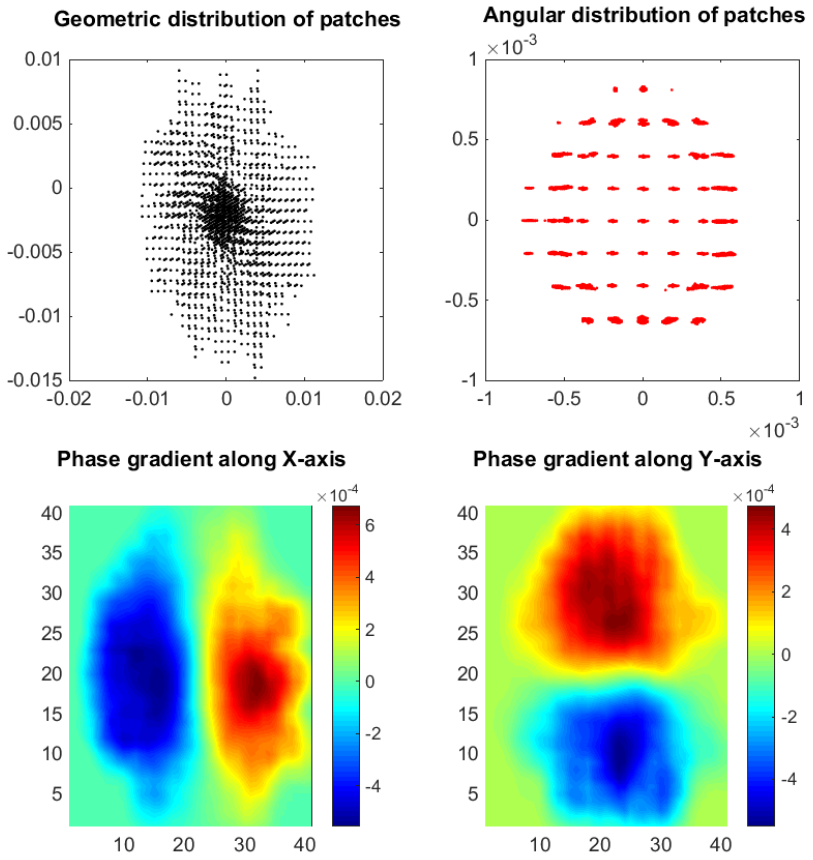

Figure 3. 11: Detailed explanation for full reconstruction algorithm on the "Defocus" phase distortion case

In figure 3.11, the upper-left plot shows the geometric distribution of light patches at optimized back tracing depth, with each dot representing a small patch (or single ray). The optimized depth (the plane of reconstruction) is determined by back propagating the rays until

the intensity distribution resembles the beam profile before encountering the phase screen (a Gaussian distribution in our experiment). The upper-right plot shows the distribution of the directions of the patches (rays), with each dot representing a small patch (or single ray). The angular distribution of patches results from the gradient of the phase change and is extracted from the image on the plenoptic sensor primarily by the block index *(M, N)* and adjusted by the actual positions of rays on the reconstruction plane. Based on the geometric and directional information of light patches (rays), the phase gradient graphs can be determined by equation (37). The results of the phase gradient along the X axis and Y axis are presented in the lower-left and lower-right plots in figure 8 respectively. With all the necessary information, algorithm step 8 can be completed to derive the results demonstrated in figure 3.10.

It is easy to see in equation (37) that the full reconstruction algorithm uses the statistical weighting average of each pixel to provide the overall results. In other words, each pixel suggests a piece of information about the phase and intensity distribution of the beam at the entrance pupil, and the reconstruction is achieved by examining through the entire image. In the full reconstruction algorithm, no information will be arbitrarily ignored and the outliers of pixels will be neutralized due to the weak law of large numbers (WLLN).

3.4.2 Fast reconstruction algorithms

Admittedly, the full reconstruction algorithm that examines every pixel in a plenoptic image provides a reliable and complete result that includes the phase and amplitude distribution of the beam. However, a lot of situations and applications don’t require full knowledge of the distorted beam. For instance, knowing the phase distortion is adequate to make significant improvement in remote imaging, free space optics (FSO)

communication and directed energy applications. Therefore, a fast reconstruction algorithm that can quickly resolve the phase front of the beam is favored over a thorough and complete solution.

In general, a fast reconstruction algorithm only requires a small portion of pixels on a plenoptic sensor. Typically, "information loss" will happen in a fast reconstruction algorithm due to the ignorance of raw image data. However, as a tradeoff, a much faster speed can be achieved and the overall AO corrections can be improved.

In this section, we will elaborate on a "Tree" reconstruction that is based on graph theory and a "Checkerboard" reconstruction based on the Poisson equation of the phase front.

"Tree" Reconstruction Algorithm:

The overall purpose of image processing is to translate a plenoptic image into executable commands on a deformable mirror (DM) that has a finite number of actuators. If the DM has N actuators, the algorithm result is an N-dimension vector. If the phase screen is reconstructed on the surface of a deformable mirror (named as the "correction plane" in the following discussion) and each recovered spot geometrically corresponds to one of the actuators in the device, the vector can be explicitly expressed as:

$$g_j = -\frac{1}{2}\delta_{ij} f_i \tag{39}$$

In equation (39), f_i is the reconstructed phase front value for the i^{th} channel of actuator on the DM. The phase front values are real numbers calculated based on a common reference point. The j^{th} actuator's displacement value is expressed by g_j and the value -1/2 accounts for the DM's reflective surface. Intuitively, equation (39) points out that a simple compensation command can be formed if the reconstruction happens on the plane of the DM and only the

spots coincide with the actuators need to be reconstructed. Therefore, the situation resembles a graph theory problem: we can generate a graph that maps the actuators in a DM into vertices and the edge connecting two vertices represents the retrieved phase difference between them.

An illustration diagram of the phase compensation can be shown as:

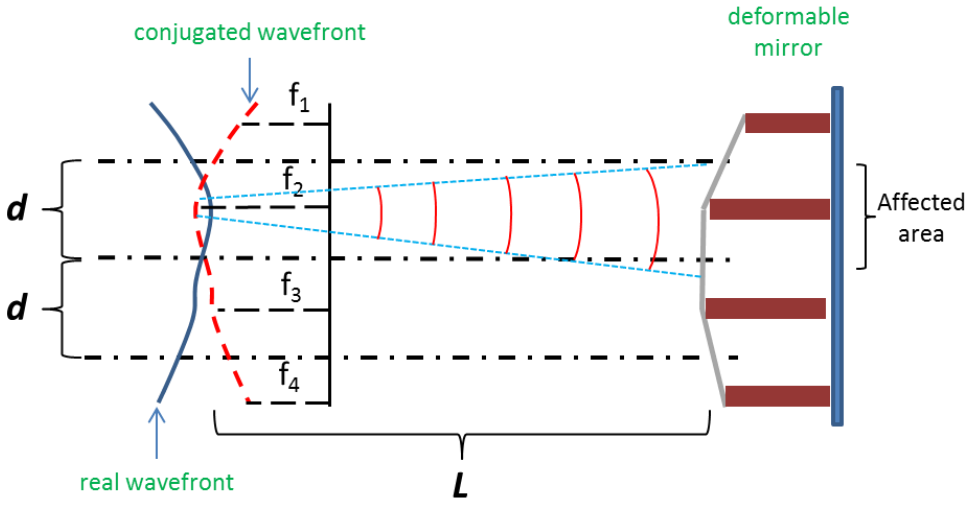

Figure 3. 12: Illustration diagram of DM's phase compensation idea

In figure 3.12, *d* is the spacing between neighboring actuators, and L is the distance between the reconstructed phase screen and the correction plane. It is assumed that the layout of g_j is identical with the layout of f_i.

The task of the fast reconstruction is to find the minimum requirement to reconstruct all the phase front values of the vertices. It is a fundamental conclusion in graph theory that for a graph with N vertices, it only requires N-1 edges to form a spanning tree that connects the graph. As shown by the full reconstruction algorithm, a more illuminated blob has larger influence on the reconstruction result. In other words, a large and bright blob in the plenoptic image tends to provide more information. If the N-1 edges correspond with the brightest blobs, a fast reconstruction can be formed.

Because the neighboring actuators in an AO device are usually equally spaced, we only make use of the shortest edges that join nearest pairs of vertices together. For example, in a Cartesian layout of actuators where neighboring elements are equally spaced, all the edges used to form a spanning tree will have the same length. Thus the total number of edges to be retrieved from a plenoptic image can be expressed as:

$$|E| = \frac{1}{2}\sum_{i=1}^{N} d_i \tag{40}$$

In equation (40), d_i is the number of nearest vertices of the i^{th} vertex, and $|E|$ denote the cardinality of the set of edges. The spanning tree with N-1 edges is a subset of the edges in equation (40), denoted as set $\{ E \}$.

We show next how to select the most informative edges to obtain the spanning tree, and therefore retrieve the phases on the vertices. For simplicity, a "dummy" AO system with only seven channels of control is used in our explanation. Its actuators form a hexagonal layout as shown in Figure 3.13:

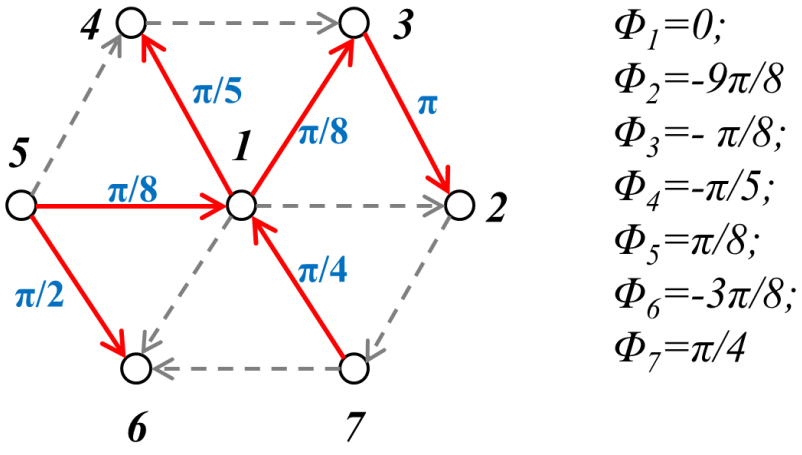

Figure 3. 13: Simple example of reconstruction diagraph

In Figure 3.13, the directional red edges represent the selected edges of the spanning tree. The numbered vertices are the geometric locations of the actuators of the device. The gray dashed

edges are not selected by the fast reconstruction algorithm. The phase information retrieved from the plenoptic sensor is marked in pair with each corresponding edge. Thus, with the selected spanning tree, the phases on the vertices are deterministic.

A normal plenoptic image and the edge selection algorithm for the spanning tree is illustrated in Figure 3.14:

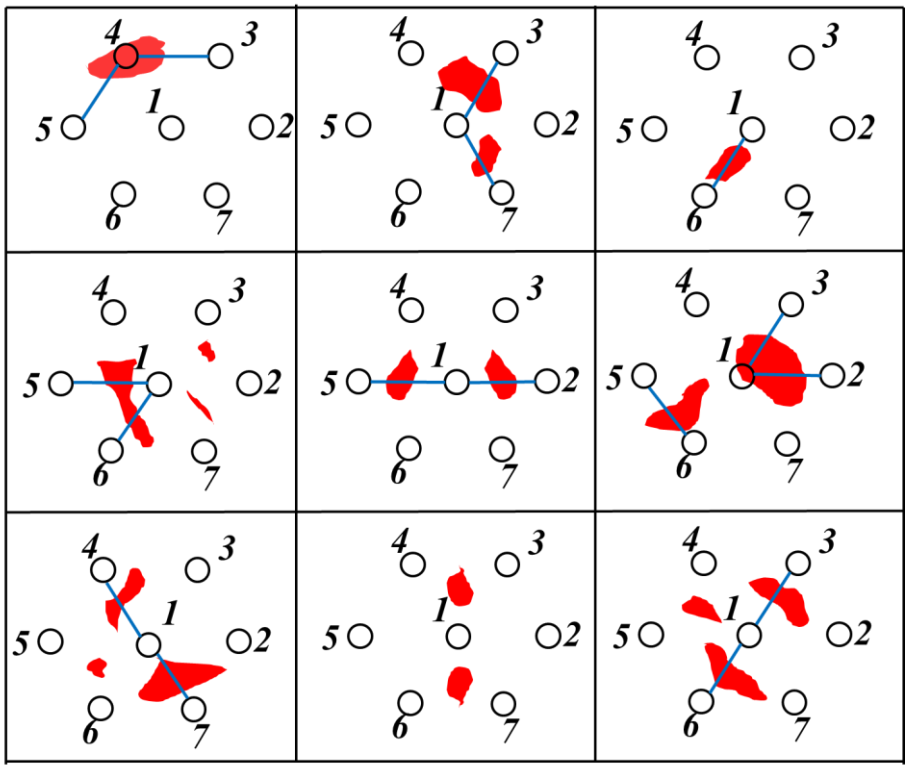

Figure 3. 14: Edge selection process on the plenoptic image for maximum spanning tree on the digraph presented by Figure 3.13

In Fig.4, the solid black lines mark the division of image cells and the red islands are the images of the light patches when the distorted wavefront is imaged by the plenoptic sensor. We virtually make copies of the layout of the vertices of the "dummy" AO into each image cell to show their corresponding locations. Based on the previous discussion, there are 12 edges in the graph: $E_{\{1,2\}}$, $E_{\{1,3\}}$, $E_{\{1,4\}}$, $E_{\{1,5\}}$, $E_{\{1,6\}}$, $E_{\{1,7\}}$, $E_{\{2,3\}}$, $E_{\{3,4\}}$, $E_{\{4,5\}}$, $E_{\{5,6\}}$, $E_{\{6,7\}}$. The

direction of these edges can be arbitrarily assigned. We then use a box counting method to sum up (over all *M* and *N* indexes) the pixel values covering each edge and rank them in descending order. Using the summed-up intensity as the weight for each edge, the edges selection process is converted into a maximum spanning tree problem [18]. The "Greedy" method [19] can be used to practically determine the structure of the tree with the following steps:

(1) Start with a graph with all the vertices and zero edge.

(2) Take the first element in the edge set E (the edge with highest weight) and put it into the graph.

(3) If the edge doesn't form a circuit in the graph, keep it.

(4) Delete the selected edge from the edge set E.

(5) Go back to step (2) until N-1 edges are selected.

Once the structure of the maximum spanning tree is determined, the phase information of the edges can be calculated by the following equation:

$$\varphi_{E_{\{j,k\}}} = \frac{\sum_{(s,t)\in E_{\{j,k\}}} I(s,t)\vec{v}_{E\{j,k\}} \cdot \left(\frac{Md_0}{f_1}, \frac{Nd_0}{f_1}\right) \cdot \frac{2\pi l_0}{\lambda}}{\sum_{(s,t)\in E_{\{j,k\}}} I(s,t)} \tag{41}$$

In equation (41), *I(s, t)* is the pixel value with coordinates *(s, t)* on the plenoptic image. *(M, N)* are the indexes for an image cell with width d_0. $\mathbf{V_E}$ is the unit directional vector of the edge and l_0 is the length of the edge. λ is the wavelength and f_1 is the focal length of the plenoptic sensor's objective lens. $E_{\{j,k\}}$ is the edge between vertices *j* and *k*. Then, by arbitrarily appointing any vertex to be the reference point $(\varphi=0)$, one can find the phases of other

vertices by traversing the tree structure and using the phase difference information carried by its branches.

If the reconstruction requires more resolution points, one can use a denser set of vertices and go through the same procedure. Accordingly, a more complex form of equation (39) should be determined to relate the higher resolution of reconstruction to the lower resolution of wavefront correction on the AO system.

The construction for the spanning tree can be shown by the following figure based on the simple example in figure 3.11:

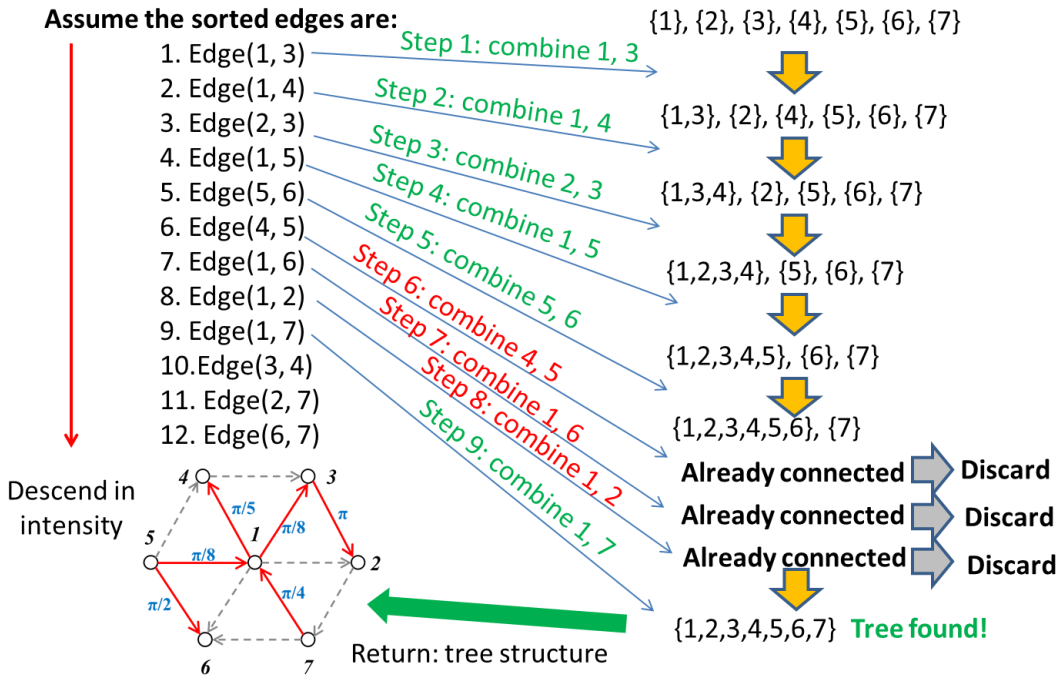

Figure 3. 15: Illustration of spanning tree formation based on "greedy" method for fast reconstruction for a plenoptic image

In conclusion, the “tree” reconstruction algorithm looks for cell indices of N-1 edges that are covered by the most illuminated blobs and resolves the local tip/tilt of neighboring actuators with priority. Therefore, instead of using 2D images for

reconstruction, the “tree” reconstruction algorithm only examine the pixels covered by the pre-defined edges (1D data).

“Checkerboard” reconstruction algorithm:

The checker board reconstruction algorithm is invented based on the Shack-Hartmann sensor’s reconstruction algorithm. A Hartmann-graph representing the sampled wavefront tip/tilt serves as an intermediate step between a Shack-Hartmann image and the reconstructed wavefront. In a wide sense, the Hartmann-graph is a small light field with reduced resolution. In fact, the geometric information of the light field is contained in the MLA indices (inter-cell) in a Shack-Hartmann sensor while the angular information of rays is reflected by the focus shift (intra-cell). Similarly, in the plenoptic sensor, the angular information is contained in the MLA cell indices (inter-cell) and the geometric information is reflected by the actual cell image (intra-cell).

It is not difficult to show that the Shack-Hartmann sensor and the plenoptic sensor have flipped representations of angular and geometric information. Therefore, a similar reconstruction algorithm to retrieve the Hartmann-graph can be achieved. However, the “Checkerboard” reconstruction algorithm typically uses a much larger data base than those used in the Shack-Hartmann reconstruction algorithm. The amount of data acquired by each sensor will be elaborated on in section 3.5.

The process of the checker board reconstruction algorithm is stated as follows:

(1) In each MLA cell image, divide the image into grids as a desirable Hartmann-gram.

(2) Search for each grid point to find the image cell index (M_i, N_i) that has the highest intensity in that grid area.

(3) The cell index for each grid is the most credible angular information, and the Hartmann-gram can be built accordingly.

For simplicity, we use the following dummy example to illustrate the “Checkerboard” reconstruction algorithm:

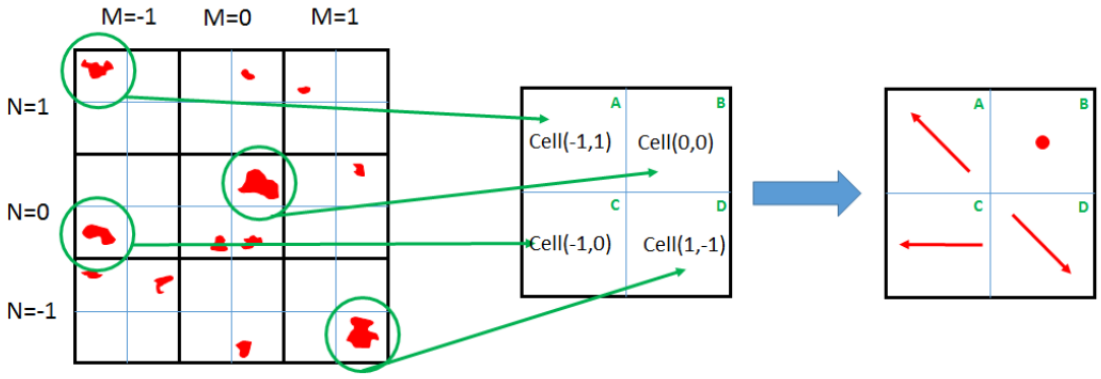

Figure 3. 16: Dummy example to illustrate the "Checkerboard" reconstruction algorithm

In figure 3.16, we use a uniform grid method to divide each cell into a 2 by 2 cell as the predefined checkerboard. The checkerboard grid has identical copies in all the cell images. Therefore, for each checkerboard unit, we only need to find which cell contains the most illuminated pixels and return the search with the cell indices. Then the overall Hartmann-graph can be retrieved based on the checkerboard’s resolution (2 by 2 in this dummy example). The rest of the reconstruction converges with the Shack-Hartmann sensor’s reconstruction. In fact, when the Hartmann-graph is derived, we get the mathematical Poisson equation of the phase front and the solution can be derived accordingly.

The complexity of the “Checkerboard” reconstruction algorithm is the same as the algorithm of a Shack-Hartman sensor. The checkerboard grid serves as the same

principle as the MLA in a Shack-Hartmann sensor. Similar to the searching of displacement in the focus points, the “Checkerboard” reconstruction looks for the brightest patch among all the possible scattering angles. In other words, the computation complexity for each spot on the Hartmann-graph is equal in both sensors.

For the same example of “Defocus” deformation as shown in the full reconstruction (section 3.4.1), the “Checkerboard” reconstruction algorithm provides its result as:

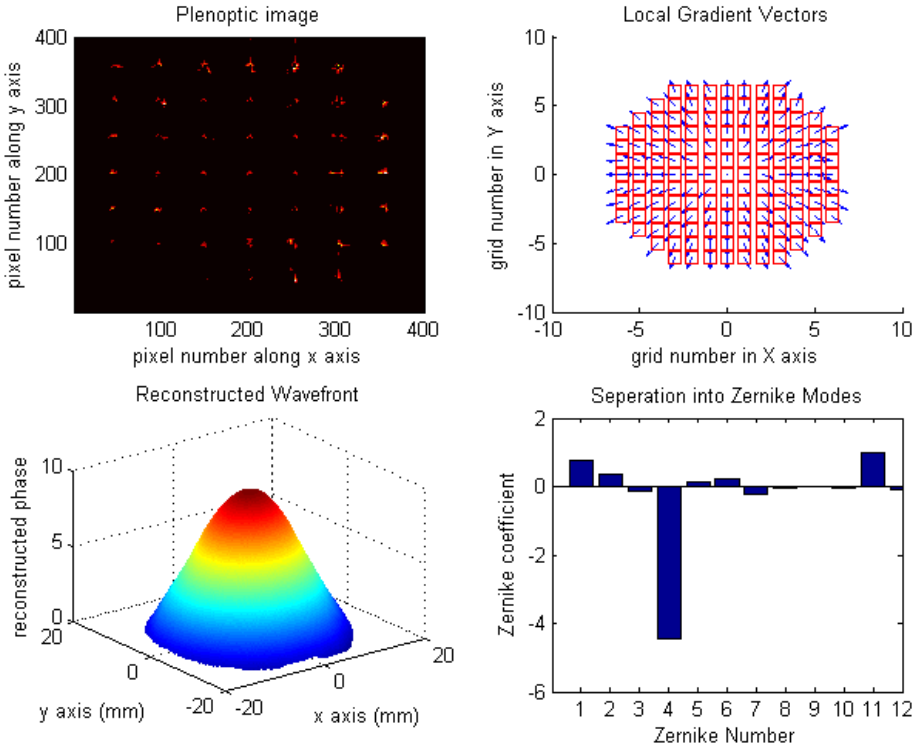

Figure 3. 17: "Checkerboard" reconstruction on "Defocus" deformation case

The result shows that the “Defocus” deformation has been reliably recognized by the “Checkerboard” reconstruction algorithm. In fact, it has 90% similarity to the Shack-Hartmann sensor’s result regardless of their respective errors. It is also interesting to point out that the “Checkerboard” reconstruction is lossy but accurate: as many other

patches that are less illuminated have been ignored in the process. A quick explanation can be shown by the following diagram:

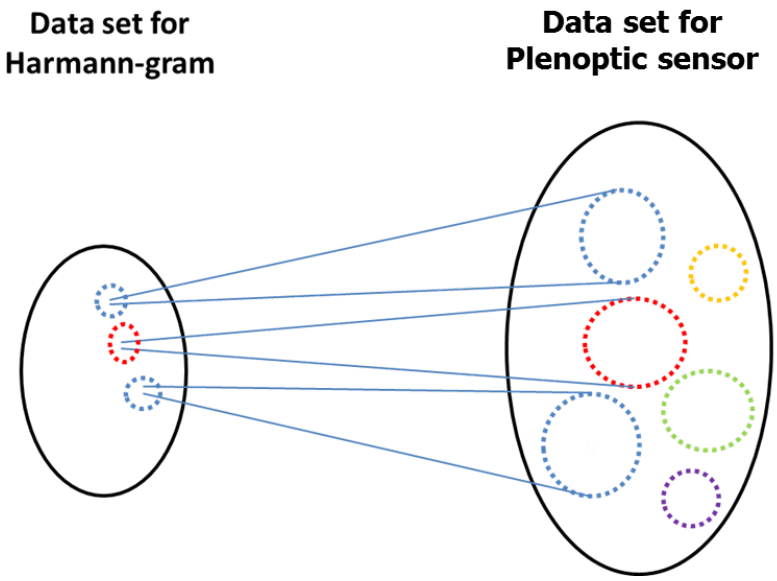

Figure 3. 18: Data compression from the plenoptic sensor's information set to the Shack-Hartmann sensor's information set

Figure 3.18 shows that the "Checkerboard" reconstruction algorithm is actually compressing its information set to fit into a Hartmann-graph. Intuitively, in each cell of a Shack-Hartmann sensor, only one sharp focusing point is allowed while the other pixels are treated as "dark" (low value pixels). However, in the plenoptic sensor, the restriction has been removed where each cell image is free to be any arbitrary pattern and each pixel is equivalently informative. Therefore, the "Checkerboard" reconstruction fetches a small portion of the plenoptic image and uses that to mimic what a Shack-Hartmann sensor would do. The associated speed up when compared with full reconstruction algorithm is obtained by using one computation thread for each spot on the Hartmann-graph. The "Checkerboard" reconstruction algorithm is

also more robust when compared with a Shack-Hartmann sensor, which will be proved later (in section 3.5).

3.4.3 Analytical phase and amplitude retrieval equations

In some occasions, detailed reconstruction is preferred over speed parameters. For example, in calibrating a deformable mirror, it is desirable to acquire the weak displacement as well as the reflectivity of the surface. In other words, if the complex field is to be reconstructed, analytical solution serves as an optional reconstruction algorithm.

In general, a complex optic field contains two real number parts for any point in space along a specified polarization direction: amplitude and phase. At least 2 equations are required to solve one spatial point of a complex optic field. Thus, to resolve an area of complex field with $N \times N$ points, $2N^2$ equations need to be listed.

The analytical equations are listed by treating each patch to be uniform in phase and assume that each point on the entrance pupil has a unique phase. Therefore, the geometric bounding conditions can be obtained on the plenoptic image and the phase bounding conditions can be obtained at the entrance pupil of the plenoptic sensor. By solving the corresponding equations group with MMSE standard, an analytical complex field result can be acquired.

"Dummy" Example:

In a discrete sample array of 3×3 points on the front focal plane, one can actually predict how they evolve into blocks of images as presented in the following figure.

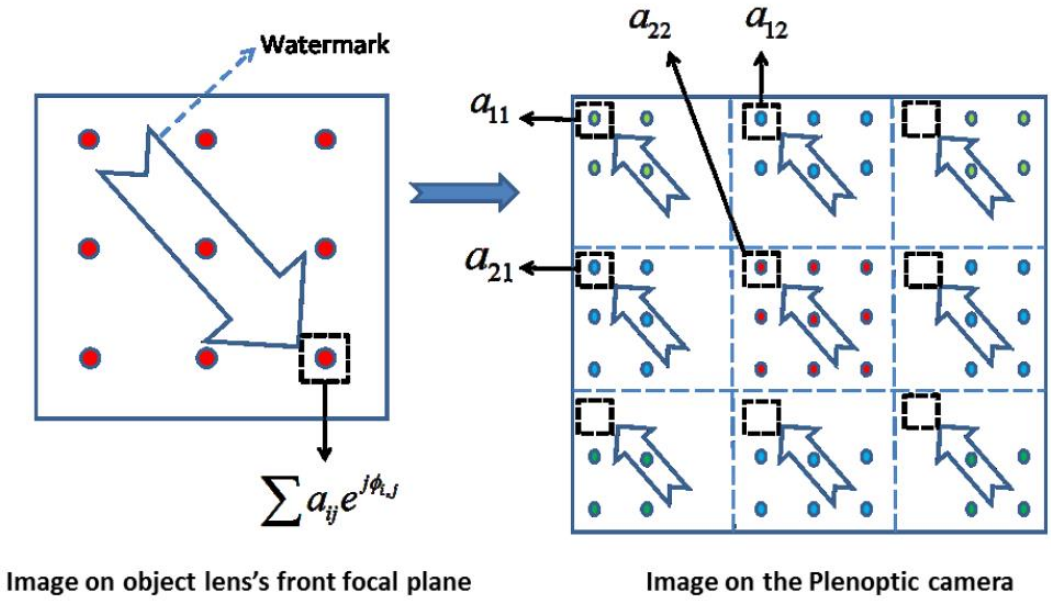

Figure 3. 19: Dummy example in analytical solution of the complex field on a plenoptic image

To reconstruct the phase information, we need the assumption that in each block, the phase change can be neglected, which results from the fact that rays within a patch of the beam would basically end up in the same block with identical angular and phase information. Hence we have the equation group:

$$\left|a_{11}e^{j\phi_{11}} + a_{12}e^{j\phi_{12}} + a_{21}e^{j\phi_{21}} + a_{22}e^{j\phi_{22}}\right| = \sqrt{a} \tag{42}$$

$$\left|b_{11}e^{j\phi_{11}} + b_{12}e^{j\phi_{12}} + b_{13}e^{j\phi_{13}} + b_{21}e^{j\phi_{21}} + b_{22}e^{j\phi_{22}} + b_{23}e^{j\phi_{23}}\right| = \sqrt{b} \tag{43}$$

$$\left|c_{12}e^{j\phi_{12}} + c_{13}e^{j\phi_{13}} + c_{22}e^{j\phi_{22}} + c_{23}e^{j\phi_{23}}\right| = \sqrt{c} \tag{44}$$

$$\left|d_{11}e^{j\phi_{11}} + d_{12}e^{j\phi_{12}} + d_{21}e^{j\phi_{21}} + d_{22}e^{j\phi_{22}} + d_{31}e^{j\phi_{31}} + d_{32}e^{j\phi_{32}}\right| = \sqrt{d} \tag{45}$$

$$\left|E_{11}e^{j\phi_{11}} + E_{12}e^{j\phi_{12}} + E_{13}e^{j\phi_{13}} + E_{21}e^{j\phi_{21}} + E_{22}e^{j\phi_{22}} + E_{23}e^{j\phi_{23}} + E_{31}e^{j\phi_{31}} + E_{32}e^{j\phi_{32}} + E_{33}e^{j\phi_{33}}\right| = \sqrt{E} \tag{46}$$

$$\left|f_{12}e^{j\phi_{12}} + f_{13}e^{j\phi_{13}} + f_{22}e^{j\phi_{22}} + f_{23}e^{j\phi_{23}} + f_{32}e^{j\phi_{32}} + f_{33}e^{j\phi_{33}}\right| = \sqrt{f} \tag{47}$$

$$\left|g_{21}e^{j\phi_{21}} + g_{22}e^{j\phi_{22}} + g_{31}e^{j\phi_{31}} + g_{32}e^{j\phi_{32}}\right| = \sqrt{g} \tag{48}$$

$$\left|h_{21}e^{j\phi_{21}}+h_{22}e^{j\phi_{22}}+h_{23}e^{j\phi_{23}}+h_{31}e^{j\phi_{31}}+h_{32}e^{j\phi_{32}}+h_{33}e^{j\phi_{33}}\right|=\sqrt{h} \tag{49}$$

$$\left|i_{22}e^{j\phi_{22}}+i_{23}e^{j\phi_{23}}+i_{32}e^{j\phi_{32}}+i_{33}e^{j\phi_{33}}\right|=\sqrt{i} \tag{50}$$

In the above equations, matrix $\begin{matrix} i & h & g \\ f & E & d \\ c & b & a \end{matrix}$ is the interference pattern observed on the front focal plane of object lens and the blocks are assigned with uniform phase information $\phi_{3\times3}$. These real numbers can be obtained by adding all the corresponding pixel intensities on the image of a plenoptic camera, or can be alternatively obtained by using a standard imaging camera and setting the image sensor at the back focal plane of lens. By solving the equation group, the patches in the light field are initially retrieved, including their relevant phases. Then further adjustments can be used in iterations to satisfy that in the reconstruction, the phase map doesn't have any discontinuities:

$$\oint \nabla S\left(\vec{r}\right)\cdot d\vec{r} \le error_{tol} \tag{51}$$

Equation (51) can be invoked under continuous phase change assumptions. However, the consumption of computation power for the analytical solution and its optimization is considerable and is not linearly tractable. For N=100, it requires 10000 interweaved equations and the complexity to solve this goes with the trend of $N^3 ln(N)$.

Therefore, it is not practical to use the analytical equations to adaptively observe and reconstruct the phase distortion caused by atmospheric turbulence. For static phase and amplitude distortions, however, the analytical algorithm provides reasonable and reliable results. In fact, it maximizes the use of all the information on a plenoptic image as all the bounding conditions have been considered.

3.5 Use basic concepts of information theory to review the plenoptic sensor

The fundamental difficulty in overcoming atmospheric turbulence is the incomplete knowledge of the turbulence situation. Simply, given the actual refractive index of the air channel, a theoretical optimization can be figured out to optimize laser beam propagation through the channel. Similarly, one can use a special coding method to ensure reliable signal communication through the channel. However, full knowledge of the turbulence distribution is unrealistic. Therefore, how much useful information about the turbulent channel can be obtained is a challenging topic. And it is very interesting to think about the turbulence channel with ideas in information theory. In fact, we will introduce a very "different" understanding of the turbulence with concepts of information entropy [22].

3.5.1 Entropy and mutual information

Entropy has been widely used to measure the size of information content. Without loss of generality, the "information" can be quantized and represented by binary strings. For example, the result of a coin toss can be represented by a 1 bit digit as "0" for the heads and "1" for the tails. If the coin is fair, with equal probability of both outcomes, the entropy is 1 bit for the coin toss game. On the other hand a biased coin with a 99% chance to show heads and 1% chance to show tails will have an entropy rate of 0.08 bit. This means that on average the biased coin provides little information for each toss since the result is almost certain.

In studying the effect of atmospheric on beam propagation, normal ideas treat the turbulence as a source of noise that degrades the beam quality in propagation, and methods of beam corrections have been developed to provide a less distorted beam

after propagation through the turbulent channel. Therefore, the noise of the atmospheric channel is time-varying without being a fixed distribution. It will be difficult to send a “message” through the atmospheric channel, where the “message” is a desired, less distorted beam at the receiver site. Innovatively, we can think in the reverse direction: the atmospheric turbulence is the source that provides the “message”, while the beam at the transmitter site is totally controllable “noise”. Thus, the highest frequency of the turbulent channel is the rate at which “information” is sent. The noise can be controlled (at least we can keep it static in the case of no applicable adaptive optics devices) to help us decode the information faster and easier.

The strength of atmospheric turbulence is measured by path-averaged values of refractive index structure constant C_n^2 (unit: $m^{-2/3}$). C_n^2 is commonly acquired by placing a point detector at the receiver site to measure the intensity fluctuation within a finite aperture. C_n^2 is usually effective in revealing the fundamental turbulence situations: whether the turbulence is weak, medium or strong at the current time. However, the structure constant C_n^2 is almost “useless” in giving actual information about the turbulence, not only because it is a statistical averaged value, but also because of its low dimensional properties. In other words, given the same value of C_n^2, the beam can be distorted in countless ways and gives no information on how to get a less distorted beam. Therefore, in terms of “information content”, the structure constant C_n^2 provides quite limited information about the channel.

Comparatively, the Shack-Hartmann sensor provides better information compared to using a point detector at the receiver site. In fact, a Shack-Hartmann sensor provides

an array of points that expands the information set from 1D (in time dimension) to 3D (2D in geometric and 1D in time dimension). Therefore, the entropy of the data provided by a Shack-Hartmann sensor will be much greater than that of a scintillometer. Without loss of generality, we express the entropy measure of an arbitrary sensor as:

$$H = -\sum_{k}\sum_{i} p_i \log_2(p_i) \qquad (bits) \tag{52}$$

In equation (52), the index *k* goes over all channels of the device and the index *i* goes over all the quantized evaluations of each individual channel. For example, suppose a scintillometer provides 8 evaluations of the turbulence per second and the analyzed C_n^2 data can equally ranges from 10^{-16} $m^{-2/3}$ to 10^{-12} $m^{-2/3}$ with "super accuracy" (in fact, it is pointless to achieve such accuracy) of 10^{-16} $m^{-2/3}$. Then the cardinality of index k is 8, and the maximum entropy (when the distribution of C_n^2 is i.i.d and uniform over the range) of the data provided by the scintillometer per second is 106 bits. For comparison, suppose a 128fps Shack-Hartmann sensor has 64×64 cells and each cell has size 16×16 $pixel^2$. It is easy to find that with each focal spot in a cell of the Shack-Hartmann sensor, its location can specify 16×16 gradient directions and its intensity values can vary from 1 to 255. Therefore, the cardinality of channels is 4096, and each channel provides 16 bits of information in maximum, so the overall maximum entropy measure of the data provided by a Shack-Hartmann sensor per second is 2^{23} bits (8,388,608 bits). Compared with a scintillometer's result (106 bits), the amount of information provided by a Shack-Hartmann sensor is abundant. Evidently, the Shack-Hartmann sensor tells much more about the details of the atmospheric turbulence when compared with a scintillometer.

The entropy measure of information content on various devices gives us an approximation of the devices' capacities in providing details of the turbulent channel. Without loss of generality, we can draw the diagram of the swapped source-channel detection as:

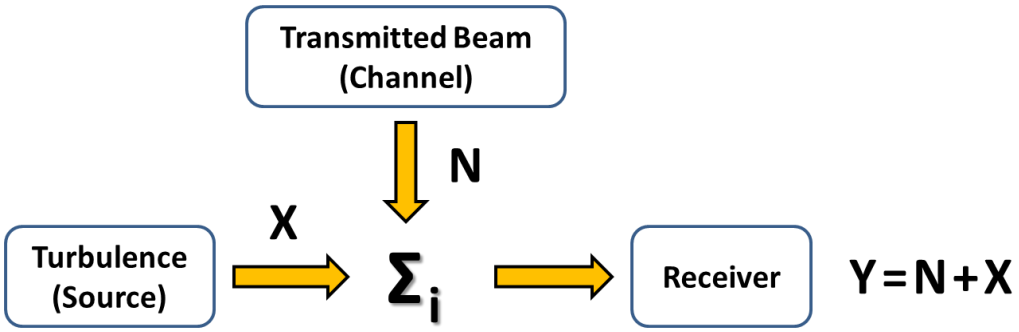

Figure 3. 20: Diagram of swapped source-channel detection in atmospheric turbulence modeling

In figure 3.20, the transmitted beam profile is injected at the transmitter site, and it can be modified with known phase and amplitude distribution with the help of AO devices such as a spatial light modulator or deformable mirror, etc. Since the receiver signal is picked up at the receiver site, the equivalent noise signal in the turbulent channel should be the projected outcome of the transmitted beam in the absence of turbulence. Regarding the fact that the optic signal is carried by the beam, all the symbols in figure 1 represent the logarithm magnitude of the original signal. Thus, the value of the turbulence signal X won't be revealed at points with zero optic intensity (Y would be -∞ for that point). By taking the logarithm of the signals we have the convenience of expressing the turbulence source in a more uniform manner for weak turbulence, deep turbulence and strong turbulence situations:

$$X \triangleq \log_2(1+\sum x_i) \tag{53}$$

In equation (53), x_i represents the amplitude and phase change in the i^{th} small segment of the channel length within which the amplitude and phase changes are trivial. On average, the real part of x_i is negative and the imaginary part of x_i reflects the phase change in each segment.

Because the noise signal is unbounded for its negative real parts, we can empirically define a finite threshold to regulate so that normalized signals below the threshold are meaningless for our detection. The process is illustrated as:

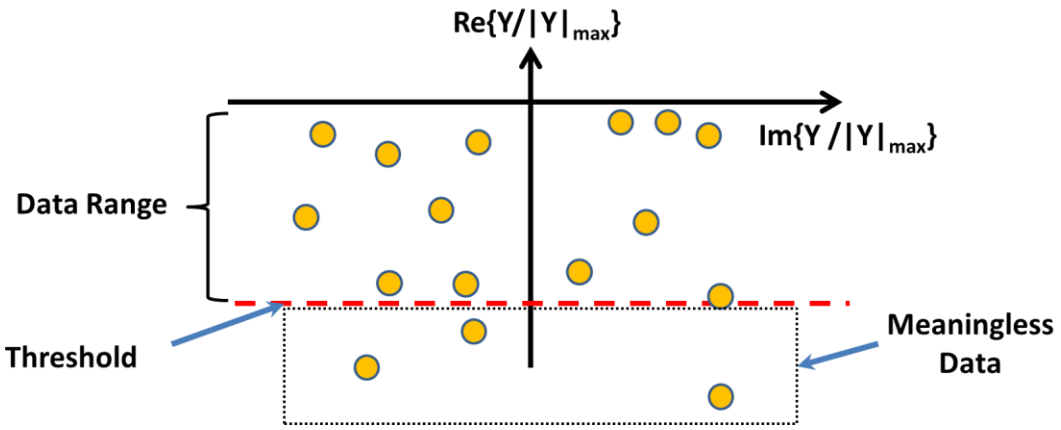

Figure 3. 21: Diagram of handling low intensity data

In figure 3.21 we show that the subset of the data with low intensity (points below the threshold) is discarded so that all the informative data points should lie within the "Data Range". In practice, however, one can simply define the corresponding dark areas (that can't provide credible information) as "Meaningless Data".

Whenever the detecting device is changed, the coding alphabet of the source signal and channel noise signal will be changed accordingly. For example, an interferometer uses the intensity variation and reference beam's profile to determine the distorted wavefront. On the other hand, the Shack-Hartmann sensor uses focus shift to tell the local phase gradient of the distorted wavefront. Therefore, it is hard to establish a

certain standard to evaluate various approaches. The entropy rate, however, can serve as a fair measure. If the maximum capacity of the device can't cover the data rate (entropy measure per second) of the turbulence channel, we know that the observation is inadequate.

Nevertheless, there are alternative ways to claim inadequate observation, but we can always quantify with the entropy concepts. For instance, one can claim that a Shack-Hartmann sensor is "inadequate" when the focal spot reaches outside the boundary pixel of a cell. Intuitively this means that the SH sensor is short of angular range to express the local tilt, while the concept of entropy will explain that outcome as an "error" code (not because the cell is empty, but because there exist 2 distinctive spots in the neighboring cell). In fact, as long as the outcome doesn't resemble a Hartmann-gram[3], the entropy way will treat the outcome as an error. This is because the maximum entropy measure of a Shack-Hartmann sensor is calculated based on an ideal Hartmann-gram.

An interesting question to ask is whether we can determine the entropy measure of the plenoptic sensor, and whether the plenoptic sensor is capable of communicating with the source at a higher data rate than the Shack-Hartmann sensor mentioned above. We can assume that the plenoptic sensor uses the same image resolution as the Shack-Hartmann sensor, and the MLA is identical in both sensors with 64×64 cells and each cell has size 16×16 pixels. Each block is an individual angular spectrum, and each cell image is a geometric copy of the real world. Thus we have $(64 \times 64 \times 16 \times 16)$ individual channels and each channel gives 8 bits information. When the plenoptic sensor is sampling at the same frame rate as the Shack-Hartmann sensor

(128 fps), with each pixel revealing 8 bits information, the maximum information content measured by the plenoptic sensor is 2^{30} bits (1,073,741,824 bits). Intuitively, this means with the same MLA and image resolution, the plenoptic sensor has 128 times more possible outcomes than the Shack-Hartmann sensor. In other words, if one wants to characterize the turbulence channel, the plenoptic sensor can provide more details than a Shack-Hartmann sensor. Note that the comparison depends on how the image resolution is divided by the MLA's property. For convenience, we can use the following chart to see the comparison between those two types of wavefront sensors:

Table 1. 1. Information size comparison between the plenoptic sensor and the Shack-Hartman sensor

Image cell size	Image cell number	Information size of a plenoptic sensor per second	Information size of a Shack-Hartmann sensor per second
64×64	16×16	2^{30} bits	~2^{19}bits
32×32	32×32	2^{30} bits	~2^{21}bits
16×16	64×64	2^{30} bits	2^{23} bits
8×8	128×128	2^{30} bits	~2^{25} bits
4×4	256×256	2^{30} bits	~2^{27} bits
2×2	512×512	2^{30} bits	~2^{28} bits

From Table 1.1, it is not difficult to see that with the changes of a MLA cell size (cell number will be changed accordingly if the MLA has fixed size), the plenoptic sensor has a constant size of maximum information output, while the Shack-Hartmann

sensor increases the total number of information output with smaller cells. However, two distinctive observations can be made:

(1) The increased amount of information on a Shack-Hartmann sensor is at the cost of smaller angular detection range.

(2) The plenoptic sensor strictly provides a larger amount of information than the Shack-Hartmann sensor with the same hardware (same MLA, same image resolution, and same frame rate).

In fact, in the limit of the Shack-Hartmann sensor (if the cell size is just 1 pixel) its information size provided in 1 second equals that of the plenoptic sensor. But the Shack-Hartmann sensor provides less meaningful information since there is no angular information provided. Thus, in the practice of changing the MLA cell size to realize tradeoffs between angular and geometric resolutions, the plenoptic sensor provides a smooth trade-off without harming the capacity of the observing device. The Shack-Hartmann sensor, however, doesn't have stable capacity in the trade-off practice. This is due to the restriction that a Shack-Hartmann sensor can only have one focus interpreted under each cell image.

Nevertheless, in low illumination conditions (such as astronomy applications), the Shack-Hartmann sensor does provide good SNR ratios. For weak illumination sources, a Shack-Hartmann sensor is more sensitive than the plenoptic sensor because all photons within a MLA cell are concentrated to 1 pixel (while the plenoptic sensor distributes the photons into many pixels). As a consequence, the Shack-Hartmann sensor may out-perform the plenoptic sensor in extreme low-illumination conditions. In normal conditions where illumination is sufficient (especially in laser imaging), the

Shack-Hartmann sensors will lose the sensitivity advantage when compete with a plenoptic sensor. In fact, the ultimate use of an image sensor's capacity is to use every pixel to resemble a ray in the light field, and the plenoptic sensor has achieved this. In other words, the plenoptic sensor is the optimized realization of light field sensing.

3.5.2 Data compression

The purpose of advanced wavefront sensing is to obtain as much information about the complex amplitude of the field as possible. It is regulated by the data processing inequality (DPI) that any reconstruction algorithm can't retrieve/recreate information lost in the wavefront sensing part. Intuitively, given a uniform beam *U(x, y)*, turbulence caused point spread function *X(s, t, x, y; L)*, and an arbitrary 2D sensor acquires an image of *Im(s, t)*. The sensing process can be expressed as a convolution result of: $U(x, y)*X(s, t, x, y; L) \rightarrow Im(s, t)$. Since the transmitted beam and the image on the wavefront sensor is known, *Im(s, t)* is treated as an indicator of the atmospheric turbulence: $X(s, t, x, y; L) \rightarrow Im(s, t)$. On the other hand, a reconstruction algorithm can be applied to use the wavefront sensing information to estimate the turbulence situation $Im(s, t) \rightarrow X^*(s, t, x, y; L)$. Then the DPI states that:

$$I\left(X, X^*\right) \leq I\left(X, \mathrm{Im}\right) \tag{54}$$

Equation (54) suggests that from any reconstruction algorithm, one can't obtain any extra information about the turbulence than the sensing process. The equality of equation (54) is achieved if and only if the reconstruction algorithm is lossless. Based on this conclusion, the full reconstruction algorithm provides more facts about the turbulence than the fast reconstruction algorithms.

As discussed in the fast reconstruction algorithm (section 3.4.2), a Hartmann-graph is a lossless reconstruction algorithm result for a Shack-Hartmann image, while it is a data compression result for a plenoptic image. For low orders of atmospheric phase distortion where a Hartmann-graph has a larger entropy measure than the distortion, the Shack-Hartmann and the plenoptic sensor should provide very similar results. However, ambiguities happen on the Shack-Hartmann sensor because the local phase gradient for each spatial point depends entirely on one MLA cell. In other words, if the cell image is interfered, the data from the same cell will be lost and the reconstruction result will be affected. Admittedly, interpolation from neighboring data points help to produce a smoother result, but the entropy measure of the data can't be increased.

However, on the plenoptic sensor's site, since we only use a subset of the plenoptic image, the remaining set of plenoptic image pixels might be useful. Thus, we can run the "checkerboard" reconstruction once again after we experience the tragic scenario where the critical information has been lost. The result is shown as:

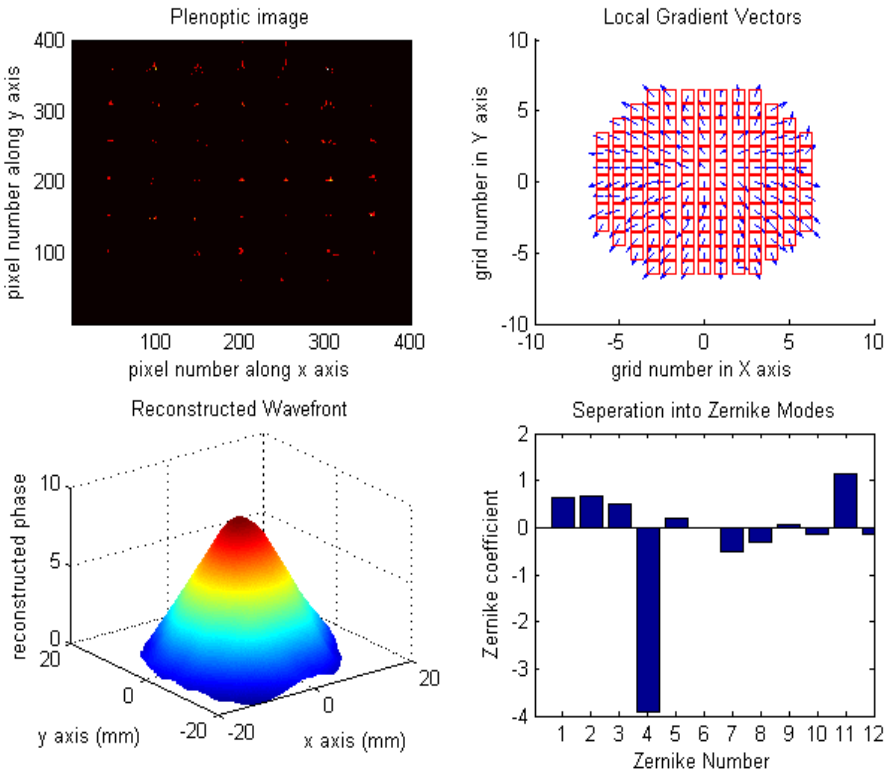

Figure 3. 22: Checkerboard reconstruction result on the plenoptic sensor when we lose all the information in the previous reconstruction practice

Figure 3.22 shows that a credible reconstruction can be conducted on the plenoptic image, even if we have removed all the pixels used in the previous reconstructions (by setting their values to zero). Since the pixels on the plenoptic image represent light rays that are mutually exclusive, there is no redundancy in the received plenoptic image. Therefore, we can see that the second reconstruction reflects the wavefront with accuracy. In fact, the correlation with the result of a Shack-Hartmann sensor is 95.4% (The first reconstruction trial has 99% agreement with the Shack-Hartmann sensor's result).

For additional interest, we run the "checkerboard" reconstruction again after removing all the pixels used for the previous reconstructions. The result is shown as:

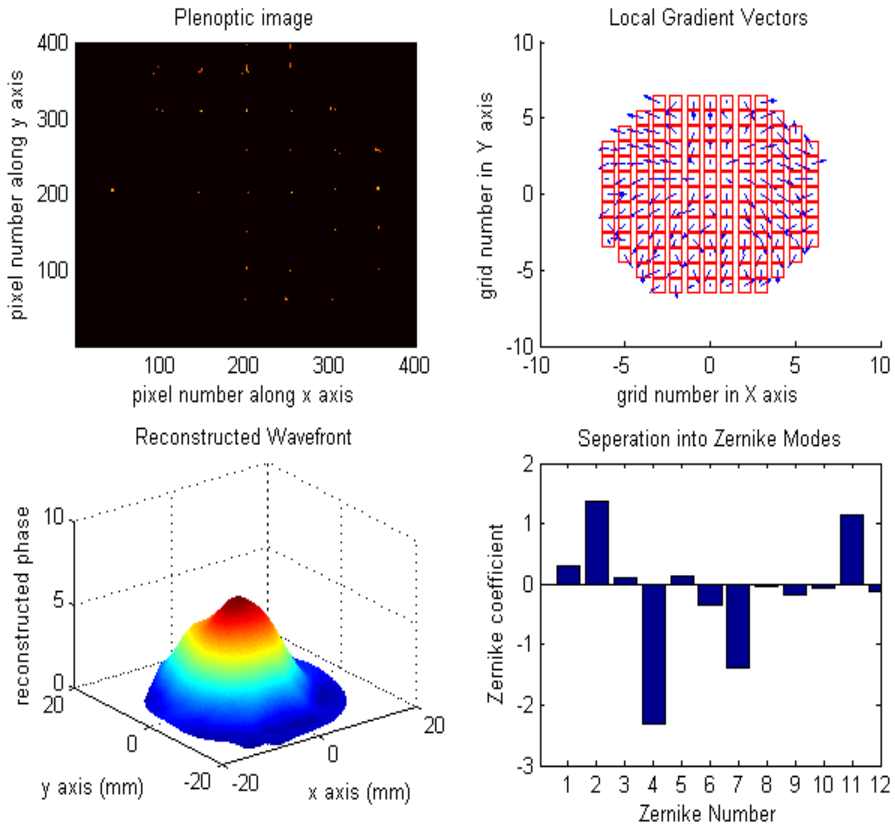

Figure 3. 23: Extra trial with checkerboard reconstruction assuming that a significant amount of information is lost

As shown in figure 3.22, we find that the dominant Zernike distortion is still "defocus", and the similarity of the third attempt drops to 74.3%. Therefore, when we iteratively remove relevant information from the data set, the reconstruction result will be increasingly affected by the irrelevant information. Thus, compared with a Shack-Hartmann sensor that provides only one copy of the Hartmann-gram, the plenoptic sensor provides extra robustness in revealing the wavefront information.

The difference in accuracy begins to show up in reconstructing a "trefoil" deformation (higher order of distortion) with both the Shack-Hartmann sensor and the plenoptic sensor. The "trefoil" deformation contains more spatial oscillations of the

wavefront and is comparatively more difficult to reconstruct than a “defocus” case. The result of the “trefoil” deformation reconstructed by a Shack-Hartmann sensor is shown in figure 3.24, while the result from a plenoptic sensor is shown in figure 3.25. As the distortion is known to be a “trefoil” case, it is evident that the plenoptic sensor reveals the details better than the Shack-Hartmann sensor with the same hardware configuration. Admittedly, we built the Shack-Harman sensor with comparatively larger image cell size (54×54 pixel^2) to reconstruct low order distortions more accurately. Therefore, when facing the higher order Zernike modes, the Shack-Hartmann sensor’s performance begin to degrade (because of lack of enough grid points in the geometry). The plenoptic sensor, however, has smooth performance in revealing higher order wavefront distortions. Thus the “trefoil” deformation is reconstructed credibly by the plenoptic sensor. In order to make a Shack-Hartmann sensor to work for higher Zernike modes, we need to make tradeoffs by reducing the angular range (the cell size of MLA) and increasing the number of grid points (the number of cells in a MLA).

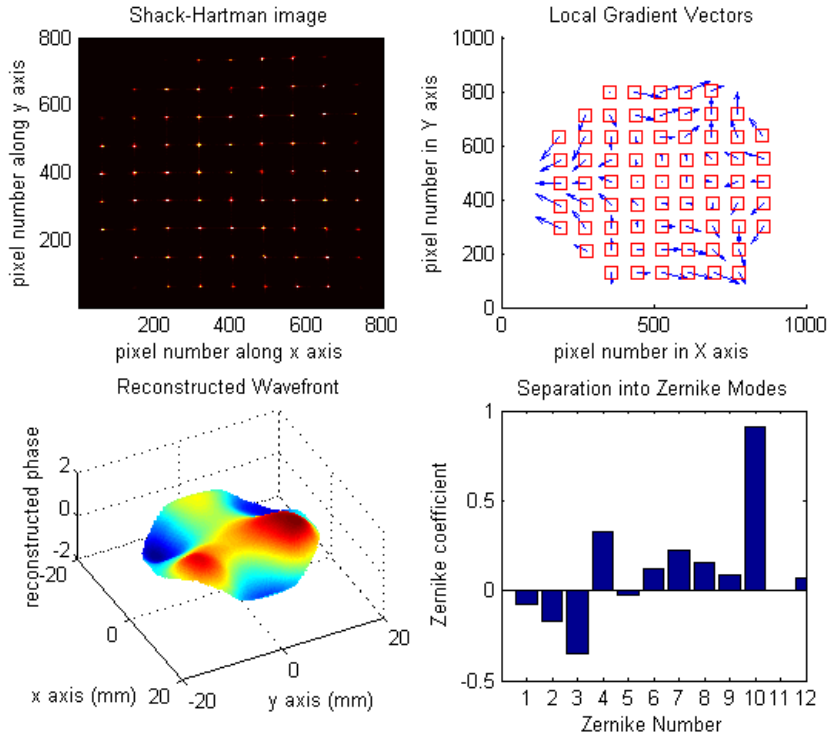

Figure 3. 24: Trefoil deformation and reconstruction by the Shack-Hartmann sensor

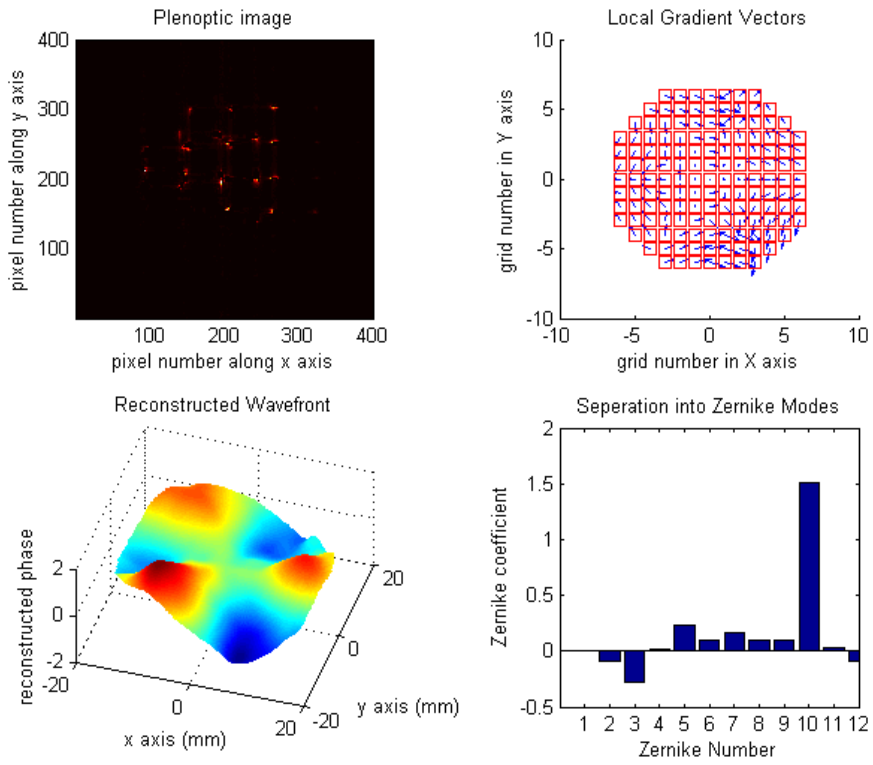

Figure 3. 25: Trefoil deformation and "checkerboard" reconstruction by the Plenoptic sensor

In conclusion, a fast reconstruction algorithm (such as the “Tree” reconstruction algorithm and “Checkerboard” reconstruction algorithm) is a data compression process on the plenoptic image, while a full reconstruction algorithm (such as the full reconstruction algorithm or the panorama reconstruction algorithm) maximizes the use of a plenoptic image.

3.5.3 Channel capacity

How to determine whether a wavefront sensor is adequate for typical atmospheric turbulence situation is of great importance. In this section, we will introduce a rule of thumb to solve this fundamental question.

As described in section 3.5.1, with a swapped source channel module, the turbulence can be viewed as a transmitter that emits signals to the receiver. And the entropy measure can be conducted on the source to determine the actual size of information variety that is achievable on the source. For simplicity, we mark the entropy measure of the source as H_s.

Similarly, the maximum entropy measure on an observing device can be determined by asymptotic equal partition (AEP) assumption where each outcome is equally possible. For simplicity, we use H_i to mark the i^{th} sensor for sensing the distorted laser beam. Then, if $H_s>H_i$, we can determine that the i^{th} sensor is inadequate in handling the current turbulence situation. In other words, there will be some different turbulence structures that can't be differentiated by the wavefront sensor. Only a lower resolution of the turbulence situation is possible when $H_s>H_i$ happens. For the cases where $H_s<H_i$, it is "possible" that the wavefront sensor is adequate to reveal the turbulence situation. The quoted word "possible" refers to the actual distribution of outcomes in the wavefront sensing. Intuitively, if the outcomes are not uniformly distributed, the entropy measure of the device H_i is overestimated and a tighter bound needs to be determined as H_i^* based on asymmetric outcome distribution. And the device is adequate for observing turbulence if $H_s<inf\{H_i^*\}$ and alignment is correct.

An extension for this theorem can be applied to AO devices under the help of a wavefront sensor (as a translator for different deformation). Without loss of generality, the entropy measure of the AO has an entropy measure of H_a with regard to the wavefront sensor it cooperates with. Then the system entropy measure can be determined as $H_{AO}=min\{Ha, inf\{H_i^*\}\}$. And similar rules can be applied to determine

whether the adaptive optics system is adequate to correct the turbulence situation by comparing H_s and H_{AO}.

References

[1] Wu, Chensheng, Jonathan Ko, and Christopher C. Davis. "Determining the phase and amplitude distortion of a wavefront using a plenoptic sensor." *JOSA A* 32, no. 5 (2015): 964-978.

[2] Ng, Ren, Marc Levoy, Mathieu Brédif, Gene Duval, Mark Horowitz, and Pat Hanrahan. "Light field photography with a hand-held plenoptic camera."*Computer Science Technical Report CSTR* 2, no. 11 (2005).

[3] Levoy, Marc, Ren Ng, Andrew Adams, Matthew Footer, and Mark Horowitz. "Light field microscopy." *ACM Transactions on Graphics (TOG)* 25, no. 3 (2006): 924-934.

[4] Levoy, Marc, and Pat Hanrahan. "Light field rendering." In *Proceedings of the 23rd annual conference on Computer graphics and interactive techniques*, pp. 31-42. ACM, 1996.

[5] Adelson, Edward H., and James R. Bergen. *The plenoptic function and the elements of early vision*. Vision and Modeling Group, Media Laboratory, Massachusetts Institute of Technology, 1991.

[6] Eslami, Mohammed, Chensheng Wu, John Rzasa, and Christopher C. Davis. "Using a plenoptic camera to measure distortions in wavefronts affected by atmospheric turbulence." In *SPIE Optical Engineering+ Applications*, pp. 85170S-85170S. International Society for Optics and Photonics, 2012.

[7] Sobierajski, Lisa M., and Arie E. Kaufman. "Volumetric ray tracing." In *Proceedings of the 1994 symposium on Volume visualization*, pp. 11-18. ACM, 1994.

[8] Wu, Chensheng, William Nelson, and Christopher C. Davis. "3D geometric modeling and simulation of laser propagation through turbulence with plenoptic functions." In *SPIE Optical Engineering+ Applications*, pp. 92240O-92240O. International Society for Optics and Photonics, 2014.

[9] Aaronson, Scott, and Alex Arkhipov. "The computational complexity of linear optics." In *Proceedings of the forty-third annual ACM symposium on Theory of computing*, pp. 333-342. ACM, 2011.

[10] Seitz, Steven M., Brian Curless, James Diebel, Daniel Scharstein, and Richard Szeliski. "A comparison and evaluation of multi-view stereo reconstruction algorithms." In *Computer vision and pattern recognition, 2006 IEEE Computer Society Conference on*, vol. 1, pp. 519-528. IEEE, 2006.

[11] Levin, Anat, William T. Freeman, and Frédo Durand. "Understanding camera trade-offs through a Bayesian analysis of light field projections." In *Computer Vision–ECCV 2008*, pp. 88-101. Springer Berlin Heidelberg, 2008.

[12] Georgiev, Todor, Zhan Yu, Andrew Lumsdaine, and Sergio Goma. "Lytro camera technology: theory, algorithms, performance analysis." In *IS&T/SPIE Electronic Imaging*, pp. 86671J-86671J. International Society for Optics and Photonics, 2013.

[13] Wu, Chensheng, and Christopher C. Davis. "Modified plenoptic camera for phase and amplitude wavefront sensing." In *SPIE Optical Engineering+ Applications*, pp. 88740I-88740I. International Society for Optics and Photonics, 2013.

[14] Wu, Chensheng, Jonathan Ko, William Nelson, and Christopher C. Davis. "Phase and amplitude wave front sensing and reconstruction with a modified

plenoptic camera." In *SPIE Optical Engineering+ Applications*, pp. 92240G-92240G. International Society for Optics and Photonics, 2014.

[15] Goodman, Joseph W. *Introduction to Fourier optics*. Roberts and Company Publishers, 2005.

[16] Southwell, William H. "Wave-front estimation from wave-front slope measurements." *JOSA* 70, no. 8 (1980): 998-1006.

[17] Liu, Ling, and Mikhail A. Vorontsov. "Phase-locking of tiled fiber array using SPGD feedback controller." In *Optics & Photonics 2005*, pp. 58950P-58950P. International Society for Optics and Photonics, 2005.

[18] Wu, Chensheng, Jonathan Ko, and Christopher C. Davis. "Using Graph Theory and a Plenoptic Sensor to Recognize Phase Distortions of a Laser Beam." *arXiv preprint arXiv:1506.00310* (2015).

[19] Tarjan, Robert. "Depth-first search and linear graph algorithms." *SIAM journal on computing* 1, no. 2 (1972): 146-160.

Chapter 4: 3D simulations

Although the real time 3D dynamic sensing of atmospheric turbulence structure is unrealistic, it is possible to perform 3D simulation of atmospheric turbulence to economically test system design and figure out solutions in overcoming turbulence effects. There are two major approaches to conduct the 3D turbulence simulation. One is based on geometric ray modeling that simulates each ray's trajectory and phase change. The other is based on wave theory and uses phase screens to resemble the changes caused by the channel. The major advantage of the geometric ray modeling is its simplicity where the fundamental task is to track individual ray in the shared atmospheric channel, while wave properties of the beam might be lost in the tracking process (no diffraction). Wave analysis keeps track of the continuous changes in the beam but the setup of the turbulence channel is based on 2D models rather than 3D models. In this chapter we will introduce both approaches and propose a "pseudo" diffraction model to account for the wave properties in geometric ray modeling.

4.1 Basic concepts in geometric optics

Geometric optics is widely applied in optical studies. It has been applied in automatic optic system design software such as Code-V and Zemax [1], computer vision [2], as well as some virtual reality studies [3]. In the field of atmospheric turbulence, geometric optics can be used to describe/analyze/simulate the beam propagation process. In fact, given the distributive refractive index of the channel and the

transmitted beam (with adequate ray samples), the resulted distorted beam can be calculated.

In general, the ray geometrics can be expressed as:

$$\frac{d}{ds}\left(n\frac{d\vec{r}}{ds} \right) = grad\, n \tag{1}$$

Where n is atmospheric refractive index and $\vec{r}$ is a single ray's geometric trajectory with regard to its path length *s*. Because the majority of rays have weak deviation from sight to sight alignment, a paraxial approximation can be generally applied. Also, by taking into account the fact that all rays collected by the receiver shares a common propagation axis, we can express the displacement equations along the transverse plane of the optical axis as:

$$\frac{d}{dz}\left((1+\delta n)\frac{dx}{dz} \right) = \frac{d(\delta n)}{dx} \tag{2}$$

$$\frac{d}{dz}\left((1+\delta n)\frac{dy}{dz} \right) = \frac{d(\delta n)}{dy} \tag{3}$$

Where atmospheric turbulence has been expressed directly by deviation in refractive index, thus by further quantizing the process in evolution steps, we have:

$$\Delta x \approx \Delta z \cdot \frac{\delta z}{\delta x}\Delta n_x(x,y) \tag{4}$$

$$\Delta y \approx \Delta z \cdot \frac{\delta z}{\delta x}\Delta n_y(x,y) \tag{5}$$

Where Δ is a symbol that handles the increments in ray propagation, and δ handles increments in the distribution of atmospheric refractive index (note that the ray simulation and turbulence simulation use different resolutions). Therefore, for any arbitrary ray in the system, the trajectory of the ray can be tracked geometrically if all

the channel distortion is known. However, the diffractive behavior of the ray has been ignored and the associated error in long range propagation conditions may cause severe deviation from reality.

4.1.1 Eikonal equation

It is of great importance to determine the source of error in using geometric optics without considering the minor effect of diffraction [4]. The original form of the wave equation can be expressed as:

$$\nabla^2 u + k_0^2 n^2(r) u(r) = 0 \tag{6}$$

In equation (6), $u(\boldsymbol{r})$ represents the complex optical field and $\boldsymbol{k_0}$ represents the wavenumber of the light rays. The refractive index of the channel is expressed by $n(\boldsymbol{r})$.

Without loss of generality, we can assume the standard solution form:

$$u(r) = A(r) e^{i\psi(r)} \tag{7}$$

In equation (7) the amplitude information is $A(\boldsymbol{r})$ and the phase information is $\psi(\boldsymbol{r})$. In general, atmospheric turbulence satisfies the following term:

$$\lambda_0 \ll L,\ L \equiv \min\left(\frac{|A|}{|\nabla A|}, \frac{|k_j|}{|\nabla k_j|}, \frac{n}{|\nabla n|}\right) \tag{8}$$

In equation (8), it is assumed that the atmospheric turbulence causes much more gradual changes (instead of rapid spatial oscillation) than the scale of the wavelength. Therefore, we can introduce a scaling parameter as:

$$\mu = \frac{1}{kL} = \frac{1}{k_0 n L} = \frac{\lambda}{2\pi L} \ll 1 \tag{9}$$

In addition, dimensionless wave equations can be obtained by the following transformation:

$$\nabla_1^2 u + n^2 u = 0,\ \nabla_1^2 \equiv \frac{\partial^2}{\partial x_1^2} + \frac{\partial^2}{\partial y_1^2} + \frac{\partial^2}{\partial z_1^2},\ x_1 = k_0 x\ y_1 = k_0 y\ z_1 = k_0 z \tag{10}$$

$$\nabla_2^2 u + \frac{n^2}{\mu^2} u = 0,\ \nabla_2^2 \equiv \frac{\partial^2}{\partial x_2^2} + \frac{\partial^2}{\partial y_2^2} + \frac{\partial^2}{\partial z_2^2},\ x_1 = \frac{x}{L}\ y_1 = \frac{y}{L}\ z_1 = \frac{z}{L} \tag{11}$$

Equation (10) and (11) are 2 different methods to derive a dimensionless wave equation. The relations between amplitude and phase scaling are expressed as:

$$A = A(\mu r_1) = A(r_2) \tag{12}$$

$$\psi(r) = \frac{\psi_1(\mu r_1)}{\mu} = \frac{\psi_1(r_2)}{\mu} \tag{13}$$

$$\nabla \psi = \frac{\nabla_1 \psi_1(\mu r_1)}{\mu} = \nabla_2 \psi_1(r_2) \tag{14}$$

Similarly, the solution for the dimensionless equation can be transformed as:

$$u = A(\mu r_1) e^{i\psi_1(\mu r_1)/\mu} = A(r_2) e^{i\psi_1(r_2)/\mu} \tag{15}$$

And the original wave equation can be reformed as:

$$\nabla^2 u + \frac{n^2}{\mu^2} u = \left\{ \frac{1}{\mu^2} [n^2 - (\nabla_2 \psi_1)^2] A + \frac{i}{\mu} (2\nabla_2 A \nabla_2 \psi_1 + A\nabla_2^2 \psi_1) + \nabla_2^2 \psi_1 \right\} \exp(i\psi_1 / \mu) = 0 \tag{16}$$

A general series solution by expanding the amplitude in powers of μ can be given as:

$$u(r_2) = e^{i\psi_1(r_2)/\mu} \sum_{m=0}^{\infty} (\mu / i)^m A_m(r_2) \tag{17}$$

By matching each power of μ, the following Eikonal equation group can be obtained:

$$
\begin{aligned}
&(\mu^{-2}) \quad (\nabla_2\psi_1)^2 = n^2,\\
&(\mu^{-1}) \quad 2(\nabla_2 A_0 \nabla_2\psi_1) + A_0\nabla_2^2\psi_1 = 0,\\
&(\mu^{0}) \quad 2(\nabla_2 A_1 \nabla_2\psi_1) + A_1\nabla_2^2\psi_1 = -\nabla_2^2 A_0,\\
&----------\\
&(\mu^{m-1}) \quad 2(\nabla_2 A_m \nabla_2\psi_1) + A_m\nabla_2^2\psi_1 = -\nabla_2^2 A_{m-1}
\end{aligned}
\tag{18}
$$

In Cartesian coordinates (x, y, z representation), the Eikonal equation group is reformed as:

$$
\begin{aligned}
&(\nabla\psi)^2 = n^2,\\
&2(\nabla A_0 \nabla\psi) + A_0\nabla^2\psi = 0,\\
&2(\nabla A_1 \nabla\psi) + A_1\nabla^2\psi = -L\nabla^2 A_0,\\
&----------\\
&2(\nabla A_m \nabla\psi) + A_m\nabla^2\psi = -L\nabla^2 A_{m-1}
\end{aligned}
\tag{19}
$$

It can be directly followed in equation (19) that geometric optics is the approximation of the first two orders of the Eikonal equations. To increase the accuracy of geometric optics, higher order equations can be taken into the system as a "perturbative" refinement. However, it is often not worthwhile in practice due to the required large computation power.

Simply, assume that the geometric parameter can be written as **r**=(q_1,q_2…), each ray's Eikonal equation can be written as:

$$
\mathrm{H}\left(\frac{\partial\psi}{\partial q_1}, \frac{\partial\psi}{\partial q_2}, ..., \frac{\partial\psi}{\partial q_n}, q_1, q_2, ..., q_n\right) = 0 \tag{20}
$$

Or equivalently, as:

$$
\mathrm{H}\left(p_j, q_j\right) = 0,\ p_j = \frac{\partial\psi}{\partial q_j},\ \psi = \psi(q_j) \tag{21}
$$

Equation (21) is a simplified form of equation (20). And the momenta of a ray is marked by p_j (j=1, 2, 3 in Cartesian coordinates). The first order differential equation can be expressed as:

$$\frac{dq_j}{\partial H / \partial p_j} = -\frac{dp_j}{\partial H / \partial q_j} = \frac{d\psi}{\sum_{j=1}^{n} p_j (\partial H / \partial p_j)} \tag{22}$$

The expression of equation (22) can be simplified by adding the differential equations:

$$\frac{dq_j}{d\tau} = \frac{\partial \mathrm{H}}{\partial p_j} \tag{23}$$

$$\frac{dp_j}{d\tau} = -\frac{\partial \mathrm{H}}{\partial q_j} \tag{24}$$

$$\frac{d\psi}{d\tau} = \sum_{j=1}^{n} p_j \frac{\partial \mathrm{H}}{\partial p_j} \tag{25}$$

In equation (23)-(25) *qj* represents the universal geometric parameter and p_j represents the universal momenta parameter. For example, in Cartesian coordinates we can express the coordinates as:

$$\frac{dr}{d\tau} = \frac{\partial \mathrm{H}}{\partial p} \tag{26}$$

$$\frac{dp}{d\tau} = -\frac{\partial \mathrm{H}}{\partial r} \tag{27}$$

$$\frac{d\psi}{d\tau} = p\frac{\partial \mathrm{H}}{\partial p} \tag{28}$$

$$p = \nabla \psi \tag{29}$$

Therefore, the Eikonal equation for a ray is a quadratic one, and the solution can be expressed in a general form as:

$$\psi = \psi^0 + \int_{\tau^0}^{\tau} p \frac{\partial \mathrm{H}}{\partial p} d\tau \tag{30}$$

$$d\tau = \frac{d\sigma}{\left|\partial \mathrm{H} / \partial p\right|} \tag{31}$$

In equation (31), arc length σ is applied as a tracing of the rays' trajectories. The remaining question is to derive the actual form of Hamiltonian equation ***H***. And due to the quadratic equation (19), the 1st form of Hamiltonian equation can be simply written as:

$$\mathrm{H} = \frac{1}{2}\left[p^2 - n^2(r) \right] = 0 \tag{32}$$

Where

$$p = \nabla \psi \tag{33}$$

Based on the above Hamiltonian form, the ray equation can be written as:

$$\frac{dr}{d\tau} = p, \ \ \frac{dp}{d\tau} = \frac{1}{2} \nabla n^2(r) \tag{34}$$

$$\psi = \psi^0 + \int_{\tau^0}^{\tau} p^2 d\tau = \psi^0 + \int_{\tau^0}^{\tau} n^2(r) d\tau \tag{35}$$

$$d\tau = \frac{d\sigma}{p} = \frac{d\sigma}{n} \tag{36}$$

Equation (34) is the geometric ray tracing function, equation (35) is the phase tracking function and equation (36) is the trajectory function.

Similarly, the 2nd form of the Hamiltonian equation can be written as:

$$H = p - n(r) = 0 \tag{37}$$

$$p = \sqrt{p^2} \tag{38}$$

Equation (37) and (38) can de derived directly from solving equation (32). Correspondingly, the ray equations are changed to:

$$\frac{dr}{d\sigma} = \frac{p}{n}, \quad \frac{dp}{d\sigma} = \nabla n \tag{39}$$

Despite the seemingly different forms of these Hamiltonian equations, a generalized expression is shown as:

$$\frac{d^2 r}{d\tau^2} = \frac{1}{2}\nabla n^2, \quad \frac{d}{d\sigma}\left(n\frac{dr}{d\sigma}\right) = \nabla n \tag{40}$$

In conclusion, geometric optics is a low order solution of the Eikonal equations in wave analysis. When the condition of equation (8) is satisfied, geometric optics can be safely applied to provide an accurate and reliable solution.

4.1.2 Meridional ray and skew rays

The meridional ray is generally used in optical fiber systems to describe the ray passing through the axis of a fiber. Skew rays refer to those rays that pass through the optic fiber in zig-zag paths/trajectories. As an extension, we can use a gradually expanding light pipe to describe the behavior of a congruence of light rays. Geometrically we call the center ray of the light pipe “Meridional ray” while rays at the edge of the light pipe as “Skew rays”.

Without loss of generality, the light pipe profiles a patch (a small wavelet that acts like a plane wave with flat phase front). Since all the rays inside the pipe are geometrically close to each other, they pass through the same turbulence cells and stays coherent at the end of the propagation channel. Based on the meridional ray and

skew rays, the analytical wave expression can be reconstructed. In other words, geometric optics and wave analysis are interchangeable in solving atmospheric turbulence problems as long as spatial resolution is adequate. With the established turbulence channel (in simulation), it is convenient to use geometric optics to simulate the propagation process in 3D.

4.2 2D phase screen simulations

Wave analysis of the turbulence effects on laser beam propagation is conventionally achieved by 2D phase screen models. In general, a phase screen characterizes the concentrated atmospheric distortion effect for a segmental channel length L. The propagation is ideally simplified to free propagation plus a one-time interaction with a phase screen. In fact, different from geometric optics, which focuses on the accuracies in describing the channel while causing inaccuracies in waveforms, phase screen methods focus on the accuracies of the waveforms but cause inaccuracies in describing the turbulent channel.

4.2.1 Mathematical model

Atmospheric turbulence has an inertial range where correlation between the fluctuations in the refractive index of the air serves as a fundamental fluid property of the air. In a simplified mathematical model (without investigating the actual viscidity of air), the correlation can be implied by the correlation and structure function of turbulence [6] as:

$$B_n\left(\vec{R_1},\vec{R_2}\right)\equiv\left\langle n_1\left(\vec{R_1}\right)n_1\left(\vec{R_2}\right)\right\rangle \tag{41}$$

$$D_n\left(R\right)=2\left[B_n\left(0\right)-B_n\left(R\right)\right] \tag{42}$$

$$\vec{R}=\vec{R_2}-\vec{R_1} \tag{43}$$

Equation (41) describes the auto-correlation function of fluctuations in the refractive index of air. In equation (42) we have made an isotropic assumption about the structure function. Anisotropic results can be saved in matrix forms similarly. The correlation can be obtained from field measurements on temperature distributions, wind speed and humidity levels. With this data, the structure properties of refractive index can be implied to the extent of equipment limits (which prevent measurements from retrieving further accuracy). For example, the refractive index structure constant C_n^2 that measures fluctuation strength can be inferred from:

$$C_n^2=\left(79\times10^{-6}\frac{P}{T^2}\right)^2 C_T^2 \tag{44}$$

Where C_T^2 is the temperature structure constant, retrieved from temperature measurements. This approach neglects other possible effects such as correlations with humidity. Alternatively, the autocorrelation function can be inferred from theoretical models, since the auto-correlation function and the spatial power spectrum density function are Fourier transform pairs of each other:

$$\Phi_n\left(\vec{K}\right)=\frac{1}{\left(2\pi\right)^3}\iiint_{-\infty}^{+\infty}B_n\left(\vec{R}\right)\exp\left(-i\vec{K}\cdot\vec{R}\right)d^3\vec{R} \tag{45}$$

In isotropic cases this equation can be simplified into a 1D situation:

$$\Phi_n\left(\kappa\right)=\frac{1}{2\pi^2\kappa}\int_0^\infty B_n\left(R\right)\sin\left(\kappa R\right)dR \tag{46}$$

Simply, one can derive the auto-correlation by using the power spectrum function as:

$$B_n\left(\vec{R}\right)=\iiint_{-\infty}^{+\infty}\Phi_n\left(\vec{K}\right)\exp\left(i\vec{K}\cdot\vec{R}\right)d^3\vec{K} \tag{47}$$

Similarly, in isotropic cases, the equation can be simplified as:

$$B_n\left(R\right)=\frac{4\pi}{R}\int_0^{\infty}\kappa\Phi_n\left(\kappa\right)\sin\left(\kappa R\right)d\kappa \tag{48}$$

Based on these facts, theoretical auto-correlation restrictions can be achieved through a Fourier transform of the spatial power spectral density functions. Several basic spatial power spectral density functions are shown in figure 4.1. For convenience, we list only 4 of the major spectra used in most research articles:

(1) Kolmogorov law is expressed as:

$$\Phi_n\left(\kappa\right)=0.033C_n^2\kappa^{-11/3}\quad 1/L_0\ll\kappa\ll 1/l_0 \tag{49}$$

(2) Tatarskii spectrum:

$$\Phi_n\left(\kappa\right)=0.033C_n^2\kappa^{-11/3}\exp\left(-\frac{\kappa^2}{\kappa_m^2}\right)\quad \kappa\gg 1/L_0\quad \kappa_m=5.92/l_0 \tag{50}$$

(3) Von Karman spectrum:

$$\Phi_n\left(\kappa\right)=0.033C_n^2\frac{\exp\left(-\frac{\kappa^2}{\kappa_m^2}\right)}{\left(\kappa^2+\kappa_0^2\right)^{11/6}}\quad 0\le\kappa<\infty\quad \kappa_m=5.92/l_0 \tag{51}$$

(4) Modified atmospheric spectrum (Hill spectrum):

$$\Phi_n\left(\kappa\right)=0.033C_n^2\left[1+1.802\left(\kappa/\kappa_l\right)-0.254\left(\kappa/\kappa_l\right)^{7/6}\right]\times\frac{\exp\left(-\frac{\kappa^2}{\kappa_m^2}\right)}{\left(\kappa^2+\kappa_0^2\right)^{11/6}} \tag{52}$$

$$0\le\kappa<\infty\quad \kappa_l=3.3/l_0\quad \kappa_0=4\pi/L_0 \tag{53}$$

Symbols l_0 and L_0 are inner and outer scales of turbulence respectively. The modified atmospheric spectrum model is also called the "Hill spectrum" in some articles.

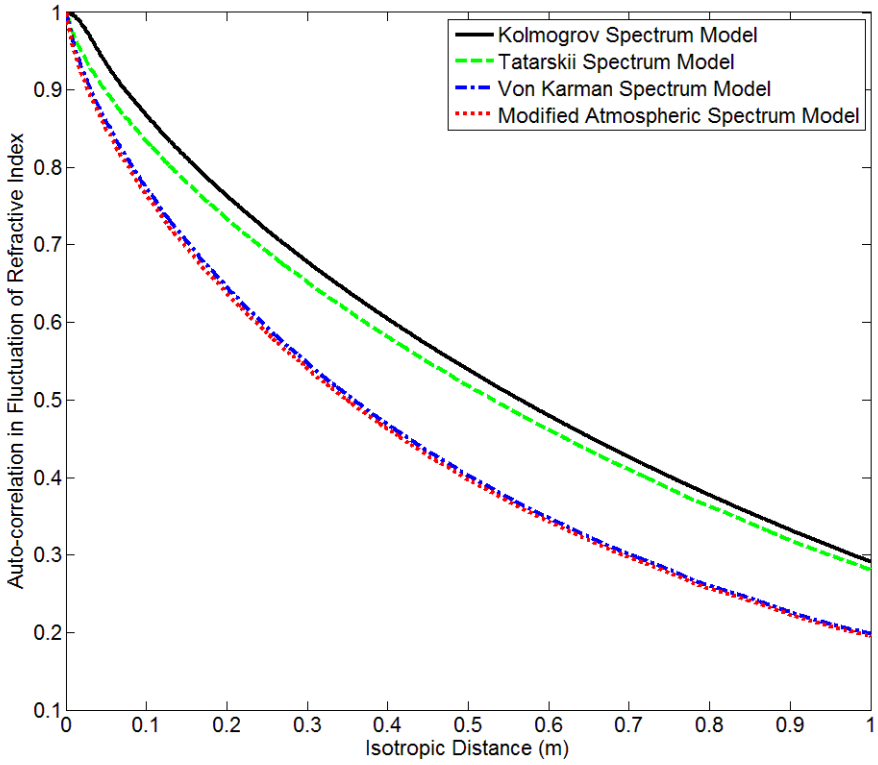

Figure 4. 1: Normalized auto correlation function for various models of spatial power spectrum density

Based on the correlation function, a 2D phase screen that satisfies the statistical analysis can be generated to add phase and amplitude modifications to the beam to mimic the atmospheric turbulence effects.

4.2.2 Generation of 2D phase screens

The generation of a phase screen is simply compression of atmospheric turbulence from 3D to 2D, expressed as [5]:

$$\phi(x,y) = k_0 \int_{z_0}^{z_0+z_s} \delta n(x,y,z)\, dz \tag{54}$$

Where k_0 is the wavenumber of the laser beam, and if the laser has a broad spectrum, an extra convolution layer can be applied to handle the situation:

$$\phi(x, y, k_0) = \int_{k_{\min}}^{k_{\max}} \delta(k - k_0) k \int_{z_0}^{z_0 + z_s} \delta n(x, y, z, k)\, dz \cdot dk \tag{55}$$

For each spectrum the phase screen is assumed to be made up of:

$$\phi(x, y) = \sqrt{2\pi z_s} k_0 \int_{-\infty}^{+\infty} \int_{-\infty}^{+\infty} e^{i(\mathrm{K}_x \cdot x + \mathrm{K}_y \cdot y)} \alpha(\mathrm{K}_x, \mathrm{K}_y) \Phi_n^{1/2}(\mathrm{K}_x, \mathrm{K}_y)\, d\mathrm{K}_x \cdot d\mathrm{K}_y \tag{56}$$

Where K_x and K_y are spatial frequencies of turbulence in the transverse plane, $\alpha(K_x, K_y)$ is a random complex amplitude with a standard normal distribution, and $\Phi_n(K_x, K_y)$ is power spectrum density along the transverse plane. Therefore, the distance along the propagation direction that a phase screen represents must satisfy the precondition:

$$z_s \gg L_0 \tag{57}$$

The symbol $\boldsymbol{L_0}$ in equation (44) is the outer scale of turbulence. This precondition gives mathematical convenience in setting up a number of phase screens to achieve similar effect of turbulence by lowering the complexity by one dimension (the propagation direction is suppressed).

4.2.3 Limitations to phase screen simulations

The limitation of phase screen simulations is the mismatch between the 2D set up of the channel structure and the actual 3D structure of the channel. Normally, the correlation between neighboring phase screens is ignored by setting them far apart. And the track of how turbulence evolves dynamically has become impossible in this model. In fact, phase screen models are rather static than dynamic due to the compression of channel structure complexity from 3D to 2D. Advanced models of 3D

phase screens have been proposed [6], which consider the correlation between phase screens that lies within the inertial range. However, the conciseness of the phase screen will be lost and the computation requirement has been greatly increased.

4.3 Pseudo diffraction functions for wave propagation

The weakness of a geometric optics approach is its inconsistency with the wave properties. Intuitively, if a plane wave passing through a tiny hole is simulated in geometric optics, the straight trajectory of light can't mimic the diffraction pattern such as Airy rings [7]. In this section, a technical "trick" is proposed to introduce a "Pseudo diffraction function" that counteracts part of the complexity in generating 3D turbulence. In other words, the 3D turbulence generation can be simplified while diffraction behavior in geometric optics can be obtained.

4.3.1 "Diffraction" in refractive index

In principle, an Airy pattern will be generated if one image beam passes through a circular hole around the similar size to the wavelength. The refractive index distribution can be described as unity everywhere besides infinity at blocking (obstructing) areas. In reality, the boundary of the channel is fixed while the wave property of photons causes the photons to end randomly (with certain distribution) behind the small optic opening. Mathematically, the diffraction pattern is mathematically described by the Fresnel diffraction equation, which computes the scaled Fourier transform of the geometry of the optic opening. In the laser beam propagation studies, the incident wavelets can be assumed to be plane waves and the

diffraction pattern can be simply computed by the geometric properties of the optical openings directly.

Based on the above facts, by a small philosophical change, if we treat an individual photon as a reference center and view/watch the small optic opening, the optic opening would have already caused diffraction. In fact, instead of calculating the diffraction patterns while the beam is propagating, one can compute the diffraction pattern first and convolute with illumination on the optic opening to get wave analysis results. Therefore geometric optics can be used directly as the setup of the media has already considered the diffraction condition. For convenience, we name this as "pseudo diffraction process" to mark the special treatment in geometric optics to diffract first and then propagate.

4.3.2 Intuitive interpretation of pseudo diffraction method

The generation of the diffracted envelope pattern is illustrated as:

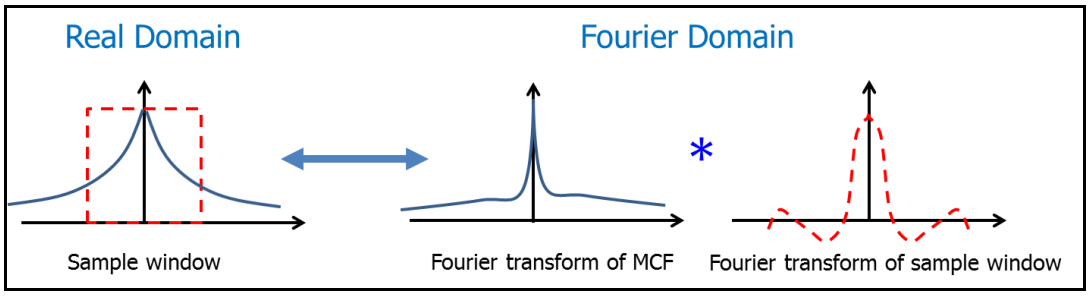

Figure 4. 2: Truncated envelope extends its influence in Fourier domain

Therefore, when the turbulence frames are generated, the hard aperture of the filter causes a similar "diffraction" pattern and a pseudo-diffraction pattern can be generated because rays passing through the general turbulence cells would be added with weak moment variations. However, we claim that our diffraction algorithm works not because it connects physics principles, but that it functions as both a relief

for computational resources and parasitic diffraction generator. In fact, one has to scale the local fluctuations on the turbulence grids to match with the wavelength used in the simulation. The philosophy that encouraged our treatment of the turbulence grids is a simple switch from the standpoint of the real world to the world of light rays, and for the light rays, it seems that the world (turbulence structure) is diffracting instead.

The "Pseudo diffraction" can be demonstrated by a simple example where a group of parallel rays pass through a tiny rectangular aperture and the far field pattern through the above algorithm gives the following diffraction pattern that resembles the Airy patterns for rectangular apertures:

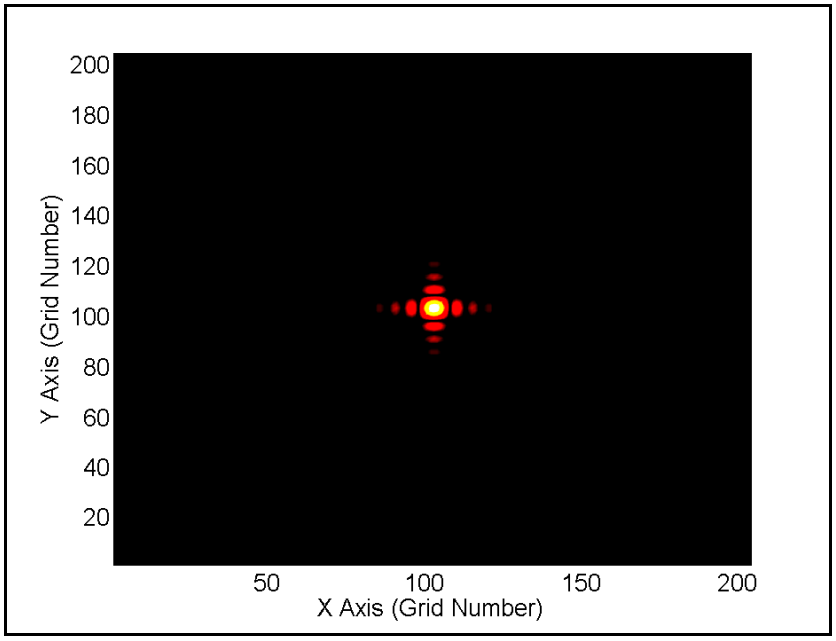

Figure 4. 3: Demonstration of pseudo diffraction mechanism

As a result diffraction can be interweaved into the process of generating turbulence grids, which will allows for future convenience in propagating rays with diffraction taken into account.

4.3.3 Benefits of pseudo diffraction processing

The pseudo diffraction processing serves as a modification of the geometric optics result that can account for the diffraction facts in long range propagation. The diffraction angle, however small, will bend the ray trajectory significantly with adequate propagation distance. Therefore, inserting the diffraction treatments to geometric optics helps to increase the accuracy of ray tracing results. However, it is obvious that extra computation power is required. In fact, for a 3D channel, the pseudo diffraction processing requires convolution between a 3D diffraction kernel and the 3D channel.

4.4 3D simulation of turbulence

In the 3D simulation of turbulence, we find a “coincidence” case exists that the extra computation process to generate a “pseudo diffraction” channel can be achieved by “sloppily” generating the 3D turbulence grid. This special arrangement seems like “killing two birds with one stone”.

4.4.1 Generation of 3D turbulence

With knowledge of the correlation functions of fluctuations in refractive index, the turbulence grids can be set up accordingly. The problem is simplified by finding a random distribution that satisfies equation (5). And a theoretical solution can be

achieved by the convolution of an envelope function and wide sense stationary random grids. A simple proof is shown as:

$$\begin{matrix} \langle E(0)E(R)\rangle = B_n(R) \\ \langle X(0)X(R)\rangle = \delta(R) \end{matrix} \Rightarrow \langle (X*E)(0)\cdot(X*E)(R)\rangle = B_n(R) \qquad (58)$$

Where "***0"*** is a reference point for simplification, which can be replaced with an arbitrary geometric coordinate ***r***. The evaluation of the RHS of equation (13) can be written as:

$$\begin{aligned} &\langle (X*E)(0)\cdot(X*E)(R)\rangle \\ &= (X*E)(0)*(X*E)^{-}(R) = \left(X(0)*E(0)*E^{-}(R)*X^{-}(R)\right) \\ &= \left(X(0)*X^{-}(R)\right)*B_n(R) = \delta(R)*B_n(R) = B_n(R) \end{aligned} \qquad (59)$$

In this evaluation we use the fact that the autocorrelation function is the convolution of a function with its "mirrored" self, where we have:

$$X^{-}(r) = X(-r); \qquad \langle X(r)X(r+R)\rangle = \int_r X(r)X^{-}(-R-r)dr = \left(X*X^{-}\right)(R) \quad (60)$$

As a result, a direct solution exists where ***X(r)*** is WSS noise (can be obtained from a 3D random matrix) and the envelope has the form of:

$$E(R) = \frac{B_n(R)}{\sqrt{B_n(0)}} \qquad (61)$$

Therefore, the turbulence grids are generated by:

$$n_1(r) = \frac{X*E(r)}{\sqrt{B_X(0)}} \qquad (62)$$

It is clear to see that the generation of 3D turbulence grids deals with a 3D convolution process. And if the situation is isotropic, it can be done separately. Otherwise, a texture filter (isotropic in 2D and anisotropic in another direction) or a

box filter (anisotropic in all directions) needs to be applied. For simplicity, we use the isotropic case that involves independent convolutions along 3 orthogonal directions. To differentiate the propagation direction and its transverse plane, we build a stock of independent 2D transverse planes first and then perform the envelope filter along the propagation direction. The diagram is shown as:

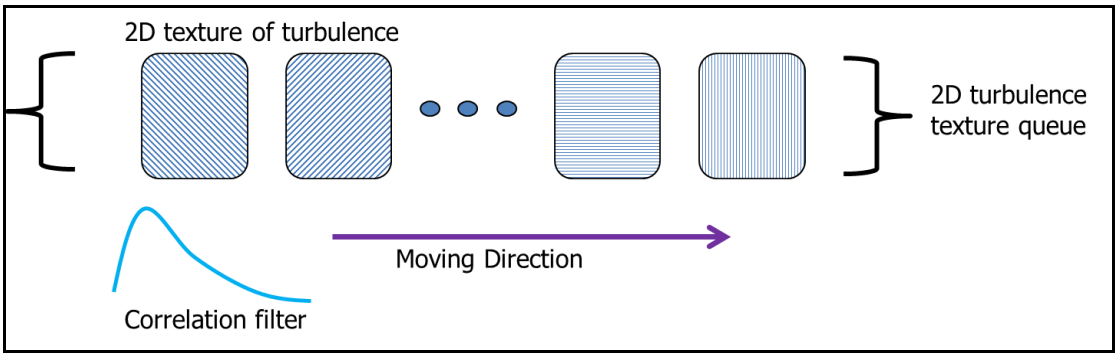

Figure 4. 4: generation of turbulence grids of refractive index

Generally, the generation sequence of turbulence can be swapped. We chose to build the transverse plane first to make the process similar to the phase screen model. However, turbulence grids allow for dense sampling along the propagation direction. In fact, if one modifies the phase screens to make them correlated for close ranges, eventually the turbulence generation process would lead to identical results. As a result, our proposed method of generating 3D turbulence grids is mathematically simple and a straightforward application of physics. For example, when we set $C_n^2 \approx 10^{-13}\ m^{-2/3}$, we present the 2 turbulence grids that are 10mm apart from each other by using the modified atmospheric spectrum model as mentioned above:

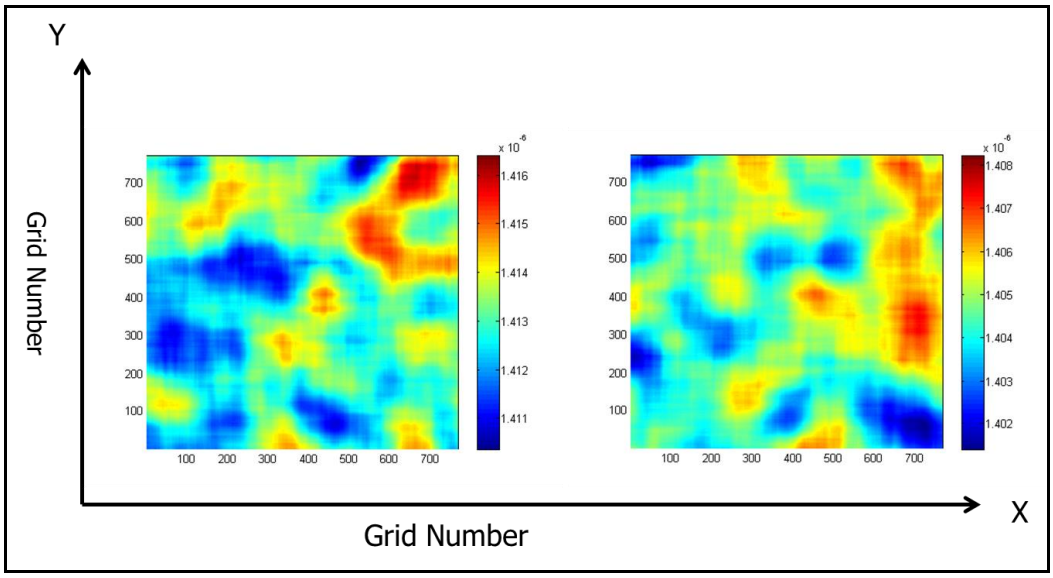

Figure 4. 5sampled 2D turbulence frames that are 10mm apart

The C_n^2 in our 3D turbulence grids generation is a reference of local fluctuation strength of refractive index.

4.4.2 Imbedded pseudo diffraction in 3D turbulence generation

It is not difficult to discover that the so called "eddies" or turbulence cells do exist and behave more or less in groups. Since the turbulence grids are just generated by WSS noise and an envelope filter, it is obvious to relate the envelope filter size to the actual controls on the diameters of turbulence cells. That is when the envelope filter is truncated at an arbitrary length within the inertial range $l_0<l_x<L_0$, it results in an aperture that matches with the turbulence cell size and it diffracts the turbulence grids a little. And it is not difficult to find the local diffraction patterns for the turbulence frames generated above.

4.4.3 Channel and signal separation

The channel and signal separation can be achieved by the "pseudo diffraction" processing where the turbulence channel and the various beam profiles are generated separately. The propagation law of the rays stays the same as in conventional

geometric optics. In general, the propagation process is an interaction between the beam and the channel. Some of the quantization steps in beam propagation process based on the "pseudo diffracted" channel are discussed as follows:

Geometric optics solves the refractive behavior of inhomogeneous media in a straightforward way. Since we have already arranged a mechanism in the turbulence channel that can cause pseudo-diffraction phenomenon for high density rays that propagate through, in the propagation algorithm we can make use of the geometric optics equations. In fact, the generation of 3D turbulence grids depends on the method of propagation. Because the beam's future behavior in diffraction has already been taken into account in the turbulent channel, it will be problematic if one propagates the beam in wave forms instead of ray forms.

To describe the propagation algorithm, we make use of a cluster of functions called "Plenoptic" functions that keep all the necessary information of a light field including ray location, momentum, phase and energy. The Plenoptic function is widely adopted by researchers in the imaging processing field[13], and we have modified it for use in turbulence simulations[14]. In general, the Plenoptic function can be written as:

$$\{P\} = \left\{\rho\left(x, y, \theta_x, \theta_y, \phi; z\right)\right\} \tag{63}$$

Where {} represents the cluster set for all rays in the light field, and x, y, θ_x, θ_y, ϕ, z are the geometric and phase parameters for each ray. $\boldsymbol{\rho(x, y, \theta_x, \theta_y, \phi, z)}$ is the weight function for the ray, and it can be amplitude or intensity for coherent or incoherent applications respectively. The convenience of the plenoptic function lies in that it is easier to describe and implement operations on the light field. For example, {2x}

means a horizontal stretching of the light field by a factor of 2. And the Plenoptic function is automatically energy preserving because:

$$\sum\{\rho\cdot\rho^{*}\}=\text{constant} \tag{64}$$

One can treat the Plenoptic function as a ***class*** in computer programing that includes parameters and functions. The function used in this thesis is simply an energy carrier (amplitude of rays) and is designed to describe the interaction between rays such as diffraction and interference. However, to avoid nonlinear functions with these behaviors, we separate the diffraction into the turbulence generation and thus the function can be kept in the simplest form. In other words, each ray is independent and can be computed in parallel. Therefore, the light field is updated at each step following the Plenoptic function:

(1) Location update:

$$\{x\}=\{x\}+\{\theta_x\}\cdot dz \tag{65}$$

$$\{y\}=\{y\}+\{\theta_y\}\cdot dz \tag{66}$$

(2) Momentum update:

$$\{\theta_x\}=\{\theta_x\}+\frac{\partial n_1}{\partial x}_{x=\{x\}}\cdot\frac{dz}{n} \tag{67}$$

$$\{\theta_y\}=\{\theta_y\}+\frac{\partial n_1}{\partial y}_{y=\{y\}}\cdot\frac{dz}{n} \tag{68}$$

(3) Phase update:

$$\{\phi\}=\{\phi\}+k\cdot n_1\cdot\left(\frac{\{dx^2\}+\{dy^2\}}{2dz}+dz\right) \tag{69}$$

(4) Energy update:

$$\{\rho\} = \{\rho\} \tag{70}$$

Clearly, propagating the beam through turbulent grids will simultaneously distort and diffract the rays. The geometric optics approach attributes the moment change by gradients in the distribution of refractive index as:

$$\frac{d}{ds}\left(n\frac{d\vec{r}}{ds} \right) = grad\, n \tag{71}$$

Where ***ds*** is the evolutional steps along the ray's trajectory and ds≈dz in the paraxial approximation. Therefore equation (67) and (68) is the quantized version of equation (71), expressed as:

$$\frac{d}{dz}\left((1+n_1)\frac{dx}{dz} \right) = \frac{dn_1}{dx} \tag{72}$$

$$\frac{d}{dz}\left((1+n_2)\frac{dy}{dz} \right) = \frac{dn_1}{dy} \tag{73}$$

The other equations in the Plenoptic function follow normal rules of linear propagation of rays.

As a result, the propagation of a laser beam through atmospheric turbulence has been reduced to updating a Plenoptic function through a turbulent grid. The computation algorithm has been designed to be a linear process and parallel computing can help speed up the calculation.

4.5 Simulation implementation and optimization with GPUs

The computation task and arrangement for the "pseudo diffraction" integrated geometric optics simulation of atmospheric turbulence needs to be carefully considered in order to be carried out on a normal GPU enabled computer. Normally, infinite computation power is not available. Therefore, we will discuss how to economically conduct the 3D geometric turbulence simulation.

4.5.1 Memory assignments and management

Although the algorithm introduced in previous sections seems feasible for a super-computer, the required data volume is overwhelming and therefore may be difficult to realize on a standard computer. For example, the spacing between grid points should be no greater than the inner scale l_0. This implies that a 2m×2m×1km channel with double precision data would require about 32TB (1TB≈2^{40} bytes). Therefore, both the algorithm and memory management must be carefully designed to reduce the computation power required. A major step of complexity compression is achieved by focusing only on the wavefront activity instead of the whole channel situation. This means that there is no need to build the turbulence channel all at once, it can be built step by step before the beam propagates through certain frames. And in the limit, one can generate one turbulence frame, propagate the wavefront and generate another and so on so forth. Therefore, the required memory storage problem is reduced to only 32MB (1MB≈2^{20}bytes), which allows computation to be done using only the memory on the GPU.

A second step is to make use of the parallel structure of GPUs to flatten the computation stacks. For each thread on the GPU, it only needs to follow a single ray's

updating problem. The recondition of this compression process is that each ray behaves relatively independently and is satisfied by our special treatment in the previous section. If careful consideration of the wave behavior is required, higher orders of the Plenoptic function are required and communication between threads is unavoidable. Therefore, all the evolutional propagation steps of the Plenoptic function are tailored to a similar image processing problem.

A third step is to generate enough of a number of independent 2D turbulence frames before the simulation and randomly load them in sequence and apply a correlation filter along the propagation axis to generate new turbulence grids. Therefore, the complexity of box convolution is reduced to 1D convolution. Also, the turbulence frame can be stored in the shared memory of a GPU to allow for parallel access by each thread.

4.5.2 Beam propagation

The arrangement of the GPU is shown as:

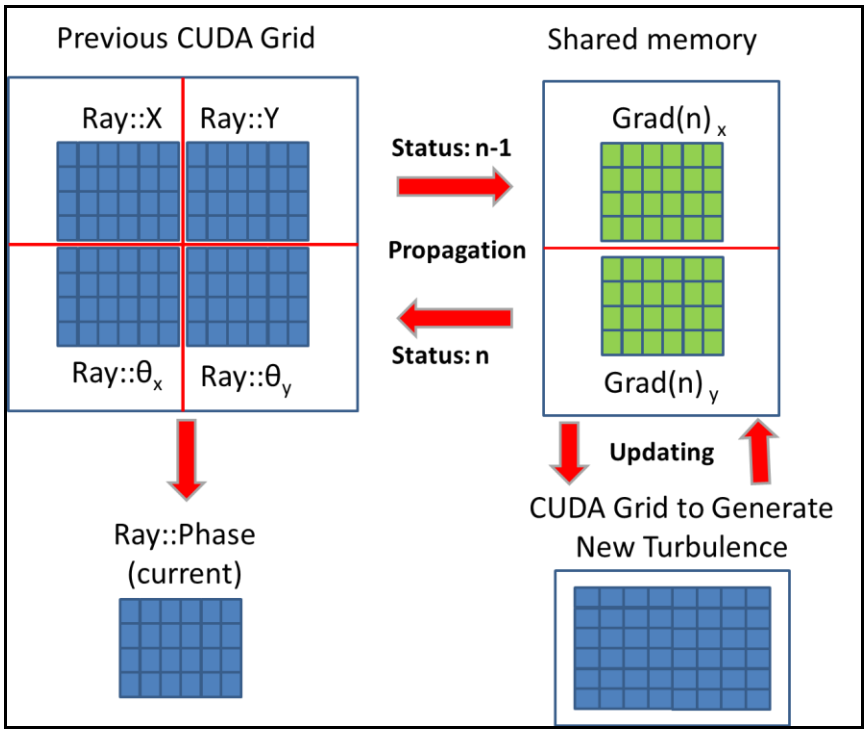

Figure 4. 6: GPU arrangement for evolutionally updating the light field through turbulence

As a result of the above efforts, the 3D turbulence simulation can be carried out by a normal computer that facilitates GPU computing. Clearly, the most resource consuming task is to generate turbulent grids that involve convolution. For example, it takes 19ms on a CUDA enabled GPU NVidia G-Force 770 ($400 general purpose GPU) to generate a new turbulence frame with 1024×1024 and filter size 255×255.And the overall complexity growth of the problem is linear with propagation distance. Thus it takes 50 min for simulating 3D beam propagation through static turbulence. If the optimization of using a pool of pre-generated 2D turbulence grids is used, the efficiency can be improved by 10 times. Yet to overcome the obstacles in field assessment with undetermined C_n^2, an additional scaling factor should be invoked because most spatial power spectra are linear with C_n^2 values.

Nevertheless, it needs to be pointed out that the arrangements of the computation resources depend on various applications. For example, if reciprocity is not considered, the past frames can be freed immediately, otherwise one has to store all the generated frames in the computer. Indeed the data volume with 3D turbulence simulation is strikingly large. This section gives general suggestions to manage the 3D simulation on a lab computer.

For some primary results, we set the turbulence channel with $C_n^2=10^{-13}$ $m^{-2/3}$ and propagation distance 1 km. The inner scale of turbulence is 1 mm and the outer scale is 1.00 m. The filter uses the modified atmospheric spectrum and is truncated at L=0.3m. The scale factor for pseudo-diffraction is selected by:

$$scl = \left(\frac{\sigma_X \cdot E(l = L)}{2\int_0^L E(l)dl} \right)^{-1} \frac{1.22\lambda}{\langle D \rangle} \tag{74}$$

Where D is the turbulence cell size, X and E represent normalized WSS noise and envelope filter respectively from the turbulence grid generation algorithm. The wavelength used is 600 nm. And for each simulation presented, $2^{20}\approx$1M rays are traced.

4.5.3 Simulation results for various turbulence conditions

For a collimated Gaussian beam with w_0=0.2 m, the beam distortion over 1km range looks like:

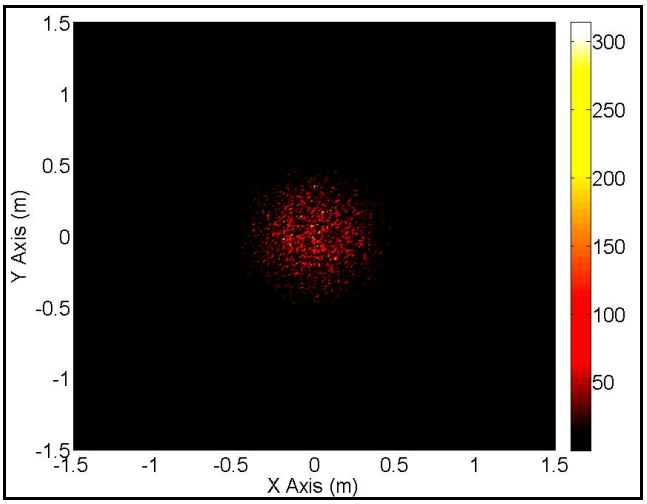

Figure 4. 7: Gaussian beam distortion through 1km turbulence (strong) channel

It is inferred from this result that the beam breaks up at the receiver aperture. If the beam is initially stretched with asymmetric w_x=0.1m, w_y=0.2m, then the result becomes:

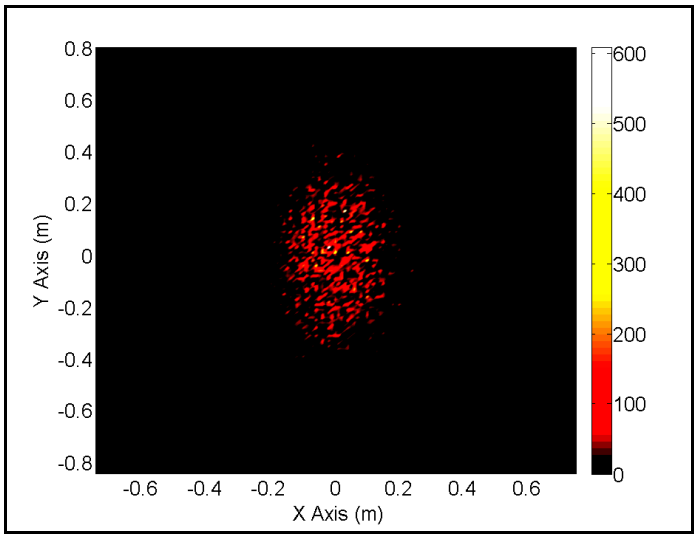

Figure 4. 8: Oval shaped Gaussian beam propagation through turbulence (strong) channel

If the turbulence gets lower with $C_n^2=10^{-14}$ $m^{-2/3}$ with all the other conditions unchanged, the result of the same Gaussian beam propagation looks like:

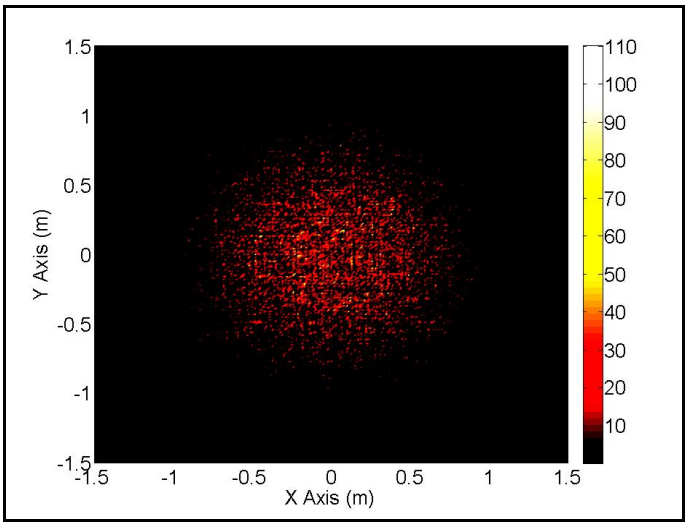

Figure 4. 9: Gaussian beam distortion through 1km turbulence (medium) channel

Though a speckle effect is still observable, the color scale suggests that the beam is less distorted since the intensity profile is more uniform. Similarly, if we stretch the initial Gaussian beam to be w_x=0.1m, w_y=0.2m, the received beam looks like:

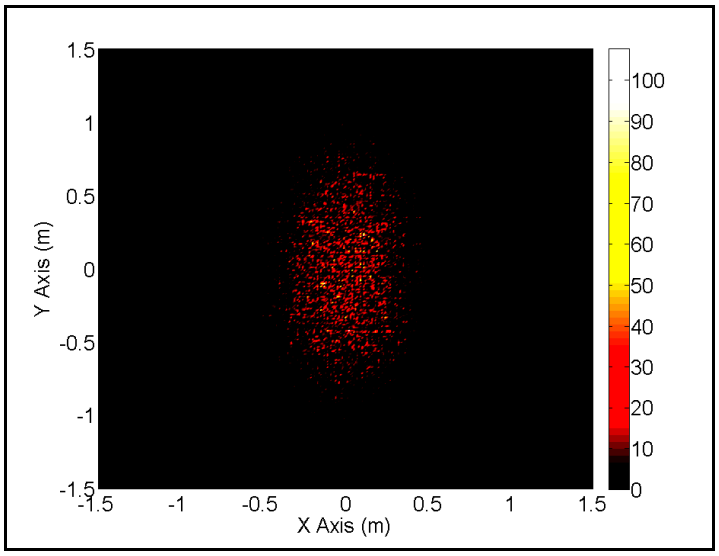

Figure 4. 10: Oval shaped Gaussian beam propagation through turbulence (medium) channel

In all of the above examples, diffractive vertical and horizontal lines are discernible since we use separable convolution to generate the turbulence grids in Cartesian coordinates. More application relevant simulations can be realized by the proposed

3D simulation algorithm. Yet in our work, we focus on the demonstration that the method of 3D geometric simulation and its individual uses for different cases can be explored similarly to the 2D phase screen models.

Since the results are presented by a ray counting method, the wave result can be derived by the methods introduced in section 4.1.2.

In conclusion, our proposed algorithm is an attempt to evolve from 2D phase screen simulation to 3D turbulence simulation. It innovatively creates a diffraction involved turbulence grid that simultaneously causes the ray refractive and diffractive behavior simply by using linear geometric ray functions. Therefore, the method is cost effective and can be computed by a normal computer with enabled GPU computation. And the invention of this 3D approach explores the aspect of turbulence's weak and continuous distorting mechanisms on the beam, which is generally neglected by 2D phase screen models. Therefore, the 3D simulation approach can serve as a more robust tool to develop and evaluate various beam correction strategies.

References:

[1] Durnin J. Exact solutions for nondiffracting beams. I. The scalar theory. JOSA A. 1987 Apr 1;4(4):651-4.

[2] Faugeras O. Three-dimensional computer vision: a geometric viewpoint. MIT press; 1993.

[3] Cruz-Neira, Carolina, Daniel J. Sandin, and Thomas A. DeFanti. "Surround-screen projection-based virtual reality: the design and implementation of the CAVE." In *Proceedings of the 20th annual conference on Computer graphics and interactive techniques*, pp. 135-142. ACM, 1993.

[4] Born, Max, and Emil Wolf. *Principles of optics: electromagnetic theory of propagation, interference and diffraction of light*. CUP Archive, 1999.

[5] Lane, R. G., A. Glindemann, and J. C. Dainty. "Simulation of a Kolmogorov phase screen." *Waves in random media* 2, no. 3 (1992): 209-224.

[6] Antonsen, Thomas M., and Dan Gordon. "Computational Accelerator Physics: Working Group Summary." *AIP CONFERENCE PROCEEDINGS*. IOP INSTITUTE OF PHYSICS PUBLISHING LTD, 2002

[7] Richards, B., and E. Wolf. "Electromagnetic diffraction in optical systems. II. Structure of the image field in an aplanatic system." In *Proceedings of the Royal Society of London A: Mathematical, Physical and Engineering Sciences*, vol. 253, no. 1274, pp. 358-379. The Royal Society, 1959.

Chapter 5: Experimental Results of the Plenoptic Sensor

In this chapter, we will demonstrate the functions of the plenoptic sensor through experimental results. The algorithms mentioned in chapter 3 will also be illustrated with intermediate steps and varying cases to help readers to gain better understanding on the principles of the plenoptic sensor.

5.1 Basic experimental platform

The basic experimental setup is shown as:

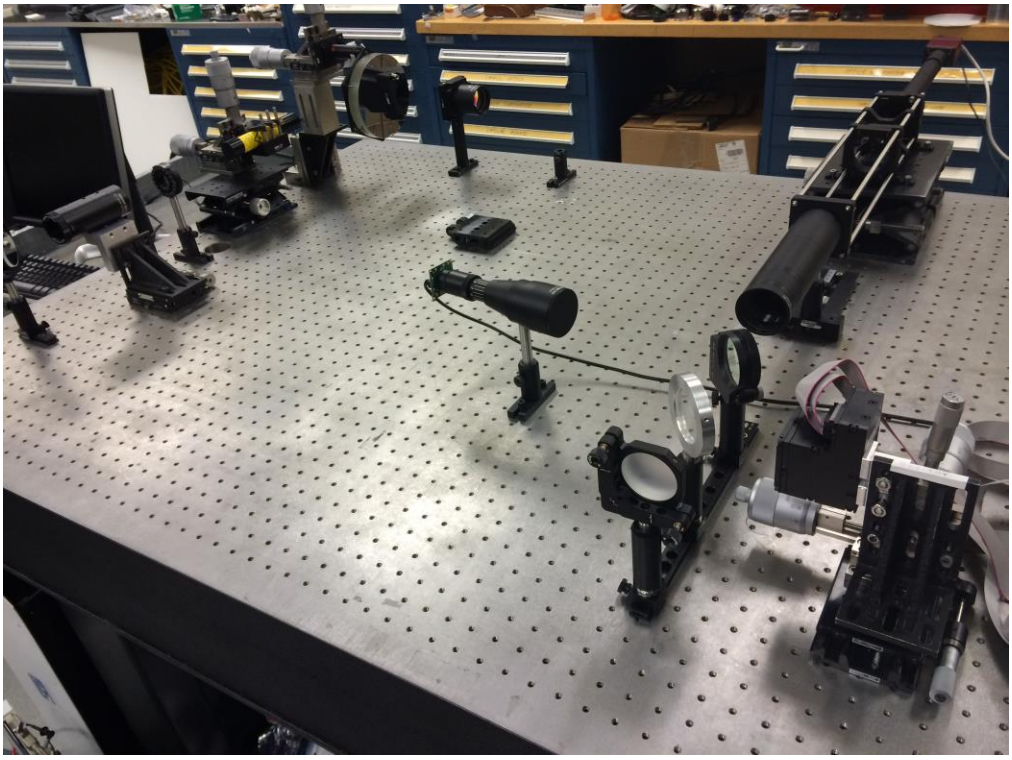

Figure 5. 1: Basic experimental setup picture

The illustrative diagram for this experimental setup can is shown as:

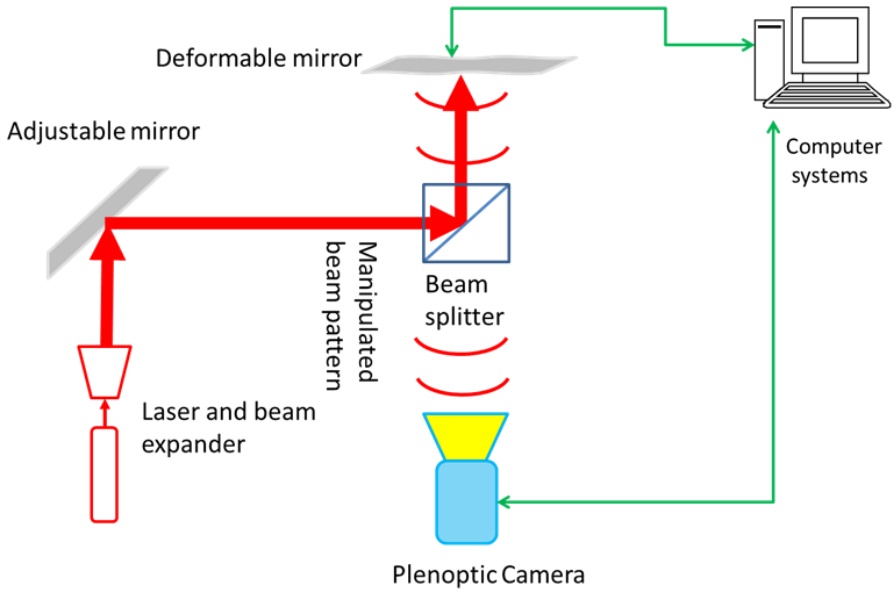

Figure 5. 2: Diagram for basic experimental setup picture

In figure 5.2, a laser beam is distorted by a deformable mirror and sensed by the plenoptic sensor. The plenoptic images are transferred to the computer and reconstruction algorithms can be applied to retrieve the distorted wavefront. To verify the algorithms' correctness, one can compare them with a known deformation applied to the deformable mirror. To implement a correction algorithm, the computer can give deformation orders to the DM based the result on the plenoptic sensor and check if the DM can be set flat again. The following experiments are built based on the basic platform.

5.2 Full reconstruction algorithm

In the full reconstruction algorithm, an OKO deformable mirror (piezoelectric, 37 actuators, 30mm diameter) is used to generate a known phase distortion. The plenoptic sensor is applied

to reconstruct the phase distortion independently. A collimated Gaussian beam is used at the transmitter's site. The detailed experiment diagram and layout are as shown [1]:

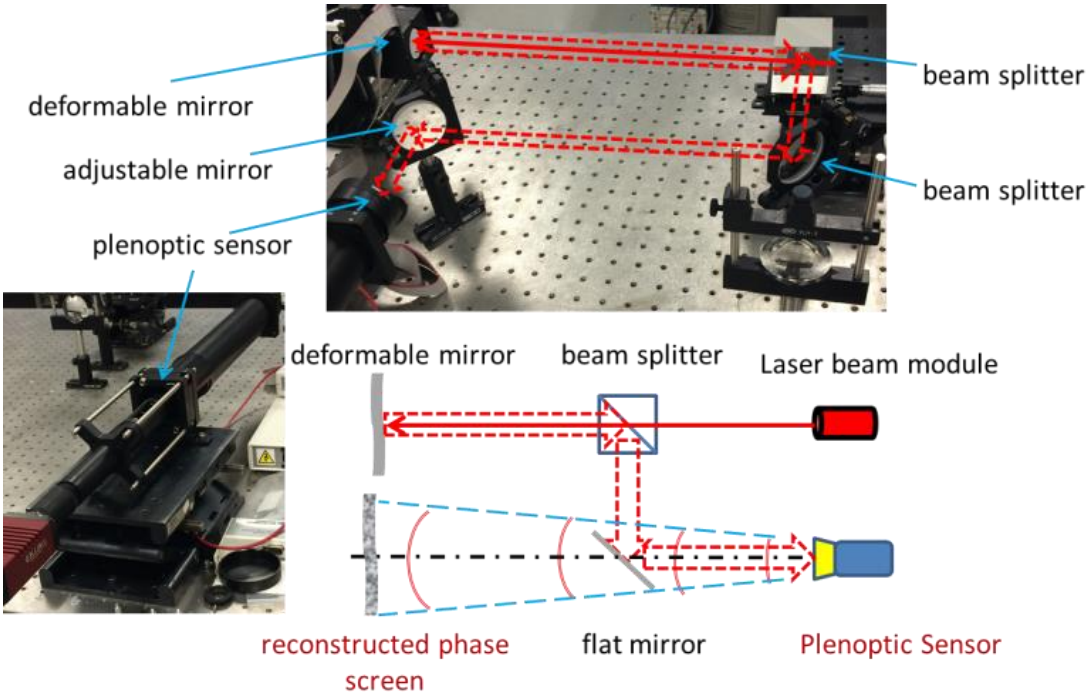

Figure 5. 3: Experimental setup for full reconstruction algorithm

The plenoptic sensor contains a thin objective lens with a 2 inch diameter and focal length of 750mm. The MLA used is 10mm by 10mm with 300μm pitch length and 1.6° divergence (EF = 5.1mm). The image sensor is an Allied Vision GX1050 monochrome CCD camera with a max frame rate at 109fps. A detailed diagram of the OKO 37-channel deformable mirror and its actuators' locations are shown in Figure 5.4.

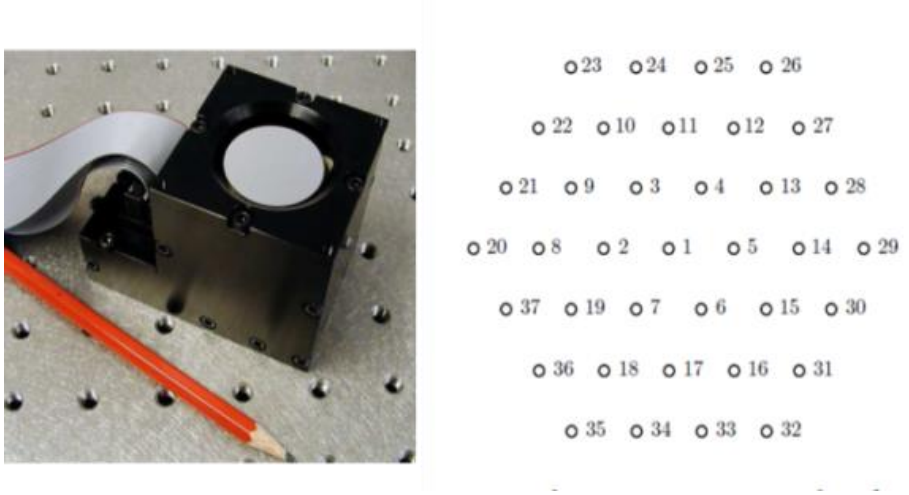

Figure 5. 4: OKO 37-channel PDM and its actuators' positions (observed from the back of the mirror)

The commands sent to the deformable mirror consist of 37 individual integer numbers ranging from 0 to 4095. The maximum number 4095 corresponds to a voltage of 150V, which drives a piezoelectric actuator in the DM to move to its full magnitude of 5.5λ (λ=632.8nm). When a deformation needs to be applied by the 37-actuators beneath the surface of the DM, one can use the experimentally determined scaling factor of 740/λ to form the distortion command.

The results for the reconstruction algorithms are shown as:

Case A:Defocus Z(2, 0) deformation

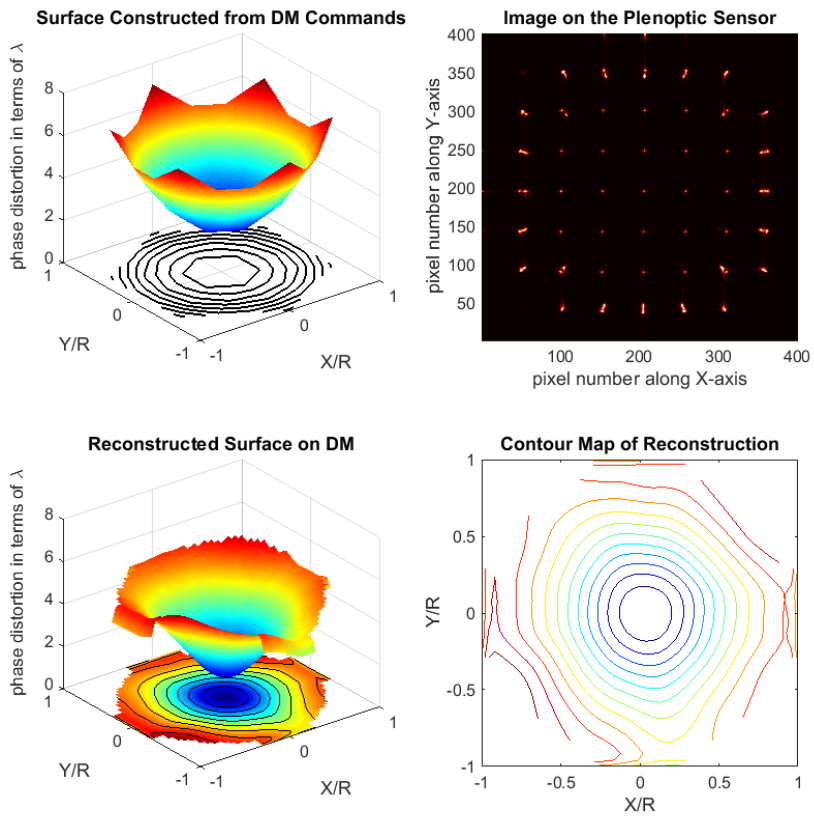

Figure 5. 5: Reconstruction results of a phase screen with Z(2, 0)

The "Defocus" can be expressed as:

$$Z_2^0(\rho,\theta) = A \cdot \rho^2 \qquad 0 \le \rho \le 1,\ \theta \in [0, 2\pi) \tag{1}$$

The symbol *"A"* in equation (1) represents the magnitude of the distortion (*A=4095* in the case of "Defocus"), while ρ and θ represent the normalized radius and angle respectively for the Zernike polynomial. Intuitively, the gradient of the "Defocus" function increases symmetrically when the radius ρ increases. The gradient at each spot *(ρ, θ)* is mapped into different blocks of the deformable mirror. Furthermore, the observation that the most outside blocks are illuminated with larger areas reflects that the gradients changes faster when the radius ρ increases.

A detailed explanation of figure 5.5 has been discussed in section 3.4.1, which will not be elaborated on here. Based on the reconstruction results, the channel (actuator) values on the deformable mirror can be quantitatively extracted by sampling the reconstructed surface at the geometries of the 37-channel actuators of the DM. Then by multiplying the same scaling factor of 740/λ, the channel based values can be compared with the original commands sent to the deformable mirror. The compact results in the "Defocus" case is listed in the table 5.1:

Table 5. 1: Channel values of "Defocus"

Channel	Distortion	Reconstruction	Error
1	0	0	0
2	455	742	287
3	455	641	186
4	455	633	178
5	455	782	327
6	455	916	461
7	455	794	339
8	1365	1828	463
9	1820	2276	456
10	1365	1862	497
11	1820	2267	447
12	1365	1904	539
13	1820	2225	405
14	1365	1716	351

15	1820	2247	427
16	1365	2064	699
17	1820	2611	791
18	1365	2045	680
19	1820	2149	329
20	3185	2671	-514
21	3185	2977	-208
22	4095	3443	-652
23	3185	3005	-180
24	3185	2976	-209
25	4095	3730	-365
26	3185	3302	117
27	3185	3229	44
28	4095	3453	-642
29	3185	2963	-222
30	3185	2821	-364
31	4095	3361	-734
32	3185	3167	-18
33	3185	3313	128
34	4095	4095	0
35	3185	3374	189
36	3185	3238	53
37	4095	3040	-1055

The first column of table 5.1 is the index of the actuators as demonstrated as in figure 5.5. The second column is the commands sent to the actuators of the DM, and the third column is the information extracted from the reconstruction at each position of the actuators. The fourth column (Error) in table 5.1 is derived by subtracting the third column by the second column. It reflects the overshoot of the reconstruction result compared with the original commands sent to the deformable mirror. Compared with the scaling factor of $740/\lambda$, most channels are reconstructed within an absolute error of $\lambda/2$ when the maximum deformation (5.5λ) is applied. Without loss of generality, we can use the correlation between the original commands and the reconstruction results to reflect how closely the deformation is recognized. A correlation value of *"1"* represents the complete recognition of the distortion; while a correlation value of *"0"* means that the reconstructed surface is completely irrelevant to the actual distortion. In the "Defocus" case, the correlation value is 0.956. According to figure 5.3, once the distortion pattern is recognized, the AO device can be intelligently arranged to compensate for the major phase distortion. The remaining distortion can be corrected by iteratively using the sensing, reconstruction, and compensation process, or by using conventional AO strategies such as SPGD [2] or SIMPLEX [3] methods.

The time consumption in a control-feedback loop in our experiment is about 13ms, which includes the image acquisition time (9.2ms), the algorithm processing time (3.1ms on CPU) and setup time for the DM (≈1ms). These times do not reflect the faster performance that could be achieved with more advanced (and costlier) components.

Other cases of Zernike polynomials expressed as *Z(m, n)* or equivalently Z_n^m can be sensed and reconstructed accordingly. For example, figure 9-12 show the reconstruction results of *Z(1, 1), Z(2, 2), Z(3, 3)* and *Z(4, 4)* respectively:

Case B: Tilt *Z(1, 1)* deformation:

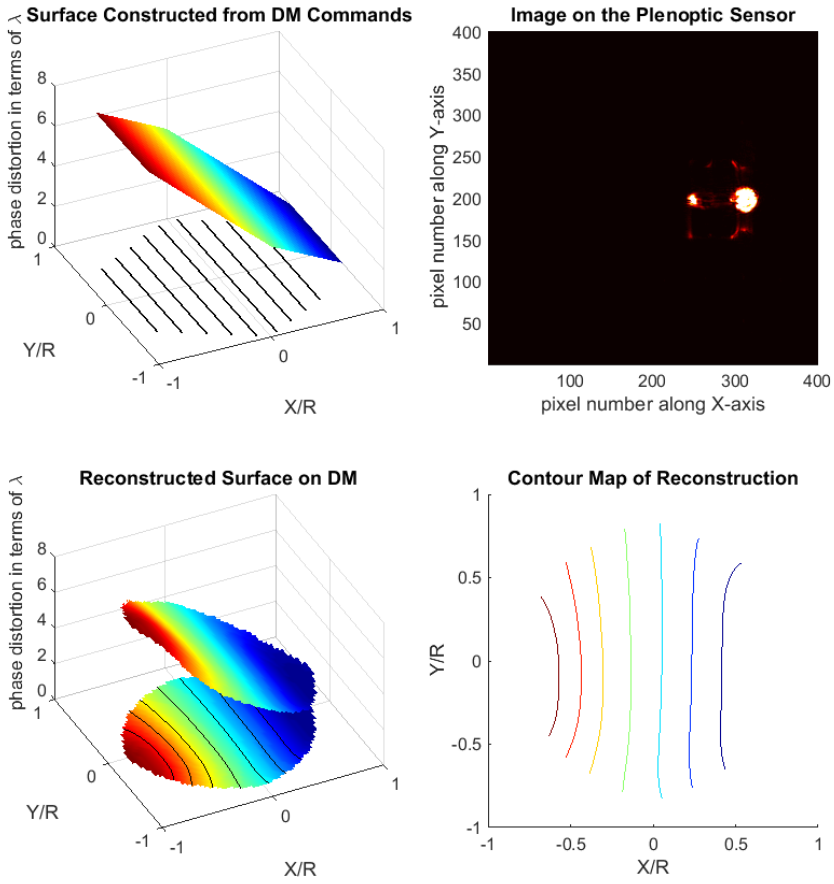

Figure 5. 6: Reconstruction results of a phase screen Z(1, 1)

The function of *Z(1, 1)* can be expressed as:

$$Z_1^1(\rho,\theta) = A \cdot \rho \qquad 0 \le \rho \le 1,\ \theta \in [0, 2\pi) \tag{2}$$

Case C: Astigmatism *Z(2, 2)* deformation:

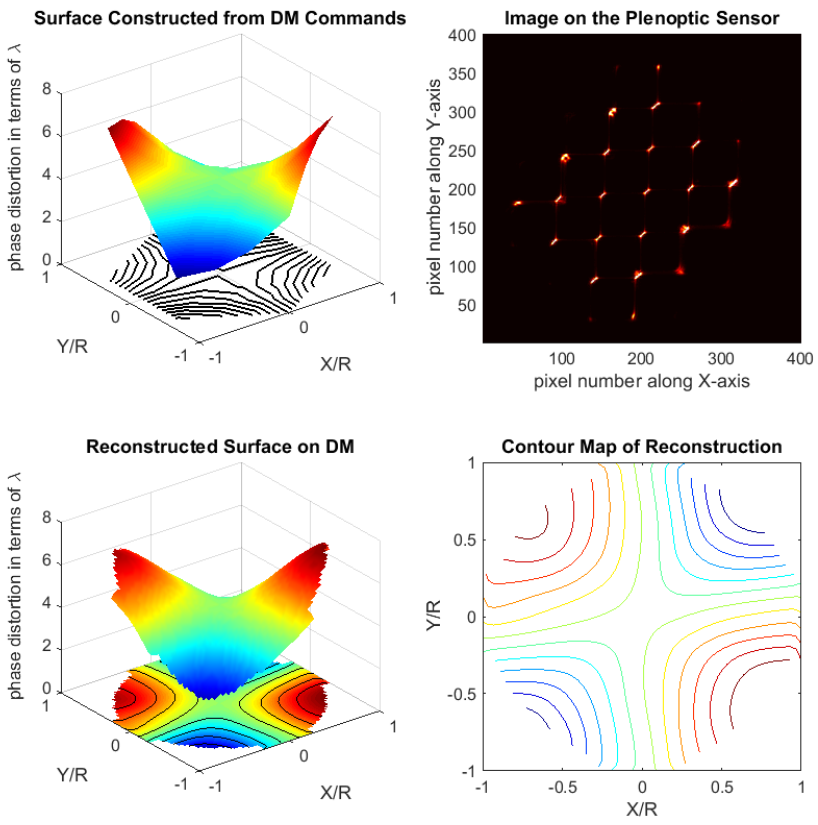

Figure 5. 7: Reconstruction results of a phase screen Z(2, 2)

The function *Z(2, 2)* can be expressed as:

$$Z_2^2(\rho,\theta) = \frac{A}{2}\left[\,\rho^2 \cdot \cos(2\theta) + 1\,\right] \quad 0 \le \rho \le 1,\ \theta \in [0, 2\pi) \tag{3}$$

Case D: Trefoil *Z(3, 3)* deformation:

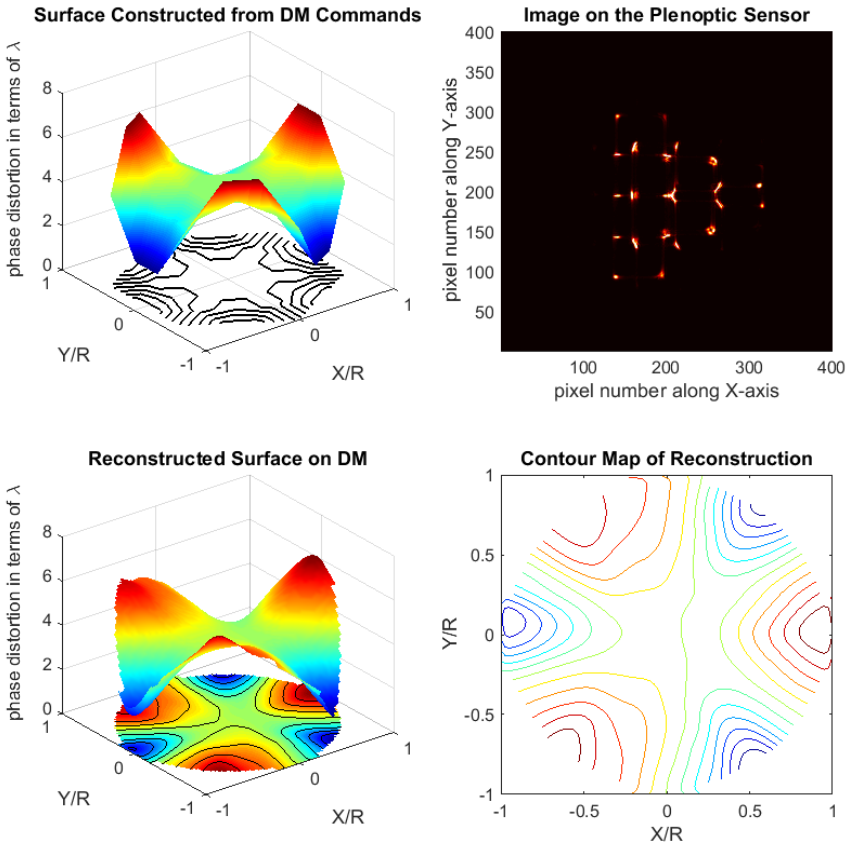

Figure 5. 8: Reconstruction results of a phase screen Z(3, 3)

The function *Z(3, 3)* can be expressed as:

$$Z_3^3(\rho,\theta) = \frac{A}{2}\left[\rho^3 \cdot \cos(3\theta) + 1\right] \quad 0 \le \rho \le 1,\ \theta \in [0, 2\pi) \tag{4}$$

Case E: Tetrafoil *Z(4, 4)* deformation

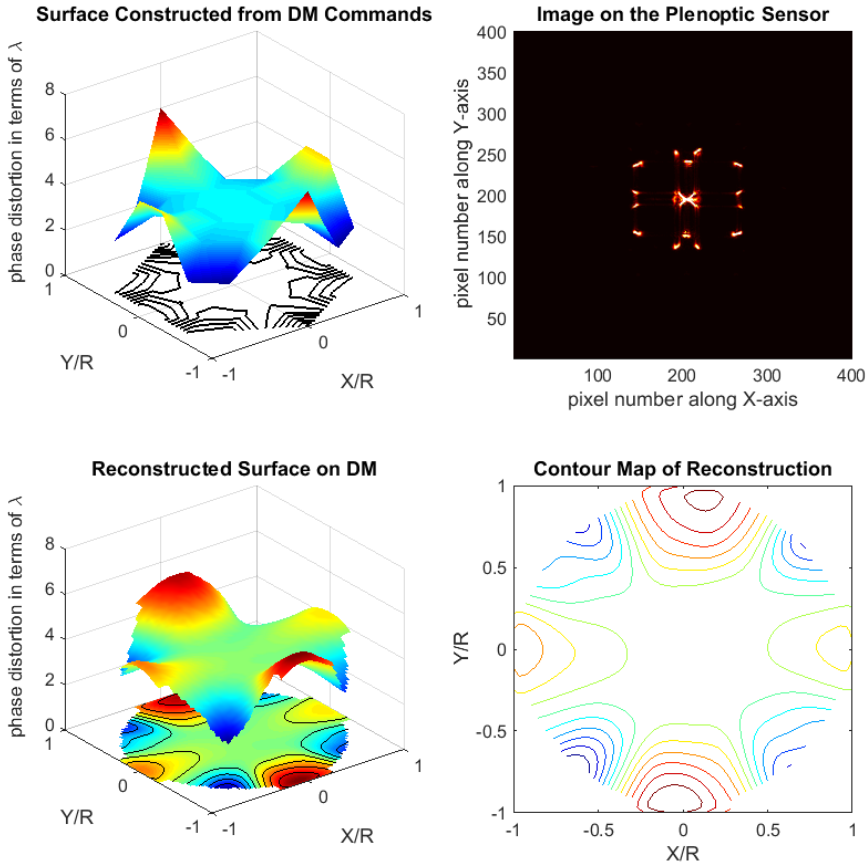

Figure 5. 9: Reconstruction results of a phase screen Z(4, 4)

The function *Z(4, 4)* can be expressed as:

$$Z_4^4(\rho,\theta) = \frac{A}{2}\left[\,\rho^4 \cdot \cos(4\theta) + 1\,\right] \quad 0 \le \rho \le 1,\ \theta \in [0, 2\pi) \tag{5}$$

The accuracies of the above reconstruction results can be evaluated similarly to the "Defocus" case by extracting the values for individual actuators and compared them with the original commands. The results are listed in table 5.2 and table 5.3:

Table 5. 2: Channel values of "Tilt" and "Astigmatism"

	Z(1, 1)		Z(2, 2)	
Channel	Distortion	Reconstruction	Distortion	Reconstruction

1	2048	2037	2048	1797
2	1367	1224	1820	1521
3	1367	1195	2275	2191
4	2048	1928	2048	1917
5	2728	2796	1820	1541
6	2728	2796	2275	2343
7	2048	2054	2048	1883
8	1367	1250	1365	1017
9	686	575	1137	934
10	686	491	2048	2011
11	686	497	2958	3010
12	1367	1213	2730	2782
13	2048	1952	2048	2023
14	2728	2777	1365	1048
15	3409	3456	1137	950
16	3409	3493	2048	2164
17	3409	3526	2958	3327
18	2728	2817	2730	2701
19	2048	2092	2048	1832
20	1336	1428	865	727
21	711	886	236	68
22	5	583	0	230
23	0	106	1418	1797

24	0	0	2677	2678
25	5	6	4095	3622
26	711	544	3859	3658
27	1336	1249	3230	2972
28	2048	1997	2048	1953
29	2759	2791	865	828
30	3384	3375	236	0
31	4090	3783	0	216
32	4095	4095	1418	1905
33	4095	4084	2677	3054
34	4090	4004	4095	4095
35	3384	3508	3859	3640
36	2759	2787	3230	2715
37	2048	2117	2048	1678

Table 5. 3: Channel values of "Trefoil" and "Tetrafoil"

	Z(3, 3)		Z(4, 4)	
Channel	Distortion	Reconstruction	Distortion	Reconstruction
1	2048	2052	1484	1591
2	2048	1871	1468	1583
3	2048	1854	1468	1545
4	2048	2281	1516	1529
5	2048	2103	1468	1634

6	2048	2174	1468	1677
7	2048	2314	1516	1590
8	1384	1258	1339	1554
9	2048	1926	1226	1286
10	2711	2845	1774	1803
11	2048	2066	1226	1515
12	1384	1557	1339	1683
13	2048	2664	2000	2606
14	2711	2955	1339	1566
15	2048	2275	1226	1462
16	1384	1416	1774	1989
17	2047	2794	1226	1445
18	2711	2992	1339	1500
19	2048	2434	2000	2354
20	0	638	1758	2407
21	0	0	0	409
22	2047	2063	178	481
23	4095	3579	2694	1955
24	4095	3844	2694	2118
25	2048	2258	178	947
26	0	256	0	1027
27	0	1070	1758	3100
28	2047	2878	4095	3834

29	4095	3518	1758	2297
30	4095	3957	0	481
31	2048	2287	178	800
32	0	364	2694	2212
33	0	1396	2694	2242
34	2047	3269	178	1007
35	4095	4095	0	0
36	4095	3343	1758	2649
37	2048	2042	4095	4095

In table 5.2 and table 5.3, the "Distortion" columns are the commanded deformation values for the DM to enforce different Zernike Polynomials. The "Reconstruction" columns are the value of the actuators extracted from the reconstructed phase distortion. The reconstructed channel values closely resemble the imposed distortions.

The largest mismatch in the case "Tilt" is actuator #22 with absolute error of 578 (equivalent to 0.78λ). The largest mismatch in the case "Astigmatism" is actuator #36 with absolute error of 515 (0.7λ). For the case "Trefoil", the largest mismatch is actuators #33 with absolute error of 1396 (1.9λ). And for the case "Tetrafoil", the largest mismatch is actuator #27 with absolute error of 1342 (1.8λ). Although the deformable mirror's surface condition is invariant under a constant shift (add the same value to each actuator), the worst reconstructed values can serve as an upper limit of the reconstruction errors. All of the largest mismatched actuators are at the edge of the DM (actuator #20 to actuator #37). This can be explained by the fact that the reconstruction algorithm integrates the gradients of the phase distortion from

the center point to the edge points of the DM's surface, and therefore the reconstruction errors accumulate and propagate to the outside actuators.

Table 5.4 provides the correlation and absolute RMS errors between the distortion values and reconstructed values for all achievable modes of Zernike polynomials on the deformable mirror. The mode Z_4^0 and modes higher than Z_4^4 can't be accurately enforced by the DM used in the experiment because the number of actuators in the DM is not adequate enough to represent spatial oscillations in the radius ($\boldsymbol{\rho}$) direction.

Table 5. 4: Difference between imposed distortions and reconstructed distortions in basic Zernike polynomials

Zernike Polynomial	Correlation	RMS Error
Tilt (Z_1^1)	0.993	0.20λ
Defocus(Z_2^0)	0.956	0.59λ
Astigmatism(Z_2^2)	0.975	0.32λ
Coma(Z_3^1)	0.936	0.49λ
Trefoil(Z_3^3)	0.932	0.62λ
Secondary Astigmatism (Z_4^2)	0.842	0.60λ
Tetrafoil (Z_4^4)	0.904	0.59λ

In table 5.4, the "Correlation" column shows that how closely the mode is recognized compared to the reconstruction results. The results show that all the basic polynomial modes

are recognized by the plenoptic sensor with the reconstruction algorithm. The "RMS Error" column demonstrates the average error for each reconstructed case of Zernike polynomials. Compared with the maximum phase distortion in each case (5.5λ), "RMS Error" accounts for on average 10% of the maximum magnitude of phase distortion.

To demonstrate a more general case where the distortion is a superposition of various Zernike polynomials, a case of half "Trefoil" + half "Tetrafoil" is shown as:

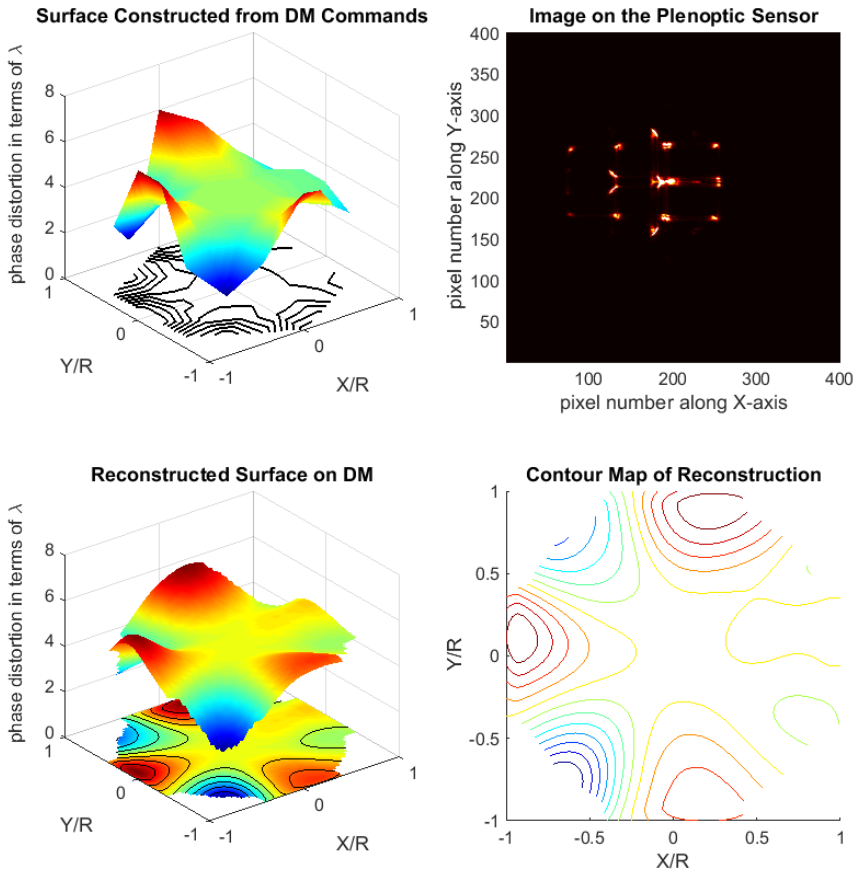

Figure 5. 10: Reconstruction results of a phase screen that combines 2 basic Zernike modes

The function of the distortion used is:

$$Z(\rho,\theta) = \frac{A}{4}\left[\,\rho^4\cos(4\theta) + \rho^3\cos(3\theta) + 2\,\right] \tag{6}$$

where the parameters satisfy:

$$0 \le \rho \le 1,\ \theta \in [0, 2\pi) \tag{7}$$

Figure 5.10 shows that for an arbitrary distortion, the plenoptic sensor is able to use a single reconstruction process to recognize the major distortions in phase. In fact, the Zernike polynomials can be treated as Eigen-modes for a phase distortion and an arbitrary distortion can be expressed with combinations of basic Zernike polynomials plus small local distortions. Therefore, the reconstruction case in figure 5.10 is as accurate as the cases of single mode Zernike polynomials. The correlation between the initial distortion and the reconstructed results in terms of channel values is 0.917 and the "RMS Error" is 0.54λ.

The detailed channel values of the initial distortion and reconstructed distortion for figure 5.10 are listed in table 5.5:

Table 5. 5: Channel values for combined Zernike Polynomial "Trefoil" + "Tetrafoil"

Channel	Distortion	Reconstruction	Error
1	2144	2266	122
2	2133	2232	99
3	2133	2330	197
4	2167	2237	70
5	2133	2317	184
6	2133	2239	106
7	2167	2400	233
8	2397	2551	154
9	1962	2016	54
10	1994	2375	381

11	1962	2428	466
12	2397	2419	22
13	2509	3005	496
14	1687	1864	177
15	1962	2196	234
16	2705	2724	19
17	1962	1696	-266
18	1687	1911	224
19	2509	3023	514
20	3434	3283	-151
21	2192	2419	227
22	1222	1842	620
23	1903	2126	223
24	1903	2488	585
25	1222	2107	885
26	2192	2701	509
27	3434	3864	430
28	3990	4095	105
29	1242	1962	720
30	0	950	950
31	1222	2074	852
32	4095	3848	-247
33	4095	3108	-987

34	1222	1142	-80
35	0	0	0
36	1242	2053	811
37	3990	3386	-604

Similar to the previous discussions in different Zernike distortion cases, the channel values from the reconstruction resemble the initial distortion imposed by the deformable mirror. Based on the full reconstruction results, corrections in the experimental setup can be quickly applied by subtracting values sampled on the reconstructed phase front. In fact, a minimum of 90% phase correction can be achieved in the one step "observe and subtract" correction algorithm in this experimental platforms.

5.3 Fast reconstruction algorithm

The experiment diagram and picture of the instruments are shown as in figure 5.11:

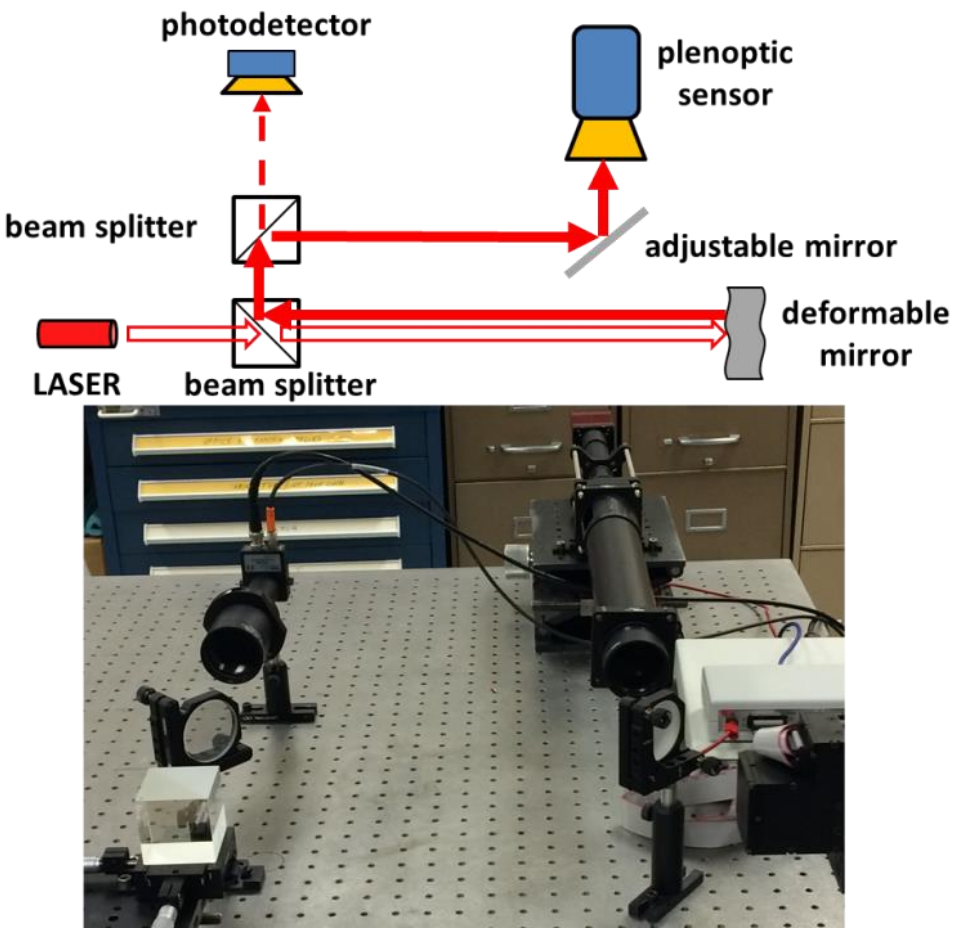

Figure 5. 11: Experimental setup for fast reconstruction algorithm

In the diagram shown in figure 5.11, a 5mW 632.8nm He-Ne laser source (Thorlabs: HNL050L) is used and expanded to a collimated beam with 40mm diameter. The beam propagates through a 50mm cubic beam splitter and reflects off the surface of the DM. The reflected beam is truncated by the DM to an aperture with 30mm diameter and a superposed phase change. Then the distorted beam with 30mm diameter is directed to the plenoptic sensor to measure the phase distortions as shown by the solid red arrows in Figure 5.11. A secondary channel directs the distorted beam to a photodetector to measure the undistorted amount of optical intensities as shown by the red dashed arrow in Figure 5.11. This secondary channel uses an aspherical lens of focal length of 150mm and a pinhole with

0.1mm diameter placed at the back focal spot of the lens. A photodetector (Thorlabs: PDA100A) is put behind the pinhole. Thus, any significant distortion will deviate part of the beam away from the focal spot and reduce the intensity value on the photodetector.

The plenoptic sensor uses an Allied Vision GX1050 monochrome camera (1024×1024 in resolution with 5.5 μm pixel width, and operating at 109 fps) as its image sensor. The objective lens has a clear aperture of 50mm and focal length of 750mm. The MLA used is a 10mm×10mm microlens array with 300μm cell width and 5.1 mm focal length (Edmund Optics: #64-476). Limited by the size of the image sensor, the plenoptic sensor has 18×18 (324) as the maximum number of image cells.

When no distortion is applied to the beam, the photodetector obtains the highest intensity value and the plenoptic sensor shows a round beam in one image cell (defined as the center block). When a distortion is applied by the DM, the photodetector shows a drop of value and the plenoptic sensor shows distributed patches in different image cells. Therefore, the goal of SPGD correction (based on the feedback from the photodetector) is to maximize the intensity value on the photodetector. The goal of guided correction (based on the feedback from the plenoptic sensor) is to rehabilitate the image of the beam to the center block.

The image metric used on the plenoptic sensor is "power out of the bucket (POB)," which measures the intensity sum outside the center block divided by a constant scaling factor. The photodetector measures the power of the undistorted optic flux and is conventionally referred to as "power in the bucket (PIB)" [4]. We choose POB as our image metric for the plenoptic sensor because of its simplicity and its complementary property with the PIB measurement on the photodetector. Based on POB, one can implement an advanced image metric that varies significantly when some patches move further away from the center block.

To initiate the phase distortion, we use the DM to mimic various modes of Zernike Polynomials with peak to peak value of 5.5λ (λ=632.8nm). This maximum deformation is experimentally determined, and a larger magnitude of deformation can't be accurately enforced by the DM due to hysteresis effects in the piezoelectric actuators. Note that the when the beam is reflected from the surface of the DM, the actual peak to peak phase distortion is <11λ. Since the Zernike Polynomials are Eigen modes of an arbitrary deformation on the DM, the expected iteration steps are bounded by the best and worst cases of correcting those Zernike modes.

To correct the phase distortion, we use an algorithm called "Guided SPGD" method, which first uses the plenoptic sensor to iteratively use our fast reconstruction algorithm to correct for the major phase distortion, and then start a conventional SPGD algorithm for optimization when the beam is almost corrected (lower than a threshold image metric value). For comparison, the "Pure SPGD" method is applied to correct the same deformation, which strictly uses SPGD algorithm for each iteration step of correction.

For convenience of illustration, we will first introduce the results on "Tree" reconstruction algorithm. The results of "Checkerboard" reconstruction has already been discussed in chapter 3 in the entropy theory part (section 3.5.2). In fact, the "Checkerboard" reconstruction is a mini version of the full reconstruction algorithm, and the speed up effect lies between the "Tree" algorithm and the full reconstruction algorithm. For simplicity, we can treat the "Checkerboard" reconstruction algorithm as a balance between the full reconstruction and the fast "Tree" reconstruction.

5.3.1 Static distortion

A detailed result of the fast reconstruction algorithm can be explained in figure 5.12 by using the Trefoil deformation as an example. The upper-left plot shows the plenoptic image when the Trefoil deformation is applied (the non-illuminated image cells are not shown in this plenoptic image). The upper-right plot is the maximum spanning tree that the algorithm derives to recognize the major phase distortion pattern. The bottom-left plot shows the original command on each actuator of the DM to generate the deformation. The bottom-right plot shows the reconstructed phase for the actuators by using the fast reconstruction algorithm. The maximum spanning tree indicates which set of pixels the fast reconstruction should use to form a "sub-optimal" reconstruction of the phases on the vertices (optimal reconstruction can be achieved by using all the pixels). In other words, the fast reconstruction algorithm makes use of the pixels that represent the location of the *N-1* edges rather than the whole 2D plenoptic image, which brings down the input data requirement from 2D to 1D. It is clear that the fast reconstruction recognizes the dominant phase distortion correctly. In other words, the one step phase compensation will be sufficient to fix most of the phase distortion in this "Trefoil" case.

Meanwhile, since the "Tree" reconstruction uses only the pixels covered by the edges and each edge represents the local tip/tilt between neighboring actuators, it is looking for the most significant and non-overlapping *N-1* local tip/tilt deformations and connect them with a "global" tree structure. Parallel algorithm can also be invoked to extract the edge information simultaneously because they are geometrically separated on the plenoptic image.

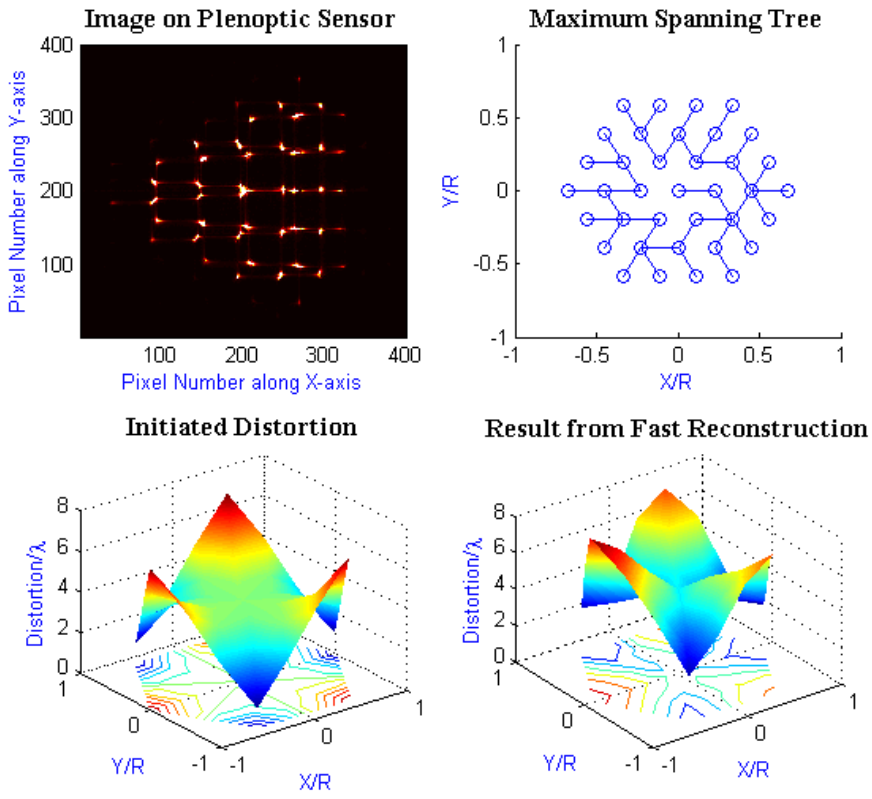

Figure 5. 12: Fast reconstruction result for "Trefoil" deformation

5.3.2 Adaptive optics corrections

To correct the phase distortion, we use an algorithm called "Guided SPGD" method, which first uses the plenoptic sensor to iteratively use our fast reconstruction algorithm to correct for the major phase distortion, and then start a conventional SPGD algorithm for optimization when the beam is almost corrected (lower than a threshold image metric value). For comparison, the "Pure SPGD" method is applied to correct the same deformation, which strictly uses SPGD algorithm for each iteration step of correction.

We start with a simple tip/tilt case in Zernike Polynomials as shown by figure 5.13:

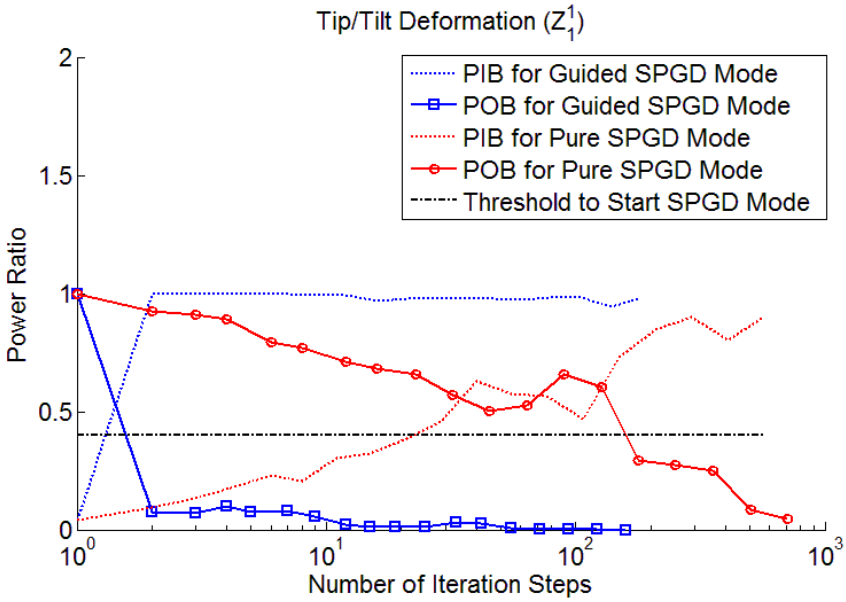

Figure 5. 13: Fast reconstruction results for correcting Tip/Tilt deformation

In Figure 5.13 a tip (or equivalently tilt) deformation is applied by the DM. The deformation can be expressed as:

$$Z_1^1(\rho,\theta) = A \cdot \rho \qquad 0 \le \rho \le 1,\ \theta \in [0, 2\pi) \tag{8}$$

In equation (8), *"A"* is the magnitude of the phase deformation ($A=11\lambda$), while ρ and θ represent the normalized radius and angle respectively.

As shown by the legend, the solid blue line represents the improving curve of the "Guided SPGD" method. It is obvious that the major correction is completed in one step through the guidance of the plenoptic sensor. Then the correction enters the SPGD mode to make tiny random iterations to minimize the image metric (or equivalently, maximize the power collected by the photodetector). At the 10^{th} iteration step, the beam has already reached the vicinity of the optimum point. This result of "Guided SPGD" mode is also reflected by the "PIB" curve on the photodetector data, which is a complement for the "POB" curve. As shown by the solid red line, when the "Pure SPGD" method is applied to correct for the same

distortion, it takes about 150 iteration steps to reach the threshold for the "Guided SPGD" method and many more iteration steps (about 800) to get close to the optimum point. The difference can be intuitively explained: when the tip/tilt deformation is applied, it moves the beam from one image cell to another on the plenoptic sensor. The movement is recorded by all the 90 edges and the spanning tree will have every branch indicating the phase tip/tilt (the deformation can be fully recognized regardless of which branches are selected). Thus the correction orders for the actuator on the DM will correct the deformation directly in the 1st step.

The "SPGD" method, on the other hand, will generate an identical and independent distribution (i.i.d) of Bernoulli *(p=0.5)* over set *{+ε, - ε}* for each actuator, where ε is a small deformation. Then, it determines the gradient of the image metric over this small step and tells the next movement whether to either forward this step (if it decreases the "POB" image metric) or reverse this step (if it increases the "POB" image metric) in proportion to the magnitude of the gradient. Thus, improvement can be guaranteed in terms of every 2 iteration steps. In practice, we make slight improvements on the SPGD to make assured convergence in roughly every 1.5 steps by empirically equalizing the magnitude of the trial step ε with the actual correcting deformation determined by SPGD. Note that we make ε linearly scaled by the image metric value to accelerate the convergence (similar to the gain coefficient γ in the formal theory of SPGD). Then, the SPGD method will either keep the deformation or reverse the deformation to make assured decreasing in 1.5 steps (the trial step is actually the correction step). However, with 37 actuators, the convergence is relatively slow because the typical result of a random trial step makes little improvement on the image metric (statistically half of the actuator get closer to the correct deformation while the other half of

the actuators get farther away from the correct deformation). Intuitively, for a DM with N actuators, each iteration step has $(1/2)^N$ chance to guess the perfect directions of movement for all the actuators. Therefore, given N=37, the chance that SPGD can generate significant improvement in the first step is almost zero. The plenoptic sensor, however, has the capability to recognize the major phase distortion and inform the actuators to move correctly not only in terms of directions, but also in terms of proper magnitude. Thus, the extra intelligence provided by the plenoptic sensor can dramatically reduce the overall steps needed for beam correction (or equivalently make convergence to optimization more quickly).

We should also account for the fact that the image based feedback loop takes longer per iteration than the time required for a photodetector feedback loop. For example, in our experiment, the image based feedback loop operates at 65 fps (9.2ms for image acquisition, 1.5ms for DM control and 4.6ms for computer process time including calculating the image metric). Comparatively, the photodetector feedback loop operates at 482 fps (1.5ms for DM control and 0.57ms for photodetector data acquisition plus computer process time). Therefore, by regarding each guidance step from the plenoptic sensor as about 8 iterations in SPGD mode, we can find the corresponding improvement in terms of time. For the tip/tilt deformation, since there is only 1 step guidance from the plenoptic sensor, the improvement by "Guided SPGD" method is still significant when compared with "Pure SPGD" method. We also stress that these execution times are currently constrained by working in a Microsoft Windows environment with its associated overhead, and the max operational speed of our current deformable mirror. Execution times per iteration can be dramatically improved by implementing FPGA operation with a faster response deformable mirror. More results are shown as follows:

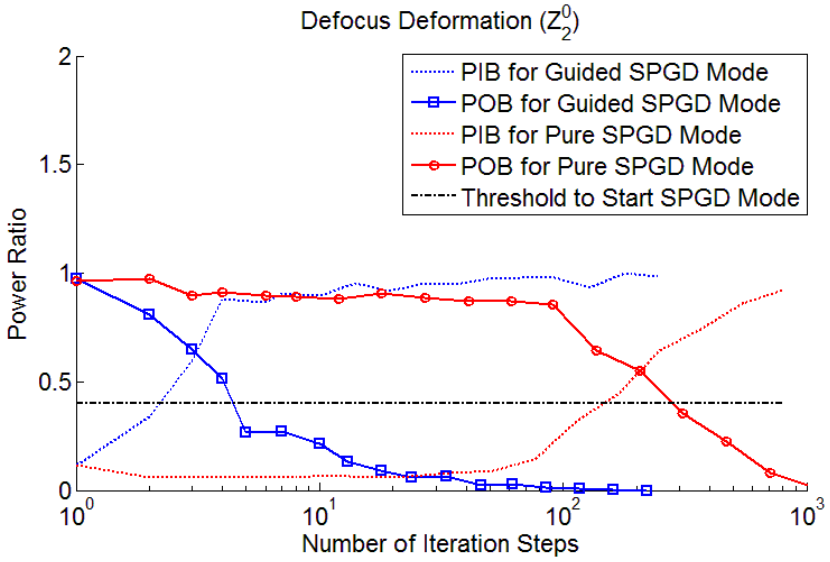

Figure 5. 14: Fast reconstruction result for correcting Defocus deformation

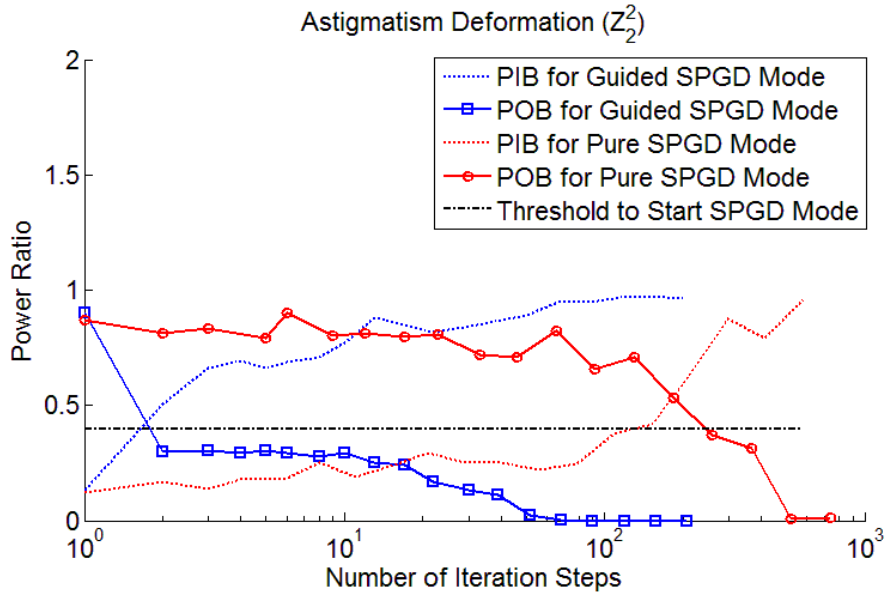

Figure 5. 15: Fast reconstruction result for correcting Astigmatism deformation

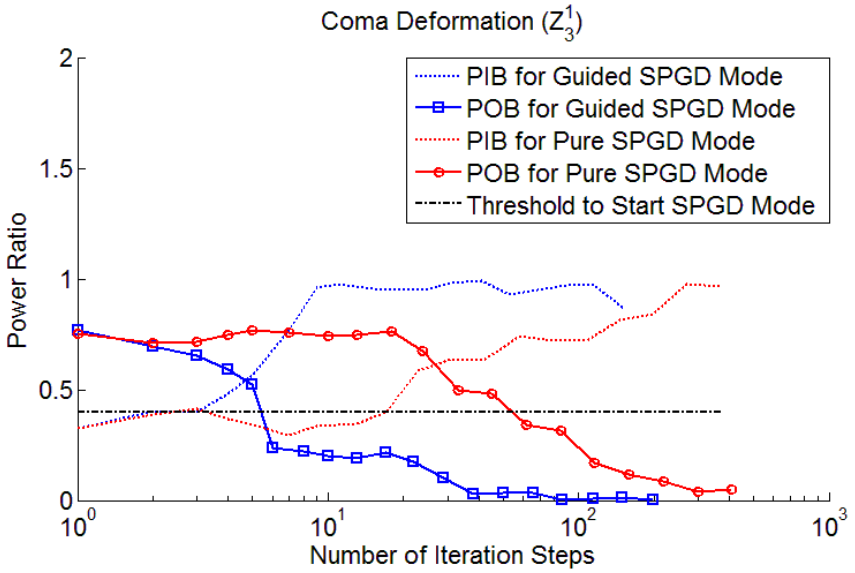

Figure 5. 16: Fast reconstruction result for correcting Coma deformation

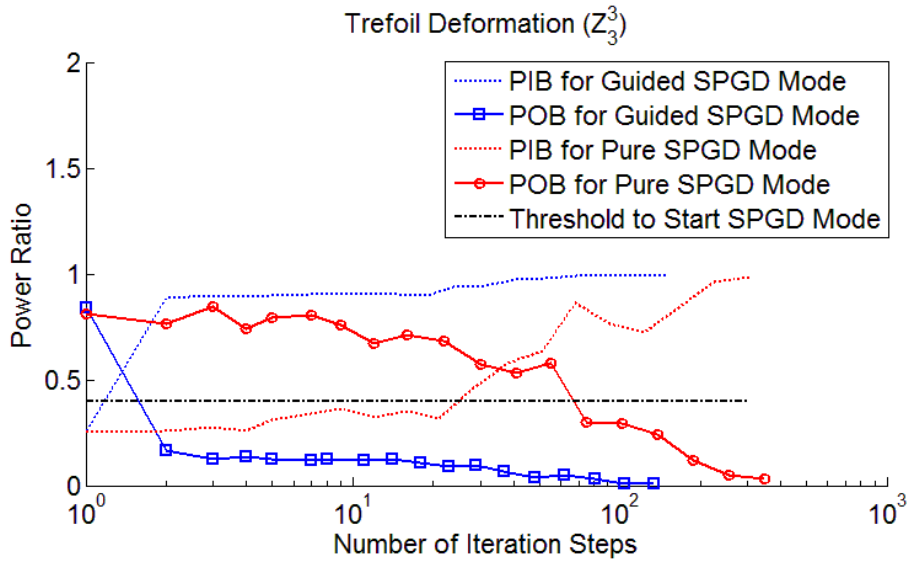

Figure 5. 17: Fast reconstruction result for correcting Trefoil deformation

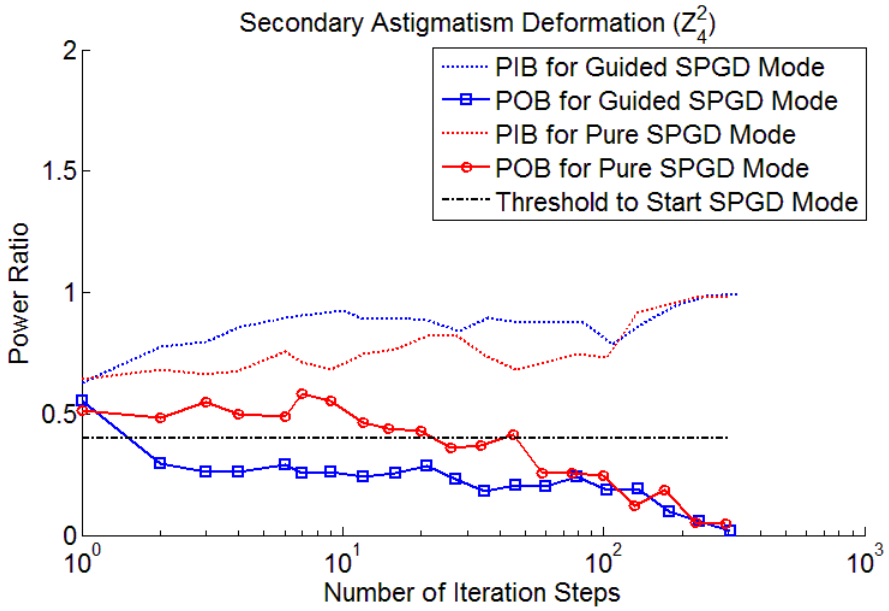

Figure 5. 18: Fast reconstruction result for correcting Secondary Astigmatism deformation

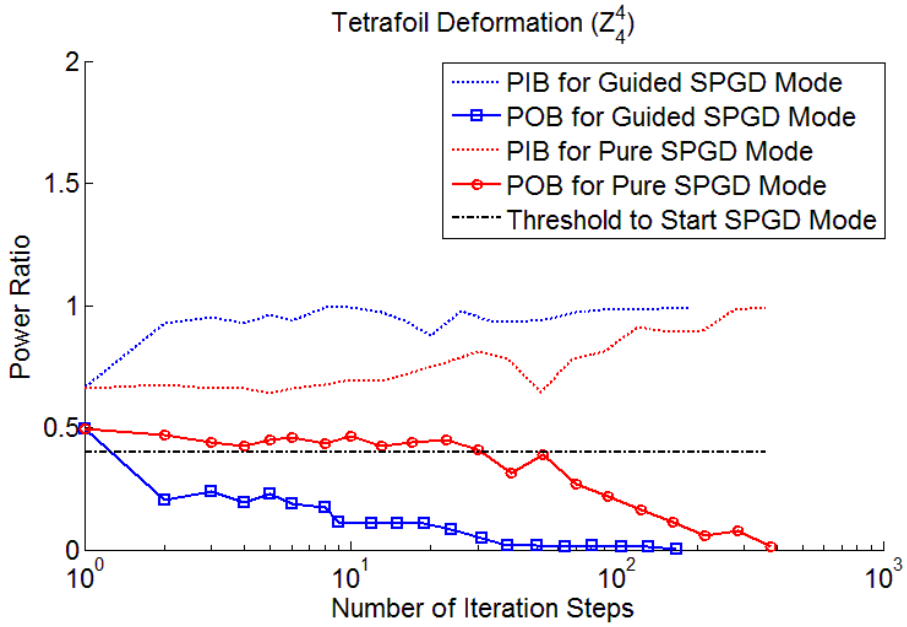

Figure 5. 19: Fast reconstruction result for correcting Tetrafoil deformation

Figure 5.13-5.19 show the comparison between the "Guided SPGD" method and "Pure SPGD" method for different orthogonal modes that are achievable on the DM. Given *"A"* as the magnitude of the phase deformation (*A=11λ)*, ρ and θ as the normalized radius and angle. We can express those deformations as:

$$Defocus: \qquad Z_2^0(\rho,\theta) = A \cdot \rho^2 \tag{9}$$

$$Astigmatism: \quad Z_2^2(\rho,\theta) = \frac{A}{2}\left[\, \rho^2 \cdot \cos(2\theta) + 1 \,\right] \tag{10}$$

$$Coma: \quad Z_3^3(\rho,\theta) = \frac{A}{2}\left[\, (3\rho^3 - 2\rho) \cdot \cos(4\theta) + 1 \,\right] \tag{11}$$

$$Trefoil: \quad Z_3^3(\rho,\theta) = \frac{A}{2}\left[\, \rho^3 \cdot \cos(3\theta) + 1 \,\right] \tag{12}$$

$$Secondary\,Astigmatism: Z_4^2(\rho,\theta) = \frac{A}{2}\left[\, (4\rho^4 - 3\rho^2) \cdot \cos(4\theta) + 1 \,\right] \tag{13}$$

$$Tetrafoil: \quad Z_4^4(\rho,\theta) = \frac{A}{2}\left[\, \rho^4 \cdot \cos(4\theta) + 1 \,\right] \tag{14}$$

The parameters from equation (9) to equation (14) should satisfy:

$$0 \le \rho \le 1, \ \theta \in [0, 2\pi) \tag{15}$$

As shown by the results in figure 5.13-5.19, the "Guided SPGD" method converges to optimized phase correction much more effectively than the "Pure SPGD" method. The blue "PIB" curve (provided by the photodetector) for the "Guided SPGD" method in each deformation shows the exponentially increasing intensity on the receiver. This is also reflected by the blue "POB" curve for the "Guided SPGD" method in each deformation. In comparison, note that the red "POB" curve for "Pure SPGD" in each deformation is generally a concave curve with regard to the logarithm of iteration steps. This reveals that

SPGD is more efficient in correcting weak distortion than in correcting strong distortion. Equivalently, the same conclusion can be drawn by inspecting the convexity of the red "PIB" for the "Pure SPGD" method in each deformation. Intuitively, the major proportion of iteration steps is conducted by SPGD in both methods, while the "Guided SPGD" uses guidance from the plenoptic sensor to find a much better starting point for SPGD than the unguided "Pure SPGD" method. It costs very few steps to find the starting point with the help of the plenoptic sensor, and therefore, much faster convergence can be achieved by the "Guided SPGD" approach.

For some cases such as "Defocus" in figure 5.14 and "Coma" in figure 5.16, the "Guided SPGD" needs more than one step to accomplish the major correction (bring the image metric value down to the threshold value of "*9*" to trigger SPGD mode for optimization). This means that one step fast reconstruction does not suffice to recognize all the major phase distortions. However, the algorithm will iteratively recognize the most "significant" phase distortion patterns and suppress them with phase compensation. Intuitively, the word "significant" means the light patches that illuminated the pixels of certain edges most. The plenoptic image sequence for the first 4 guided correction steps in the "Defocus" case (figure 5.14) are shown by figure 5.20.

The step-by-step plenoptic images of the guided corrections show how the initial 4 correction steps by the plenoptic sensor can effectively make a distorted beam converge to an almost corrected form and trigger SPGD to perform the optimization. The upper-left image shows the collimated beam on the plenoptic sensor. The upper-middle image shows how the deformation distorts the beam on the plenoptic sensor. Since "Defocus" deformation introduces a hyperbolic phase deformation to the collimated beam and makes the beam

diverges over a range of angles, the plenoptic image sees all kinds of patches in different blocks. The fast reconstruction algorithm picks up the outside patches (since they are largest and most illuminated compared with other patches) and uses them to reconstruct the phases on the actuator to form a phase compensation suggestion for the next iteration. The upper-right image shows the result of first step correction. Clearly, the large and bright patches in the outside image cells are eliminated and packed into inner image cells. Then, similar corrections are formed iteratively in the second iteration (bottom left image), third iteration (bottom middle image) and fourth iteration (bottom right image). After the fourth guided correction step, the defocus is almost compensated as most of the optic flux is directed back to the center image cell. If the image metric drops below the threshold value of 9, the fast reconstruction will not see significant phase changes between vertices and we can invoke the SPGD method to make further optimization with a few iterations.

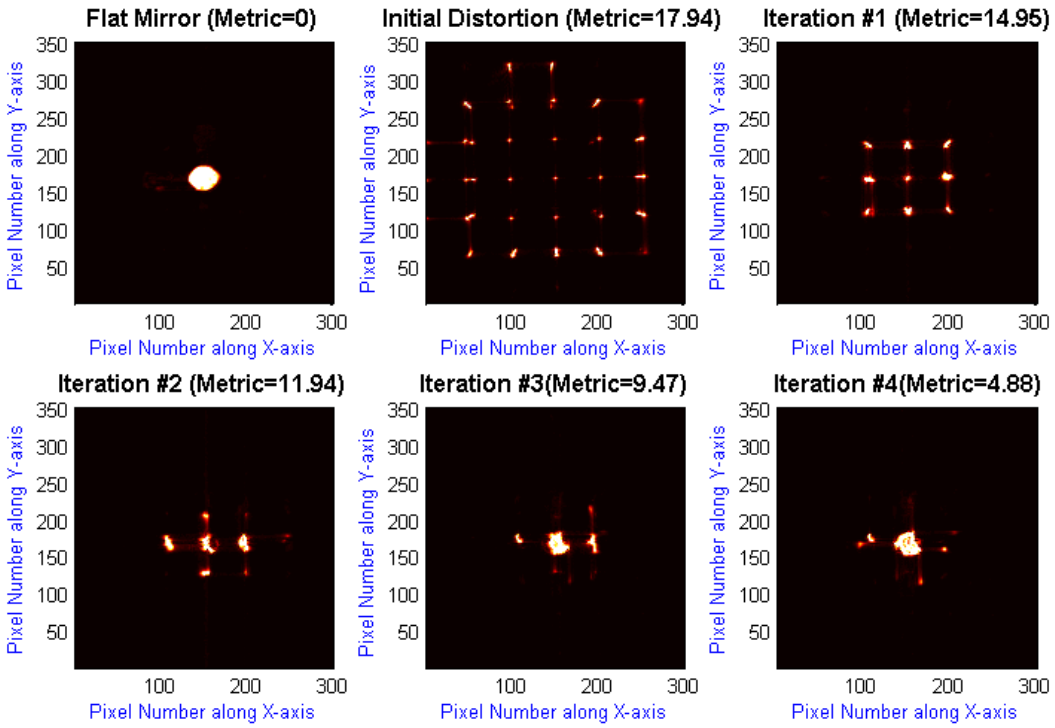

Figure 5. 20: Plenoptic images for each guided correction for "Defocus" deformation case (4 guided correction steps were taken)

The image metric values over the first 10 iteration steps with the "Guided SPGD" method for all the applicable Zernike modes (as shown in figure.5.12~5.19) on the DM are presented in Figure 5.21.

It can be concluded from figure 5.21 that the major phase correction can be done by the plenoptic sensor and its fast reconstruction algorithm within few iteration steps ($N \leq 5$ in our experiments). Whenever the image metric value drops below the threshold value (M=9), the SPGD optimization process will be triggered to fix the remaining weak distortions in phase. Since SPGD utilizes random guesses ($+\varepsilon$ or $-\varepsilon$, where ε is an arbitrary and small iteration step size) on each actuator of the AO device, the actual number of iteration steps fluctuates a lot to achieve correction for the same distortion. Thus it can be argued as "unfair" to compare the "Guided SPGD" and "Pure SPGD" methods by plotting outcomes from a single experiment

since the "Pure SPGD" may get unlucky and result in a long convergence sequence. To rule out "bad luck" we repeated 100 trials using the "Pure SPGD" method to correct each Zernike Polynomial phase distortion case and selected the best correction case that requires minimum steps to converge. The minimum step is denoted by an integer n_0, where starting with $n>n_0$, the normalized variation of intensity on the photodetector is less than 2% (equivalently, the image metric value is smaller than 2). The results are shown in table 5.6. The correction uses the "Pure SPGD" method where the metric is the photodetector readouts.

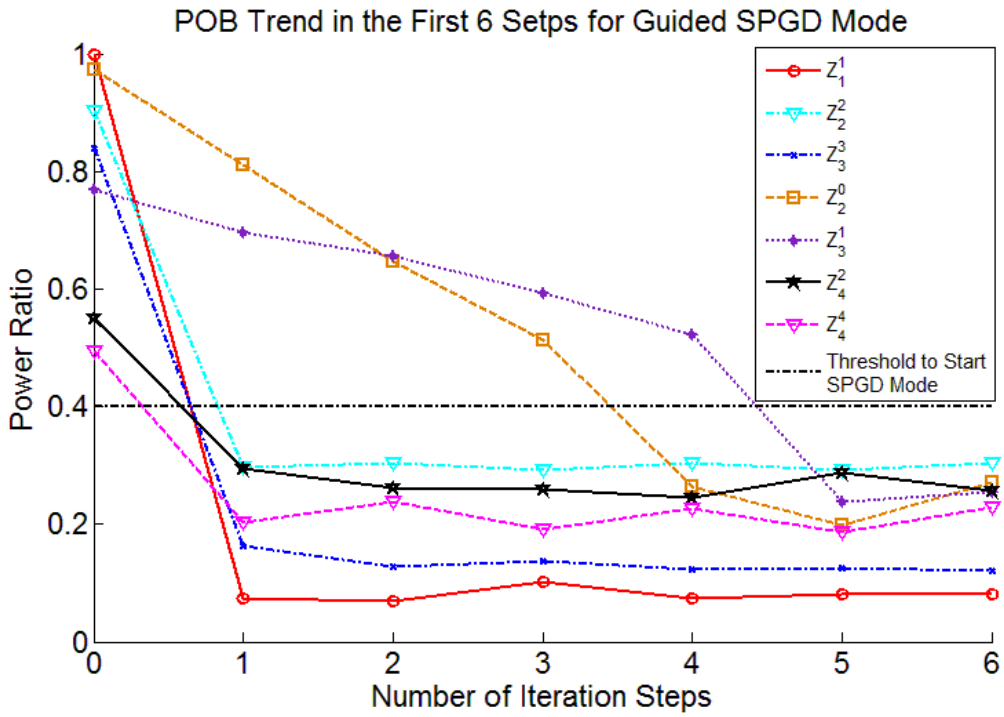

Figure 5. 21: First 10 corrections steps for each deformation case by using "Guided SPGD" method

Table 5. 6: Minimum iteration steps using "Pure SPGD" method (best result through 100 repeated corrections in each case)

Zernike Polynomial	Minimum Number of

Modes	SPGD Iterations
Tip/Tilt (Z_1^1)	199
Defocus(Z_2^0)	238
Astigmatism(Z_2^2)	162
Coma(Z_3^1)	214
Trefoil(Z_3^3)	240
Secondary Astigmatism(Z_4^2)	304
Diamond(Z_4^4)	210

It is easy to find that in the case of a 37-channel AO device, the best "Pure SPGD" results cost around 200 iteration steps. Those results still can't beat the "Guided SPGD" method without best case selection. The presented "Guided SPGD" corrections typically completes at around 100 iterations. Thus, it is evident that the guided steps strongly speed up the convergence of correction.

In fact, the philosophy behind the improvement is that we have implemented a wavefront sensor that can extract the major phase distortion within the channel. Therefore, with deterministic direction and magnitude instructions for individual actuators in the AO device, the phase distortion is significantly suppressed within few iteration steps (for example, ≤5 in our experiments). For the remaining weak distortion, the plenoptic sensor can't provide further guidance since the center block will become the most illuminated cell, and SPGD can be invoked to complete the correction (perform optimization).

5.3.3 Real time correction for strong turbulence distortion

Based on the fast reconstruction algorithm, laser beam distortions caused by strong atmospheric turbulence effects can be accomplished in real time. Because the frequency of atmospheric turbulence, which predominantly varies from 10Hz to 100Hz, real time correction is possible when the correction speed of the adaptive optics system exceeds 100Hz. The lab-scale experimental platform is shown as:

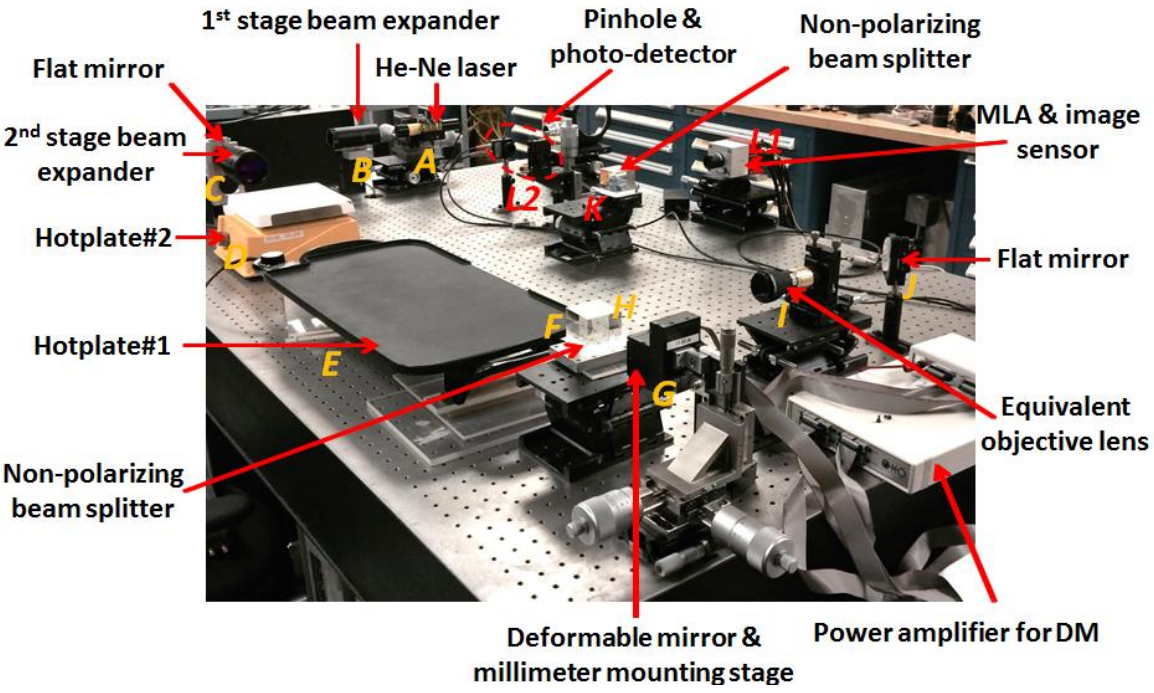

Figure 5. 22: Experimental platform of real time correction of strong turbulence effects

In figure 5.22, a He-Ne laser source with wavelength of 633nm is located near position label "A". In propagation, the laser beam first propagate through a 10X beam expander near position label "B" and expanded to a collimated beam with diameter of 10mm. The collimated beam is re-directed by a flat mirror near position label "C" into a second stage beam expander to be expanded into a 50mm wide beam. Then the expanded beam propagates through an extremely turbulent channel (2m) simulated by a hotplate (near position label "D") and a large griddle plate (near position label "E").

The surface temperature of the hotplate and the griddle is typically larger than 200 ℉, and the associated strong turbulence effects will cause significant interference patterns on the laser beam. At the end of the propagation channel, the distorted laser beam propagates through a 50mm wide non-polarizing cubic beam splitter (near position label “F”) and arrives at a deformable mirror (OKO DM with 37 actuators, near position label “G”). The deformable mirror takes commands from the reconstruction results to add a controllable phase to the distorted beam through reflection. Because the deformable mirror has a diameter of 30mm, the correction is focused to the center area of the 50mm wide beam. The phase modulated 30mm wide beam is reflected from the DM’s surface to the beam splitter (near position label “H”) and re-directed into the equivalent objective lens in the plenoptic sensor (near position “I”). The objective lens has an effective focal length of 3000mm and 30mm diameter. The flat mirror near position label “J” and the 50mm wide non-polarizing beam splitter near position label “K” reroute the light path after the objective lens into the microlens array (MLA) and fast frame rate camera near position label “L_1”. The MLA used is an Edmund optics MLA with pitch length of 500μm and effective focal length of 46.7mm. The fast frame rate camera used is an AVT bonito camera with 400 fps. In order to assist measuring the quality of the correction, we also setup a side branch from the beam splitter near position label “K” to a tiny pinhole (<1mm in diameter) and a photodetector near position label “L_2” to measure power in the bucket (PIB). The PIB value helps to indicated how much power of the corrected beam can be directed into a target area. Intuitively, without any turbulence and phase modulation on the DM, the PIB reflects the entire power of the 30mm wide beam at

the diffraction limited focal spot after the objective lens. When turbulence is involved, the distorted beam can't be focused into a tight spot due to the phase and amplitude distortion on the beam. And the goal of the correction is to compensate the phase distortion in the beam so that a relatively tight focus can be achieved on the photodetector.

In the correction process, the plenoptic sensor acquires a plenoptic image on the distorted laser beam and the fast reconstruction algorithm quickly analyzes the plenoptic image and forms a correction command to the DM. The DM will instantly apply the phase correction to finish a unit iteration step of wave-front sensing, analyzing and correction. As a result, the correction helps to maintain a good optic link and high PIB value. To show the difference with/without the correction, we added a control signal to periodically turn on/off the correction.

The result of the PIB is shown as follows for various turbulence levels (all of them fall in strong turbulence regime):

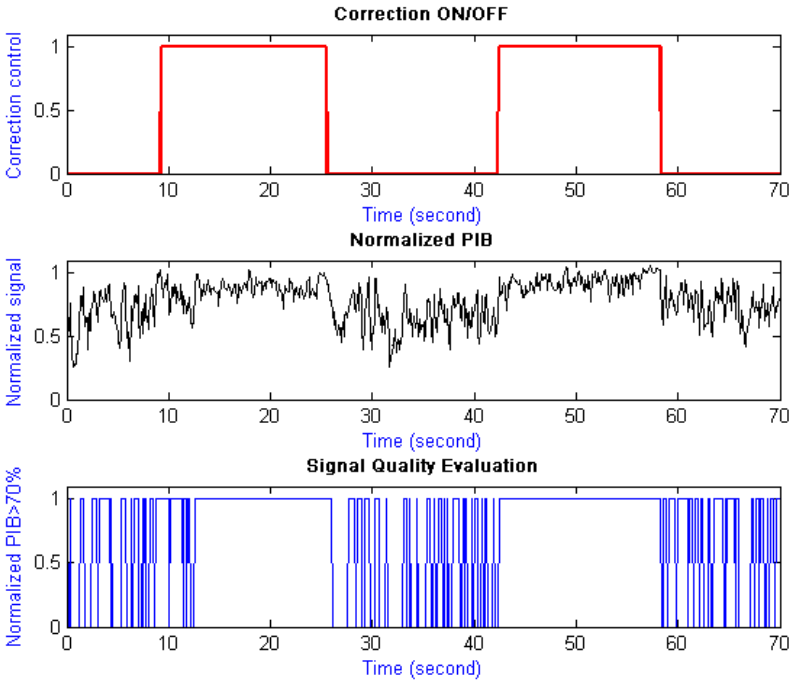

Figure 5. 23: Correction result for 180 ℉

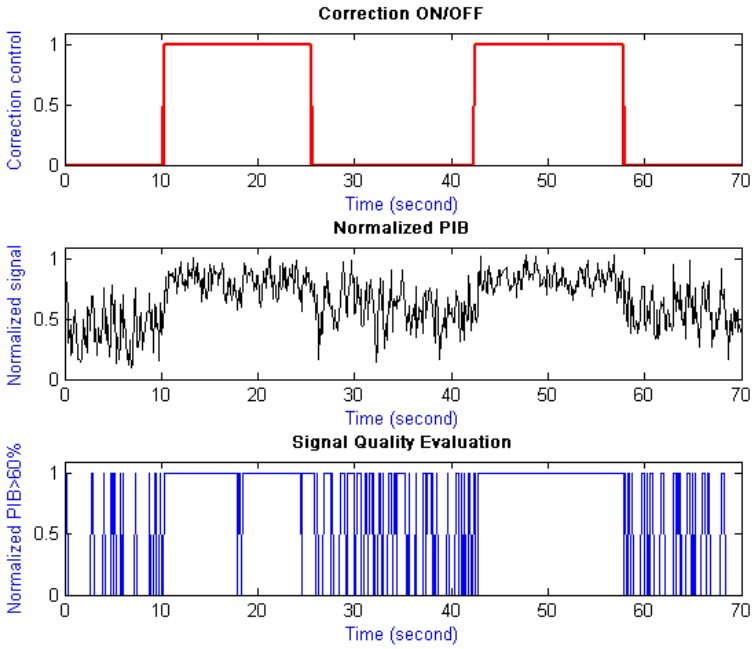

Figure 5. 24: Correction result for 250 ℉

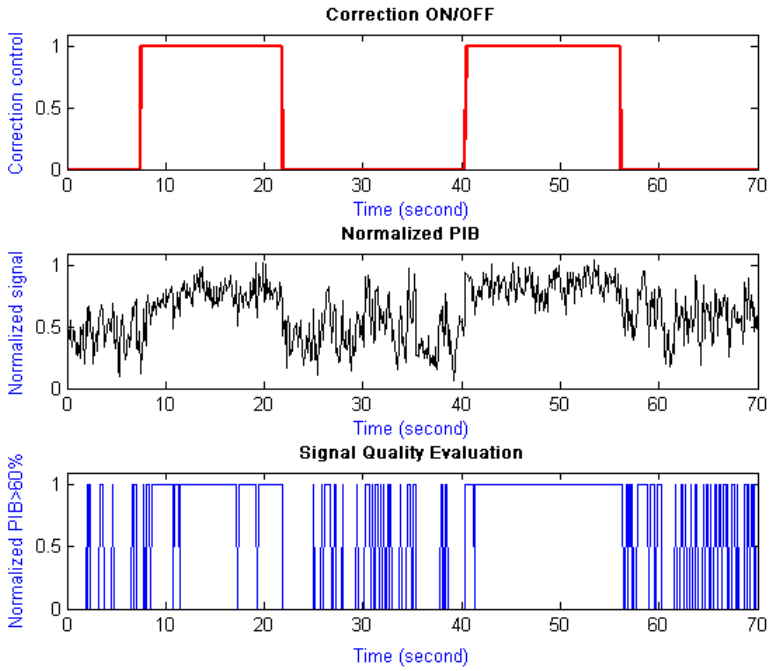

Figure 5. 25: Correction result for 325 Ŧ

In figure 5.23-5.25, we show the control signal, PIB signal and quantized evaluation of the PIB signal respectively with the red, black and blue curves in each plot. When the red curve reaches level "1", the guided correction from the plenoptic sensor is on. When the red curve reaches level "0", the correction is turned off and the DM is set flat. The black curves are plotted by the readout on the photodetector divided by the corresponding readout without turbulence (ideal alignment). The blue curves reflect the logical outcomes of whether the instant PIB value passes a basic threshold value. As shown in the previous section (5.3.2), the fast reconstruction can correct a major beam distortion with almost one step (the worst case may require 5 steps). The major correction will guarantee a PIB of 60% for correcting static distortion cases. It is evident to show the same conclusion in correcting real time turbulence. The overall FPS of the correction is 200, which means there are 200 iterative corrections in each

second. In other words, each correction step takes only 5ms, where 2.5ms is the image acquisition time, 1.5ms is the processing time for the fast reconstruction algorithm and 1ms is the setup time for the DM. Therefore, a good optic link can be maintained when the correction is on. Note that we have slightly increased the threshold value from 60% to 70% in the 180℉ case to show that when turbulence gets weaker, the correction will produce a better result (because correction will also become easier).

The correction is not perfect (restoring 100% PIB) as there is still a 5ms time delay before each correction is applied. In other words, the correction doesn't account for the small changes in the turbulence structure within the 5ms time delay. Therefore, the real time correction is good enough to maintain a major power of the beam on the desirable target area by considering this small imperfection reason due to limited correction speed. In fact, the $C_n^2 \times L$values can be determined on the plenoptic sensor by measuring the angle of arrival. The $C_n^2 \times L$ values are 3.3×10^{-9} $m^{1/3}$, 1.7×10^{-8} $m^{1/3}$, 3.8×10^{-8} $m^{1/3}$ respectively for figure 5.23-5.25 respectively. These data is equivalent to normal C_n^2 values of strong turbulence (from 10^{-13} $m^{-2/3}$ to 10^{-12} $m^{-2/3}$) for at least 3km channels. In application, it shall greatly benefit free space optics (FSO) communication systems and directed energy (DE) applications, where the effective range of a laser beam is severely limited by time-varying atmospheric turbulence.

References:

[1] Wu, Chensheng, Jonathan Ko, and Christopher C. Davis. "Determining the phase and amplitude distortion of a wavefront using a plenoptic sensor."*JOSA A* 32, no. 5 (2015): 964-978.

[2] Liu, Ling, and Mikhail A. Vorontsov. "Phase-locking of tiled fiber array using SPGD feedback controller." In *Optics & Photonics 2005*, pp. 58950P-58950P. International Society for Optics and Photonics, 2005.

[3] Sandalidis, Harilaos G., Theodoros A. Tsiftsis, and George K. Karagiannidis. "Optical wireless communications with heterodyne detection over turbulence channels with pointing errors." Journal of Lightwave Technology 27, no. 20 (2009): 4440-4445.

[4] Ji, Xiaoling, and Baida Lü. "Turbulence-induced quality degradation of partially coherent beams." *Optics Communications* 251, no. 4 (2005): 231-236.

[5] Wu, Chensheng, Jonathan Ko, and Christopher Davis. "Object recognition through turbulence with a modified plenoptic camera." In *SPIE LASE*, pp. 93540V-93540V. International Society for Optics and Photonics, 2015.

[6] Roggemann, Michael C., Byron M. Welsh, and Bobby R. Hunt. *Imaging through turbulence*. CRC press, 1996.

Chapter 6: Combined Turbulence Measurements: From Theory to Instrumentation

In this chapter we will introduce some practical platforms/approaches that facilitate the study of atmospheric turbulence. In section 6.1, a resistor temperature detector (RTD) system will be discussed that can measure the local turbulence level by measuring the coherence structure in weak temperature fluctuations. In section 6.2, a large aperture LED scintillometer systems will be introduced that can measure strong turbulence levels. The transmitter of the large aperture scintillometer also has a laser module that facilitates the measure of lower levels of turbulence. In section 6.3, we will talk about the modification of our plenoptic sensor into a remote imaging platform that can identify the distribution of turbulence distortion in image formation. With our plenoptic image processing algorithm, we can remove most of the turbulence distortion. In section 6.4, we show an enhanced back scattering (EBS) system that exploit the reciprocity of a turbulent channel, which shows high potential in turbulence analysis as well as aiming, tracking, and imaging applications.

The above instrumentations, when combined with advanced wavefront sensing of the plenoptic sensor, will be able to push turbulence studies to new levels. In fact, as the phase and intensity distribution of a distorted beam can be obtained, it expands the statistical characterization of turbulence experiments from intensity fluctuation to the complex field of a laser beam. For example, EBS improves beam alignments between the transmitter and the receiver, the knowledge of distributed turbulence level by RTD as well as imaging analysis of the target can be combined into the wavefront

sensing result by a plenoptic sensor to form more intelligent analysis to improve beam propagation by an adaptive optics (AO) system.

6.1 Resistor Temperature Measurement (RTD) system

Local atmospheric turbulence is primarily results from temperature fluctuations in the air. As the equilibrium in local air pressure is dynamically maintained, Charles' law regulates that increased air temperature results in decreased density of air and refractive index. Therefore, for point measurement on the atmospheric turbulence levels, one can use the temperature fluctuations to indicate the refractive index fluctuations. In other words, we can use a precise temperature probe system to estimation local C_n^2.

In general, by extending Komogorov theory of structure functions to statistically homogenoeous and isotropic temperature fluctuations[1], a power law can be derived as:

$$D_T(R) = \left\langle \left(T_1 - T_2\right)^2 \right\rangle = C_T^2 R^{2/3}, \qquad l_0 \ll R \ll L_0 \tag{1}$$

In equation (1), T_1 and T_2 are temperature measurements at two close spots (separated within inertial range of atmospheric turbulence). The directionless spacing between the spots is represented by R and the inner scale and outer scale of atmospheric turbulence are represented by l_0 and L_0 respectively. To verify this power law we we made use of 4 ultra precise air and gas RTD sensors (OMEGA P-L-1/10-1/8-6-1/8-T-3) for point measurement of temperature as shown in figure 6.1:

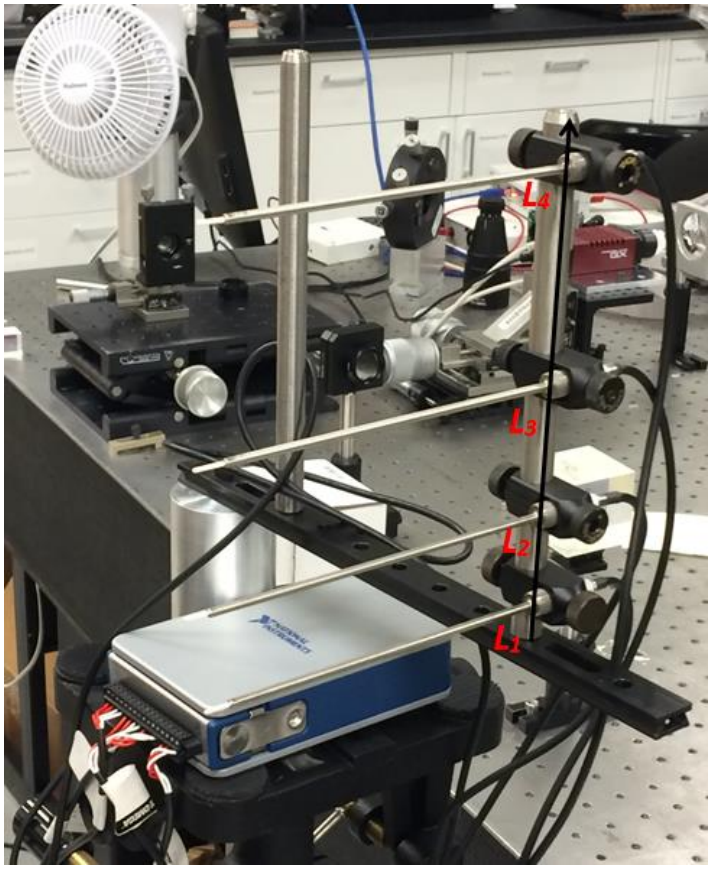

Figure 6. 1: Experimental platform of using RTD system to estimate local C_n^2 values

After callibration, these probes can respond sensitively to a temperature change of 0.002K. As a result, if roughly arranged R≈1cm-50cm, the 2/3 law of temperature fluctuation structure is generally satisfied:

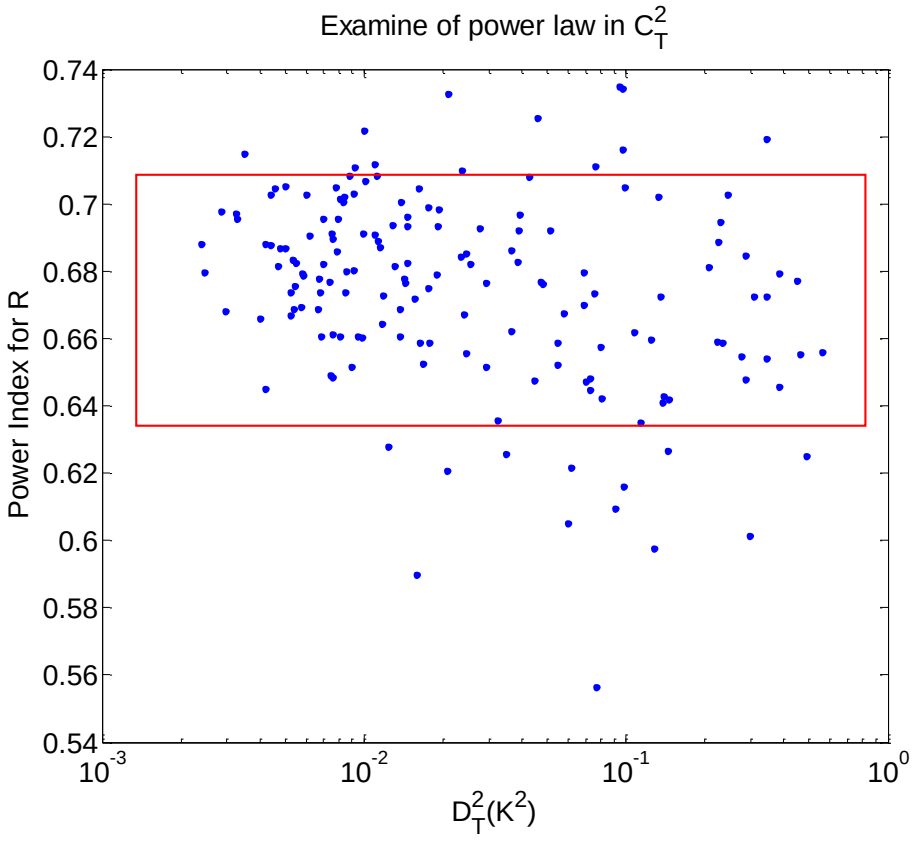

Figure 6. 2: Examination of the 2/3 degradation power law in spatial structure of air temperature fluctuation

Thus the turbulence parameter C_n^2 can be inferred from temperature measurement of C_T^2 as:

$$n(\vec{R}) = 1 + 77.6\times10^{-6}(1 + 7.52\times10^{-3}\lambda^{-2})\frac{P(\vec{R})}{T(\vec{R})} \tag{2}$$

$$C_n^2 \approx (79\times10^{-6}\frac{\langle P\rangle}{\langle T^2\rangle})^2 C_T^2 \tag{3}$$

Consequently, the 3D spectrum of temperature fluctuations is expressed as:

$$\phi_T(\kappa) = 0.033C_T^2\kappa^{-11/3}, \quad \frac{1}{L_0} \ll \kappa \ll \frac{1}{l_0} \tag{4}$$

Due to the precision of temperature measurement, this requires a minimum value of C_n^2 to satisfy:

$$C_{n,\min}^2 \geq N \times C_{n,error}^2, \quad C_{n,error}^2 \approx 4 \times 10^{-14}\ m^{-2/3} \tag{5}$$

This suggests that the temperature measurement approach wouldn't be accurate for weak turbulence cases. However, for strong turbulence levels, it can effectively provide C_n^2 data where saturation can become a problem for conventional scintillometers.

In order to verify the RTD system in providing reliable C_n^2 values, we combined the 4 RTD probes, a data acquisition and memory module, adapting mounts as well as weather proof housing into a compact platform and compared with data from commercial available scintillometers. The platform is shown in figure 6.3:

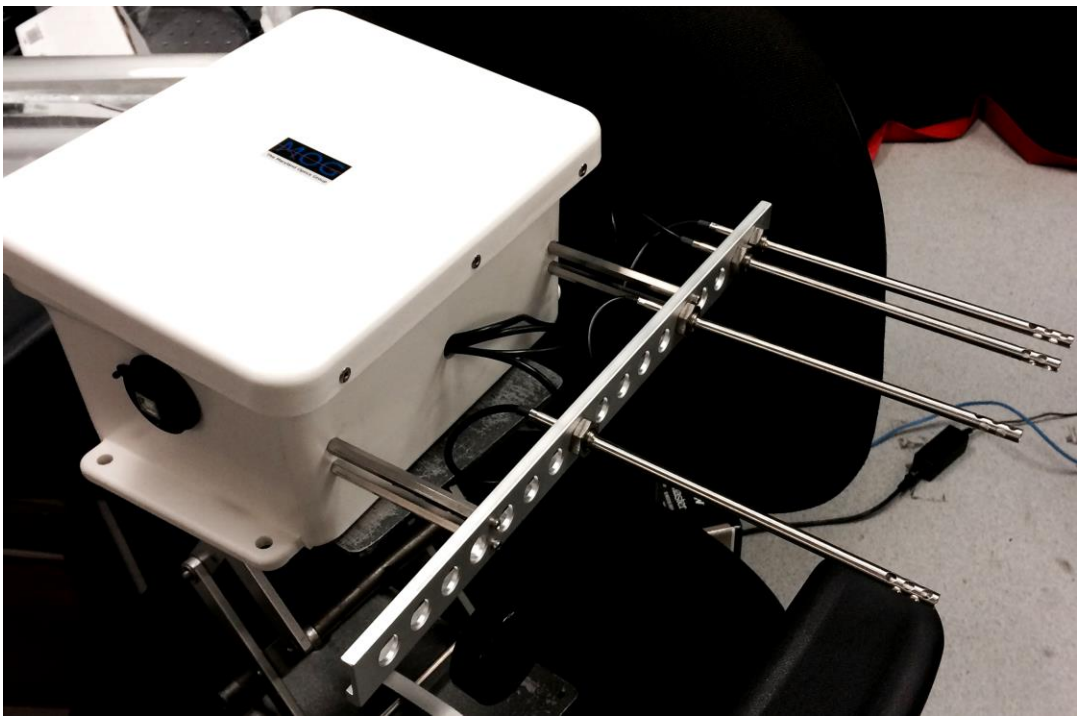

Figure 6. 3: Instrumentation of point C_n^2 measurement with RTD probe system

The verification experiment was conducted from Thursday, October 22 to Friday October 23. Simultaneous measurements of C_n^2 were made with two conventional optical scintillometers, the Scintek BLS 900 and the Scintek SLS 20, and two RTD temperature probe systems that measure C_T^2 directly and convert this to C_n^2.

The measurements were made on the 1 km long TISTEF range at the Kennedy Space Center. The BLS 900 was deployed over the full range with the transmitter at the far end of the range and the receiver at the near end of the range (adjacent to the buildings.) The SLS20 was deployed over a 200 m range near to the buildings. Two RTD temperature probe units were deployed, one at the far end of the range, near the BLS 900 transmitter, and one at the near end of the range near the SLS 20 receiver. At the beginning of experiments the two RTD units were operated next to each other in the laboratory to verify that they were providing readings in good agreement. All the computers collecting and storing data were time synchronized so that diurnal variations of C_n^2 from the scintillometers and C_n^2 measurements from the RTD units could be computed. Figure 6.4 shows a composite of all the results obtained.

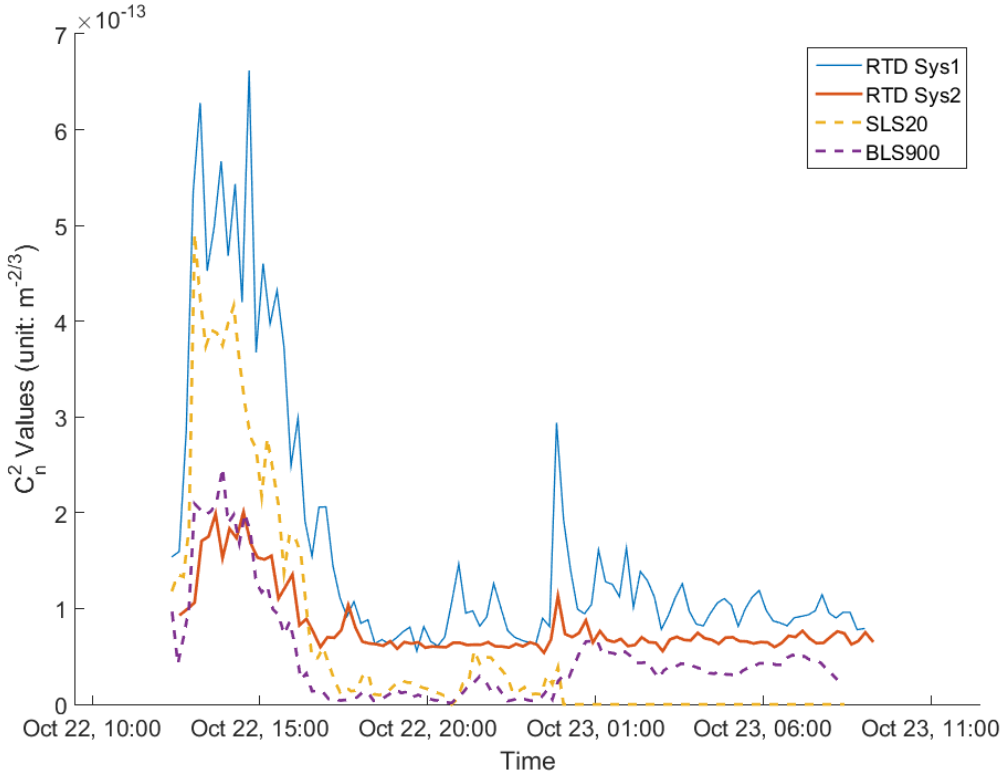

Figure 6. 4: Scintillation data from two optical scintillometers and two RTD systems

It is interesting to note that the SLS20 system and RTD system near it agree quite well, and the BLS 900 and the RTD system near its transmitter also agree quite well. But, the C_n^2 data from the full range and the C_n^2 from the region near the buildings are quite different. During periods of low turbulence the RTD systems generate some noise and can't measure the smallest C_n^2 values directly. All these effects are shown in detail in Figure 6.5.

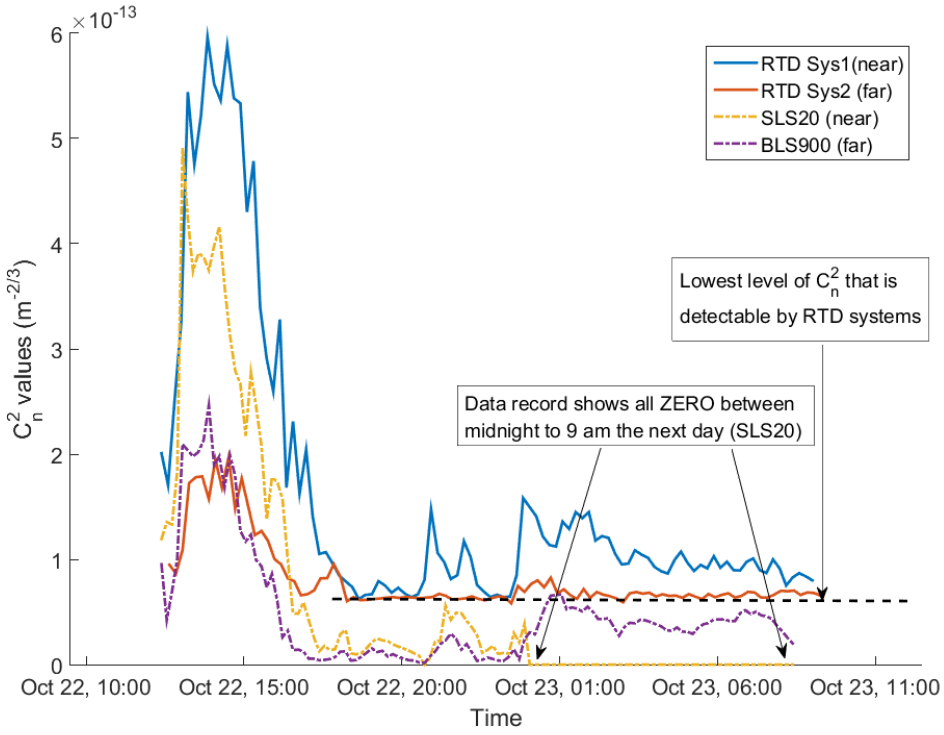

Figure 6. 5: Scintillation data with comments

Figure 6.6 shows the correlation between the BLS 900 and the far RTD system. These data have been corrected for the RTD system by subtracting the effects of the average noise on the measurements so as to increase the lower turbulence measurement range of the RTD system.

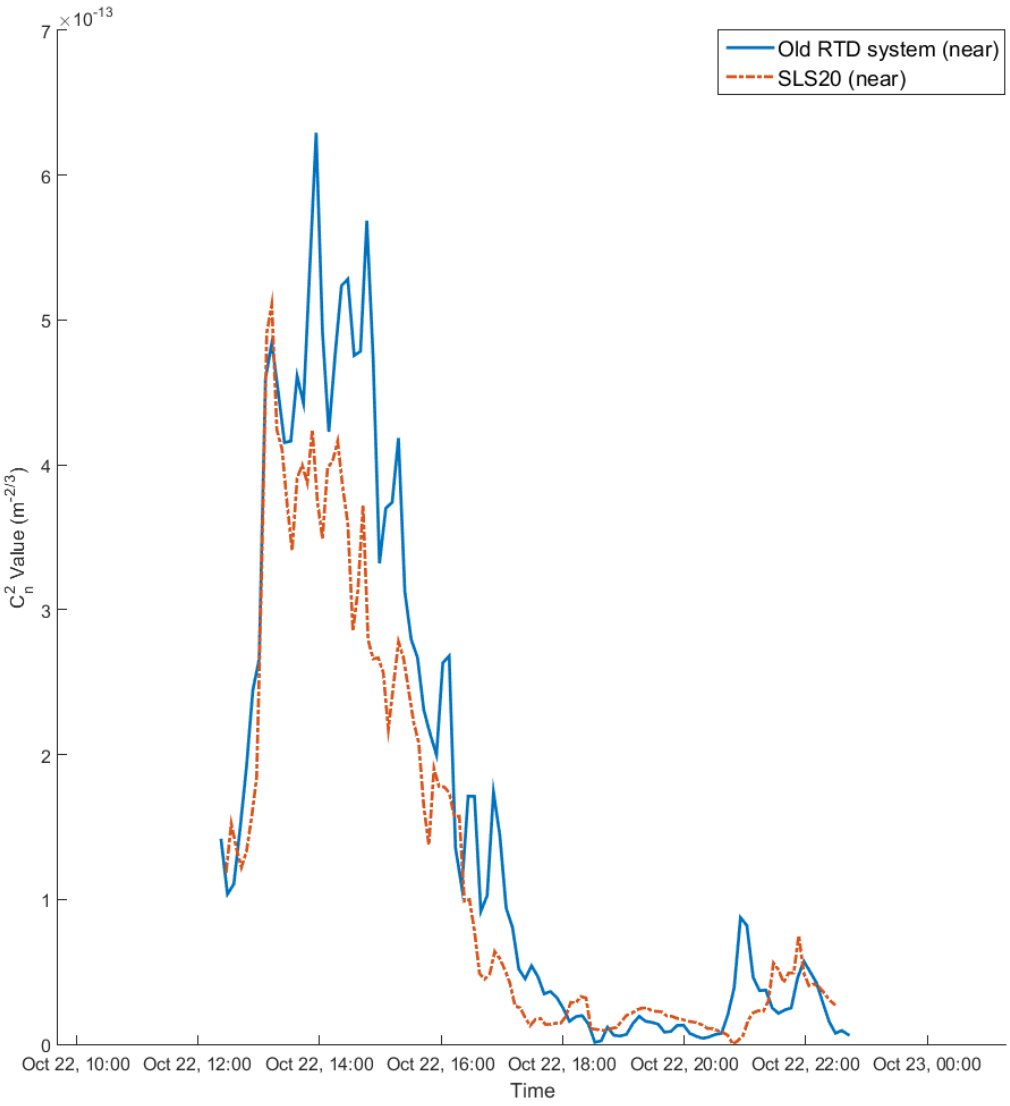

Figure 6. 6: Correlation between measurements made with the SLS 20 and the adjacent RTD system

Figure 6.7 shows the correlation between the BLS 900 and the adjacent RTD system. These data have been corrected for the RTD system by subtracting the effects of the average noise on the measurements so as to increase the lower turbulence measurement range of the RTD system.

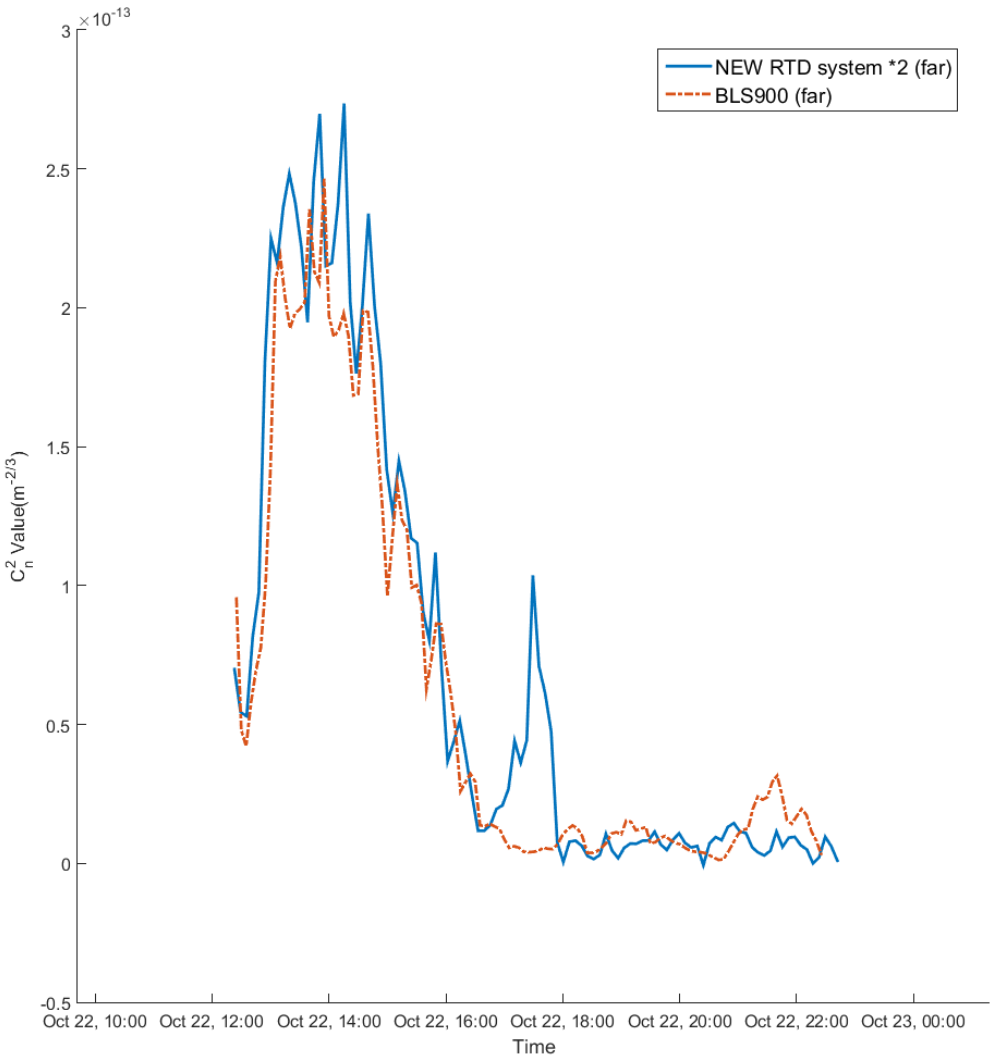

Figure 6. 7: Correlation between measurements made with the BLS 900 and the adjacent RTD system

We conclude from these measurements that the C_n^2 values measured on the range are not uniform along its length. The data suggest that the turbulence is stronger near to the buildings at the near end of the range. It is also interesting to note that if the BLS 900 data is multiplied by a factor of 2 then the data from the two scintillometers lines up quite well. Given the assumption that C_n^2 is gradually declining (from the near end to the far end) over the test range of 1km, the following expectation should be satisfied:

1) C_n^2 close to the building (old RTD system)>C_n^2 for short range average near the building (SLS20) > C_n^2 for the full range average (BLS900)> C_n^2 close to the end (new RTD system)
2) Averaged C_n^2 values for RTD systems at both end ~ C_n^2 for the full range average (BLS900)

Figures 6.6-6.8 show the good agreement between the expected results and experimental outcomes.

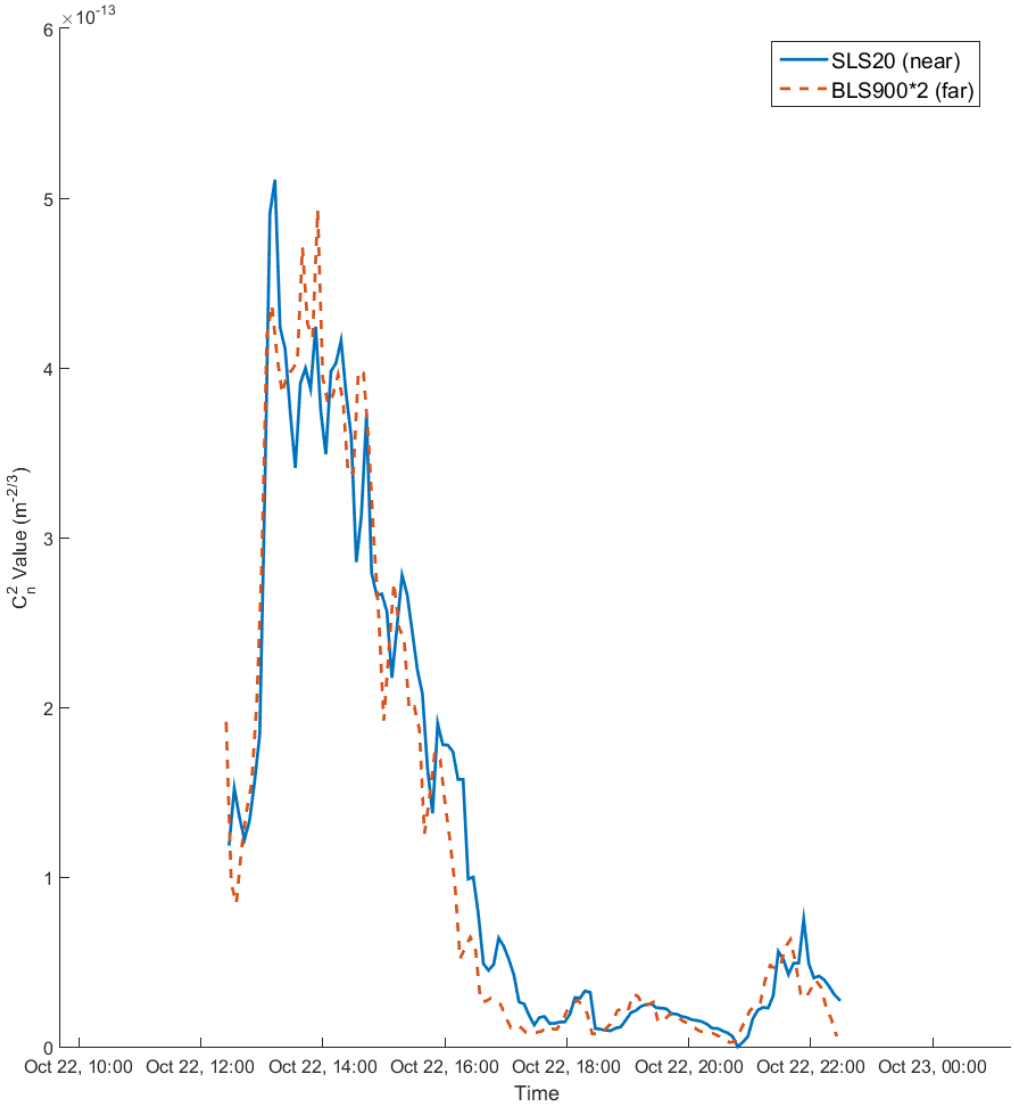

Figure 6. 8: Comparison of data from the two scintillometers

Thus, we are confident that it is adequate to use a precise RTD system to obtain good estimates of local C_n^2 data.

6.2 Large Aperture Scintillometers

Commercial scintillometers can be used to measure path averaged C_n^2 values. In principle, a digital on/off signal is sent through the transmitter and collected by the receiver in a commercial scintillometer pair. C_n^2 is measured by the scintillation effects of the received signal. Due to aperture averaging effects, the sensitivity and measuring range of a scintillometer varies with different configurations. Especially in measuring strong and deep turbulent channels, conventional scintillometer tend to saturate because the significant scattering degradation and beam wandering effects on the transmitted signal. Therefore, we customized our own large aperture scintillometer to assist field measurement for strong turbulence conditions. In addition, to supply C_n^2 data when turbulence is relatively weak, we implement a laser transmitter in the same channel.

The experimental platform of our laser and LED integrated scintillometer transmitter can be shown as:

Figure 6. 9: Laser and LED integrated scintillometer's transmitter

The scintillometer's transmitter in figure 6.3 uses a 10 inch wide LED beam that sends 25Hz on/off signals. When the LED signal is off, the ambient sunlight signal is measured and when the LED signal is on, the summed signal of ambient light and LED signal is measured and the actual LED signal can be detected by subtraction (assuming that sunlight changes much slower than the transmitted signal). On top of the scintillometer, there is a 2 inch diameter laser beam transmitter that sends 50Hz on/off signals.

The field deployment of our customized scintillometer pair is shown in figure 6.10:

Figure 6. 10: Pictures of scintillometer in experiments

To verify that our scintillometer provides reliable data, we made side by side comparison with commercial scintillometers over a 240m channel. The results are shown in figure 6.11. This is sufficient to show that our scintillometer provides reliable data on C_n^2 when compared with data provided by commercial scintillometers. Note that a systematic ratio (2-3) between our large aperture LED scintillometer data and commercial scintillometer data can be seen. This is not surprising since different scintillometers give different results for various reasons, such as sampling rate, height above the ground, range length, etc. But the general up/down trends over time should agree with each other.

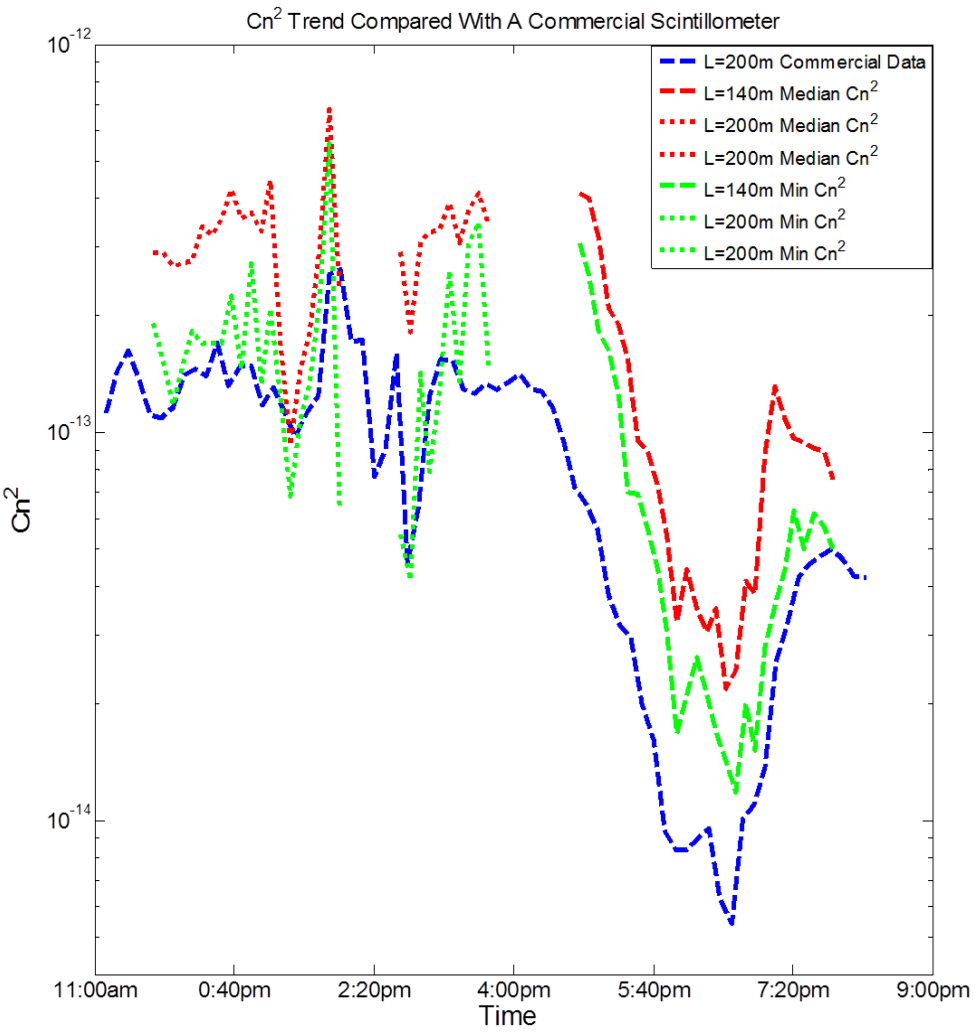

Figure 6. 11: Side by side comparison between our customized LED large aperture scintillometer and a commercial scintillometer (Kipp and Zonen LAS MK II)

6.3 Remote imaging system

Imaging through atmospheric turbulence in horizontal directions has been widely studied over the past decades. Progresses in imaging through atmospheric turbulence can be made through both hardware and software approaches. The hardware approach will typically use a deformable mirror (or other adaptive optics device) to modify the distorted wavefront so that the point spread functions on the image will be resolvable.

The software approach generally uses image/video processing algorithm to retrieve images that are relatively clear of turbulence effects. Both approaches have been proved to be effective in specific well-defined cases. No general (wide-sense) solution to imaging through atmospheric turbulence problems has been developed. In fact, most of the approaches are based on 2D imaging models and require external references. It is evident from a light field angle that conventional 2D images don't provide adequate information about turbulence. And cooperative references, such as guide stars, will be absent in general applications.

The idea of using a light field camera to tactically solve the problems of imaging through turbulence in 4D provides a new direction. In this section, we will demonstrate a few convenient methods of using a plenoptic sensor to record images through turbulence and retrieve the undistorted image. The major trick is to use a plenoptic sensor to further analyze a traditionally formed image behind a camera lens. Without loss of generality, we assume that the image is formed at the entrance pupil of the plenoptic sensor. Intuitively, if the light field at the entrance pupil of the plenoptic sensor happens to be light patterns of a focused image, each MLA cell will form an image in uniformly distributed sub-angular space. In other words, each MLA cell images the same object with slightly different light path from each other. Therefore, a 3D lucky imaging algorithm can be realized on the plenoptic sensor. The word "3D" refers to 1D in time dimension and 2D in spatial dimensions. In other words, besides the image sequence acquired over time, the extra 2 dimensions are provided by the MLA cells (as an image array).

Mechanisms:

When the optical signal of a scene propagates through an atmospheric turbulent channel, the light field that carries the information will suffer from random temporal and spatial changes. For example, the image may be wandering around when we take a sequence of images. Without loss of generality, one can simply express the distortion of an image by the superposition law as:

$$t_1(x, y) = t_1^*(x, y) + \delta t(x, y) \tag{6}$$

In equation (6), $t_1^*(x, y)$ is the ideal image without turbulence, $\delta t(x, y)$ is the change in the image caused by atmospheric turbulence. For simplicity, we will call $\delta t(x, y)$ distortion, which is a 2D random variable. The ideal image $t_1^*(x, y)$ can be generally regarded as the mutual information for the image sequence collected at different timestamps.

Intuitively, if the distortion is weak and purely identical independent distributions (i.i.d) over time, the imaging processing algorithm will be strikingly simple: averaging over many frames. Unfortunately, the actual turbulence has correlations within an inertial range marked by outer scale (L_0) and inner scale (l_0). The wandering of an image is typically caused by turbulence structures comparable to the outer scale, while the local intensity scintillation and oscillation of pixels are typically caused by turbulence structures comparable to the inner scale. If an image processing approach just blindly uses the averaging methods, the sharp features of the image will be blurred.

However, lucky imaging turns out to be a useful alternative approach. In general, one can make segments on the imaging area, and collect an image sequence over a time to select the best features in each segment to assemble the overall less distorted image.

In other words, the lucky imaging approach is to search for the minimum distortion moment for each segment and stitch them together.

With the plenoptic sensor, the image is an array of cell images that are differentiated by slightly different viewing angles. Two extra spatial dimensions can be added to the lucky imaging process. In fact, since the point spread function for a spot in the scene is distributed into an array of point spread functions in different image cells, it facilitates the selection of a cell image that contains the sharpest point spread function. Therefore, besides the time dimension, the plenoptic sensor provides 2 extra geometric dimensions to perform the lucky imaging process, as shown by figure 6.12:

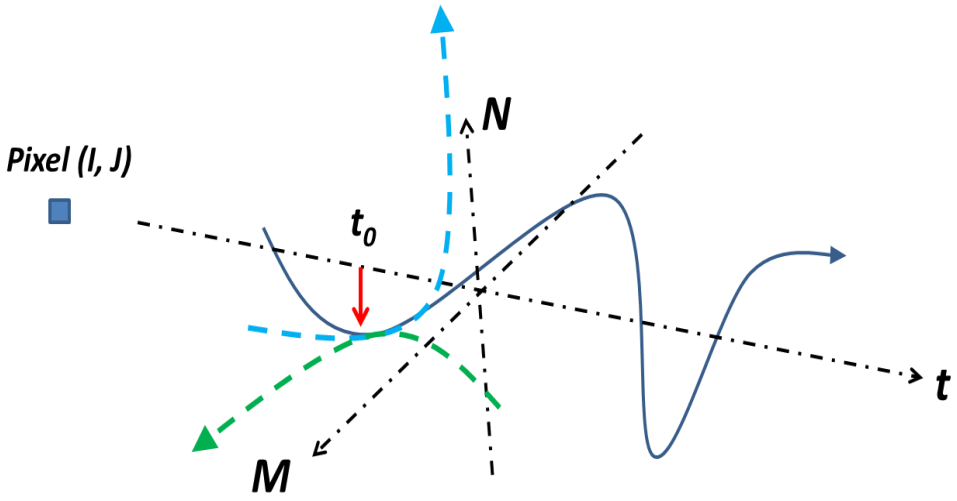

Figure 6. 12: Diagram of selecting the most stable pixels in 3D lucky imaging method on the plenoptic sensor

In figure 6.12, we show the principle of 3D lucky imaging in finding the most stable spot (in the scene) over time and space. Intuitively, the stableness in time represents the minimum scintillation. The stableness over space (M and N indices) represents the compensating gradient of the distorted wavefront. In other words, the first order

of local phase distortion can be directly compensated by a certain image cell that represents the same tip/tilt. Therefore, the 3D lucky imaging not only provides points that are stable over scintillations, but also stable over wavefront tip/tilt. For convenience, we call the set of pixels selected in the 3D lucky imaging process "steady patterns". Once the steady patterns are determined for each spot in the scene, one can assemble the patterns to form an image that is strictly better than any cell image in the recorded image space (the plenoptic image sequence). The assembling process can be demonstrated with the following diagram:

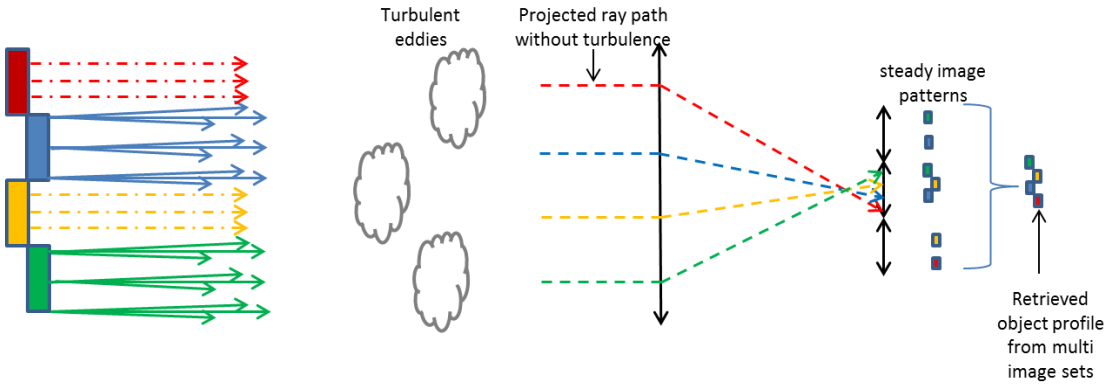

Figure 6. 13: Assembling process for the steady patterns

Figure 6.13 shows that when the image pattern is spatially disrupted by atmospheric turbulence, the spatial oscillation of a spot will cause minor movement of pixels inside an image cell, and the angular oscillation of a spot will cause intensity redistribution of the corresponding pixels between the image cells. Therefore, by using 3D lucky imaging to select the best features among all the collected cell images, a strictly better image can be obtained. And in circumstances where traditional lucky imaging can't be used, the plenoptic sensor still has extra 2 dimensions of spatial freedom to perform lucky imaging.

Practically, the 3D lucky imaging on the plenoptic sensor requires solving a few more technical problems. One of the problems is how to perform the image stitching once the best patterns are acquired from the set of plenoptic images. This is because each MLA cell has a slightly different view of the scene, and there is pairwise wandering of cell images between any two arbitrary cells. This wandering between neighboring cells can be solved by finding the maximum spot in the cross correlation function between 2 cell images (since the majority of the pixels describe the same scene). The different view of the scene can be handled by re-projection to remove the trivial difference of viewing angles. The image stitching problem can be illustrated by the following diagram:

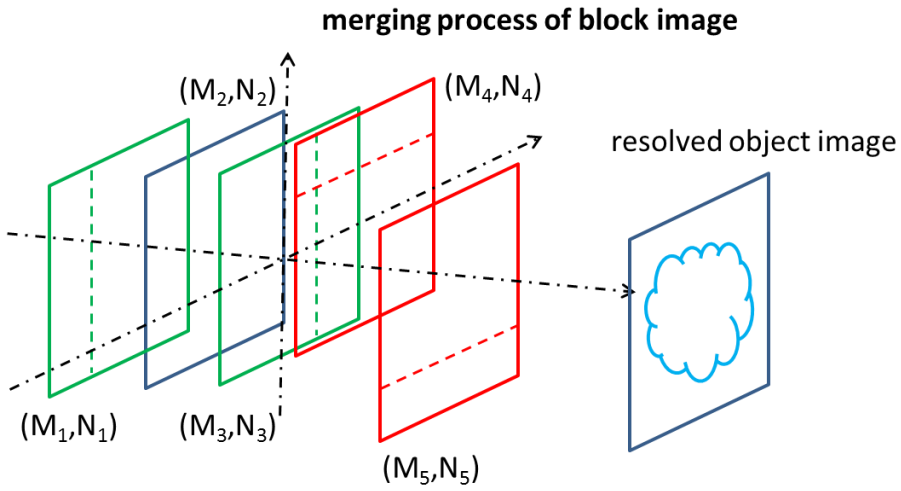

Figure 6. 14: Image stitching problem to assemble the 3D lucky image

The second problem is to track the pixels in a uniform pattern. Intuitively, a pixel corresponds to a spot in reality, and if the neighborhood of a pixel is a uniform pattern, it will be hard to track the spot's movement. Thus, the stability of the spot's representative pixels on the plenoptic sensor is hard to determine. To solve this problem, we use the feature points for each cell image instead of all the pixels. The

feature points are points with sharpest local features in an image that can describe the pixels with significant gradient to its vicinity. In other words, the feature points can be traced much more easily than ordinary points in the image. The pixel tracing problem can be illustrated by the following diagram:

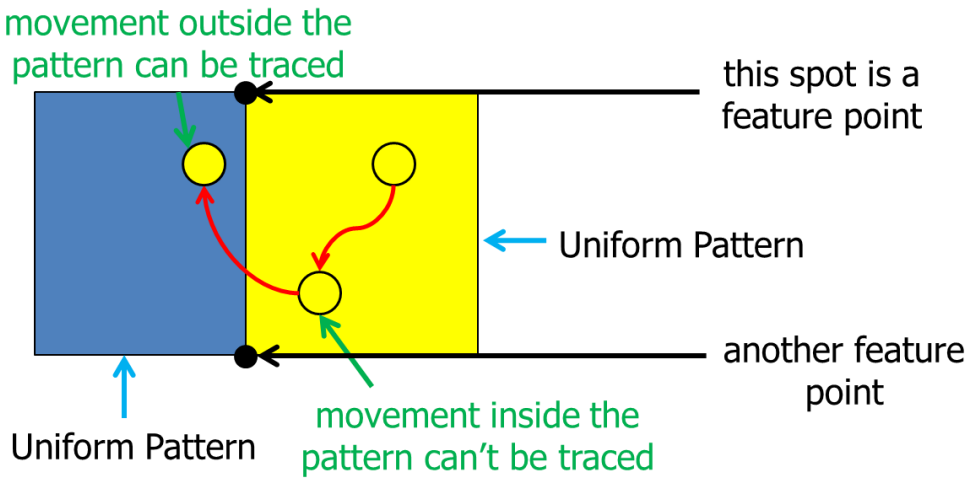

Figure 6. 15: Diagram of using feature points to replace ordinary points for 3D lucky imaging on the plenoptic sensor

Without loss of generality, we use a "Harris" corner detector to determine the feature points in each cell image on the plenoptic sensor. The "Harris" corner detector uses the gradient of the image intensity map to find the corners of an image pattern. Since all the cell images are on the same scale, we are not worried about the scaling variant problem of the "Harris" corner detector. Intuitively, the scaling variant problem means if the image is magnified, some corner features will become smoother and the "Harris" corner detector may be affected.

For example, if we use the plenoptic sensor to image a checkerboard, by applying the "Harris" corner detector, we can capture its grid points as shown by figure 6.16:

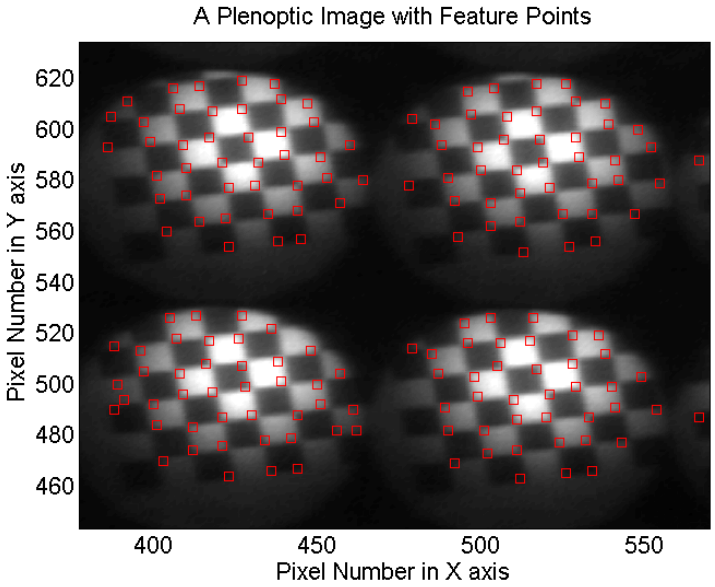

Figure 6. 16: Feature point detector on a plenoptic image

In Figure 6.16, we show that the feature points describe the corners of the checker board. By using these feature points, we can describe the stableness of the cell image. In other words, the 3D lucky imaging can be simplified to tracking the stability of those feature points. If a local feature becomes unstable, it may appear/disappear among various frames as well as its neighboring cells. Therefore, an image cell is stable at a certain frame if and only if it captures the maximum number of stable features. A feature is stable if and only if it is repeatedly discovered by other cell images (consensus between different cell images). The stable feature points determine where to fetch information to reconstruct the image that is turbulence free.

The third problem is to identify the same feature point over different image cells. Because small atmospheric turbulence structures cause local distortions, distortion on local features inside a cell image will cause errors in alignment with neighboring cells. Typically the displacements for corresponding feature points in two image cells (can be viewed as a straight line between the two feature points) are not equal.

Therefore, we need to apply random sample consensus (RANSAC) test for the feature points in 2 image cells to rule out the outliers. The outliers include:

(1) Temporal formation of feature points caused by turbulence.

(2) Pairs of feature points that deviate significantly from the displacement between corresponding cell centers.

(3) Pairs of feature points that don't have enough number of similar supporting pairs.

For the above categories for outliers, point (1) refers to the image elements that have been severely distorted by atmospheric turbulence. Intuitively, if part of an image has been significantly distorted by turbulence, the corresponding feature points will be temporal and the easiest to detect (because they are not repeatable in a probability sense). Point (2) means if we treat the feature points in 2 cells as a bipartite group and draw straight lines between them, the lines that deviate significantly from the line connecting the image cell centers should be discarded. This is because the line connecting the image cell centers can be served as a reference to matching corresponding feature point pairs (although it excludes the fact that each cell image has a slightly different view). Therefore, any large deviation from that reference line should be treated as wrong pairing of feature points. Point (3) means that if the cell image doesn't have enough feature points to pair correctly with another cell, at least one of them have been distorted (or they can be both be distorted in uncorrelated ways).

Once the RANSAC has been done, we can pick the center cell as reference view to stitch/replace patterns that are found more stable in other neighboring cells. There are two minor aspects to mention:

(1) For minor distortions between the pairs of feature points that passed the RANSAC test, we can re-project to the center cell's view to correct for the distortion.

(2) For the illumination differences when we replace an original patch with a more stable (less distorted) patch from another cell, one should also multiply by the illumination ratio (the sum of pixel values in original patch divided by the sum of pixel values in the replacement patch).

Since the overall process for the image reconstruction is very similar to the panorama process in imaging processing, we call the algorithm "panorama" reconstruction. As long as C_n^2 of turbulence is strong enough ($>10^{-14}$ $m^{-2/3}$), the "panorama" reconstruction will be able to select patches from different time and space and we get a synthetic image that is strictly less distorted than all the cell images collected by the plenoptic sensor. Intuitively, the whole process looks like using a camera array to observe the target in very close angles with each one contributing their best observation to the final 3D lucky imaging.

Experimental results:

Strong turbulence over a short distance often causes blurring and shimmering effects. Those effects can be commonly seen in a hot summer day, when one looks horizontally along the road and sees objects floating around. Intuitively, the hot and fast air flow will cause relatively large refractive gradient and the overall effects of

strong turbulence in a short distance works as a randomly placed lens/wedge. Therefore, the visual effect is as if the image is moving around with uncertain blurry parts.

The experimental platform is shown as:

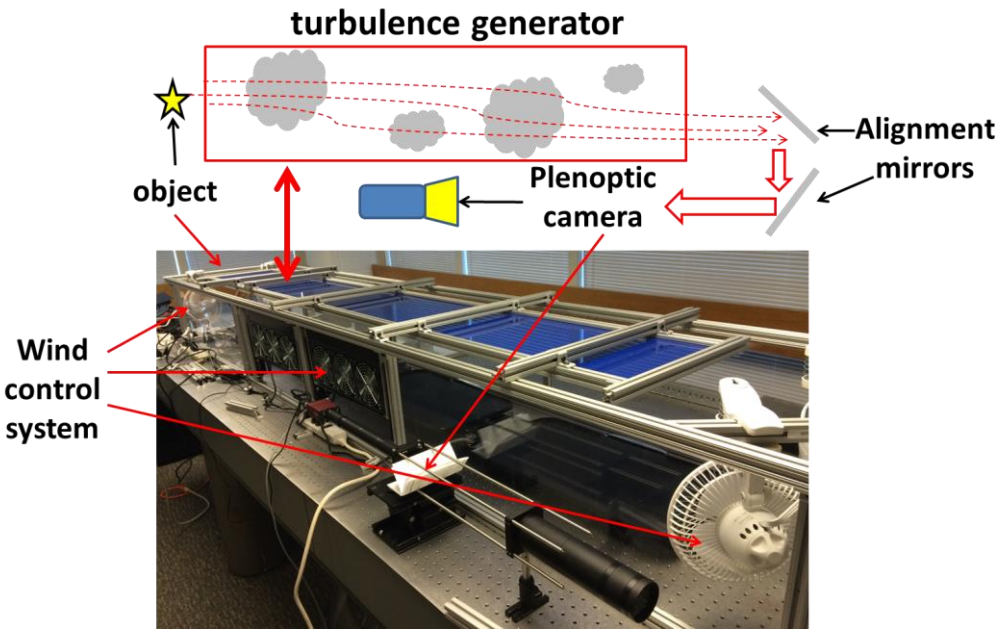

Figure 6. 17: Experimental platform to generate lab scale turbulence and apply imaging with plenoptic sensor

In Figure 6.17, the protected area contains 4 heating strips that can generate the total volume of $0.3 \times 3.3 \times 0.25$ m^3 of turbulent hot air and also introduce air flow in multiple directions. The target is a 50 mm×50 mm checkerboard that is located 6 meters away from the plenoptic camera. An average temperature of 50 $^{\circ}$C is simulated by the system, and the camera (Allied Vision GX1050) captures the image though this turbulence environment at 109 fps with resolution 1024×1024. We collected 25 frames of plenoptic images in sequence (time span is about 0.25 second). Then we apply the "panorama" reconstruction to process the plenoptic video.

The intermediate steps for the “panorama” reconstructions are shown as:

(1) Most stable cells over time:

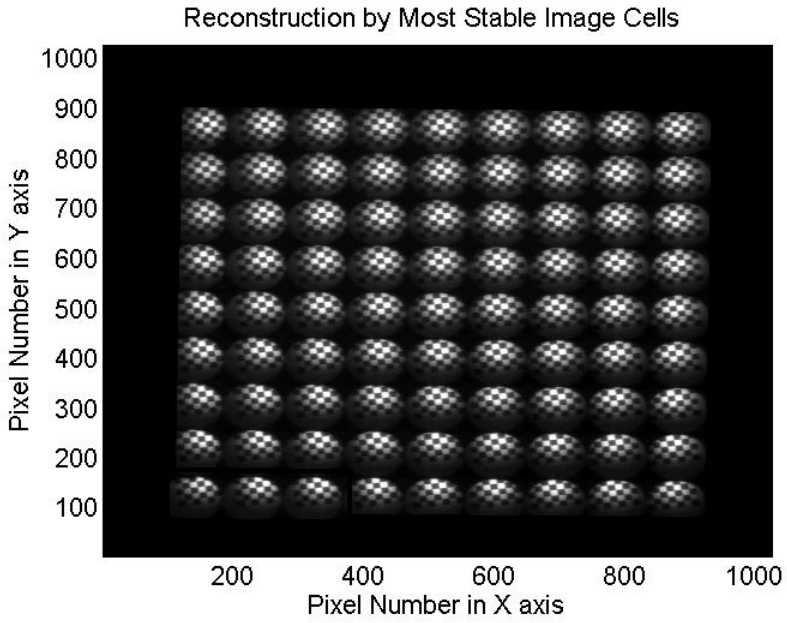

Figure 6. 18: synthetic plenoptic image made by the most stable cells over time

Figure 6.18 shows the assembled plenoptic image by selecting the most stable image cells over time sequence. The method used for the selection is to count for each cell’s feature points and track their scintillations (deviation from averaged intensity over time). The most stable frame for a cell image can be determined if that frame contains the most stable feature points.

The frame indices for the most stable cells in Figure 6.18 are shown by the following table:

Table 6.1: Frame indices for the most stable image cells selected from the plenoptic video

15	12	12	11	11	11	15	12	12
15	12	12	12	15	15	15	12	12
15	12	12	12	15	15	15	12	12
12	12	12	11	15	15	15	12	12
12	12	12	15	15	15	15	12	12
15	12	12	15	15	15	15	12	12
12	12	12	15	15	15	12	12	12
12	12	12	15	15	15	15	12	12
15	12	15	15	15	15	15	12	15

(2) RANSAC and panorama reconstruction:

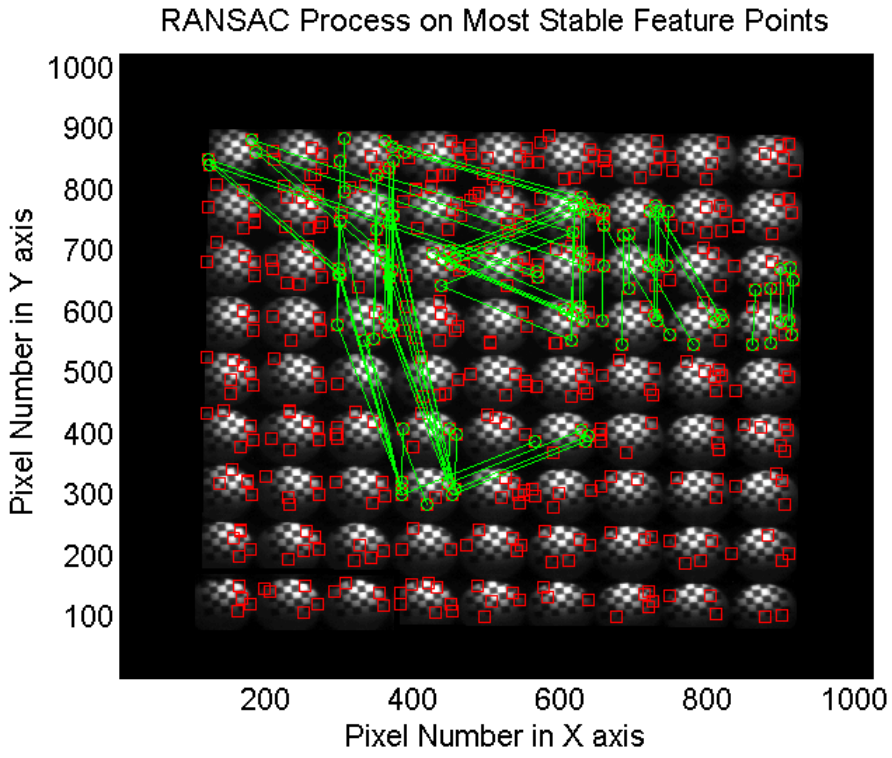

Figure 6. 19: Result of RANSAC process to determine how to stich the cell images

Figure 6.19 shows the most stable features on the synthetic plenoptic image (figure 6.18). Compared with the dense feature points in Figure 6.16, only a small portion has remained due to the removal of unstable features. Then, all the cell images that are connected by the green lines in figure 6.19 are selected to assemble the final image. The result is shown as:

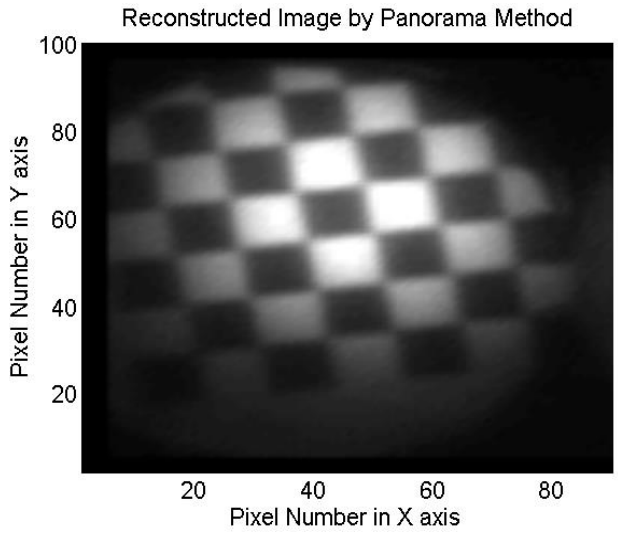

Figure 6. 20: Reconstructed image by panorama algorithm

For comparison, we can turn off the turbulence, and use the center image of the plenoptic sensor as the goal of image retrieval, as:

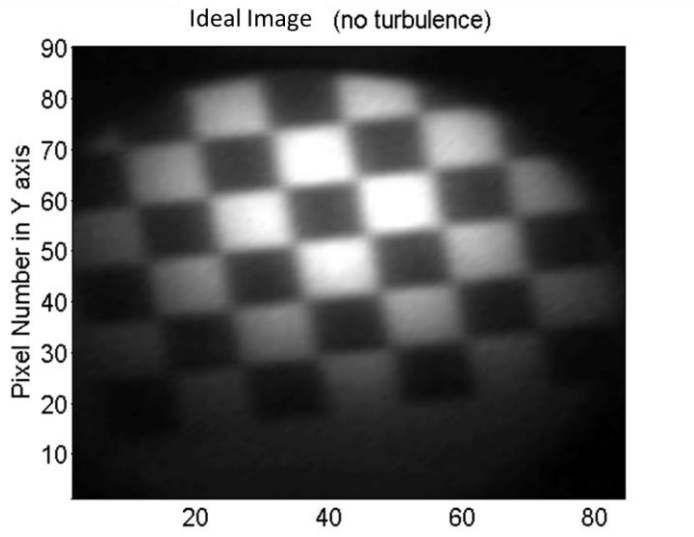

Figure 6. 21: Ideal image for reconstruction (no turbulence)

Note that the reconstruction result in figure 6.20 shows a slightly larger area than figure 6.21 because of the image stitching. In other words, more stable features are added to the result by combining the view from different image cells. The similarity (image correlation) between the ideal image and the reconstructed result is 98.2%. Therefore we can see that turbulence effects are significantly removed. Besides, the sharpness of an image depends on many factors such as lens aberration, illumination conditions, and depth variation of the object as well as post stage image processing. Based on these facts, our algorithm only aims at turbulence removal. Further image processing algorithms such as resampling and deburring can be applied to further improve the image quality.

If an ordinary camera is used to perform imaging through turbulence at the same location of the plenoptic sensor, the image obtained by the same level of artificial turbulence is shown as:

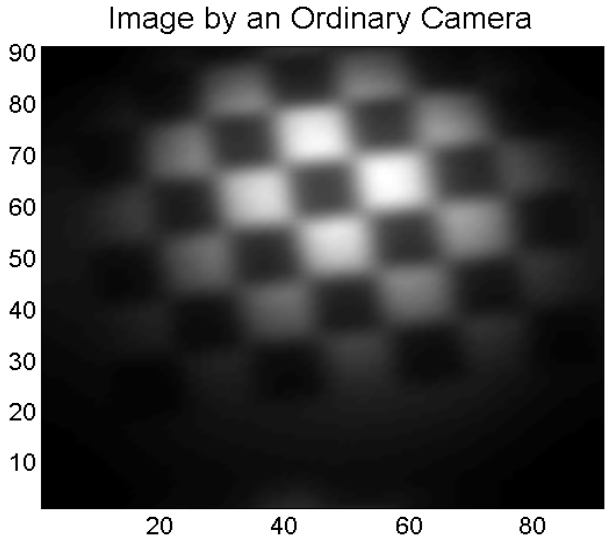

Figure 6. 22: Image obtained by a normal camera through turbulence

Not surprisingly, turbulence causes more blurring effects on a normal camera image. This is caused by the superposition law of adding all deviated rays on the image plane. Comparatively, the plenoptic sensor can distinguish the blurring and wandering effects and make corresponding corrections. Thus turbulence can be safely removed by the panorama algorithm on a plenoptic image.

Another strong turbulence condition can be found in water, whose refractive index has a much greater gradient when turbulence gets involved. In fact, the underwater vision distortion will be more obvious and slower than the strong turbulence effects happening in the air. Therefore, the panorama treatment won't be effective because of the lack of consensus between neighboring cells. Instead, direct 3D lucky imaging is performed for imaging through water turbulence (which makes the algorithm much simpler).

The common diagram of the system is shown as:

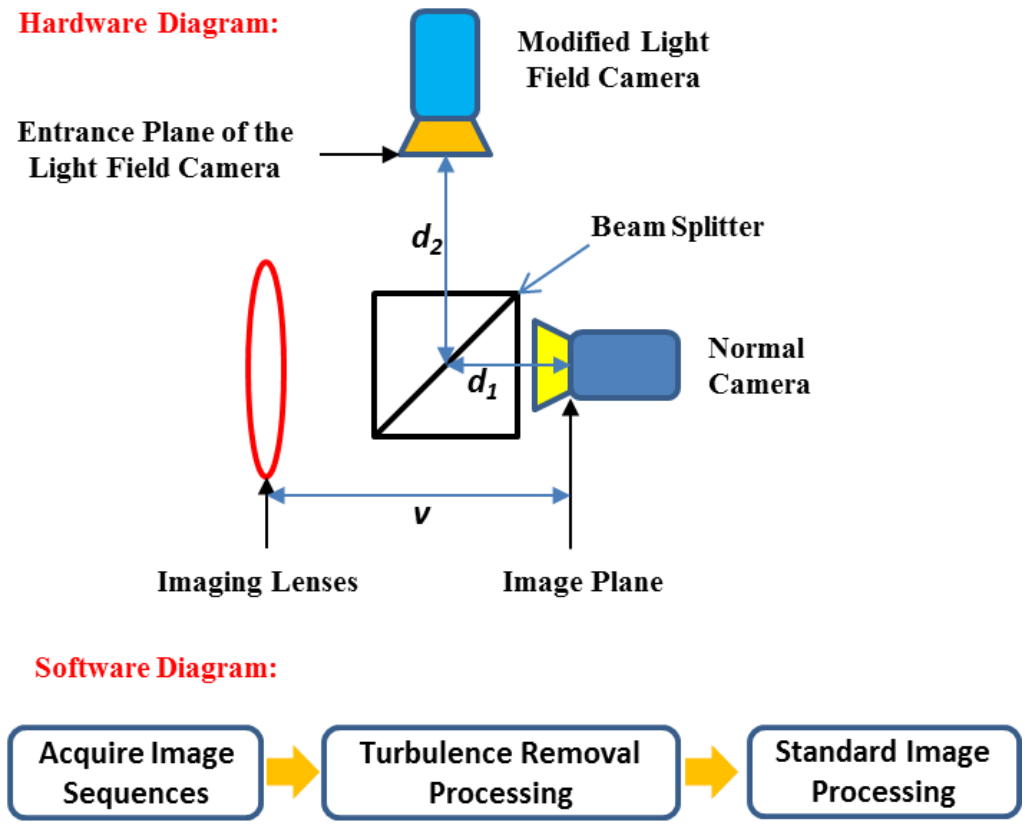

Figure 6. 23: Hardware Diagram for simultaneously imaging with normal camera and plenoptic sensor

The imaging lenses in the diagram are used to zoom and focus on the object of interest. We insert a beam splitter to form 2 identical copies of the image. One copy of the image is sampled by a camera directly, which forms a normal image of the object of interest. The other copy of the image is sampled by the modified light field camera to form an array of images in the image's sub-angular space. The extra propagation distance of the second image before it enters the modified light field camera is marked by d_2-d_1, which equals the focal length (f_1) of the objective lens in the modified light field camera.

Without turbulence distortion, all the image cells present an array of identical images. When turbulence is involved, each image cells begin to show difference with its neighboring (top, bottom, left, right, previous, next) cells. In general, the cell image difference can be measured by mean square errors of pixel values between the neighboring cell images. The gradient of the cell difference can be defined as the difference between the cell differences. Larger cell image difference means more turbulence effect is concentrating in the corresponding cell when compared with other cell images collected at the same time.

The “Laplacian Metric” is defined to be the multiplication of the gradient of cell image difference along horizontal (M) direction, vertical (N) direction and progressive time (t) direction. The best image cell (targeted lucky image cell) can be proved to be located at the cell with maximum magnitude of Laplacian Metric.

We can show the result by a twisted letter “A” through the following experimental platform:

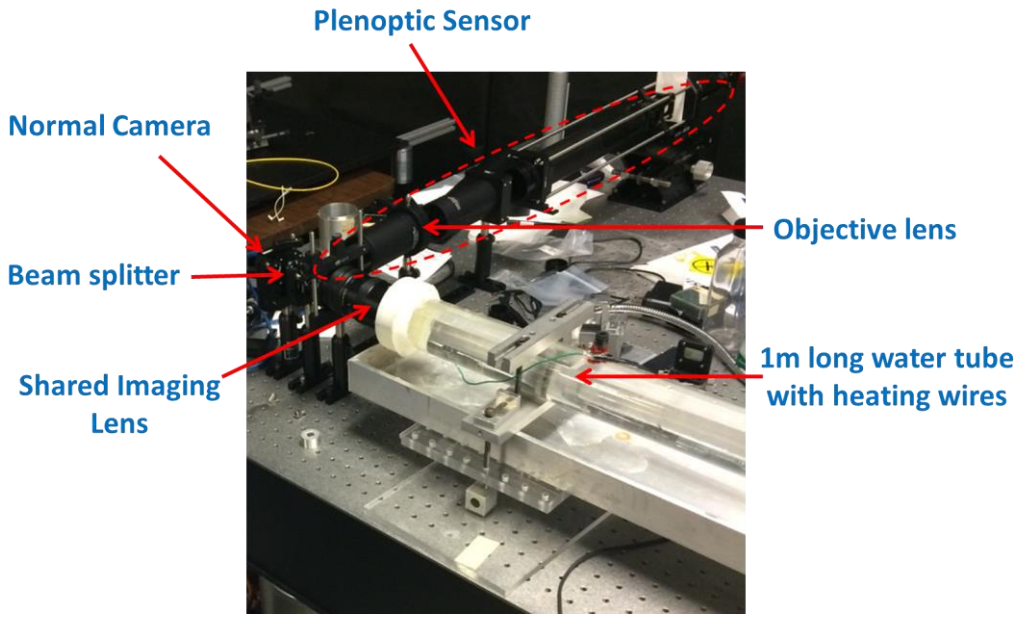

Figure 6. 24: Experimental platform for water vision distortion and correction

The results for the plenoptic video processing for the best image cell are shown as:

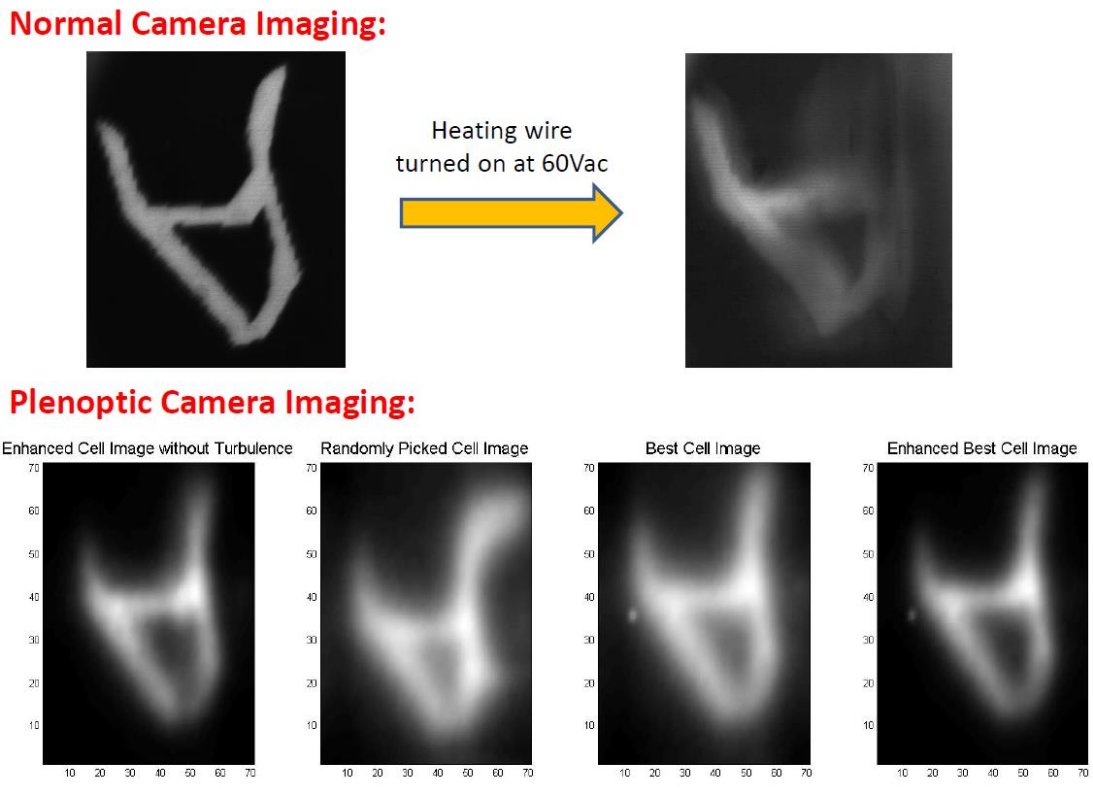

Figure 6. 25: 3D lucky imaging results on the plenoptic sensor

The results suggest that by differentiating images formed at different propagation path in strong turbulence, blurring and shimmering effects caused by turbulence distortion can be intelligently avoided.

Similar experiments can be conducted in extremely strong air turbulence caused by hot plates. The observing platform is shown as (will be elaborated on in chapter 6):

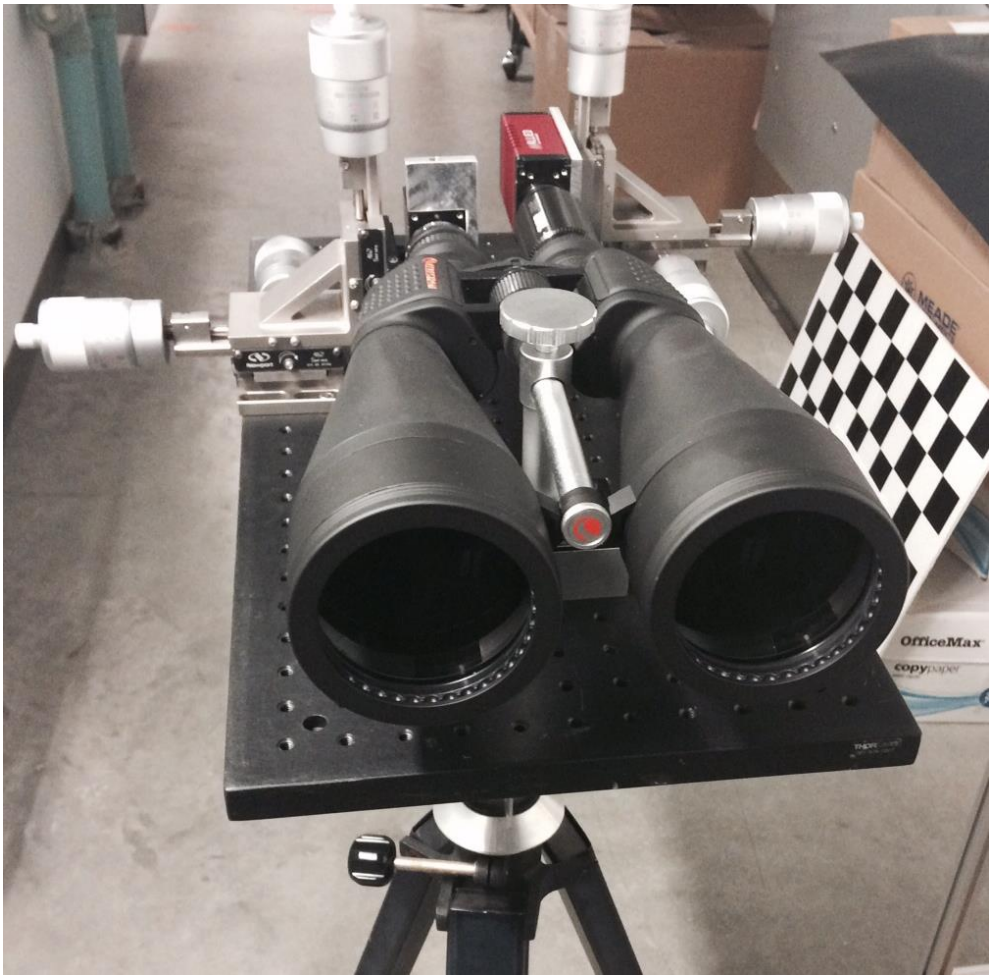

Figure 6. 26: Experimental platform for remote imaging through atmospheric turbulence

In figure 6.26, a long range binocular is used to render the view. Each front objective lens in the binocular has a diameter of 3 inches. One branch of the binocular is

connected with a normal camera, while the other branch connects to a plenoptic sensor. Therefore, the plenoptic sensor can resolve imaging problems caused by a hot plate similarly as the water tube. The results are shown as (with an object letter “H”):

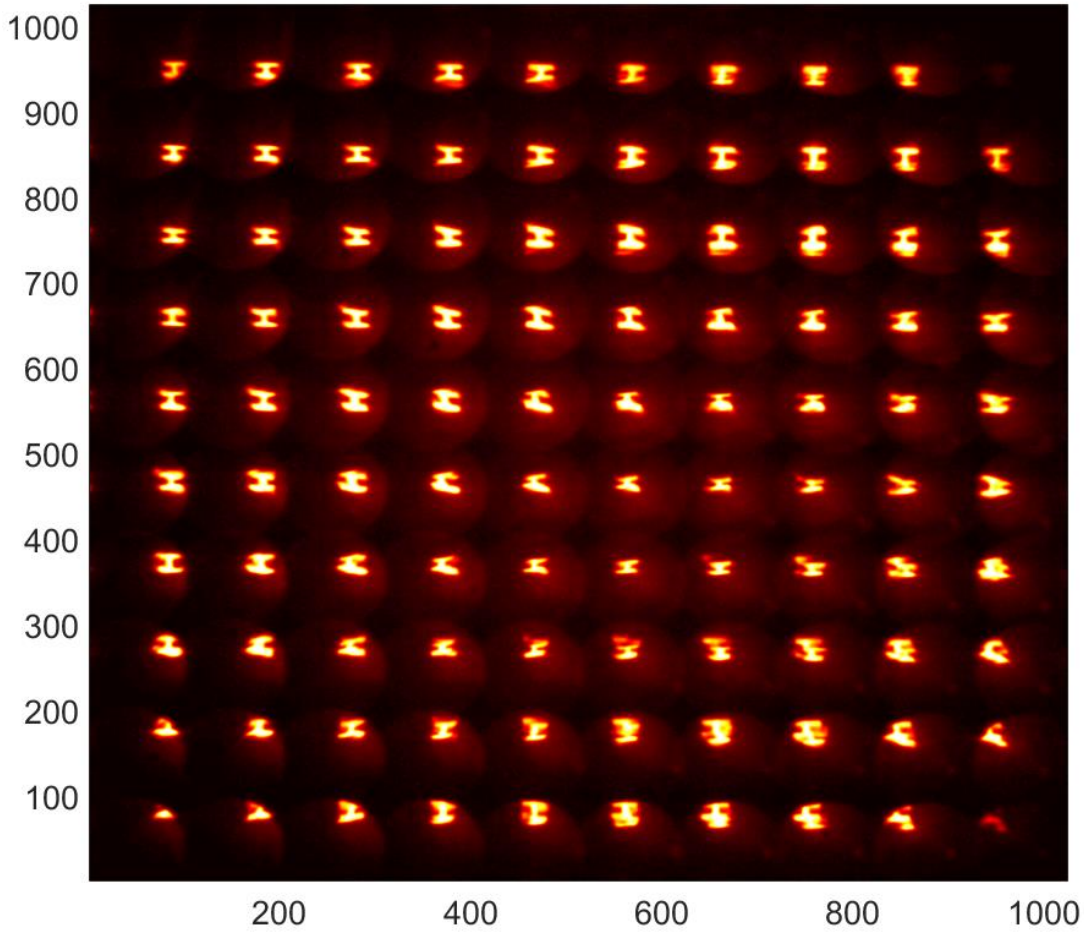

Figure 6. 27: Randomly selected plenoptic image in the recording process when the hot plate is turned on and the object is placed 60 meters away

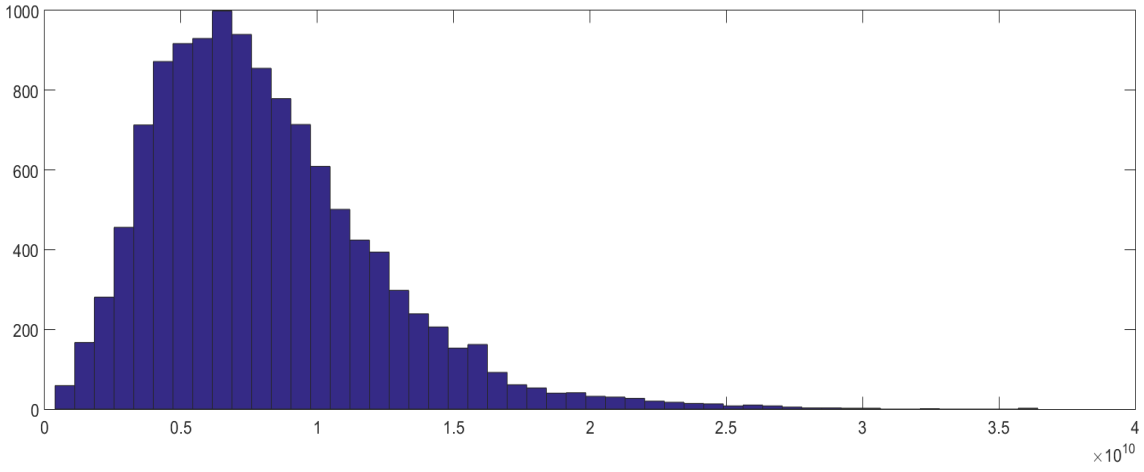

Figure 6. 28: Image cell counting for different metric values in the 3D lucky imaging process

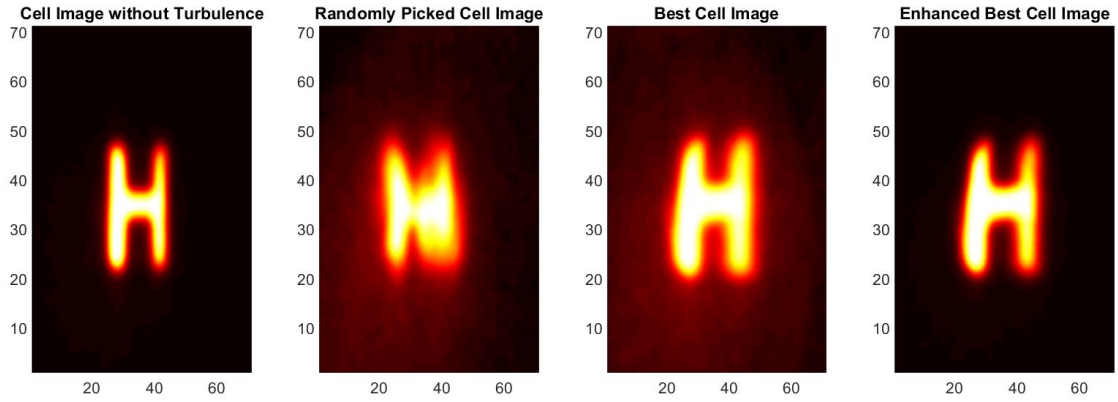

Figure 6. 29: Processing results of 3D lucky imaging on the plenoptic sensor

Figure 6.27 shows a randomly picked plenoptic image, where it is easy to notice the cell image difference caused by air turbulence generated by the hotplate. Figure 6.28 shows the box counting results for different metric values. The best image is selected at the tail, which is shown in figure 6.29. The result states that the "Mutated Laplacian Metric" is effective in retrieving a relatively undistorted image.

Another experiment was done by cascading the hotplate and the water tube to cause combined distortion effects on the image. The system picture and the result are shown as:

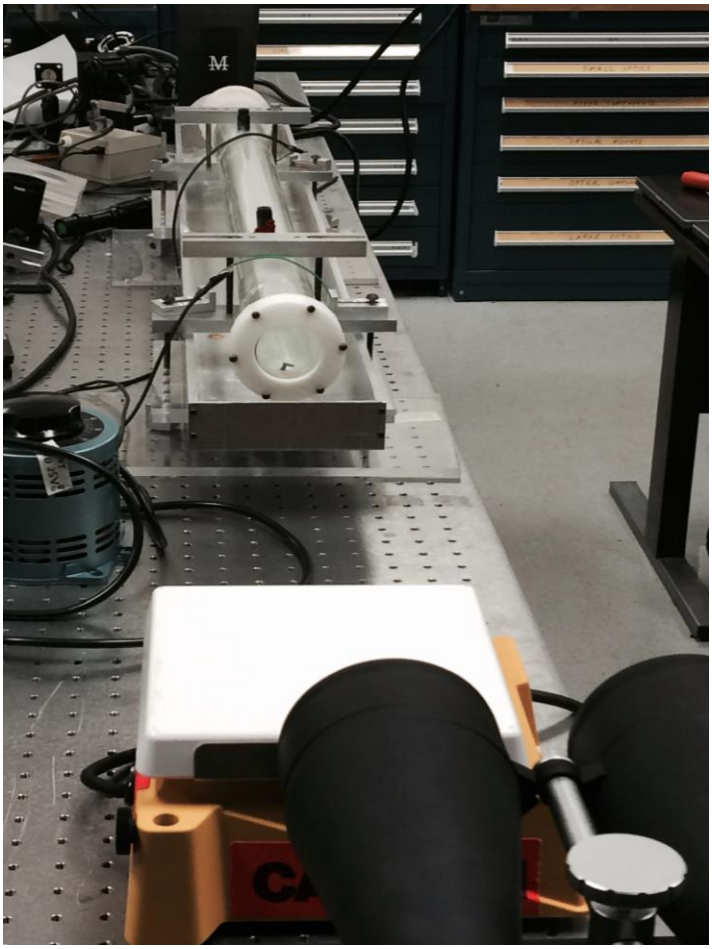

Figure 6. 30: System picture for combined lab-scale turbulence experiment

Figure 6.30 shows the experimental platform of using the plenoptic sensor branch in our remote imaging platform to resolve image distortion caused by the water tube and a hot plate. With the help of the water tube, we could concentrate severe turbulence distortions to lab scale experiments. The imaging distance is 3m, with a 1.5m length water tube to generate large distortions and a hotplate at the end to generate high frequency distortions.

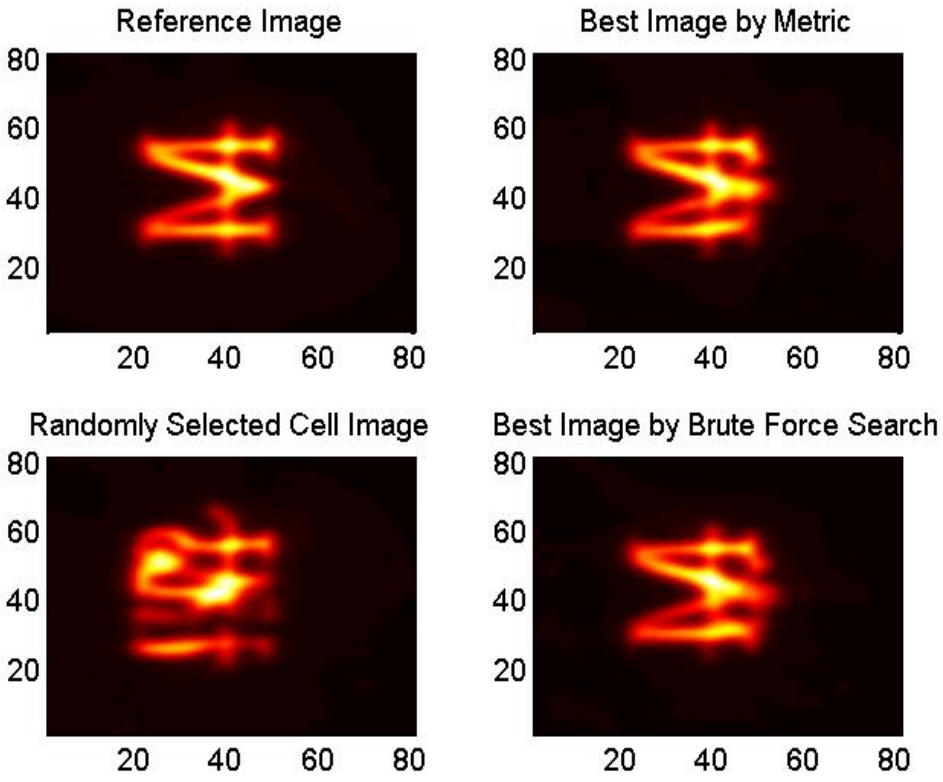

Figure 6. 31: Processing results of 3D lucky imaging on the plenoptic sensor

The result in figure 6.31 shows that the auto-selection metric (mutated Laplacian metric) is effective in resolving imaging problems under severe turbulence distortions. The upper-left plot is the reference image without turbulence. After turbulence is turned on, the upper-right image is selected for the cell with maximum metric value. The lower-left image is a randomly selected cell image and the lower-right image is cell image that has the maximum correlation with the reference image. Since the lower-right image is selected through brute force search, it is the best image under turbulence condition. However, as there is no reference image to compare to, it is impossible to realize the brute force search. Therefore, the best result is picked by the metric in reality. In fact, the correlation between the lower-right image and the

reference image is 0.9768, while the upper right image is 0.9729 correlated with the reference image. Therefore, the metric can reliably select an optimized image cell.

6.4 Enhanced back scatter system for alignment and tracking purposes

A huge challenge in directing laser energy to a confined area on an arbitrary target's surface is to find robust guidance. Atmospheric turbulence plays a disruptive role in messing up phases on the wavefront. For example, for 0.01ppm deviation in refractive index, the range of phase deviation on the wavefront would match up to 15λ per kilometer in propagation. In addition, the turbulence is varying swiftly over time with major oscillation frequencies from 10Hz to 100Hz. Therefore, even for advanced adaptive optics system that can operate at 1 kHz or even higher, the maximum number of trials to find optimized adjustments for the transmitted beam is around 20, which is too few to enforce satisfying corrections at random selected start points.

A promising approach to overcome the above difficulties lies in using the reciprocity of atmospheric turbulence in the propagation channel. In other words, if the wavefront is phase conjugated and propagated backwards, the exact initial beam can be achieved. Yet this approach is technically "impossible" for point to point observation and operation on the wavefront.

A more realistic approach is to use a phenomenon called "enhanced back scattering" (EBS) resulted from the reciprocity of the turbulent channel. The theory of enhanced back scattering predicts that for long range beam propagation through random medium, the part of the echo wave near the optic axis of alignment would show some

coherent effects. If the echo wave is collected by a lens, there exists ONE point on the focal plane of the lens that shows both doubled average intensity and doubled scintillation index. Besides the echo wave's ability in revealing the location of an object, our study on the echo wave of a laser beam demonstrates that the parasite EBS effects shows high potential in providing an excellent starting point to perform adaptive optics.

The principal of enhanced back scattering can be illustrated by the following ray tracing diagrams:

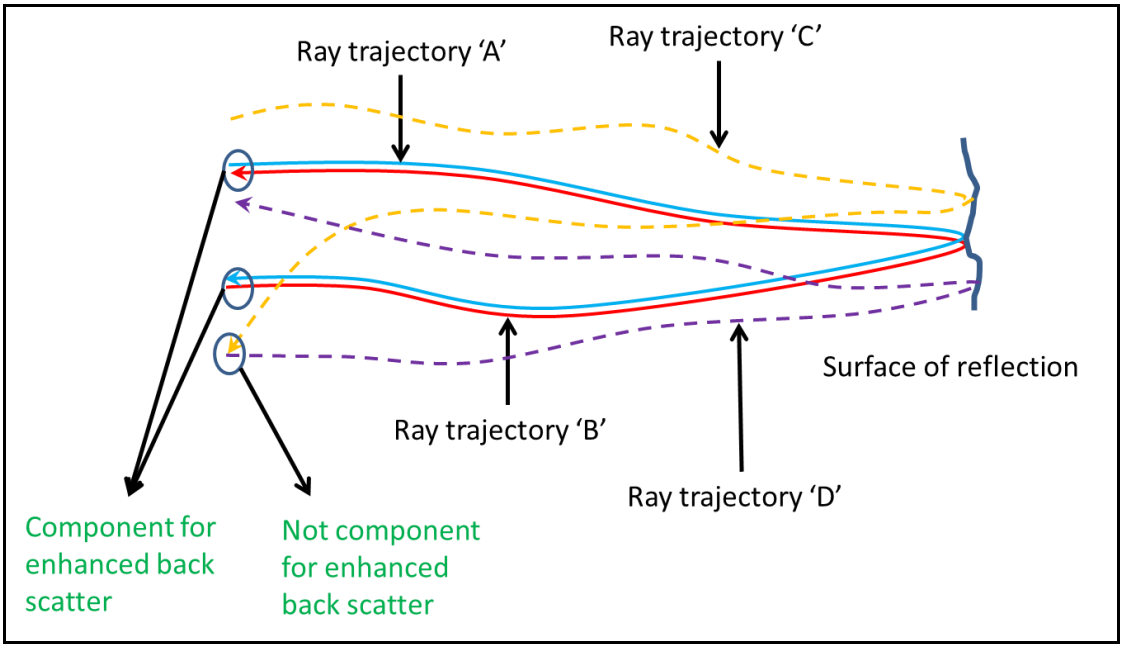

Figure 6. 32: Ray tracing diagram to illustrate the enhanced back scatter

It is not surprising to discover that the process of encouraging enhanced backscatter is to regulate the coherence of the echo beam. This leads to the instinctive thought that if the EBS kernel part of the echo wave (round trip) is more coherent, it is highly possible that the coherence target beam's wavefront (single trip) can be improved. The improvement of EBS kernel's coherence is demonstrated in the following graph:

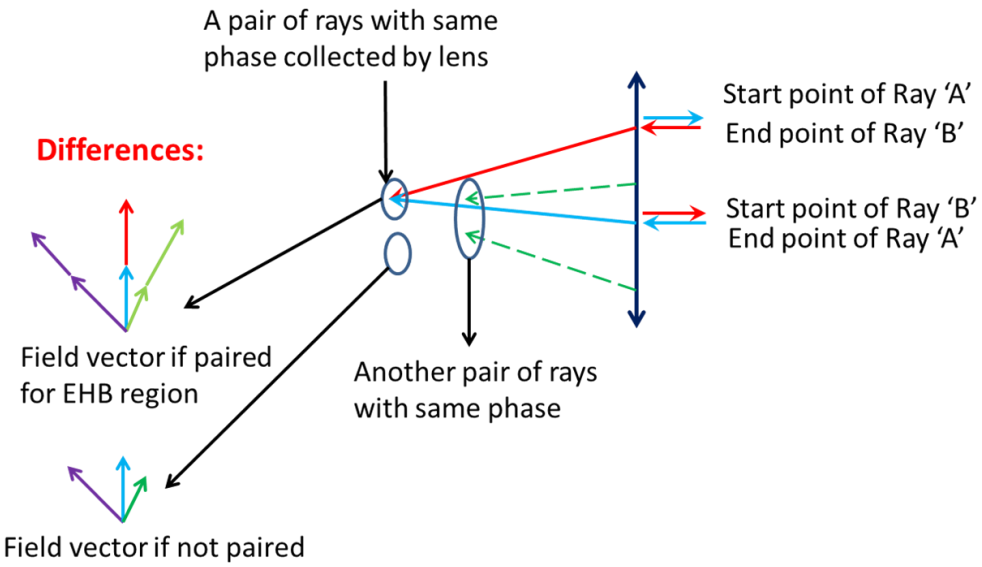

Figure 6. 33: Extraction of the EBS by using a thin lens to image the focal plane

As an experimental demonstration, we show the weak-localization (also called "enhanced backscatter") effects with the following platform:

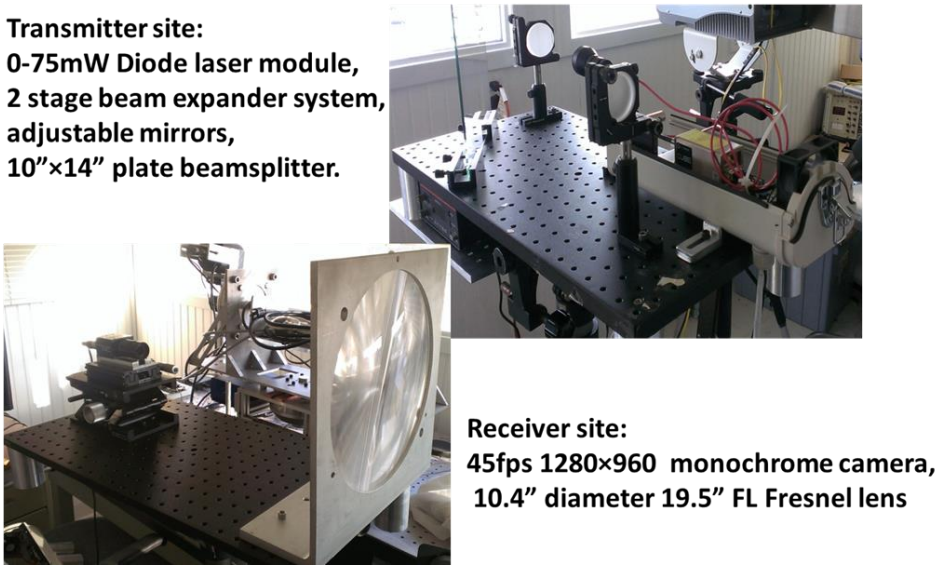

Figure 6. 34: Experimental platform for studying weak localization effects

Intuitively, the experimental structure of figure 6.34 can be illustrated by the following diagram:

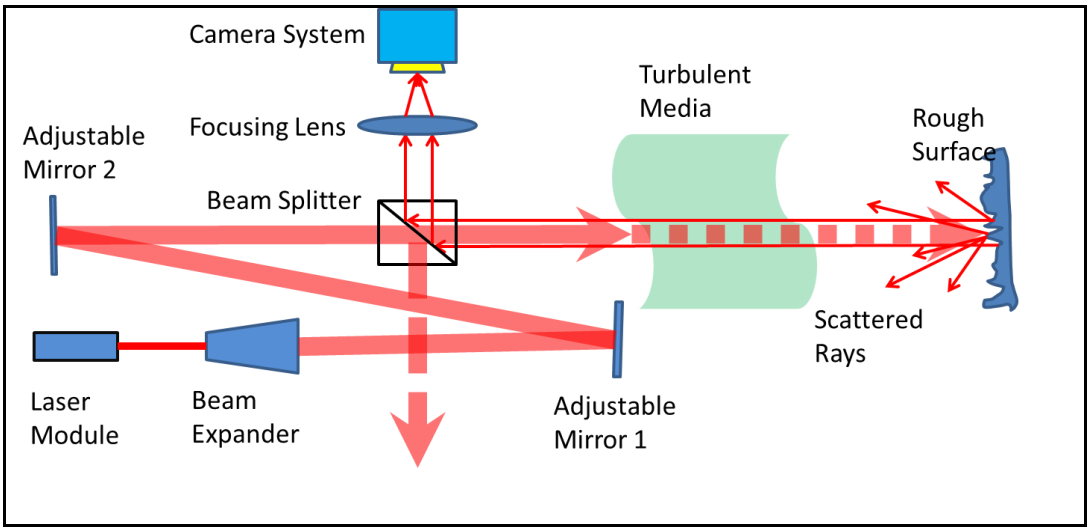

Figure 6. 35: Illustration diagram for figure 6.34

When the back-scattered beam is Fourier transformed, there exists a spot that doubles the scintillation and intensity when compared with spots in the vicinity. And the slope of ambient intensity near the spot determines the small tip/tilt between the pointing laser and the surface normal of the target. The results are shown as:

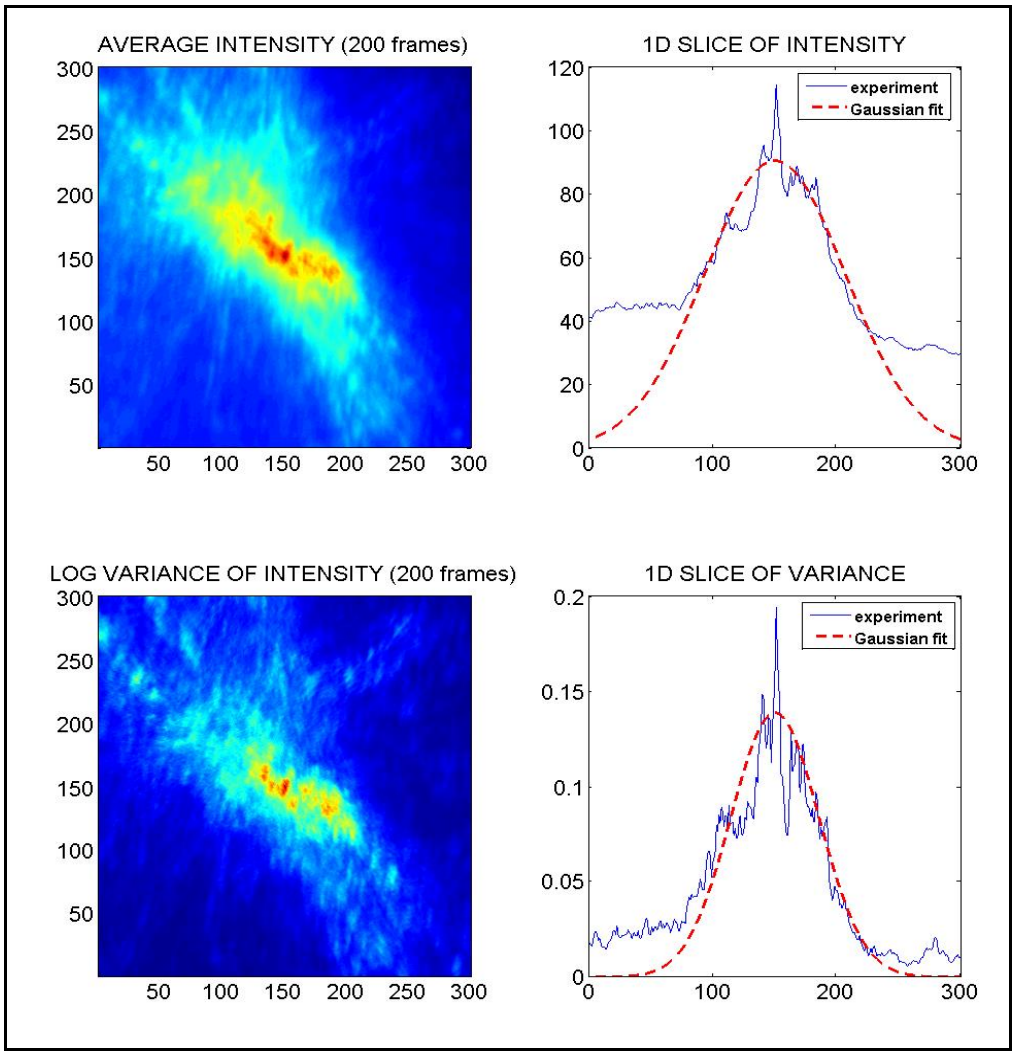

Figure 6. 36: Weak localization effect when the incident beam is normal to the target's surface

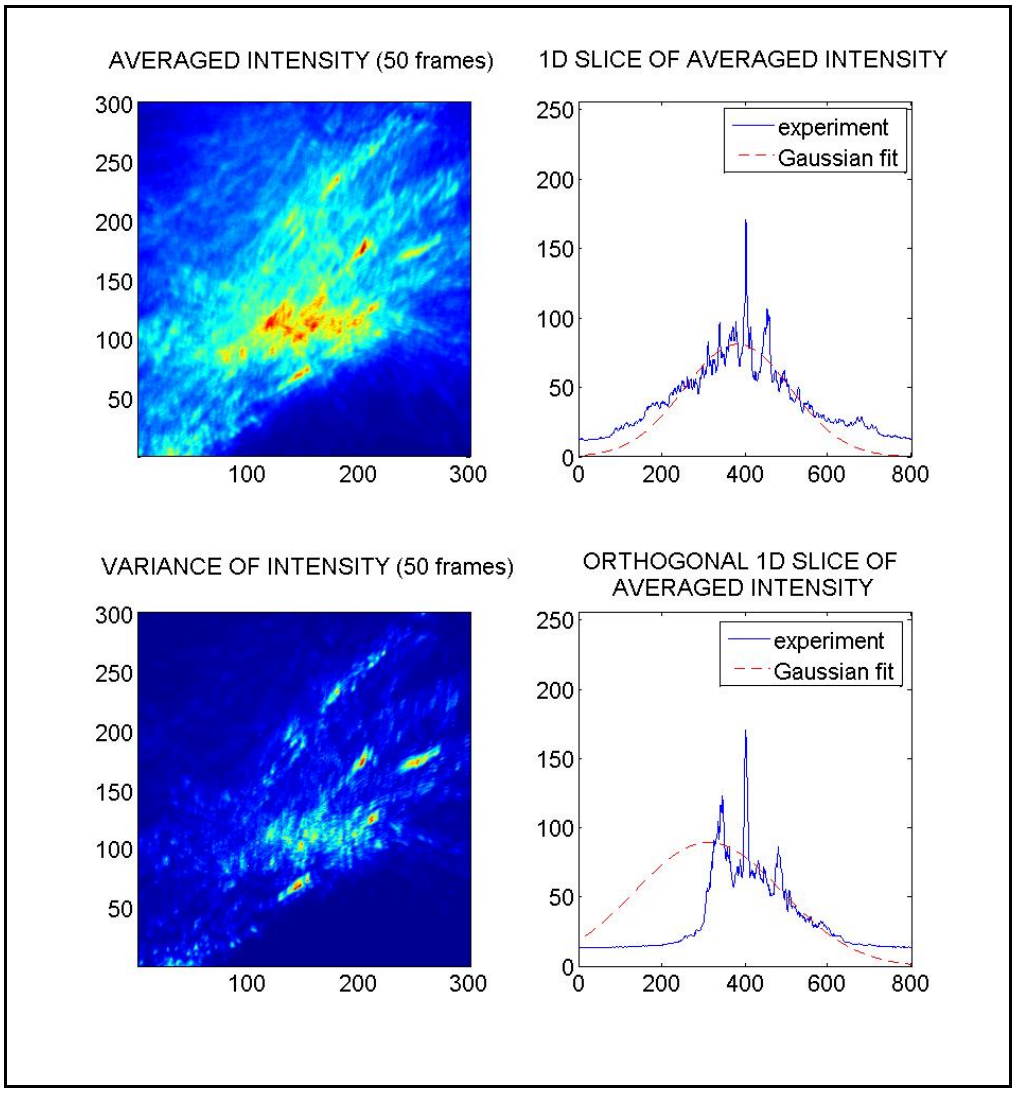

Figure 6. 37: Weak localization effect when the incident beam is tilted with the surface normal of the target

The above results show that by exploiting the details of the backscattered wave, extra information can be obtained. Note that on the above figure a cliff is observed on a 1D slice of averaged intensity due to the limited aperture of our optical components. If the entire echo wave can be collected, it shall resemble the Gaussian fit curve as shown in the graph. We also reduced the number of frames to get the EBS effect in the misaligned case by slowing the frame rate of the camera, yet the overall time to

distinguish the EBS effect from randomness remains the same as about 3-4 seconds. As a result, it is sufficient to point out:

(1) EBS effect exists in a variety of cases of coherent echo waves, whose location and shape depend mostly on the transmitter site.

(2) EBS is a good indicator for maintaining a good alignment with a remote target in adaptive optics.

6.5 Combined turbulence measurements with new instrumentations

In this section, we will discuss the benefits of combined turbulence measurements and list a few examples on how those instruments can be combined to characterize or solve atmospheric turbulence problems.

The plenoptic sensor maximizes the efficiency of using an image to extract phase and amplitude information of a distorted beam. The RTD system provides the convenience in sampling turbulence levels at an arbitrary spot and orientation. The large aperture scintillometer pair provides a larger data range in measuring C_n^2 values. The Remote imaging system helps visualize the beam pattern on the target area. The EBS can be used to optimize alignments with the receiver and facilitate tracking of a moving target.

For example two plenoptic sensors can be deployed on both sides of a free space optics (FSO) communication channel to realize a feedback loop of complete knowledge of the beam's phase and amplitude information. The diagram can be shown as:

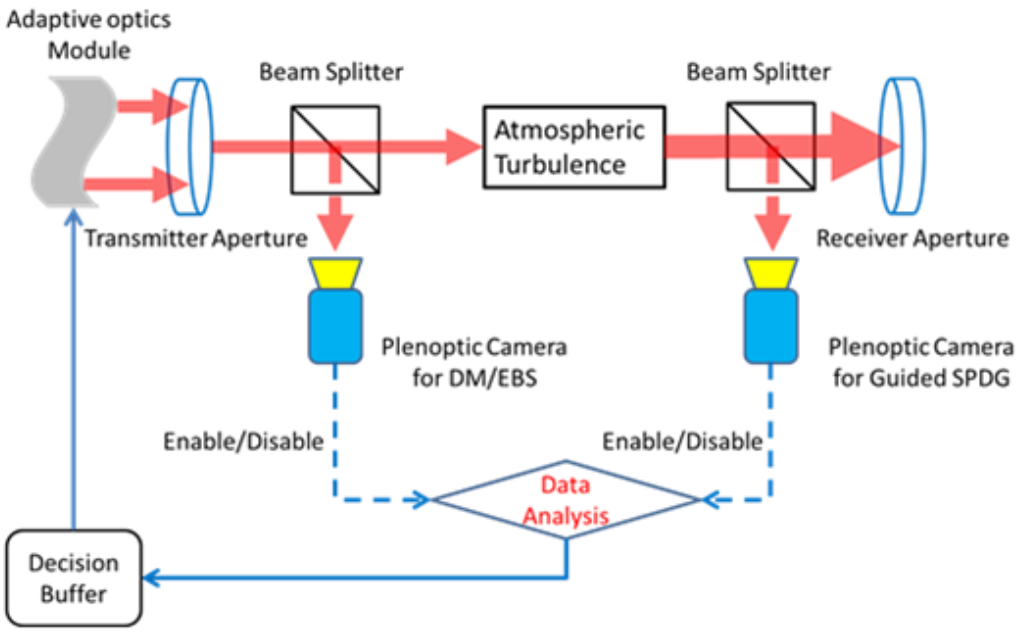

Figure 6. 38: A turbulent channel featured with plenoptic sensor on both sides

In figure 6.38, the two observed wavefront data are instantly compared and analyzed to instruct an adaptive optics (AO) module to perform beam correction. Intuitively, if the previous transmitted beam is collimated Gaussian beam, one can use the reciprocity and phase conjugation idea to impose the conjugated phase for the correction. Then a relatively clean beam can be obtained on the target and the plenoptic images are swapped and flipped on the sensors. Also, one can use the complete waveforms on both sensors to extract/characterize the system function of the turbulent channel.

Another example of combined turbulence study is to combine several RTD systems, the scintillometer pair and the plenoptic sensor to characterize deep turbulence. The RTD systems can sample the turbulence level at various spots in the channel. The scintillometer provides the path averaged measurement of turbulence level. The plenoptic sensor describes the wavefront behavior at various levels of atmospheric turbulence. Thus, the combination of the devices provide insight into how an overall

C_n^2 value is made up of distributed turbulence conditions at different locations of the channel as well as how the C_n^2 is related to the distorted wavefront. A verification experiment for this idea can be shown as:

Figure 6. 39: Experimental picture of using the plenoptic sensor to observe scintillation index

In figure 6.39, a plenoptic sensor with the objective lens replaced by a Cassegrain telescope lens with 6" diameter is connected to a Lenovo W550 workstation and a power generator to detect the optical turbulence parameter C_n^2. The test range is located at the ISTEF range with 1 km distance. The recording speed is 30fps on the plenoptic sensor and 15 continuously acquired plenoptic images are shown as:

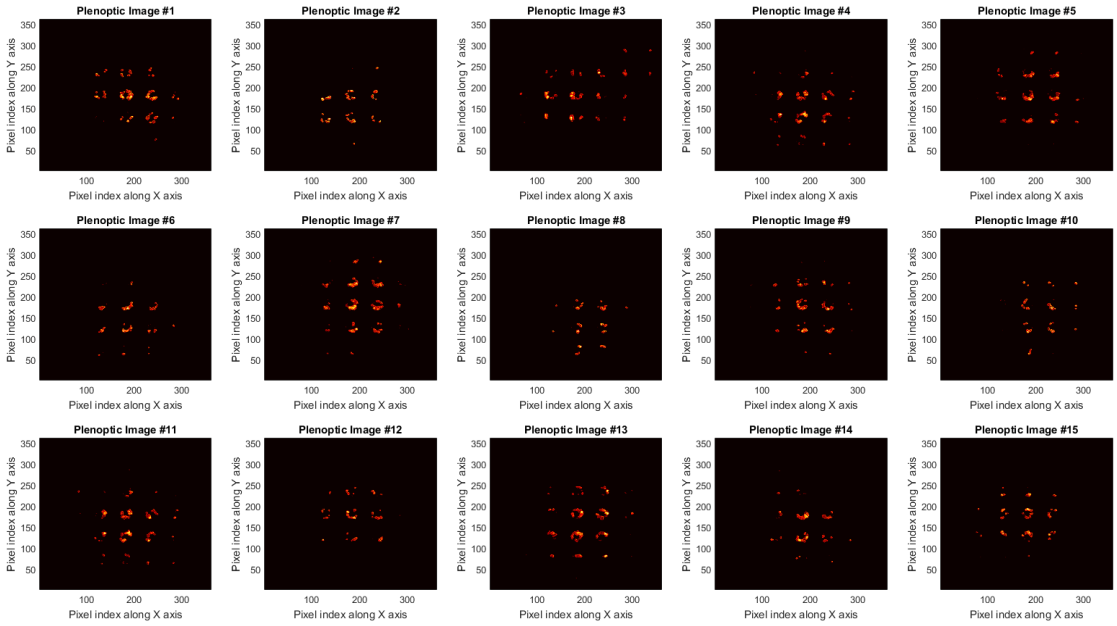

Figure 6. 40: 15 frames of continuously acquired plenoptic images on a distorted laser beam

Correspondingly, the beam intensity at the aperture of the objective lens can be reconstructed as:

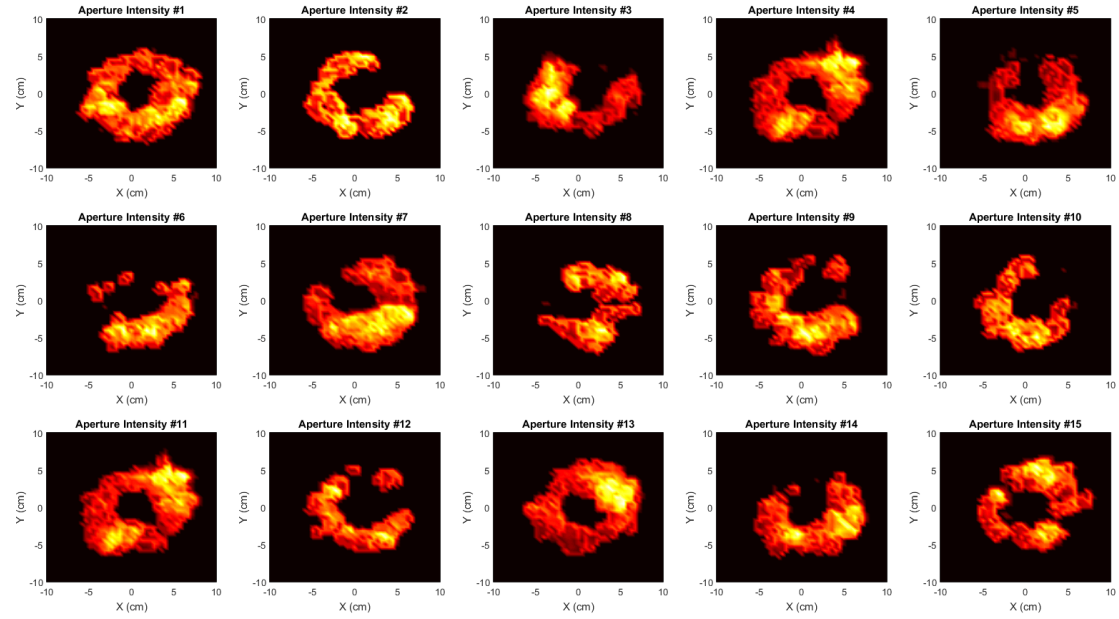

Figure 6.41: Reconstructed beam intensity profile on the aperture of the objective lens

Based on the intensity profile shown in figure 6.41, the C_n^2 value can be evaluated by the intensity scintillation on the receiving aperture as:

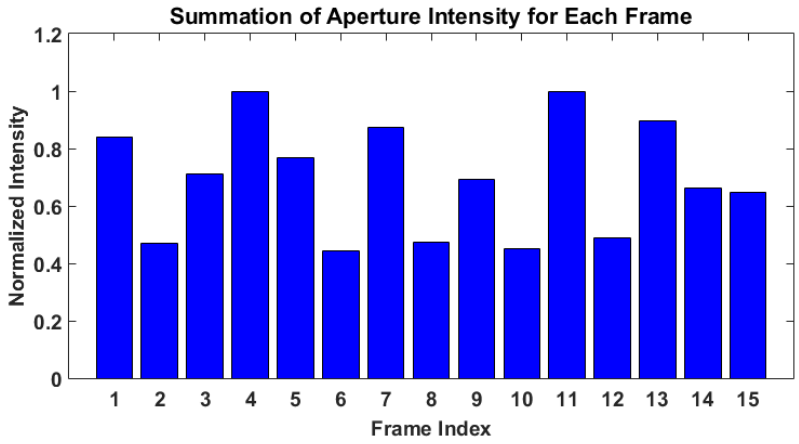

Figure 6. 42: Normalized intensity on the receiving aperture after reconstruction

Equivalently, the C_n^2 value is 7.124×10^{-13} $m^{-2/3}$ at the corresponding time (03/21/2016, 15:09). Comparatively, the C_n^2 value from the record of a commercial scintillometer pair over the same channel is 8.41×10^{-13} $m^{-2/3}$, which indicates that the plenoptic sensor's evaluation is quite accurate. Similarly, the plenoptic sensor can also be used to analyze the angles of arrival of the beam, which are shown as:

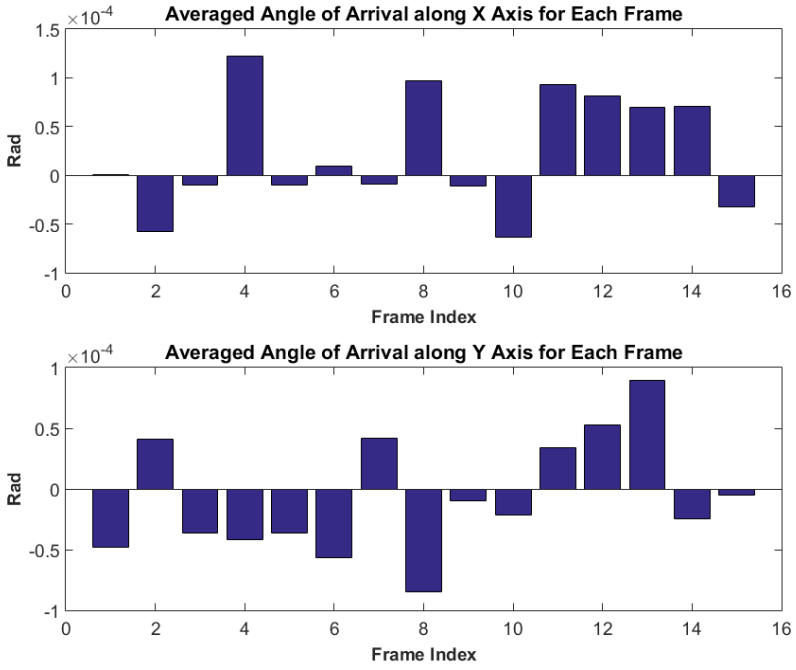

Figure 6. 43: Angle of arrival of the laser beam after the plenoptic sensor's reconstruction

Based on the angle of arrival, the C_n^2 contribution from X (horizontal) and Y (vertical) axis are $5.29\times10^{-13}\,m^{-2/3}$ and $6.99\times10^{-13}\,m^{-2/3}$ respectively, which also agree with the data on the scintillometer. Therefore, the plenoptic sensor can be used as a comprehensive tool to reveal detailed information in the beam distortion. In addition, the reconstructed wavefront of the 15 continuously required frames is shown as:

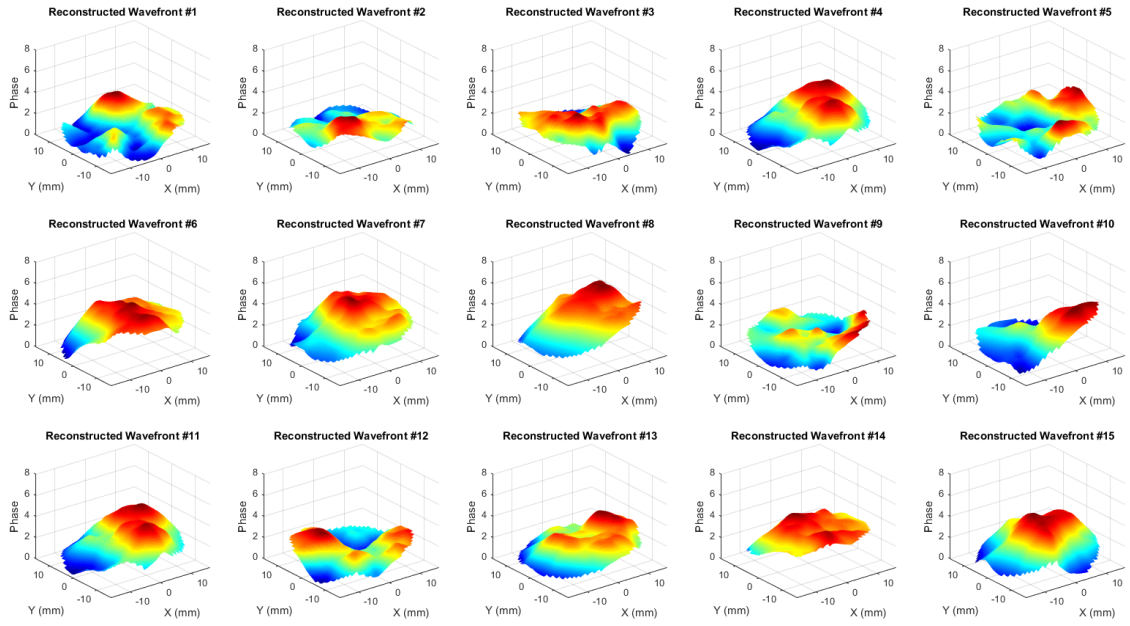

Figure 6. 44: Reconstructed wavefront distortion for the arriving beam after propagating through the 1 km turbulent channel

Without loss of generality, turbulence effects can be comprehensively understood by combining the results on the plenoptic sensor, the RTD systems and the scintillometer pairs together. In fact, there are countless algorithms and experimental configurations that can be applied to the field of studying atmospheric turbulence. A general trend in experimental study of atmospheric turbulence (especially deep turbulence, which affects the effective range of FSO and DE systems) is to use a much larger dataset and computation power to analyze more detailed structure of the turbulent channel. We believe that the plenoptic sensor greatly enhances the study of atmospheric turbulence.

Conclusions and Future Work

The plenoptic sensor introduced in this thesis is a valuable system to solve turbulence problems. Accurate and robust wavefront sensing for all kinds of turbulence situations guarantees the successfulness of optical communication, laser defense as well as remote surveillance applications. In general, an arbitrary beam with phase and amplitude distortions will be mapped to a plenoptic image that contains an image array. All the wavelets with same wavefront gradient will be casted into the same image cell, while their intensity distribution over the entrance pupil is linearly scaled and reversed on each cell image. When all the cell images are combined, the phase and amplitude distortion of the incident beam can be uniquely determined. The innovation of the plenoptic sensor, shall find numerous applications including: FSO communication, directed energy and remote imaging/surveillance.

Future work will be dedicated to integrating the plenoptic sensor into a comprehensive system including sensing and analyzing. Efforts in several areas will be made:

(1) The processing speed will be increased with hardware upgrade and software optimization. The minimum speed specification will be larger than 300Hz.

(2) Plenoptic sensor with large format objective lens will be developed to capture wider/more complex beam distortions.

(3) Past models of atmospheric turbulence will be re-examined with actual experimental data collected by the plenoptic sensor to verify their correctness.

(4) Several application platforms will be improved. This includes: the remote imaging platform, the adaptive optics platform, and the scintillometer platform.

(5) Extend the advanced wavefront sensors to wider application areas.

Bibliography

1. Lawrence, Robert S., and John W. Strohbehn. "A survey of clear-air propagation effects relevant to optical communications." *Proceedings of the IEEE* 58, no. 10 (1970): 1523-1545.
2. Fried, Do L., G. E. Mevers, and JR KEISTER. "Measurements of laser-beam scintillation in the atmosphere." *JOSA* 57, no. 6 (1967): 787-797.
3. Andrews, Larry C., Ronald L. Phillips, Richard J. Sasiela, and Ronald Parenti. "Beam wander effects on the scintillation index of a focused beam." In *Defense and Security*, pp. 28-37. International Society for Optics and Photonics, 2005.
4. Feit, M.D. and, and J. A. Fleck. "Beam nonparaxiality, filament formation, and beam breakup in the self-focusing of optical beams." *JOSA B* 5, no. 3 (1988): 633-640.
5. Fried, Daniel, Richard E. Glena, John D.B. Featherstone, and Wolf Seka. "Nature of light scattering in dental enamel and dentin at visible and near-infrared wavelengths." *Applied Optics* 34, no. 7 (1995): 1278-1285.
6. Clifford, S. F., G. R. Ochs, and R. S. Lawrence. "Saturation of optical scintillation by strong turbulence." *JOSA* 64, no. 2 (1974): 148-154.
7. Roddier, Francois. *Adaptive optics in astronomy*. Cambridge University Press, 1999.
8. Keller, Joseph B. "Accuracy and Validity of the Born and Rytov Approximations*." *JOSA* 59, no. 8 (1969): 1003.

9. Vorontsov, Mikhail, Jim Riker, Gary Carhart, V. S. Rao Gudimetla, Leonid Beresnev, Thomas Weyrauch, and Lewis C. Roberts Jr. "Deep turbulence effects compensation experiments with a cascaded adaptive optics system using a 3.63 m telescope." *Applied Optics* 48, no. 1 (2009): A47-A57.
10. Tyler, Glenn A. "Adaptive optics compensation for propagation through deep turbulence: initial investigation of gradient descent tomography." *JOSA A* 23, no. 8 (2006): 1914-1923.
11. Vela, Patricio A., Marc Niethammer, Gallagher D. Pryor, Allen R. Tannenbaum, Robert Butts, and Donald Washburn. "Knowledge-based segmentation for tracking through deep turbulence." *IEEE Transactions on Control Systems Technology* 16, no. 3 (2008): 469-474.
12. Chehbouni, A., C. Watts, J-P. Lagouarde, Y. H. Kerr, J-C. Rodriguez, J-M. Bonnefond, F. Santiago, G. Dedieu, D. C. Goodrich, and C. Unkrich. "Estimation of heat and momentum fluxes over complex terrain using a large aperture scintillometer." *Agricultural and Forest Meteorology* 105, no. 1 (2000): 215-226.
13. Fugate, Robert Q., D. L. Fried, G. A. Ameer, B. R. Boeke, S. L. Browne, P. H. Roberts, R. E. Ruane, G. A. Tyler, and L. M. Wopat. "Measurement of atmospheric wavefront distortion using scattered light from a laser guide-star." (1991): 144-146.
14. Roddier, Fran ̧ois. "The effects of atmospheric turbulence in optical astronomy."*In: Progress in optics. Volume 19. Amsterdam, North-Holland Publishing Co., 1981, p. 281-376.* 19 (1981): 281-376.

15. Wang, Fugao, and D. P. Landau. "Efficient, multiple-range random walk algorithm to calculate the density of states." *Physical Review Letters* 86, no. 10 (2001): 2050.
16. Smith, Matthew H., Jacob B. Woodruff, and James D. Howe. "Beam wander considerations in imaging polarimetry." In *SPIE's International Symposium on Optical Science, Engineering, and Instrumentation*, pp. 50-54. International Society for Optics and Photonics, 1999.
17. Dios, Federico, Juan Antonio Rubio, Alejandro Rodr ́guez, and Adolfo Comer ́on. "Scintillation and beam-wander analysis in an optical ground station-satellite uplink." *Applied Optics* 43, no. 19 (2004): 3866-3873.
18. Willebrand, Heinz, and Baksheesh S. Ghuman. "Fiber optics without fiber."*Spectrum, IEEE* 38, no. 8 (2001): 40-45.
19. Fried, David L. "Aperture averaging of scintillation." *JOSA* 57, no. 2 (1967): 169-172.
20. Mamaev, A. V., M. Saffman, D. Z. Anderson, and A. A. Zozulya. "Propagation of light beams in anisotropic nonlinear media: from symmetry breaking to spatial turbulence." *Physical Review A* 54, no. 1 (1996): 870.
21. Andrews, Larry C., and Ronald L. Phillips. *Laser beam propagation through random media*. Vol. 1. Bellingham, WA: SPIE press, 2005.
22. Lane, R. G., A. Glindemann, and J. C. Dainty. "Simulation of a Kolmogorov phase screen." *Waves in random media* 2, no. 3 (1992): 209-224.
23. Hardy, John W. *Adaptive optics for astronomical telescopes*. Oxford University Press, 1998.

24. Kobayashi, Michikazu, and Makoto Tsubota. "Kolmogorov spectrum of superfluid turbulence: Numerical analysis of the Gross-Pitaevskii equation with a small-scale dissipation." *Physical Review Letters* 94, no. 6 (2005): 065302.
25. Dogariu, Aristide, and Stefan Amarande. "Propagation of partially coherent beams: turbulence-induced degradation." *Optics Letters* 28, no. 1 (2003): 10-12.
26. Recolons, Jaume, Larry C. Andrews, and Ronald L. Phillips. "Analysis of beam wander effects for a horizontal-path propagating Gaussian-beam wave: focused beam case." *Optical Engineering* 46, no. 8 (2007): 086002-086002.
27. Avila, Remy, Aziz Ziad, Julien Borgnino, François Martin, Abdelkrim Agabi, and Andrey Tokovinin. "Theoretical spatiotemporal analysis of angle of arrival induced by atmospheric turbulence as observed with the grating scale monitor experiment." *JOSA A* 14, no. 11 (1997): 3070-3082.
28. Andrews, Larry C., Ronald L. Phillips, and Cynthia Y. Hopen. *Laser beam scintillation with applications*. Vol. 99. SPIE press, 2001.
29. Andrews, Larry C. "Field guide to atmospheric optics." SPIE, 2004.
30. Primot, J., G. Rousset, and J. C. Fontanella. "Deconvolution from wave-front sensing: a new technique for compensating turbulence-degraded images."*JOSA A* 7, no. 9 (1990): 1598-1608.
31. Marshall, Robert, Jill Kempf, Scott Dyer, and Chieh-Cheng Yen. "Visualization methods and simulation steering for a 3D turbulence model of

Lake Erie." In *ACM SIGGRAPH Computer Graphics*, vol. 24, no. 2, pp. 89-97. ACM, 1990.

32. Wu, Chensheng, William Nelson, and Christopher C. Davis. "3D geometric modeling and simulation of laser propagation through turbulence with plenoptic functions." In *SPIE Optical Engineering+ Applications*, pp. 92240O-92240O. International Society for Optics and Photonics, 2014.
33. Platt, Ben C. "History and principles of Shack-Hartmann wavefront sensing." *Journal of Refractive Surgery* 17, no. 5 (2001): S573-S577.
34. Hardy, John W. *Adaptive optics for astronomical telescopes*. Oxford University Press, 1998.
35. Dayton, David, Sergio Restaino, John Gonglewski, Joe Gallegos, Scot McDermott, Steve Browne, Sam Rogers, Mohan Vaidyanathan, and Mike Shilko. "Laboratory and field demonstration of a low cost membrane mirror adaptive optics system." *Optics Communications* 176, no. 4 (2000): 339-345.
36. Jiang, Wenhan, Hao Xian, and Feng Shen. "Detection error of Shack-Hartmann wavefront sensors." In *Optical Science, Engineering and Instrumentation'97*, pp. 534-544. International Society for Optics and Photonics, 1997.
37. Petrov, Valentin V. "Limit theorems of probability theory." (1995).
38. Buzbee, Billy L., Gene H. Golub, and Clair W. Nielson. "On direct methods for solving Poisson's equations." *SIAM Journal on Numerical analysis* 7, no. 4 (1970): 627-656.

39. Sun, Jian, Jiaya Jia, Chi-Keung Tang, and Heung-Yeung Shum. "Poisson matting." *ACM Transactions on Graphics (ToG)* 23, no. 3 (2004): 315-321.
40. Martin, Rainer. "Noise power spectral density estimation based on optimal smoothing and minimum statistics." *Speech and Audio Processing, IEEE Transactions on* 9, no. 5 (2001): 504-512.
41. Roddier, Francois, and C. Roddier. "Curvature sensing and compensation: a new concept in adaptive optics." In *European Southern Observatory Conference and Workshop Proceedings*, vol. 30, p. 667. 1988.
42. Rigaut, François, Brent L. Ellerbroek, and Malcolm J. Northcott. "Comparison of curvature-based and Shack–Hartmann-based adaptive optics for the Gemini telescope." *Applied Optics* 36, no. 13 (1997): 2856-2868.
43. Wyant, James C. "Use of an ac heterodyne lateral shear interferometer with real–time wavefront correction systems." *Applied optics* 14, no. 11 (1975): 2622-2626.
44. Schnars, Ulf, and Werner P.O. Jüptner. "Digital recording and reconstruction of holograms in hologram interferometry and shearography." *Applied Optics* 33, no. 20 (1994): 4373-4377.
45. Elster, C., and I. Weingärtner. "Exact wave-front reconstruction from two lateral shearing interferograms." *JOSA A* 16, no. 9 (1999): 2281-2285.
46. Deng, Yuqiang, Zubin Wu, Lu Chai, Ching-yue Wang, Keisaku Yamane, Ryoji Morita, Mikio Yamashita, and Zhigang Zhang. "Wavelet-transform analysis of spectral shearing interferometry for phase reconstruction of femtosecond optical pulses." *Optics Express* 13, no. 6 (2005): 2120-2126.

47. Haumann, H-J., Harald Kobolla, Frank Sauer, Juerg Schmidt, Johannes Schwider, Wilhelm Stork, Norbert Streibl, and Reinhard Voelkel. "Optoelectronic interconnection based on a light-guiding plate with holographic coupling elements." *Optical Engineering* 30, no. 10 (1991): 1620-1623.

48. Andersen, Geoff P., Luis Dussan, Fassil Ghebremichael, and Kenny Chen. "Holographic wavefront sensor." *Optical Engineering* 48, no. 8 (2009): 085801-085801.

49. Noll, Robert J. "Zernike polynomials and atmospheric turbulence." *JOSA* 66, no. 3 (1976): 207-211.

50. Ng, Ren, Marc Levoy, Mathieu Brédif, Gene Duval, Mark Horowitz, and Pat Hanrahan. "Light field photography with a hand-held plenoptic camera." *Computer Science Technical Report CSTR* 2, no. 11 (2005).

51. Ramos, José Manuel Rodriguez, Fernando Rosa González, and José Gil Marichal-Hernández. "Wavefront aberration and distance measurement phase camera." U.S. Patent Application 12/161,362, filed January 18, 2007.

52. Rodríguez-Ramos, J. M., et al. "2D-FFT implementation on FPGA for wavefront phase recovery from the CAFADIS camera." *SPIE Astronomical Telescopes+ Instrumentation*. International Society for Optics and Photonics, 2008.

53. Rodríguez, J. M., et al. "The CAFADIS camera: a new tomographic wavefront sensor for Adaptive Optics." *1st AO4ELT conference-Adaptive Optics for Extremely Large Telescopes*. EDP Sciences, 2010.

54. Rodr ́guez-Ramos, J. M., et al. "Wavefront and distance measurement using the CAFADIS camera." *SPIE Astronomical Telescopes+ Instrumentation*. International Society for Optics and Photonics, 2008.
55. November, Laurence J. "Measurement of geometric distortion in a turbulent atmosphere." *Applied Optics* 25, no. 3 (1986): 392-397.
56. Cover, Thomas M., and Joy A. Thomas. *Elements of information theory*. John Wiley & Sons, 2012.
57. Wu, Chensheng, Jonathan Ko, and Christopher C. Davis. "Determining the phase and amplitude distortion of a wavefront using a plenoptic sensor." *JOSA A* 32, no. 5 (2015): 964-978.
58. Levoy, Marc, Ren Ng, Andrew Adams, Matthew Footer, and Mark Horowitz. "Light field microscopy." *ACM Transactions on Graphics (TOG)* 25, no. 3 (2006): 924-934.
59. Levoy, Marc, and Pat Hanrahan. "Light field rendering." In *Proceedings of the 23rd annual conference on Computer graphics and interactive techniques*, pp. 31-42. ACM, 1996.
60. Adelson, Edward H., and James R. Bergen. *The plenoptic function and the elements of early vision*. Vision and Modeling Group, Media Laboratory, Massachusetts Institute of Technology, 1991.
61. Eslami, Mohammed, Chensheng Wu, John Rzasa, and Christopher C. Davis. "Using a plenoptic camera to measure distortions in wavefronts affected by atmospheric turbulence." In *SPIE Optical Engineering+ Applications*, pp. 85170S-85170S. International Society for Optics and Photonics, 2012.

62. Sobierajski, Lisa M., and Arie E. Kaufman. "Volumetric ray tracing." In *Proceedings of the 1994 symposium on Volume visualization*, pp. 11-18. ACM, 1994.

63. Wu, Chensheng, William Nelson, and Christopher C. Davis. "3D geometric modeling and simulation of laser propagation through turbulence with plenoptic functions." In *SPIE Optical Engineering+ Applications*, pp. 92240O-92240O. International Society for Optics and Photonics, 2014.

64. Aaronson, Scott, and Alex Arkhipov. "The computational complexity of linear optics." In *Proceedings of the forty-third annual ACM symposium on Theory of computing*, pp. 333-342. ACM, 2011.

65. Seitz, Steven M., Brian Curless, James Diebel, Daniel Scharstein, and Richard Szeliski. "A comparison and evaluation of multi-view stereo reconstruction algorithms." In *Computer vision and pattern recognition, 2006 IEEE Computer Society Conference on*, vol. 1, pp. 519-528. IEEE, 2006.

66. Levin, Anat, William T. Freeman, and Frédo Durand. "Understanding camera trade-offs through a Bayesian analysis of light field projections." In *Computer Vision–ECCV 2008*, pp. 88-101. Springer Berlin Heidelberg, 2008.

67. Georgiev, Todor, Zhan Yu, Andrew Lumsdaine, and Sergio Goma. "Lytro camera technology: theory, algorithms, performance analysis." In *IS&T/SPIE Electronic Imaging*, pp. 86671J-86671J. International Society for Optics and Photonics, 2013.

68. Wu, Chensheng, and Christopher C. Davis. "Modified plenoptic camera for phase and amplitude wavefront sensing." In *SPIE Optical Engineering+*

Applications, pp. 88740I-88740I. International Society for Optics and Photonics, 2013.

69. Wu, Chensheng, Jonathan Ko, William Nelson, and Christopher C. Davis. "Phase and amplitude wave front sensing and reconstruction with a modified plenoptic camera." In *SPIE Optical Engineering+ Applications*, pp. 92240G-92240G. International Society for Optics and Photonics, 2014.
70. Goodman, Joseph W. *Introduction to Fourier optics*. Roberts and Company Publishers, 2005.
71. Southwell, William H. "Wave-front estimation from wave-front slope measurements." *JOSA* 70, no. 8 (1980): 998-1006.
72. Liu, Ling, and Mikhail A. Vorontsov. "Phase-locking of tiled fiber array using SPGD feedback controller." In *Optics & Photonics 2005*, pp. 58950P-58950P. International Society for Optics and Photonics, 2005.
73. Wu, Chensheng, Jonathan Ko, and Christopher C. Davis. "Using Graph Theory and a Plenoptic Sensor to Recognize Phase Distortions of a Laser Beam." *arXiv preprint arXiv:1506.00310* (2015).
74. Tarjan, Robert. "Depth-first search and linear graph algorithms." *SIAM journal on computing* 1, no. 2 (1972): 146-160.
75. Durnin J. Exact solutions for nondiffracting beams. I. The scalar theory. *JOSA A*. 1987 Apr 1;4(4):651-4.
76. Faugeras O. Three-dimensional computer vision: a geometric viewpoint. MIT press; 1993.

77. Cruz-Neira, Carolina, Daniel J. Sandin, and Thomas A. DeFanti. "Surround-screen projection-based virtual reality: the design and implementation of the CAVE." In *Proceedings of the 20th annual conference on Computer graphics and interactive techniques*, pp. 135-142. ACM, 1993.

78. Born, Max, and Emil Wolf. *Principles of optics: electromagnetic theory of propagation, interference and diffraction of light*. CUP Archive, 1999.

79. Lane, R. G., A. Glindemann, and J. C. Dainty. "Simulation of a Kolmogorov phase screen." *Waves in random media* 2, no. 3 (1992): 209-224.

80. Antonsen, Thomas M., and Dan Gordon. "Computational Accelerator Physics: Working Group Summary." *AIP CONFERENCE PROCEEDINGS*. IOP INSTITUTE OF PHYSICS PUBLISHING LTD, 2002

81. Richards, B., and E. Wolf. "Electromagnetic diffraction in optical systems. II. Structure of the image field in an aplanatic system." In *Proceedings of the Royal Society of London A: Mathematical, Physical and Engineering Sciences*, vol. 253, no. 1274, pp. 358-379. The Royal Society, 1959.

82. Liu, Ling, and Mikhail A. Vorontsov. "Phase-locking of tiled fiber array using SPGD feedback controller." In *Optics & Photonics 2005*, pp. 58950P-58950P. International Society for Optics and Photonics, 2005.

83. Sandalidis, Harilaos G., Theodoros A. Tsiftsis, and George K. Karagiannidis. "Optical wireless communications with heterodyne detection over turbulence channels with pointing errors." *Journal of Lightwave Technology* 27, no. 20 (2009): 4440-4445.

84. Ji, Xiaoling, and Baida Lü. "Turbulence-induced quality degradation of partially coherent beams." *Optics Communications* 251, no. 4 (2005): 231-236.